DEPARTMENT OF OCEANOGRAPHY
UNIVERSITY OF CAPE TOWN

THE MOZAMBIQUE CHANNEL EDDIES: CHARACTERISTICS AND MECHANISMS OF FORMATION

A Thesis in
Numerical Modelling of the Mesoscale Ocean Circulation

ISSUFO F. M. HALO

Thesis Presented for the Degree of
DOCTOR OF PHYLOSOPHY
in the Department of
Oceanography

UNIVERSITY OF CAPE TOWN

September 2012

The present work has been supervised* and collaborated by the following members:

*Supervisor 1:
Dr. Pierrick Penven
Laboratoire de Physique des Oceans - UBO, UMR6523, IFREMER, IRD, CNRS, Plouzané, France

*Supervisor 2:
Dr. Isabelle Ansorge
Department of Oceanography, University of Cape Town, 7700 Rondebosch, Cape Town, South Africa

Collaborators:
Description of the Regional Oceanography
Prof. Johann Lutjeharms†
Department of Oceanography, University of Cape Town, 7700 Rondebosch, Cape Town, South Africa

Hydrodynamic Modelling
Dr. Bjorn Backeberg
Department of Oceanography, University of Cape Town, 7700 Rondebosch, Cape Town, South Africa

Ecosystem Modelling
Dr. Olivier Amont
Institut de Recherche pour le Développement (IRD), UMR6523, CNRS, Plouzané, France

Ecosystem Modelling
Dr. Olivier Maury
Institut de Recherche pour le Développement (IRD), UR 109 Thetis, CRH, av. Jean Monnet, B.P. 171, 34203 Séte Cedex, France

*Signatures are on file in the Science Faculty.

† Deceased.

Abstract

An ocean model configuration has been designed for the South-West Indian Ocean (SWIM) to study the mesoscale eddy properties and the physical mechanisms of their formation in the Mozambique Channel. The model spans from 0 to 77.5°E, and 47.5°S to 3°S and runs at $\frac{1}{5^\circ}$ grid resolution. The evaluation of the results has shown a good agreement between the model simulation and observations. It reproduced well the mean-state of the main features of the Agulhas system: the pathway of the currents correlating closely to observation, as well as the mean volume transports. However SWIM overestimated the seasonal cycle of the transport in the narrows of the channel, the EKE and the RMS of SSH by 50% in the central Mozambique Channel. The model also has captured the presence of the main water masses of the region, while failing to reproduce accurately their spreading.

The model outputs and the satellite data have shown a number of cyclonic and anticyclonic eddies being generated within the Mozambique Channel. The eddies were identified using a newly designed eddy detection algorithm. The algorithm has shown that cyclonic eddies appeared to be more ubiquitous than the anticyclonic and had a single mode size-distribution. On the other hand, the anticyclonic eddies seemed to have a favorite site for their formation, and have shown a bi-modal size-distribution. Both the cyclones and the first mode of the anticyclones were centered around a typical scale of the first baroclinic Rossby radius of deformation for the South-West Indian Ocean region, suggesting that their origin be associated with the baroclinic instabilities of the flow. In contrast the second mode of the anticyclonic eddies were relatively larger, beyond the first baroclinic

Rossby radius of deformation, and appeared to be generated by barotropic instabilities. Their annual frequency is consistent with the in-situ observations derived from LOCO moorings at the narrows of the channel. The eddy detection algorithm has shown that these eddies are generated in the north and at the narrows of the channel, and propagate mostly southwestwards. They are deep reaching and interact with the Mozambican continental shelf. On the other hand, the first mode of the anticyclonic eddies are generated mostly in the eastern part of the central region of the channel. A number of cyclonic and anticyclonic eddies also have been generated in the south of Madagascar.

The eddy census have suggested that cyclonic eddies dominate over the anticyclones in the Mozambique Channel. However, despite their abundance the analysis of the eddy mean properties have shown that the anticyclonic eddies are generally larger, have a higher amplitude, are highly energetic and have a longer life-time than the cyclonic eddies, thus being regarded as the predominant features of the circulation. Comparisons with altimetry suggested that SWIM produced relatively larger eddies. Throughout the channel the eddies appeared to be larger in the north and smaller in the south, while their mean amplitude and annual frequencies were lower in the north and higher in the south. The energy budget has suggested that despite localized sites within the different subregions of the channel being dominated by baroclinic instability, the overall dominant eddy formation mechanism throughout the channel is the barotropic instability.

Declaration

The present work has been originally written by me, with the full support of my supervisors: Dr. Pierrick Penven and Dr. Isabelle Ansorge, at the Department of Oceanography, University of Cape Town (South-Africa). Important contributions on the approach used in this study are clearly acknowledged by referencing it within the text.

Publication in review based on the present work:

- Halo. I, B. Backeberg, P. Penven, I. Ansorge, C. Reason and J. E. Ullgren. (2012): Eddy Properties in the Mozambique Channel: A comparison between Observations and two Numerical Ocean Circulation Models. *Deep Sea Research II*, "Special issue".

Introduction

The global ocean is dominated by small scale circulation features such as filaments, fronts, meanders and mesoscale eddies (Robinson, 1983, Chelton et al., 2007). These mesoscale eddies (length scale $\sim$ 10-500 km, time scale $\sim$ months - year) are turbulent vortices, rotating about nearly vertical axes, and can extend throughout the water column (Robinson, 1983). They are very efficient in trapping in their cores passive tracers and transporting them over long distances (Provenzale, 1999, Cushman-Roisin and Beckers, 2009).

The ocean dynamics in the Mozambique Channel, and by extension in the South-West Indian Ocean, is characterized by a strong mesoscale activity dominated by anticyclonic eddies (De Ruijter et al., 2002, Ridderinkhof and De Ruijter, 2003, Schouten et al., 2003, De Ruijter et al., 2005). Studies suggest that these eddies play a role on several aspects:

For the climate, it has been demonstrated that at the Agulhas retroflection region these eddies modulate the timing and the frequency in which warm and salty Indian Ocean waters enters into the south Atlantic (Schouten et al., 2002b, Penven et al., 2006c, Biastoch et al., 2008b), mainly in the form of Agulhas Rings (Gordon, 1986, Reason et al., 2003). These inter-ocean exchange of properties (Gordon, 1986, De Ruijter et al., 1999) are thought (De Ruijter et al., 1999, Biastoch et al., 2008a) to play a decisive role on the strength of the global meridional overturning circulation, and consequent global climate of the Earth (Weijer et al., 1999, Biastoch et al., 2008b, Beal et al., 2011).

On the ecosystems context, some studies (Weimerskirch et al., 2004, Tew-Kai and Marsac, 2009, Omta et al., 2009) have shown that the Mozambique Channel eddies play also an important role for the biological properties, such as chlorophyll-a, nutrients and

marine living organisms for the whole food chain.

On the perspective of atmospheric dynamics, there is evidence that the Mozambique Channel eddies could intensify tropical cyclones in the region (Goni et al., 2009). However, there is no conclusive result in the matter, and thus it remains an open discussion.

The eddy activity in the Mozambique Channel is very complex. In addition there are few oceanographic datasets suitable to resolve satisfactorily the mesoscale dynamics of the region. Therefore, many oceanographic processes associated to their origin and dynamics are still unknown. For instance, during their study De Ruijter et al. (2002) did not find cyclonic eddies in the Mozambique Channel. Furthermore a detailed description of the eddy properties in this region is still incomplete. These bring a range of research questions that are addressed in this study:

Eddy characteristics

- Are there cyclonic eddies in the Mozambique Channel?
- Why is the flow in the Mozambique Channel dominated by anticyclonic eddies?
- What are their physical properties (both anticyclonic and cyclonic eddies)?
- How do the Mozambique Channel eddies vary their properties throughout the channel?

Eddy generation processes

- What eddy generation mechanisms are dominant at the different subregions of the Mozambique Channel?
- What role the eddy-mean flow interaction plays on the circulation in the Mozambique Channel?

With the recent increasing capability of computer power and availability of the ocean circulation models to resolve small scale processes (eddy permitting models), a good progress has been achieved in the studies of mesoscale eddies. Therefore to address the questions of this study we have built a realistic ocean model configuration for the South-West Indian Ocean, based in ROMS model.

The finding of this study brings additional knowledge that enhances the current understanding and description of the mesoscale ocean circulation in the Mozambique Channel.

This dissertation is written with the following structure: after the introduction, the literature review provides a general historical background of the oceanography of the Indian Ocean, and the circulation of the main currents in the South-West Indian Ocean

(Chapter-1). A special description of the mesoscale circulation in the Mozambique Channel is presented in Chapter-2. The key research questions and the aims of this study are also included in Chapter-2. The methodology in Chapter-3 gives a general description of the model and the datasets used to evaluate the model simulation. The evaluation of the model configuration, answering the first key question is presented in Chapter-4. The Chapter-5 describes the design and evaluation of an automatic eddy detection algorithm used to identify and track the eddies in the Mozambique Channel. The results about the eddy properties addressing the second, third, fourth and fifth key questions are presented in Chapter-6. The results about the formation mechanisms and the role of the eddy-mean flow interaction addressing the sixth and seventh key questions are presented in Chapter-7. The conclusion of the thesis and a set of recommendations are presented in Chapter-8, which also conclude the present dissertation. Some auxiliar information can be found in the appendix section.

Table of Contents

List of Figures

List of Tables

List of Symbols

ρ - Sea-water density

ρ_o - Sea-water density of reference

ρ_{air} - Density of atmospheric air

α - Thermal expansion coefficient

∇ - Gradient operator

Δ_x, Δ_y - Horizontal grid resolution

ϕ - Dynamic Pressure

θ - Latitude

$\vec{\Omega}$ - Earth rotation frequency

Ω - Transformed vertical velocity

f - Coriolis parameter

γ_1 - Coefficient of linear bottom friction

γ_2 - Coefficient of quadratic bottom friction

σ - Terrain following vertical coordinate

θ_b, θ_s - s-coordinate stretching parameters

c_D - Non-dimensional wind-drag coefficient

g - Acceleration due to gravity

E_r - Evaporation rate

h - Water depth

H - Total ocean depth

r - Topographic slope parameter

K_v - Coefficient of vertical eddy viscosity

K_T, K_S - Coefficient of vertical eddy diffusivity

F_u, F_v, F_T, F_S - Possible forcings terms

D_u, D_v, D_T, D_S - Dissipative terms

T - Temperature

t - Time

τ_s^x, τ_s^y - Surface wind stress components

τ_b^x, τ_b^y - Bottom stress components

S - Salinity

P_r - Precipitation rate

P - Total Pressure

P_o - Oceanic Pressure

P_a - Atmospheric Pressure

Q_{net} - Net heat flux

ξ - Vorticity

S_n, S_s - Normal and shear components of strain tensor

W - Okubo-Weiss parameter

X - Generalized distance in a non-dimensional property space

R - Earth radius

R_0 - Characteristic eddy radius

$\bar{L}$ - Mean Eddy diameter

ζ - Sea surface height

$\bar{P}$ - Mean potential energy

P' - Turbulent potential energy

$\bar{K}$ - Mean kinetic energy

K' - Turbulent kinetic energy

$\vec{v}$ - Three dimensional vector velocity

u, v, w - Three dimensional velocity components

x, y, z - Cartesian directions

List of Acronyms

AABW	- Antartic Bottom Water
AAIW	- Antartic Intermediate Water
AAMW	- Australasian Mediterranea Water
ACSEX	- Agulhas Current Source Experiment
AC	- Agulhas Current
ACC	- Antartic Circumpolar Current
ADCP	- Acoustic Doppler Current Profiler
ARC	- Agulhas Return Current
ASLOW	- Arabian Sea Low Oxygen Water
ASW	- Arabian Sea Water
AVISO	- Archiving Validation Interpretation of Satellite Oceanographic data
BBW	- Bay Bengal Water
CARS09	- CSIRO Atlas of Regional Seas 2009
CDW	- Circumpolar Deep Water

CNES - National Center for Spatial Studies

COADS - Comprehensive Ocean Atmosphere Dataset

CTD - Conductivity Temperature Depth

EACC - East Africa Coastal Current

EMC - East Madagascar Current

EKE - Eddy Kinetic Energy

GEBCO1 - Global Earth Bathymetric Chart of the Oceans (1-minute resolution)

ICW - Indian Central Water

IDW - Indian Deep Water

IEW - Indian Equatorial Water

IHO - International Hydrographic Organization

IIOE - International Indian Ocean Expedition

ITCZ - Intertropical Convergence Zone

ITF - Indonesian Through-Flow

LOCO - Long-term Ocean Climate Observation

MDT - Mean Dynamic Topography

MEKE - Mean Eddy Kinetic Energy

MZC - Mozambique Channel

MZTF - Mozambique Through-Flow

NADW - North Atlantic Deep Water

NEMC - North East Madagascar Current

NOAA - National Oceanic and Atmospheric Administration

OBCs - Open Boundary Conditions

OGCM - Ocean General Circulation Model

PGW - Persian Gulf Water

QG - Quasi-Geostrophic

ROMS - Regional Ocean Modelling Systems

RSW - Red Sea Water

RMS - Root Mean Square

SAF - Subantartic Front

SAMW - Subantartic Mode Water

SEC - South Equatorial Current

SEISAMW - South East Indian Subantartic Mode Water

SEMC - South East Madagascar Current

SICC - South Indian Counter-current

SSH - Sea Surface Height

SSH - Sea Surface Salinity

SST - Sea Surface Temperature

STSW - SubTropical Surface Water

SWIM - South West Indian Ocean Model

TSW - Tropical Surface Water

WOA05 - World Ocean Atlas 2005

WOCE - World Ocean Circulation Experiment

Acknowledgments

There are many people that I would like to thank them in writing, but if I did so, I am sure that the world would not have enough scrolls. Nevertheless at least I can start in a chronological order by saying: Thanks to Dr. Olivier Maury, for his initiative of building an end-2-end ecosystem modelling for the South-West Indian Ocean, and for inviting me to work on the package of hydrodynamic ocean modelling, that gave start to this PhD project.

Secondly, I would like to thank my supervisors: Dr. Pierrick Penven and Dr. Isabelle Ansorge, that kindly worked with me to achieve the goals of this study. For Dr Penven, my remarks are specially regarded to his outstanding input, starting from the writing of this PhD Thesis proposal, application of the IRD-DSF research grant, his time and good will for teaching, reading and discussion of this manuscript during the different stages of this project. His tireless contribution has no scale.

For Dr Ansorge, my remarks are also very high. Thanks for her support in many ways: scientific discussion and the English writing style of the manuscript, that are very difficult for a non-english speaker. Thanks also for my collaborators: Prof. Johan Lutjeharms†, Dr. Bjorn Backeberg, Dr. Olivier Amont and Dr. Olivier Maury for their contribution. Many thanks to Prof. Frank Shillington (former head of Oceanography Department), and Prof. Chris Reason (current head of Oceanography Department) for their supportive leadership. I will never forget also the IRD-DSF (France), NRF (South-Africa), MARE-BASICS (South-Africa) and Nansen Tutu Center (Norway and South-Africa) research grants, that made possible to start and finish this study with sufficient financial support. Important to thank also the financial administrators, Mr. Farid Saadoun (Montpellier, France), Ms. Francoise Cudenec and Dr. Claude Roy (Brest, France) and Mr. Emlyn Balarin (Cape-Town, South-Africa) for their assistance. Also remark goes to the Ifremer

Research Center in Brest, France, for hosting me during my stay in France, and also making available their facilities to setup the SWIM model configuration used in this study by using their high performance computer (Caparmor). The stay in Brest was great: Thanks to Dr. Pierrick Penven, Dr. Eva Bucciarelli, Dr. Dominique Dagorne, Mr. Gerard Hennecart and his family, Luc Trackart and his family for accommodating me comfortably. Thanks also to Dr. Jenny Vetch, Dr. Natali Burls, Dr. Sebastian Swart, Ms. Yonss José, Mr. Dewi Lebars, Dr. Alberto Mavume, Dr. Eric Machu, Dr. Olivier Amont, Dr. Vamara Koné and Dr. Xavier Cape, for their outstanding company in Brest. My colleagues at UBO, LPO, Ifremer, UCT, UEM, CSIR and for all those that I may have forgotten, I send to them a big thanks. At last, but by no means least, is my wife Olanca Ntondo and my relatives for their emotional support, and bearing with me during all these years that I have been engaged in this project.

[†]Deceased

Dedication

I specially dedicate the present work to my parents:
Father, Mário Halo† and my mother, Chaurina Ferrão†.

†Deceased

CHAPTER 1

Indian Ocean: historical background

1.1 Geographical setting in the global ocean

According to the International Hydrographic Organization (IHO), the Indian Ocean is the smallest ocean in the world, after the Pacific and the Atlantic (IHO, 1953, Domopoulos et al., 2003). For a long time, its geographical boundaries were considered as follows: to the North, bounded by the southern limits of the Arabian Seas, Laccadive Seas, the Bay of Bengal, the East Indian Arquipelago and the Great Australian Bight (IHO, 1953). To the South, it was bounded by the Antartic continent, making a north-south distance of about 9600 km (Tomczak and Godfrey, 1994, Domopoulos et al., 2003). To the West, the Indian Ocean is bounded by the Atlantic Ocean, lying from the Cape Agulhas, South-Africa, along the meridian line of 20°E, South to the Antartic continent. To the East, is bounded by the Pacific Ocean, lying from the south-east Cape of the southern point of Tasmania, Australia, along the meridian 146. 55"°E, South to Antartic continent (IHO, 1953) (see Figure 1.1), making an east-west distance of about 7800 km (Tomczak and Godfrey, 1994). The surface area was estimated in 74.1×10^6 km^2, with a mean depth of about 3890 m, and a volume of about 28.6 $\times10^7$ km^3 (Domopoulos et al., 2003). However, the most recent criteria of delimitation of the world's oceans, termed the *"Spring Deci-*

sion" (http://www.cia.gov/cia/publications/factbook/geosoo.htlm), in year 2000, have culminated with the inclusion of the Southern Ocean among world's oceans, and the integration of the northern seas, namely, Red Sea, Arabian Seas and the Gulf Persian Seas, as integrated parts of the Indian Ocean. Therefore the northern and southern limits of the Indian Ocean have changed to a new geographical coordinates: 60°S - 30°N, and 20°E - 147°E. Thus, the Indian Ocean has now a surface area of about $\sim 48.1\times10^6$ km^2, and a volume of about 18.7×10^6 km^3.

Figure 1.1. Geographic map of the Indian Ocean.
http://earth-info.nga.mil/GandG/coordsys/onlinedatum/IndianOceanMap.html

The summary presented in this chapter, is mostly based on the textbook by Tomczak and Godfrey (1994), which is essentially a review of the results published by different authors.

1.2 Hydrographic expeditions in the Indian Ocean

The Indian Ocean is situated far away from the world's nations leading scientific oceanographic research (e.g. USA, and some European countries), and is surrounded by economically poors countries. Therefore, it was the latest being exploited, and remains less known when compared to the Pacific and the Atlantic (Tomczak and Godfrey, 1994, Domopoulos et al., 2003). Few oceanographic research vessels have entered in the Indian Ocean before the 1960's. Among such, are to consider: The Challenger 1873 - 1876, and Valdivia Expeditions 1888 - 1889; John Murray Expedition 1930; Swedish Deep Sea Expedition 1947 - 1948; and Galathea 1950 - 1952.

An important phase in history for the Indian Ocean hydrographic research has emerged with the launch of the International Indian Ocean Expedition (IIOE), during 1962 - 1965. Oceanographic data collected in this expedition allowed K. Wyrtki to compile the Atlas of the Indian Ocean, and it was regarded as the main reference textbook for Indian Ocean research (Wyrtki, 1971). Though the IIOE included surface and deep layer observations, the studies of the dynamics were essentially based on the analysis of ship drift data that did not reach below the surface layer (Tomczak and Godfrey, 1994). Therefore many oceanic processes were not investigated. After the IIOE, important oceanographic research programs have also followed: The Indian Ocean Experiment (INDEX) campaign during 1976 - 1979, and the World Ocean Circulation Experiment (WOCE), 1990 - 1998. During the INDEX campaign, long term current meter moorings were deployed for the first time in the Indian Ocean. Today several instruments can be found scattered in this ocean, most of these under WOCE's approach. WOCE is regarded as the largest Internationally coordinated oceanographic program ever conducted (Figure 1.2). WOCE provides a global data collection including ADCP, CTD, XBT, current meters, profiling floats, sea-level, sea surface T/S, subsurface floats, surface drifters, hydrography, nutrients and tracers. From WOCE the Atlas of the Indian Ocean water masses and properties distribution has been compiled (Antonov et al., 1988, Boyer et al., 1988, Levitus et al., 1994, Levitus and Boyer, 1994b, Conkright et al., 2002). WOCE data have provided a better insight for many oceanographic processes in the Indian Ocean, which can now be satisfactory characterized.

A brief description of the main water mass properties in the south-west Indian Ocean (region of interest in the present study) is presented in the next section.

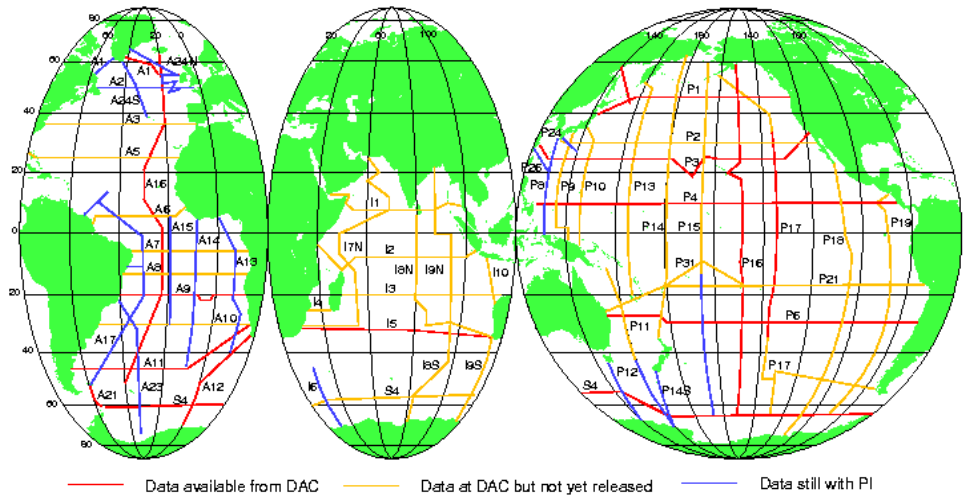

Figure 1.2. Global schematic of the hydrographic transects, and reference stations (inserted symbols), occupied during the WOCE surveys. Note that the Indian Ocean (middle panel), was the least surveyed, when compared to other oceans. [Courtesy: WOCE].

1.3 Water Masses of the South-West Indian Ocean

In our description of the south-west Indian Ocean water masses, we pay more attention to the water masses that have been reported by Beal et al. (2006), as they dominate our region of interest, namely, the Mozambique Channel, and by extension, the greater Agulhas Current system. A representation of these water masses in terms of their site of formation, and the main route of propagation towards the greater Agulhas Current system is that portrayed in Figure 1.3 (Beal et al., 2006).

Since the oceanic water masses conserve their properties for a long time, they can be used to trace the pathway of the ocean currents (Emery, 2001). It is a common practice among the oceanographers to classify the water masses of the world oceans according to their physical and biological properties, such as, temperature, salinity, nutrients, dissolved oxygen, etc. By their vertical distribution throughout the water column they can be classified as: abyssal or bottom, deep, intermediate, and surface waters (Defant, 1961).

A temperature versus salinity diagram used to identify the main water masses in the Indian Ocean Basin, as well as the main currents responsible to their transport is presented in Figure 1.4.

In regards to its relatively small size, the Indian Ocean has a complex upper water

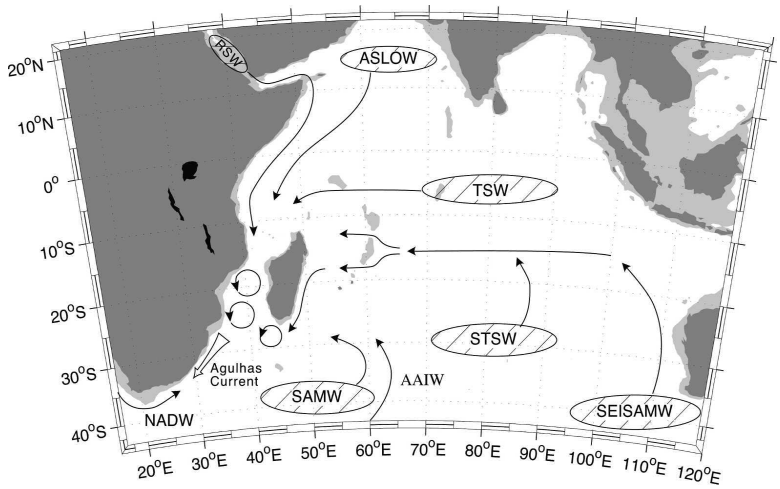

(a) Indian Ocean water masses

Figure 1.3. Schematic representation of the main water masses of the Indian Ocean and their path of propagation towards the Greater Agulhas Current System. The encycled water masses indicates their local formation, while the others, are imported from the other oceanic basins. For the meaning of the acronyms, see the text [After: Beal et al. (2006)].

mass structure. This complexity is mostly related to factors such as: its enclosure by the Asian continent at the subtropics, the regime of the monsoonal winds which control the dynamics of the currents on the upper layers in the northern Indian Ocean, and the unbalanced rates of precipitation between the eastern and western Indian Ocean (Wyrtki, 1971, Tomczak and Godfrey, 1994, Schott and McCreary, 2001, Schott et al., 2009).

1.3.1 Upper waters

At the surface and sub-surface layers (0 - 500 m depth), the south-west Indian Ocean is mainly occupied by tropical and subtropical water masses. The tropical surface water (TSW) is originated close to the equatorial band, at the central Indian Basin. Its formation is a result of excessive precipitation over evaporation in the tropics (Wyrtki, 1971, Toole and Warren, 1993), and the influence of the low salinity waters of the Indonesian Throughflow, also refered as the Australasian Mediterranean Sea Waters (AAMW) (Tomczak and Godfrey, 1994, Gordon et al., 1997). Characterization of the TSW based on neutral density layer criteria (Jackett and MacDougall, 1997), suggests that this water mass is characterized by a salinity values inferior to 35.5 and a neutral density γ below 25.5 kg.m^{-3} (Beal et al., 2006). Its specific values of salinity and temperature were found to range between 34.91 and 35.31, and between 24.7°C and 26.3°C respectively (Donohue

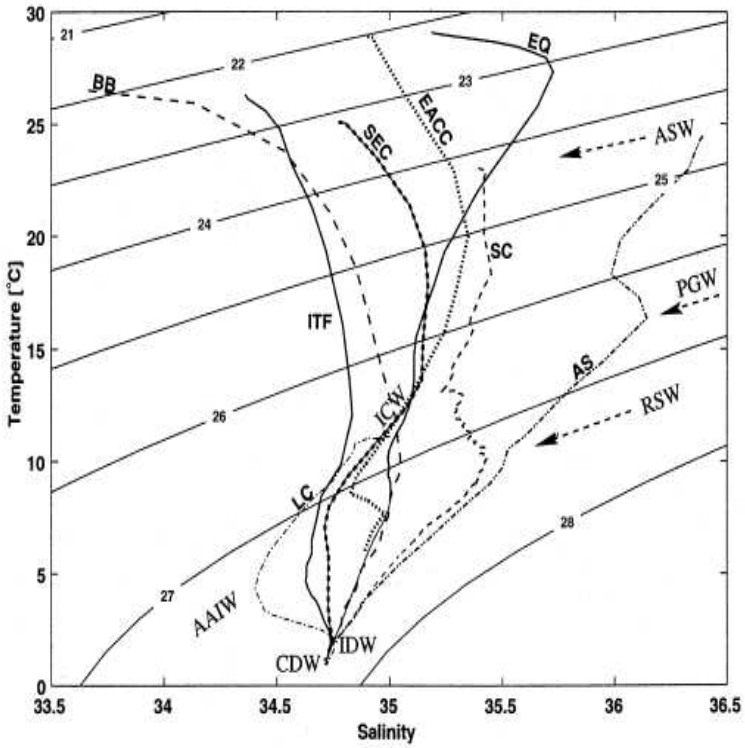

(a) Indian Ocean water mass properties

Figure 1.4. Temperature-Salinity diagram of Indian Ocean water masses from Levitus and Boyer (1994a,b). The climatology are for: The Bay of Bengal (BB), Arabian Seas (AS), equatorial region of western basin (EQ), South Equatorial Current (SEC), western exit of the Indonesian Throughflow (ITF or AAMW), and Leeuwin Current (LC). The core water masses indicated are Circumpolar Deep Water (CDW), Indian Deep Water (IDW), Antarctic Intermediate Water (AAIW), Indian Central Water (ICW), Red Sea Water (RSW), Persian Gulf Water (PGW), and Arabian Sea Water (ASW). The Somali Current (SC) curve is from August 1993 measurements in northern upwelling wedge. The Profiles are for respective winter seasons in each hemisphere [After: Schott and McCreary (2001)].

and Toole, 2003). Some studies (Swallow et al., 1988, Schott et al., 1988), suggest that the TSW enters in the subtropics via the branches of the South Equatorial Current (SEC), propagating along the east coast of Madagascar, and also along the east coast of Africa main land (detailed description of the branches of the SEC is presented later). The main route taken by the TSW during its southward propagation is through the Mozambique Channel (Figure 1.3) (Beal et al., 2006, Swallow et al., 1988).

At the sub-surface, or thermocline layers (200-500 m depth), the flow is mainly dominated by the subtropical surface water (STSW) and the AAMW. The STSW is formed within the subtropical gyre of the south Indian Ocean, to the east of 90°E (Wyrtki, 1971),

and between latitudes 25°S and 35°S (Tomczak and Godfrey, 1994, DiMarco et al., 2002). Its formation is attributed to the excess of evaporation over precipitation (Wyrtki, 1971). The water mass is characterized by a salinity values greater than 35.5 and a neutral density that ranges between γ=25.5 kg.m^{-3} and 26.4 kg.m^{-3} (Beal et al., 2006). This water mass is transported westwards mostly by the SEC, and enters into the greater Agulhas Current system by the flow of the southern extension of the East Madagascar Current (Beal et al., 2006). According to Donohue and Toole (2003), a distinction between TSW and STSW is made by a strong boundary between them, formed at about 28°S, where it generates a sharp gradient of temperature and salinity. The AAMW is originated in the tropical regions, derived from the Pacific Central Waters. This water mass enters on Indonesian Throughflow (ITF), Indian Ocean between Timor and the islands east of Bali, and forms one of the strongest thermocline front in the world (Tomczak and Godfrey, 1994). It is characterized by temperature values between 8°C and 23°C, and salinity between 34.4 and 35.0 (Emery, 2001).

Another subsurface water mass observed in our region of study is the Subantartic Mode Water (SAMW). This water mass is formed at the subtropical convergence front, mainly between 46°E and 62°E (Fine, 1993), due to the winter cooling and deep convection to the south of the front (McCarthy, 1977). This water mass subducts into the thermocline and propagates northwards into the subtropical gyre (Toole and Warren, 1993). The core of SAMW is located at about 500 m depth, and holds an oxygen maximum (DiMarco et al., 2002). To the north of about 28°S, the potential temperature and density of SAMW varies from 13°C and γ = 26.65 kg.m^{-3} at about 28°S, to values close to 11°C and γ = 26.8 kg.m^{-3} at 20°S (Donohue and Toole, 2003). The zonal gradient of temperature, salinity, and density along the southern Indian Ocean Basin, and the entrainment of the SAMW in the subtropical gyre results in a subtropical distribution of this water, with highest values of oxygen found to the southeast Indian Ocean (Donohue and Toole, 2003). This extension is also termed South-East Indian Subantartic Mode Water (SEISAMW) and is characterized by a concentration of oxygen above 4.9 ml.l^{-1}, and a neutral density γ= 26.8 kg.m^{-3} (Wyrtki, 1971). This water mass enters into our area of interest through the westward branch of the subtropical gyre (Donohue and Toole, 2003). Similar to SAMW is the Indian Central Waters (ICW). The ICW is also originated in the subtropics, and is characterized by values of temperature ranging between 8°C and 25°C, and salinity between 34.6 and 35.8 (Emery, 2001). Beal et al. (2006), has observed this water mass at a depth below the thermocline $\sim$ 300 m deep.

1.3.2 Intermediate waters

At the intermediate layers, or below thermocline waters (500 - 1500 m depth), the west Indian Ocean is mostly occupied by the Antartic Intermediate Waters (AAIW), in the southern hemisphere, and the Red Sea Waters (RSW) and the Arabian Sea Low Oxygen Waters (ASLOW) (Beal et al., 2006), in the northern hemisphere (Wyrtki, 1971). The AAIW is thought to be formed in the southeastern Pacific, and enters into the Atlantic Ocean through the Drake Passage, and continue flowing eastward along the Subantartic front (McCarthy, 1977). Once in the Indian Ocean, at about 60°E, this water mass flows northwards into the subtropical gyre (Fine, 1993, Beal et al., 2006). However it does not cross the 10°S latitude, because its propagation is blocked by the equatorial current systems (Tomczak and Godfrey, 1994). The fresher AAIW is characterized by a minimum in salinity ranging between 33.8 and 34.6, and temperature between 2°C and 10°C (Emery, 2001). On the other hand, the RSW is very saline. This water mass is formed in the Red Sea Basin (Figure 1.3), as a result of excessive evaporation over precipitation, which leads to a sinking of surface waters in the Gulf of Aden (Wyrtki, 1971, Tomczak and Godfrey, 1994). This process induces a local formation of maximum salinity values, and minimum oxygen concentration (DiMarco et al., 2002). The RSW is characterized by a potential temperature of about 22°C, salinity of about 39, and a density of 27.25 kg.m^{-3} (Tomczak and Godfrey, 1994). It flows southwards, concentrated along the African coast, below the Zanzibar Current (Wyrtki, 1971, Beal et al., 2000, Donohue and Toole, 2003), and pass through the Mozambique Channel and reaches the Agulhas Current (Beal et al., 2000, Donohue and Toole, 2003).

The ASLOW is originated in the Arabian Basin (Figure 1.3). This water mass has been observed at about 1200 m depth (Beal et al., 2006), and is characterized by high values of salinity, a relatively lighter neutral density $\gamma = 25.5$ kg.m^{-3}, and low oxygen, less than 3.8 ml.l^{-1}. Such minimum oxygen concentrations are due to the high consumption rates associated to the seasonal high productivity (Olson et al., 1992). The ASLOW propagates southwards, concentrated along the western boundary of the Indian Ocean (Figure 1.3). During its journey it also enters in the Mozambique Channel. The ASLOW is a result of a mixing process between the Arabian Sea Water (ASW) and Bengal Bay Water (BBW). The ASW is characterized by values of temperature ranging between 24°C and 30°C, and salinity between 35.5 psu and 36.8 psu, while the BBW is characterized by temperature ranging between 25°C and 29°C, and salinity between 28 and 35.0 (Emery, 2001).

1.3.3 Deep and Abyssal waters

The deep layer of the Indian Ocean is filled by the Indian Deep Water (IDW). To the north of the equator this water mass is usually termed as the NIDW, and in the south as the SIDW. To the north of 45°S this water mass ranges between 1500 and 3800 m depth, while to the south of this latitude it shallows to about 500 m depth (Tomczak and Godfrey, 1994). The IDW is characterized by a salinity greater than 34.8 in the western side of the Indian Ocean, and by 34.75 in its eastern side (Tomczak and Godfrey, 1994). According to these authors, this water mass is formed in the Atlantic Ocean as a remaining part of the North Atlantic Deep Water that did not convert into the intermediate waters within the Atlantic sector. The IDW is carried eastwards by the Antartic Circumpolar Current (ACC). In the South Indian Ocean, it propagates northwards, concentrated along the western boundary. On reaching the northern Indian Ocean, at Somali Basin, this water mass flows eastwards, and upwells in the Arabian Seas and in the Bay of Bengal (Wyrtki, 1971). The deep circulation is below the permanent thermocline and is influenced by the inflow of the RSW and Persian Gulf Waters (PGW).

To the bottom, below 3800 m, the Indian Ocean is dominated by the Antartic Bottom Water (AABW), also called Circumpolar Deep Waters (CDW). This water mass is characterized by a range of potential temperature between 1°C and 2°C, and salinity between 34.62 and 34.73 (Emery, 2001). It is formed in the Southern Ocean, and enters into the South-West Indian Ocean via the Mozambique and Madagascar Basins, through the deep fractures of the South-West Indian Ocean Ridge, near 30°S, and 56°E - 59°E (Tomczak and Godfrey, 1994). In the southeast, this water mass enters in the Indian Ocean through the South Australasian Bight, around 50°S and 124°E (Tomczak and Godfrey, 1994). The flow in the Mozambique Basin is blocked within the Mozambique Channel by the Davie Ridge. In the Madagascar Basin, the water propagates further north and forms a western boundary current, along the continental slope of the east coast of Madagascar. In the south of Australia, it flows along the southern and western slope of Australia, and further north it escapes to the central Indian Ocean, and propagates along the eastern slope of the Ninetyeast Ridge (Tomczak and Godfrey, 1994). After crossing through the fractures of the Ridge, the water flows westwards and eventually reaches the northeast coast of Africa. Through the slope of the African continent it gradually upwells to form the North Indian Deep Waters.

A summary of the water masses characteristics in the South-West Indian Ocean is presented in Table 1.1. For a detailed inventory of the water mass characteristics of the Indian Ocean see You (1997).

	Temp [°C]	**Salinity**	**Density [kg.m^{-3}]**	**Depth [m]**
TSW	24 - 28	34.91 - 35.31	25.50 - 26.50	0 - 200
STSW	8 - 25	35.60 - 35.80	25.50 - 26.40	200 - 500
AAMW	8 - 23	34.40 - 35.00	26.50 - 26.70	300 - 450
RSW	7 - 22	34.75 - 39.00	27.25 - 27.70	500 - 1500
AAIW	2 - 10	33.80 - 34.60	27.20 - 27.40	800 - 1200
IDW	4 - 7	34.75 - 34.80	27.10 - 27.30	1500 - 3800
AABW	1 - 2	34.62 - 34.73	27.50 - 27.70	3800 - bottom

Table 1.1. Characteristics of the main water masses in the southwest Indian Ocean, based on temperature, salinity, density and typical depth. For the acronyms of the water masses, see the text.

1.4 Large-scale flow in the South-West Indian Ocean

The oceanic wind-driven circulation, in the South-West Indian Ocean, to the south of 10°S, is mainly dominated by the waters of the westward flowing South Equatorial Current (Wyrtki, 1971, Tomczak and Godfrey, 1994, Stramma and Lutjeharms, 1997). The SEC receives its tributary mostly from the Subtropical gyre of the South Indian Ocean, and from the Indonesian Throughflow (Quadfazel and Swallow, 1996, Gordon and McClean, 1999, Schott et al., 2009) (Figure 1.5). In the eastern Indian Ocean (East of $\sim$ 105°E), the SEC has been observed in a broad band between 7°S and 15°S (Quadfazel and Swallow, 1996). In the West Indian Ocean, this current has been observed between 10°S and 20°S. Hydrographic measurements suggest that the volume transport of the SEC, measured around Mascarene Plateau, between 10°S and 16°S, is about 50 Sv - 55 Sv (New et al., 2007). This estimates is consistent with former studies (Swallow et al., 1988, Schott and McCreary, 2001). On reaching the east coast of Madagascar, between 17°S and 20°S, the SEC circulates around the Island of Madagascar in two opposite branches, as the Northern and Southern extension of the East Madagascar Current (Schott et al., 1988, Chapman et al., 2003, DiMarco et al., 2002) (Figure 1.5). The northward extension (NEMC) carries about 30 Sv, while the southward (SEMC), carries about 20 Sv (Swallow et al., 1988, Schott et al., 1988). The former turns around the northern tip of Madagascar, Cape-Amber, then flows westward towards the African continent. This current has about 200 km in width, is about 1100 m deep, and has a propagation speed of about 0.5 m s^{-1} (Schott et al., 1988). On reaching the African coast at about 11°S, the flow splits also in two branches (Figure 1.5). The northward branch forms the East African Coastal Current (EACC), along the Tanzanian coastal zone (Schott et al., 1988), while the southward branch flows through the Mozambique Channel, as formerly believed by the Mozambique Current (Saëtre and da Silva, 1984, Tomczak and Godfrey, 1994, Schott and McCreary, 2001). However, recent studies suggest that the flow through the Mozambique Channel is in form of mesoscale eddies (De Ruijter et al., 2002, Ridderinkhof and De Ruijter, 2003, Schouten et al., 2003) (a detailed description of the flow field throughout the channel is given later).

The branch of the southward SEMC along the east coast of Madagascar, is described as a small western boundary current (Schott et al., 1988), with about 120 km in width, 650 km length (Nauw et al., 2008), 1100 m deep (Siedler et al., 2009), and has a propagation speed of about 110 cm s^{-1}. At the southern tip of Madagascar, the SEMC separates

from the continental shelf, and undergoes through a very complex regime. Lack of in-situ data in this region made quite difficult to describe the fate of the Current, after the flow has passed the Cape Saint-Marie. Lutjeharms et al. (1981), was the first to suggest that the Current retroflects, to flow eastwards as an East Madagascar Return Current. But others (Quartly and Srokosz, 2002, DiMarco et al., 2002), refuted such hypothesis. (see also DiMarco et al. (2002), for a more detailed description of the suggested hypothesis). A study based on in-situ data from a hydrographic cruise (ACSEX II, (De Ruijter et al., 2004)) in 2001, dedicated especially to investigated the sources of the Agulhas Current, suggested that the flow of the SEMC, after passing the Cape Saint-Marie, establish an intermittent link with the Agulhas Current (AC). These authors suggest that such a link is modulated by mesoscale eddies and dipolar vortex which are generated locally, and drift in a southwest direction.

A recent work by Siedler et al. (2009) reconciles the different hypothesis presented in this matter. The work seems to be more conclusive: Based on satellite remote sensed data and a high resolution nested model, they infer that the SEMC holds two different modes, which switches from one regime to the other. The two modes depend of the intensity of the SEMC. In one mode the connection between the SEMC and the AC is a straight forward link, when the flow of the SEMC is mostly westwards. Whereas on the second mode, the SEMC retroflects and moves eastwards, when the flow of the SEMC is mainly southwestwards.

At the southern mouth of the Mozambique Channel, the outflow from both the channel and the south of Madagascar merges and propagates southwestwards to feed the poleward flowing Agulhas Current at the southeastern coast of South-Africa (Lutjeharms, 2006). The Agulhas Current represents the westernmost limb of the subtropical Indian Ocean wind driven gyre (Stramma and Lutjeharms, 1997). The current reaches its southwesternmost limits at the southwestern tip of the Agulhas Bank, South-Africa. The Agulhas Current retroflects there and its waters propagate partially to the South-East Atlantic (Gordon, 1986). However, the majority of the Agulhas waters flows eastwards (Lutjeharms and Ansorge, 2001), as the Agulhas Return Current, between 35°S and 40°S. Thus, the Agulhas Return Current represents the southernmost limb of the subtropical wind driven gyre of the South Indian Ocean. The region to the south of Madagascar is also inferred as being a place where the Subtropical Indian Ocean Countercurrent (SICC) is formed (Siedler et al., 2006, Palastanga et al., 2007). This recently discovered current (Siedler et al., 2006, Palastanga et al., 2007) propagates predominantly eastwards in

opposite direction to the flow of the SEC.

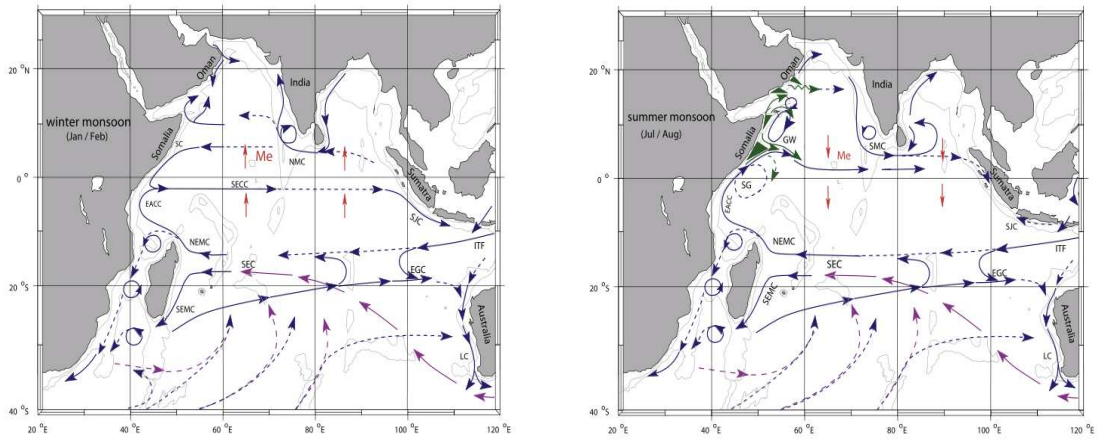

(a) Winter Monsoon currents (b) Summer Monsoon currents

Figure 1.5. Schematic diagram of the large scale surface circulation of the Indian Ocean. The left panel (a) portrays the currents during the summer monsoon, and the right panel (b) for the winter monsoon. The inserted acronyms indicates the main currents [After: Schott et al. (2009)].

1.4.1 Features of the greater Agulhas Current System, and its global scale importance

What may be considered to be the greater Agulhas Current system (Lutjeharms, 2006) extends from south of Africa to equatorward of Madagascar (Figure 1.6). It has been shown that the greater Agulhas Current System plays a key role in the global thermohaline circulation (Gordon, 1986) and a possibly decisive role in the Meridional Overturning Circulation of the Atlantic Ocean (Biastoch et al., 2008a, 2009, Beal et al., 2011). The system encompasses the following oceanic features: The branches of the South Equatorial Current, flowing southwards and northwards along the east coast of Madagascar, forming the the SEMC and NEMC respectively, as already discussed, the southward propagating flow through the Mozambique Channel, the Agulhas Current proper, the Agulhas Retroflection, and the Agulhas Return Current (Lutjeharms, 2006).

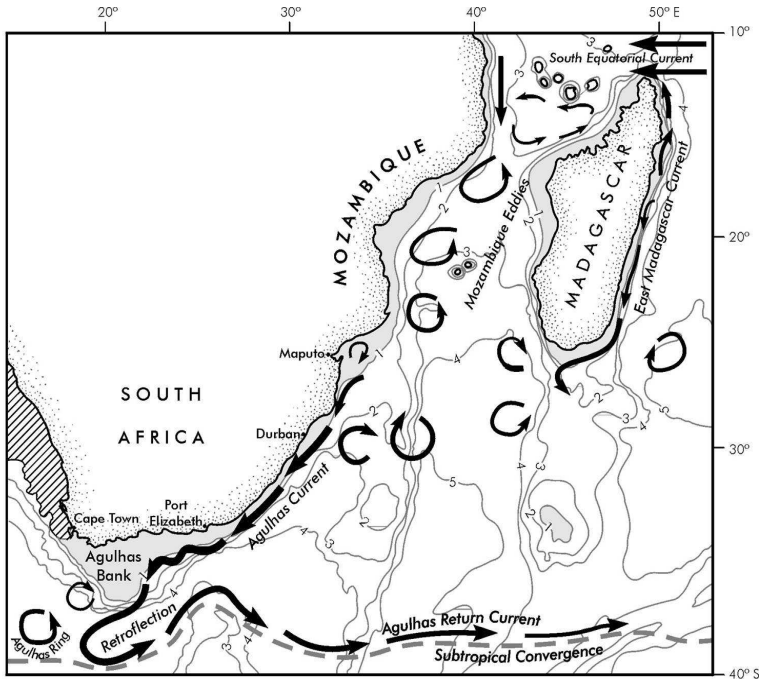

(a) The greater Agulhas Current system

Figure 1.6. Schematic diagram of the ocean dynamics in the greater Agulhas Current System. The curvilinear features portrays mesoscale eddies, and arrows the ocean currents. See the insert labels for their specification. The bathymetric contours are expressed in km [After: Lutjeharms (2006)].

1.4.1.1 The Agulhas Current

The main circulation feature on the greater Agulhas system is the poleward flowing the Agulhas Current. To-date the actual point where this current is formed is not yet known. However, Lutjeharms (2006), suggests that the current is formed somewhere to the north of Durban, east coast of South-Africa. The current is regarded as the strongest western boundary current of the southern hemisphere (Biastoch et al., 2008a). Its characteristics reveals that the Current is narrow, with a width of about 90 km, measured in-situ at 32°S (Casal et al., 2009). It reaches about 2500 m deep (Donohue and Toole, 2003), flowing closely attached to the steep slope of the continental shelf (De Ruijter et al., 1999). According to De Ruijter et al. (1999), the steep slope of the shelf provides the northern extension of the current a stable regime. However, between the cities of Durban and Richards Bay (Natal Bight), southeast coast of South-Africa, the Agulhas Current occasionally overshoots seawards (Lutjeharms, 2006). This process occurs due to the generation of an intermittent cyclonic meander at the inshore edge of the current, termed

the Natal Pulse (Lutjeharms and Roberts, 1988a). Natal Pulses have been observed to grow as they move downstream with the current, at a propagation speed of about 20 km per day (van Leeuwen et al., 2000). They have a mean diameter of about 200 km, extending throughout the water column of the Agulhas Current (Lutjeharms et al., 2001). To the south of Port Elizabeth, along the south coast of South-Africa, the continental shelf is very different from that to the north, due to the presence of the Agulhas Bank (Figure 1.6). The shallow bathymetry of the bank induces a more unstable regime on the Agulhas Current. Therefore a meandering behaviour strongly characterizes the flow field of the current in this region (De Ruijter et al., 1999). Hydrographic measurements taken along the path of the Agulhas Current (Gründlingh, 1980, Gordon, 1986), suggest that the main core of the Agulhas Current has surface temperatures ranging from 22°C to 28°C, salinity of about 35.4 psu, and a propagation speed exceeding 2 m s^{-1}. Estimated volume transport is around 70 Sv: Gründlingh (1980) suggested about 72 Sv, Beal and Bryden (1999), about 69.7 ±4.3 Sv, and Donohue and Toole (2003) suggested 76 Sv. These measurements were made throughout the water column, including the northward flowing, Agulhas Undercurrent. At the south-westernmost point of the Agulhas Bank, the Agulhas Current separates from the continental shelf and loses the bathymetric control (De Ruijter et al., 1999). The current rotates on itself in a large revolving loop known as the Agulhas Retroflection (Figure 1.6).

1.4.1.2 The Agulhas Retroflection

The retroflection of the Agulhas Current is a regular feature of the system, that occurs between 16°E and 20°E (Lutjeharms and van Ballegooyen, 1988b). The retroflection loop has an average diameter of about 340 ±70 km (Lutjeharms, 2006). From the retroflection, a series of rings, eddies, and filaments are also shed (Reason et al., 2003). These mesoscale features have been observed to migrate into the oceanic environment in the South-East Atlantic (Gordon, 1986, De Ruijter et al., 1999). It is suggested that such migration plays a decisive role on the strenght of the meridional overturning circulation, with consequent impact on the Global Climate System (Weijer et al., 1999, 2002, Biastoch et al., 2008a, 2009, Beal et al., 2011). The Indian Ocean properties such as heat and salt, are transported far beyond the subtropical region of the south Atlantic (Gordon, 1986), hence their overall effect could reach the North Atlantic Ocean (Biastoch et al., 2009). The transfer of such oceanic properties are mostly carried by the Agulhas Rings

(Reason et al., 2003). Van Ballegooyen et al. (1994) estimated a volume flux by the Agulhas Rings of about 7 Sv, for waters warmer than 8°C, heat flux of about 0.9 PW, and a salt flux of about $\sim 78\times10^{12}$ kg per year. These estimates suggest that their influence may not be neglected. They may have potential to impact significantly the surrounding water mass properties. Hydrographic observations suggested that the Agulhas Rings have an average diameter of about $\sim$ 240 $\pm$40 km, and they can extend throughout the water column (about 4500 m), drifting at a speed of about 5 - 8 km per day (Olson and Evans, 1986). The Rings lose quickly their energy (about 70 percent of their energy), after their shedding (Schouten et al., 2000). The lost is either to the surrounding oceanic environment, or to the atmosphere (Walker and Mey, 1988, Olson et al., 1992) via heat flux. After the retroflection of the Agulhas Current, a significant part of the flow also returns to the Indian Ocean, as an eastward current, known as the Agulhas Return Current.

1.4.1.3 The Agulhas Return Current

The flow of the Agulhas Return Current (ARC) propagates eastwards, as far as to the east of 70°E (Lutjeharms and Ansorge, 2001). It has been considered as being an outflow of the Agulhas Current System (Lutjeharms, 2007). The ARC constitutes the northern boundary of the Subtropical Convergence Front (Figure 1.6), and bounds the warmer and salty Indian Ocean waters to the north, from the colder and relatively fresher water from the south. It is thought that friction caused by the interaction of the Agulhas Return Current with the Subtropical Convergence, induces instabilities responsible for the enhancing mesoscale variability in the region (Lutjeharms, 2007). The ARC lies within a region of very irregular seafloor topography, which may also have an influence on the meandering of the flow, and spawning of mesoscale eddies (Gründlingh, 1978). High chlorophyll-a concentrations has been observed along the path of the ARC (Weeks and Shillington, 1996). This fact suggests that the region may play an important role on the marine ecology, as it holds a high primary productivity. As the ARC moves farther east, its volume transport gradually diminishes, while it loses part of the flow into the subtropical gyre of the South Indian Ocean (Lutjeharms and Ansorge, 2001). The remaining flow which keeps moving farther east of 75°E, is usually attributed to the flow of the South Indian Ocean Current. Drifting buoys released along the path of the flow of the ARC suggested that the propagation speed of the ARC varies from 130 cm s^{-1} in the west, to 40 cm s^{-1} between 55°E and 62°E (Gründlingh, 1978). Estimates of the volume transport for the

upper 1500 m, on the path of the ARC, near the retroflection region, suggest that the Current transports eastward about 55 Sv.

Several studies have shown that the variability of the Agulhas Current is also related to the varibility of the flow in the upstream regions (van Leeuwen et al., 2000, Schouten et al., 2002b, De Ruijter et al., 2005): Mozambique Channel and the region to the south of Madagascar, regarded as the main sources of the Agulhas Current. A general description of the flow field in these regions is presented in the next chapter.

CHAPTER 2

The Mozambique Channel

2.1 Description of the study area

It was about 165 million years ago when Madagascar separated from the African main land, to about 420 km to the east and formed the so called the Mozambique Channel (Nairn and Stehli, 1982). the channel lies on the westernmost part of the South-West Indian Ocean (Figure 2.1), and forms the northern extension of the greater Agulhas Current system. the channel is bounded to the North by the zonal line stretching from the Rovuma River Estuary, Mozambique, at about (10°.28'S, 40°.26'E), to Cape-Amber, northern tip of Madagascar (11°.57'S, 49°.17'E). To the South it is bounded by the line stretching from the Ponta de Ouro (26°.53'S, 32°.56'E), south of Maputo, Mozambique, to Cape Saint-Marie, the southern tip of Madagascar (IHO, 1953).

2.1.1 Geomorphology

The Mozambique Channel is approximately 1600 km long, and its width varies from 420 km to 1000 km (Piton et al., 1981), forming a surface area of about 1.5×10^6 km^{-2}. The narrowest part of the channel (between 16°S to 18°S), is also the shallowest in the

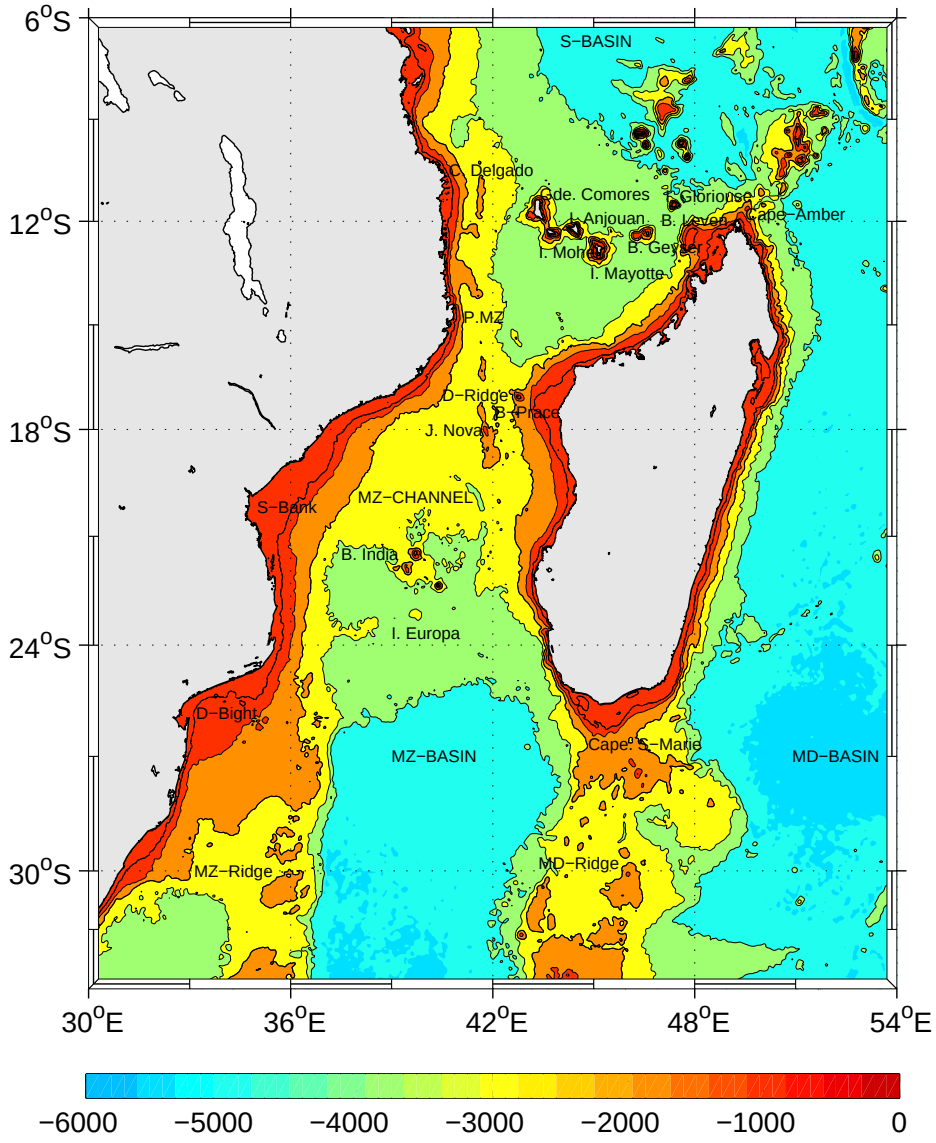

Figure 2.1. Bathymetry of the region. Meaning of the acronyms: S-BASIN: Somali Basin, MZ-Basin: Mozambique Basin, MZ-Channel: Mozambique Channel, MD-Basin: Madagascar Basin, S-Bank: Sofala Bank, P. MZ: Ponta Mozambique, D-Ridge: Davie Ridge, MD-Ridge: Madagascar Ridge, D-Bight: Delagoa Bight, J. Nova: Juan de Nova, B. Pracel: Bank Pracel, B-India: Bassas da India, I: stands for Islands. The colours indicates the ocean depths. Data derived from ETOPO2.

region (the maximum depth is about 2800 m). To the North of the channel, the maximum depth is about 3600 m, and lies within the Comores Basin, while to the South, the maximum depth is about 4000 m, and lies at the northern extension of the Mozambique Basin (Soares, 1975). The seafloor topography within the Mozambique Channel is very irregular, and it follows a north - south orientation. Many Islands and shallow banks are observed throughout the channel: The northern sector encompasses the Islands of Comores and Gloriousa, as well as the Banks of Geyser and Leven. The southern sector hosts the Islands of Europa and Bassas da India. At the center, lies the Davies Ridge and the Island of Juan Nova (Figure 2.1). It is thought that these bathymetric relief plays a significant role on the generation process and path of propagation of the eddies in the channel (DiMarco et al., 2002, Quartly and Srokosz, 2004). The continental plateau is almost inexistent, except at Sofala Bank (Beira, Mozambique), between 19°S and 21°S; and Pracel Bank, at Cape Saint-André, Madagascar, between 16°S and 18°S; and the Nosy-Bé Bank, Madagascar between 12°S and 14°S (Piton et al., 1981). Both eastern and western boundaries of the channel are also very irregular, with potentials to influence in many ways the dynamics of the flow, the Mozambican coast line being the longest with about 2700 km.

2.1.2 Hydrology

The climate of the region is tropical, with two main characterizing seasons: humid or wet (October - March), and dry (April - September). The rains are more abundant in the northern parts of the channel, around Comores, and Nosy-Bé, in the northwest of Madagascar (Piton et al., 1981). Three main rivers flows into the channel: the Mangoky and Betsiboka Rivers, to the north of Pracel Bank (at about 22°S) and Leven Bank (at about 16°S), are located at the eastern boundary of the channel. On the western boundary flows the Zambézi River, on Sofala Bank, Mozambique (at about 19°S). The contribution of these rivers in terms of sediments, nutrients, and freshwater volume inflow into the channel are very important (especially for the marine ecosystems). The annual mean freshwater inflow are estimated as follows: Zambézi (7000 m^3 s^{-1}, the most important), the Betsiboka (1000 m^3 s^{-1}), and Mangoky River (500 m^3 s^{-1}) (Piton et al., 1981). The ecology of the channel is characterized by a pristine ecosystem, with high biological diversity and several endemic and endangered species (Hoguane, 2007). It encompasses

important ecological domains: The Delagoa Bight to the south of the channel, and the Sofala Bank to the center.

Throughout the year, the northern Mozambique Channel, between 12°S and 20°S, stands as the warmest place in whole South-West Indian Ocean. In this region, the range of temperatures during summer season varies from 28°C to 29°C, and in winter it varies from 25°C to 26°C (Piton et al., 1981). To the South of 25°S it ranges from 26°C to 27°C in summer, to 22°C to 23°C in winter. The thermocline depth defined by the isotherms of 20°C (typical for midthermocline tropical oceans (Schott et al., 2009)) varies from 70 m to 220 m, with higher variations observed in the north of the channel than in the south.

2.1.3 Atmospheric forcings

The upper Ocean in the Mozambique Channel is generally influenced by the Indian Ocean southeasterly winds throughout the year, especially to the South of about 20°S (Tomczak and Godfrey, 1994). To the North of that latitude, it is influenced by the northern monsoonal winds, especially during the winter monsoon regime (Figure 2.2). Two types of atmospheric pressure system dominate over the Mozambique Channel (Figure 2.2): a high pressure (anticyclonic), and a low pressure system (cyclonic depression). According to Piton et al. (1981), the anticyclonic system is frequent during the months of May to September, when the high pressure system is established close to Madagascar between 25°S and 30°S, and 55°E and 75°E. In this regime, the winds are in general from the southeast (Figure 2.2), and the Intertropical Convergence Zone (ITCZ) is pushed to the north, beyond the equator, between 20°S and 25°N. On the other hand, the low pressure system is exclusively in winter, when the cyclonic depression dominates the system. In this regime, the local winds in the channel are predominantly from the north and northwest, especially to the North of the ITCZ (Figure 2.2). On the other hand, to the South of the ITCZ the winds are southeasterlies. In this regime, the ITCZ is pushed southwards, around 17°S (Figure 2.2), bringing along severe rains.

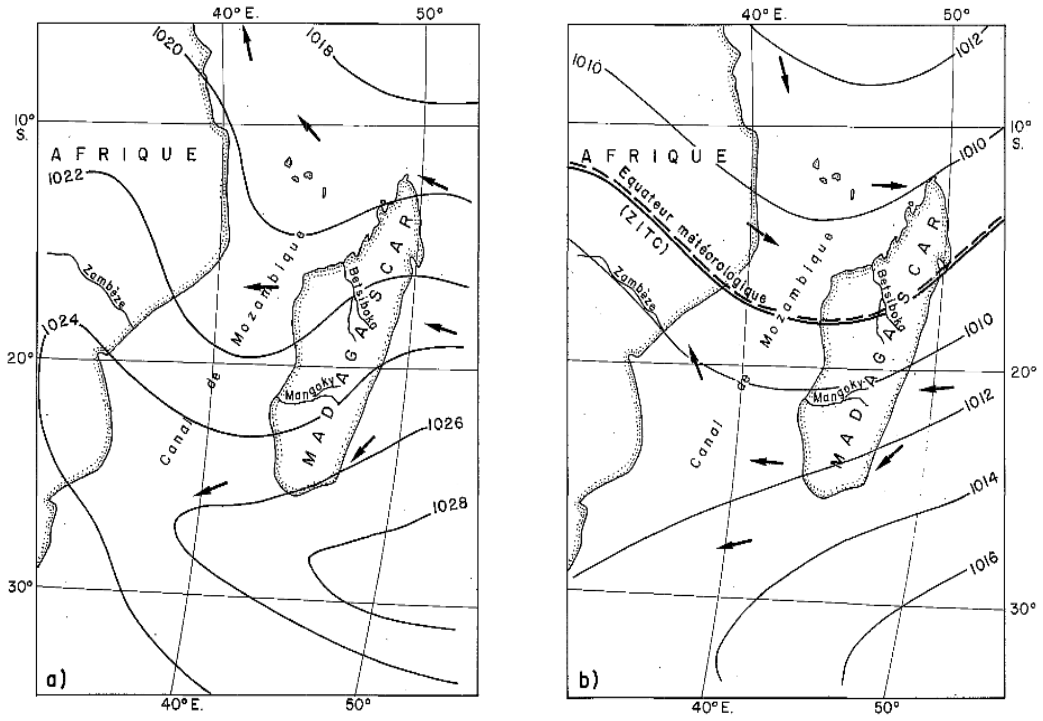

(a) (b)

Figure 2.2. Map of the atmospheric seasonal circulation over the Mozambique Channel. The contours represent the atmospheric pressure in milibars, over the sea surface. Panel (a) is for summer season, a high sealevel pressure system, and winter season (b) is for a low pressure system. The arrows indicates the seasonal wind direction [After: Donque (1973)].

2.1.4 Oceanic circulation

The water flowing southwards in the Mozambique Channel is mostly derived from the South Equatorial Current. It has been always recognized that the flow field in this region is complex, and also poorly understood (Gründlingh, 1993, Tomczak and Godfrey, 1994, DiMarco et al., 2002). The reasons behind this is the lack of useful oceanographic data (i.e. with good resolution in time and space), to allow a scientific study able to provide reliable and conclusive results.

2.1.4.1 Old conceptual description of the circulation

Based on a sparse dataset available to the oceanographic community, different portrayals of the oceanic surface circulation in the region have been proposed (Saëtre and da Silva,

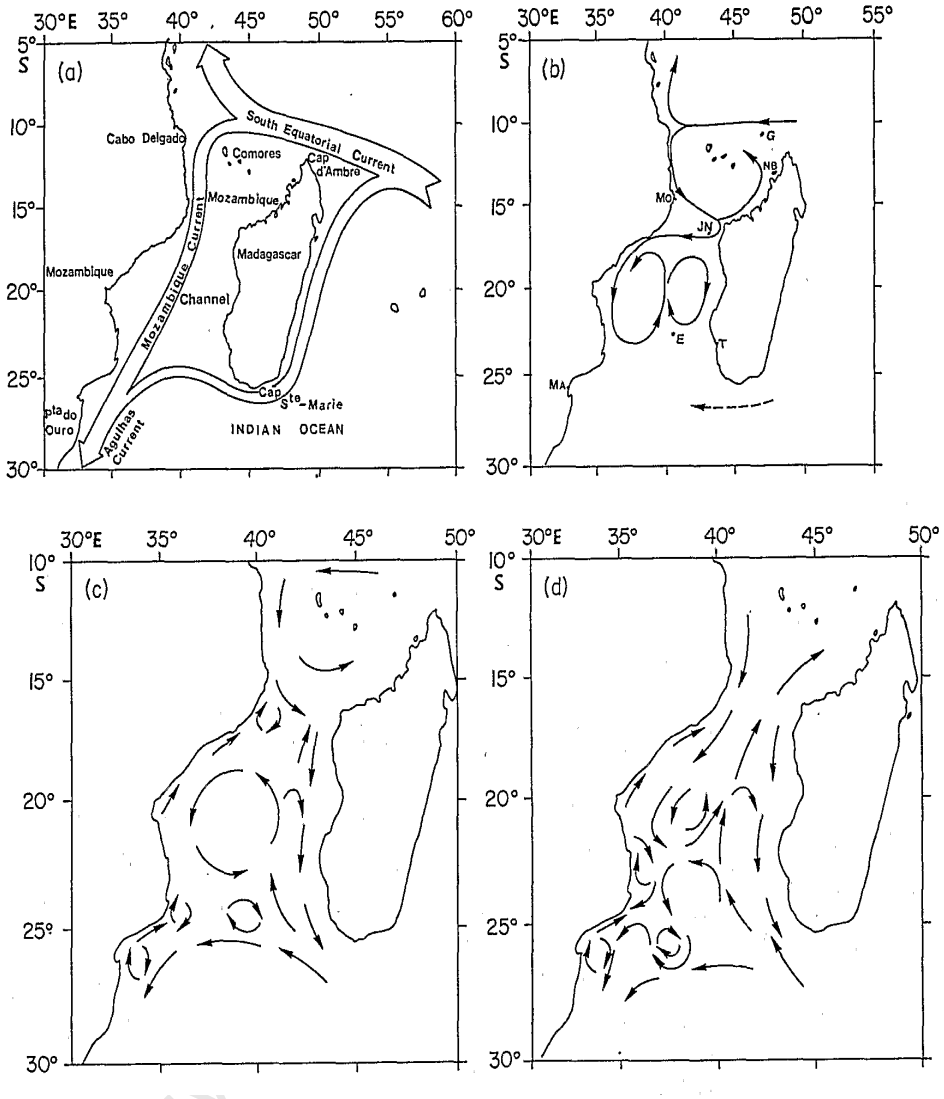

Figure 2.3. Different diagrams proposed to characterize the nature of the flow in the Mozambique Channel. Panel (a) - proposed by Saëtre (1985), based on historical data. Panel (b) - proposed by Soares (1975), based on meteorological data, and tide Gauge stations. Panels (c: summer, d: winter) - proposed by Saëtre and da Silva (1984) [After: Donguy and Piton (1991)].

1984, Saëtre, 1985, Tomczak and Godfrey, 1994, Donguy and Piton, 1991). Based on historical data, old textbooks have suggested that the surface circulation in the channel was mainly dominated by a southward flowing, western boundary current along the Mozambican coastline, known as the Mozambique Current (Saëtre, 1985, Tomczak and Godfrey, 1994). Saëtre and da Silva (1984) when addressing the question whether the flow field in the Mozambique Channel was continous or not, they proposed a circulation

scheme which was seasonally dependent (panels c, d, Figure 2.3). During the northern summer monsoon, it was mainly characterized by three anticyclonic cells, with the larger one standing at the center of the channel (Figure 2.3c). During the winter monsoon, it was dominated by a larger number of small scale circulation cells (Figure 2.3d). Based on surface drifter data, Saëtre (1985), has shown that there is strong evidence of a possible occurence of a discontinous flow in the channel, but no definite conclusion has been given.

2.1.4.2 Recent conceptual description of the circulation: Mesoscale eddy dynamics

In recent years, a scientific research effort to understand the nature of the flow in the Mozambique Channel, and by extension in the whole South-West Indian Ocean have been conducted. Hydrographic stations, at the narrow section of the Mozambique Channel by the Agulhas Current Source Experiment (ACSEX) cruise (De Ruijter et al., 2002) provided results that seem to close the debate about whether the flow in the channel was continous or not. They show that the circulation is discontinous and dominated by a series of anticyclonic eddies (De Ruijter et al., 2002, Ridderinkhof and De Ruijter, 2003). A relatively larger dataset by the Long-Term Ocean Climate Observation (LOCO) moorings, also deployed at the narrow of the channel, as well as altimetric remote sensed data, also support the concept of a flow through the channel dominated by a series of mesoscale anticyclonic eddies (Schouten et al., 2003, Harlander et al., 2009). These findings have put out of-date the concept of a continous southward flowing Mozambique Current.

However a pertinent question remaining is: how and where are these eddies generated? And what are their characteristics and variability?

Three different regions of enhanced mesoscale variability in the channel have been found (North: 5°S - 16°S, Center: 17°S - 19°S, South: south of 20°S) of the channel (Schouten et al., 2003). Several mechanisms of formation of these eddies have been proposed: De Ruijter et al. (2002), and Ridderinkhof and De Ruijter (2003), have suggested that these eddies are generated at the narrow of the channel, by conservation of potential vorticity. The flow is constricted through the Davie Ridge, favoring generation of eddies. On the other hand modelling studies suggest that these eddies are generated at the north of Madagascar, by barotropic instability between the South Equatorial Current and the northernmost tip of Madagascar (Biastoch and Krauss, 1999). Nevertheless, to-date, the

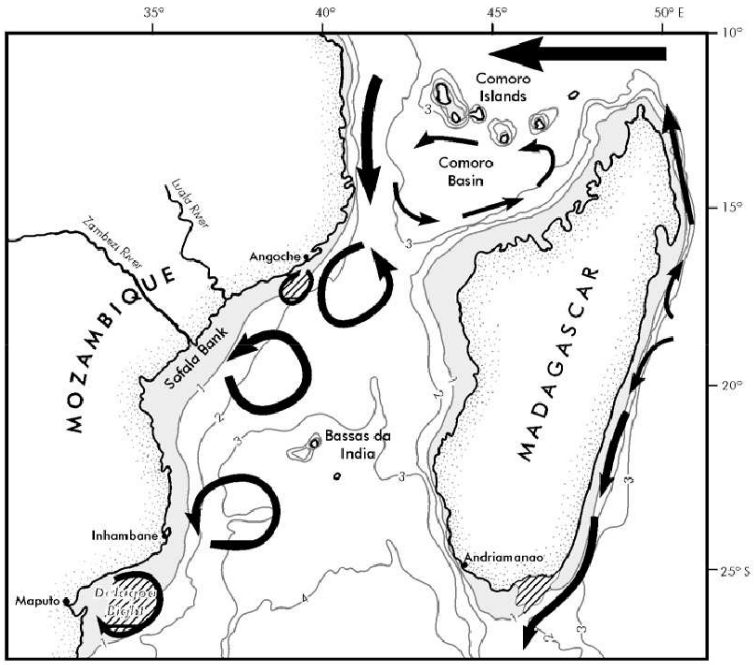

(a) The flow field in the Mozambique Channel

Figure 2.4. Schematic diagram of the ocean circulation in the Mozambique Channel, based on the recent description of the flow. The curvilinear features portrays mesoscale eddies, and arrows the ocean currents. The shaded areas on the continental shelves are shallower than 1 km. The hatched areas denote upwelling cells. [After: Lutjeharms (2006)].

mechanisms of eddy formation in the channel is not fully known. Investigations of their frequency of occurence in the different regions show that in the northern part of the channel, the eddies have been observed at a larger frequency of about 7 per year. In the central region they have a frequency of about 4 - 5 per year, while in the southern region they have been observed at a rate of 3 - 4 per year (Schouten et al., 2003). Records of anomalies of sea surface height in these regions suggest that these eddies increase their heights as they propagate from north to south (North: 20 cm, South: 35 cm) (Schouten et al., 2003). These eddies are predominantly anticyclonic (anticlockwise), southward propagating, and are observed at a regular basis. At the narrow channel they have an advecting speed of bout 4.5 km per day (De Ruijter et al., 2002), and an angular velocity of about 0.1 m s^{-1}. They have a diameter of about 300 km to 350 km, are surface intensified, with a strong barotropic component, extending throughout the water column (of about 2800 m depth, at that location) (De Ruijter et al., 2002, Schouten et al., 2003, Ridderinkhof and De Ruijter, 2003, Harlander et al., 2009). These eddies induce a southward volume transport

of about 15 Sv - 20 Sv ($1Sv = 10^6 m^3\ s^{-1}$), measured for the upper 1500 m (Schouten et al., 2003, Ridderinkhof and De Ruijter, 2003). They are oligotrophic (low nutrients (Swart et al., 2010)), and trap in their core different water masses such as RSW, AAIW and TSW. These eddies propagate mostly southwestwards along the Mozambican coastline. Their larger diameter and the relatively smaller width of the channel, favors these eddies to interact with the continental shelf, removing coastal waters and transporting them into the open ocean.

2.1.4.3 The Role of the Mozambique Channel eddies

There is a strong evidence that the mesoscale eddies in the Mozambique Channel play an important role on the large scale ocean circulation (Biastoch et al., 2008a). In a global scale perspective, the role of the mesoscale eddies from the Mozambique Channel have been investigated at the downstreams of the Agulhas Current system, at the boundary between the Southwest Indian and the Southeast Atlantic Oceans. The connection between these ocean basins allows an exchange of anomalous heat and salt content to cross into the Atlantic Ocean (Gordon, 1986). Such an exchange of oceanic properties seems to play a crucial role on the strenght of the global thermohaline circulation, and impact the global climate system (Weijer et al., 1999, 2002, Biastoch et al., 2009, Beal et al., 2011). Altimetry observations and model simulations suggest that the Mozambique Channel eddies cross the full length of the channel, and eventually reach the Agulhas Retroflection region (Schouten et al., 2002b). There, they modulate the timing and frequency which the Agulhas Rings are shed into the south Atlantic (Schouten et al., 2002b, Penven et al., 2006c, Biastoch et al., 2008a). Upstreams of the retroflection region, at the Natal Bight, these eddies also play a significant role. In this region they cause perturbations on the path and behaviour of the Agulhas Current, leading to a generation of Natal Pulses (De Ruijter et al., 1999, van Leeuwen et al., 2000). A Natal Pulse (a cyclonic meander at the inshore edge of the Agulhas Current (Lutjeharms and Roberts, 1988a) can lead to an eventual earlier retroflection of the Agulhas Current (Lutjeharms, 2006). An earlier retroflection of this current could have an impact on the required amount of Agulhas leakage necessary to keep an equilibrium of the global thermohaline circulation, and the global climate system. At the regional scale, the role of Mozambique Channel eddies have been investigated in the context of ecological perspectives (Weimerskirch et al., 2004, Tew-Kai and Marsac, 2009, Omta et al., 2009). It has been observed from in-situ mea-

surements as well as from satellite observations (Quartly and Srokosz, 2004) that during their course of propagation, the Mozambique Channel eddies could transport from the coastal environment to the offshore coastal water properties, such as sediments, nutrients, or chlorophyll. They control in this way the spatial and temporal distribution of the ecosystem for all trophic levels. In fact, Freagate birds have been observed foraging at the edges of these eddies (Weimerskirch et al., 2004). Nevertheless, very little so far is known about the Mozambique Channel eddy properties. In this study, we provide further information about their properties and mechanisms of formation.

2.2 Key Study Questions and Objectives

The literature review presented in this chapter, has shown that despite the new knowledge recently gained on the nature of the flow field through the Mozambique Channel, several questions remain open on the origin, characteristics and formation mechanisms of these eddies. We design a ROMS based model configuration: the South-West Indian Ocean Model (SWIM) to address the questions in more details. However the first question to consider is the ability of the model:

ROMS performance

- Does the SWIM model simulate satisfactorily the oceanographic features of the Mozambique Channel?

Eddy characteristics

- Are there Cyclonic eddies in the Mozambique Channel?
- Why is the flow in the Mozambique Channel dominated by anticyclonic eddies?
- What are the physical properties (statistical census, polarity, site of formation, trajectory, lifetime, amplitude, diameter, frequency) of the Mozambique Channel eddies (both anticyclonic and cyclonic eddies)?
- How do the Mozambique Channel eddies vary their properties throughout the channel?

Eddies generation process

- What eddy generation mechanisms are dominant at the different subregions of the Mozambique Channel?
- What role the eddy-mean flow interaction plays on the circulation in the Mozambique Channel?

We expect that findings of the present study will be of great importance, both for academic purposes and marine management plans.

Objectives of the study

The main objective of this study is threefold. Firstly: obtain an assessment of the mean properties of the Mozambique Channel eddies. Secondly: improve current understanding and description of the flow field in the Mozambique Channel, and thirdly: test the robustness of an adapted mixed eddy detection scheme in the waters of the Mozambique Channel. The methodology used to achieve our expectations is presented in the next chapter.

CHAPTER 3

Material and Methods

3.1 Model and Data

A review of the current knowledge of the circulation in the Mozambique Channel presented in the previous chapters, have shown that the eddies activity in the Mozambique Channel is complex, and poorly understood. One of the reasons outlined in the previous chapters, with regard to such limited knowledge is the lack of satisfactory in-situ oceanic data (sufficiently sampled in time and space) to resolve small-scale oceanic processes and variability. Nevertheless, alternative research tools such as numerical ocean circulation models could be used to provide insight on some processes of the system. Ocean circulation models can generate a large an amount of information at a desired resolution. This allows one to derive a synoptic view of a large number of targeted parameters in a large oceanic domain.

In this study, we use an ocean model, as our main research tool. The reproduced model results are compared to available observational data derived from different sources, such as: World Ocean Atlas 2005 (WOA05), CSIRO Atlas of Regional Seas 2009 (CARS09), Satellite altimetric observations from the Archiving Validation and Interpretation of Satellite Oceanographic data (AVISO), French Space Agency 2009 (CLS-CNES09), and in-situ

mooring data from the Long Term Ocean Climate Observation program (LOCO). The details of these dataset are presented later.

3.2 Model: The Regional Ocean Modelling System

3.2.1 User's Motivation in the model

There are several types of ocean circulation models distributed around the world (for an extensive list of ocean circulation models, see $http://stommel.tamu.edu/\sim baum/ocean\ models.html$). It is left to the user's criteria to decide which one suits best to address his research problem. In our case we used the Regional Ocean Modelling System (ROMS) (Shchepetkin and McWilliams, 2005). Our choice in this model is motivated by compelling reasons associated with the model advantageous features:

ROMS has been designed especially to resolve realistically basin-scale and coastal ocean processes, at higher resolution, and at relatively low computational costs. Such an efficiency is guaranteed by its advanced numerical schemes, for space and time differencing (Shchepetkin and McWilliams, 2005). Also by its parallel computing capabilities, and optimal use of the computer processors caches (local fast memory) (Shchepetkin and McWilliams, 2005), and by its compactibility with the nesting tools (that enhances the spatial resolution in a defined sub-domain) (Debreu and Blayo, 2008, Debreu et al., 2012).

3.2.2 Model description

ROMS is a new generation of ocean circulation models: It is a split-explicit hydrodynamic kernel, where barotropic and baroclinic momentum equations are solved separately, important for computational efficiency (Shchepetkin and McWilliams, 2005). It explicitly allows free surface movements (important for tidal motions, surface gravity waves, etc). The numerics are based on finite differences, discretized horizontally in an Orthogonal-Curvilinear coordinate system. This can be used to follow the coastlines for irregular lateral boundaries, important for coastal processes. In the vertical it is discretized in a generalized σ - coordinate system: following the irregularites of the bottom topography (Song and Haidvogel, 1994) (thus is of great importance for flow topography interaction). The variables are computed on a numerical staggered Arakawa C grid (Arakawa and Lamb, 1977).

ROMS solves the primitive equations of motion in a planetary rotating frame, and complies with the Boussinesq and hydrostatic approximations. In Boussinesq approximation, seawater density variations are small enough, so that their contribution in the horizontal momentum equation can be neglected, while in the vertical, density variations can not be neglected (when multiplied by the gravitational acceleration $\vec{g}$, it forms the buoyancy force $\rho\vec{g}$ in the vertical momentum equation). The Hydrostatic approximation assumes that the vertical pressure gradient $[\frac{\partial P}{\partial z}]$ is in balance with the buoyancy force. (ocean depth is smaller when compared to the horizontal basin-scale, so vertical accelerations can be neglected).

The model uses an adaptive mixed passive-active implicit radiation scheme at the open boundaries, that connects the model solution to the surrounding oceanic environment (that prevents spurious reflections, and guarranty the stability, and accuracy of the solution) (Marchesiello et al., 2001). Also the model employs an improved numerical algorithms that minimizes the pressure gradients errors, while achieving more accurate hydrostatic balance terms for the generalized sigma-coordinate formulation (Shchepetkin and McWilliams, 2003). The model holds an advanced centered fourth-order horizontal tracer advection scheme for potential temperature and salinity, with a biharmonic diffusion operator rotated to follow the isopotentials (SPLITUP) (Marchesiello et al., 2009): this minimizes the problem of spurious diapycnal diffusion, which can occur using upstream schemes in σ - coordinate models. The vertical σ - coordinate discretization, is generalized to enhance vertical resolution at the sea surface or at the seafloor (Song and Haidvogel, 1994). The K-Profile PBL surface and bottom boundary layer parameterization scheme (KPP), parameterizes subgrid-scale vertical turbulent mixing processes (Large et al., 1994). Good representation of oceanic processes at the upper layers of the ocean column are important, especially for the biology, and climate studies. At the ocean bottom, a good representation of the processes is important especially for the deep flows, benthic life, and some geological processes (e.g, sediment transports). These features make the model code suitable to expand its applications in order to simulate several processes such as: ecosystem dynamics, biogeochemical cycling (Plattner et al., 2005, Gruber et al., 2006), erosion and depositions of the sediments (UCLA and USGS, 2003, Blaas et al., 2007), and climate variability; provided a suitable coupling models approach is achieved.

3.2.3 Model Formulation

3.2.3.1 Governing Equations

The primitive equations of motion for an incompressible ocean (under Boussinesq and hydrostatic approximations) can be discretized in the Cartesian coordinate system as:

$$\frac{\partial u}{\partial t} + \vec{v}.\nabla u - fv = -\frac{\partial \phi}{\partial x} + F_u + D_u \tag{3.1}$$

$$\frac{\partial v}{\partial t} + \vec{v}.\nabla v + fu = -\frac{\partial \phi}{\partial y} + F_v + D_v \tag{3.2}$$

$$\frac{\partial T}{\partial t} + \vec{v}.\nabla T = F_T + D_T \tag{3.3}$$

$$\frac{\partial S}{\partial t} + \vec{v}.\nabla S = F_S + D_S \tag{3.4}$$

$$\frac{\partial \phi}{\partial z} = -\frac{\rho g}{\rho_o} \tag{3.5}$$

$$\frac{\partial u}{\partial x} + \frac{\partial v}{\partial y} + \frac{\partial w}{\partial z} = 0 \tag{3.6}$$

$$\rho = \rho(T, S, P) \tag{3.7}$$

The equations (3.1) and (3.2) express the horizontal momentum balance in the x and y directions respectively. The equations (3.3) and (3.4) are the tracer advection-diffusion,

that govern the time evolution of potential temperature T and salinity S. The hydrostatic and the mass balance are expressed by the equations (3.5) and (3.6) respectively. The equation (3.7) is the equation of state for seawater (Jackett and MacDougall, 1995). These equations are subject to boundary conditions at the sea surface and at the sea floor.

3.2.3.2 Vertical Boundary Conditions

- **At the sea surface**: $z{=}\zeta(x, y, t)$

$$K_v \frac{\partial u}{\partial z} = \frac{\tau_s^x}{\rho_o}(x, y, t) \tag{3.8}$$

$$K_v \frac{\partial v}{\partial z} = \frac{\tau_s^y}{\rho_o}(x, y, t) \tag{3.9}$$

$$K_T \frac{\partial T}{\partial z} = \frac{Q_T}{\rho_o c_P} \tag{3.10}$$

$$K_S \frac{\partial S}{\partial z} = \frac{(E_v - P_r)S}{\rho_o} \tag{3.11}$$

$$w = \frac{\partial \zeta}{\partial t} \tag{3.12}$$

- **At the seafloor**: $z{=}-H(x,y)$

$$K_v \frac{\partial u}{\partial z} = \frac{\tau_b^x}{\rho_o}(x,y,t) \tag{3.13}$$

$$K_v \frac{\partial v}{\partial z} = \frac{\tau_b^y}{\rho_o}(x,y,t) \tag{3.14}$$

$$K_T \frac{\partial T}{\partial z} = 0 \tag{3.15}$$

$$K_S \frac{\partial S}{\partial z} = 0 \tag{3.16}$$

$$-w + \vec{v}.\nabla H = 0 \tag{3.17}$$

The equations (3.8) and (3.9) express the horizontal momentum transfered into the ocean by atmospheric wind stress at the sea surface, in x and y directions respectively. The equations (3.10) and (3.11) are the thermal and fresh-water fluxes at the sea surface, and the equation (3.12) express the vertical velocities associated with the variation of the sea surface. Similarly, at the bottom, the equations (3.13) and (3.14) express the momentum transfered into the ocean by friction at the seafloor. The equations (3.15) and (3.16) prescribe non-occurrences of a vertical thermal and salt fluxes at the seafloor. The equation (3.17) express the non-crossing of the topography by the flow at the seafloor.

The components of the surface wind stress τ_s are given by:

$$\tau_s^x = \rho_{air} c_D \sqrt{{u_{10}}^2 + {v_{10}}^2}.u_{10} \tag{3.18}$$

$$\tau_s^y = \rho_{air} c_D \sqrt{{u_{10}}^2 + {v_{10}}^2}.v_{10} \tag{3.19}$$

For a variable topography, at the seafloor $z = -H(x, y)$, the horizontal bottom velocities have a parameterized bottom stress which can be a choice between linear, quadratic, or logarithmic terms (Hedström, 2009). The Bottom friction is perscribed as:

$$\tau_b^x = (\gamma_1 + \gamma_2 \sqrt{u^2 + v^2}).u \tag{3.20}$$

$$\tau_b^y = (\gamma_1 + \gamma_2 \sqrt{u^2 + v^2}).v \tag{3.21}$$

In the equations:

- x, y, z - are zonal, meridional, and vertical directions $[m]$ in the Cartesian coordinate system.
- u, v, w - are components of the vector velocity $\vec{v}$ $[\frac{m}{s}]$ in x, y, z, respectively.
- t - is time in seconds $[s]$.
- f - is the Coriolis parameter $[\frac{1}{s}]$.
- ϕ - is the dynamic pressure, $\phi = \frac{P}{\rho_o} [\frac{m^2}{s^2}]$.
- F_u, F_v, F_T, F_S - are the possible forcings terms.
- D_u, D_v, D_T, D_S - are the dissipative terms (explicit Laplacian or biharmonic viscosity and diffusion, or implicit in the numerical computation of advective terms.
- T - is the potential temperature $[^\circ C]$.
- S - is the salinity.
- $\vec{g}$ - is the acceleration of gravity, g $[\frac{m}{s^2}]$.

- ρ - is the seawater density, $[\frac{kg}{m^3}]$.
- ρ_o - is the mean seawater density, $[\frac{kg}{m^3}]$.
- P - is the total pressure, $\frac{\partial P}{\partial z}$= - ρg $[\frac{N}{m^2}$ or $\frac{kg}{ms^2}]$.
- ζ - is the sea surface variation $[m]$.
- τ_s^x, τ_s^y - are the surface wind stress $[\frac{N}{m^2}]$, in x and y directions respectively.
- τ_b^x, τ_b^y - are the bottom stress $[\frac{N}{m^2}]$, in x and y directions respectively.
- Q_T - is surface heat flux $[\frac{W}{m^2}]$.
- K_v - is coefficient of vertical eddy viscosity $[\frac{m^2}{s}]$.
- K_T, K_S - are coefficient of vertical eddy diffusivity $[\frac{m^2}{s}]$.
- E_r - is the evaporation rate $[\frac{cm}{day}]$.
- P_r - is the precipitation rate $[\frac{cm}{day}]$.
- c_P - is the heat capacity of seawater $[\frac{J}{kg.^oC}]$.
- H - is the total ocean depth $[m]$.
- u_{10}, v_{10} - are the horizontal components of the wind vector in x and y respectively measured at 10 m above sea level.
- c_D - is non-dimensional wind-drag coefficient.
- ρ_{air} - is the density of atmospheric air $[\frac{kg}{m^3}]$.
- γ_1 - is the coefficient of linear bottom friction.
- γ_2 - is the coefficient of quadratic bottom friction.

3.2.3.3 Forcing formulation (Ocean - Atmosphere interaction)

Gridded observational dataset is used as forcing fields at the sea surface. It requires wind stress, heat and fresh-water fluxes. In our case we use a monthly mean climatology, gridded at $\frac{1}{2^\circ} \times \frac{1}{2^\circ}$, derived from the Comprehensive Ocean Atmosphere Dataset (COADS 2005 Da Silva et al. (1994)).

In regard to the sea surface temperature (which have a direct implication on the surface heat flux), the term $\frac{\partial Q}{\partial SST}$, of the equation (3.22) accounts for a linearization of the Bulk formula, taking into account the effect of SST on heat flux (Q). To prevent the model results to drift away from the observational data, induced by the ocean-atmosphere exchange, in the forcing formulation a correction term is added to coupling ocean-atmosphere feedback term (Barnier et al., 1995). This restoring term is obtained by relaxing the model derived SST towards the SST climatology (observation), as prescribed:

$$Q_T = Q_{net} + \frac{\partial Q}{\partial SST_{clima}}(SST_{model} - SST_{clima}) \tag{3.22}$$

The amplitude of the restoring term depends on how far away the model solution has drifted from its observed climatologic value.

The components of the surface heat flux are: The incoming short-wave radiation (rate of inflow of solar energy at the sea surface), the outgoing long-wave radiation (rate of heat loss by the ocean to atmosphere and space by back radiation), Latent heat flux (rate of heat loss/gain by evaporation/condensation), and Sensible heat flux (rate of heat loss/gain through the sea surface by conduction).

There is a slight difference in the case of salinity. Changes in surface salinity does not have a direct feedback on evaporation and precipitation. But since $(E_r - P_r)$ product is of poor quality, a non-physical correction is added to the equation (3.11). Therefore the salinity flux is perscribed as:

$$K_S \frac{\partial S}{\partial z}\Big|_{z=0} = \frac{(E_r - P_r).SSS_{clima}}{\rho_o} + \frac{1}{\tau}(SSS_{clima} - SSS_{model}) \tag{3.23}$$

In these equations:

- Q_{net} - is the net heat flux $[\frac{W}{m^2}]$.
- $\frac{\partial Q}{\partial SST_{clima}}$ - is the relaxation coefficient (linearization of the reference of Q to SST).
- SST_{clima} - is the climatology sea surface temperature $[^oC]$.
- SST_{model} - is the model derived sea surface temperature $[^oC]$.
- $K_S \frac{\partial S}{\partial z}\Big|_{z=0}$ - is the salt flux at the sea surface $[\frac{PSU.cm}{day}]$.
- SSS_{clima} - is the climatology sea surface salinity SSS $[PSU]$.
- SSS_{model} - is the model derived sea surface salinity SSS $[PSU]$.
- $\frac{1}{\tau}$ - is the relaxation constant (also called inverted time). It prevents the model SSS to drift too far away from its climatologic value. This term is usually kept equivalent to $\frac{\partial Q}{\partial SST_{clima}} \sim$ 30 - 40 days.

3.2.3.4 Horizontal Boundary Conditions

Appropriate lateral boundary conditions are provided for u, v, T, S and ζ. The model code is built to deal successfully with cases in which lateral boundaries might be closed (land bounded) or opened. In case of closed (masked) boundary, the prescription is simple: A numerical masking scheme adjusts the prescribed input according to a no-slip or free-slip conditions (Hedström, 1997, 2009).

- **Open Boundary Conditions (OBCs)**

Open boundaries (OBCs) require a special treatment (because OBCs have a crucial impact on the inner domain solution). In regional domains, OBCs for realistic simulations utilizes external fields derived from gridded observational data set, or from OGCM outputs. In our case, the external data are derived from a global monthly climatology, gridded at 1°×1°, World Ocean Atlas (WOA2005) (Conkright et al., 2002). Temperature and salinity are used to calculate the geostrophic velocities at the open boundaries (we have defined a reference level of 1000 m, because slower motions in the ocean occur below

this level). The wind field are also used for the estimation of Ekman velocities at the boundaries. These input of the prescribed observational data into the model interior, and their out-going (as information leaving the model domain), are controlled by an adaptive open boundary radiation scheme (Marchesiello et al., 2001). The scheme prevents spurious reflections of the solution, while guarantee a realistic stable state equilibrium for long periods. Detailed description of the scheme is presented by Marchesiello et al. (2001).

3.2.3.5 Spatial and temporal discretization

3.2.3.6 Horizontal and vertical discretization

Given its high resolution capabilities, ROMS employs a regular numerical staggered C-grid (Arakawa and Lamb, 1977), both in horizontal (Figure 3.1) and in the vertical (Figure 3.2) directions. In Arakawa C-grid type, the quantities such as ζ, H, f, ρ, Ω, are defined at the grid center, while u, v are defined half way of the grid center. For example the East-West component of velocity u, is displaced half a grid to the west of the center, and the North-South component v is displaced half a grid to the south of the center (Figure 3.1).

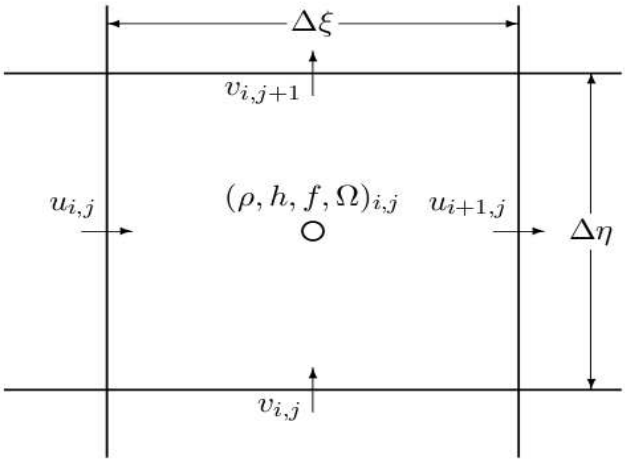

Figure 3.1. Horizontal placement of variables in a C-grid [After: Hedström (1997)].

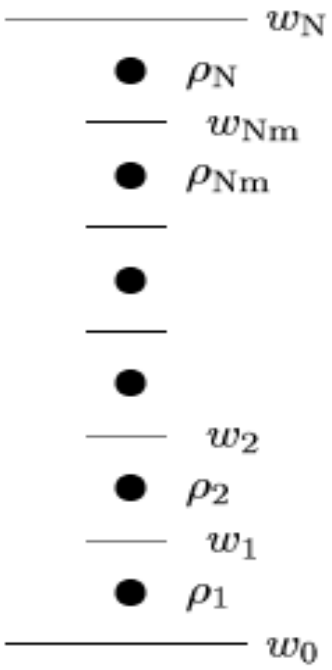

Figure 3.2. Vertical variables in a staggered Arakawa C-grid [After: Hedström (1997)].

3.2.3.7 Time-stepping and Mode-splitting

In ROMS, a suitable numerical algorithm has been implemented to deal with the issues of an optimal combination between time-stepping and mode-splitting: preserving the consistency, accuracy, and stability of the solution. This time-stepping algorithm, functions in a way that after each time-step of the momentum equations, the derived velocities are without delay used in the calculation of tracer transport and mass balance equations (Shchepetkin and McWilliams, 2005). The numerical schemes for solving the time-dependent equations are specially designed in a way that the time-steps of the barotropic (fast) mode are advanced in a series of shorter and faster time-steps, within each baroclinic (large and slow) time-steps. The scheme uses a leap-frog and Adams-Moulton 3-order predictor-corrector, which provides a better numerical stability of the time-steps.

To minimize the mode-splitting errors, the barotropic equations are re-defined to take into consideration the non-uniformity of the seawater density. Here the pressure gradient force is derived as a vertical integral of 3-D field variations, caused by oscillations on the free-sea-surface.

The advantages of the time-step and mode-splitting algorithms used in ROMS are: increase on the gain of numerical stability; increase of permissible time-step sizes; increase of computational efficiency; exact preservation and constancy of tracer properties; accurate resolution of barotropic processes, while preventing aliasing of unresolved barotropic signals into the baroclinic motions. For a detailed description of the time-step and mode-splitting algorithms, see Shchepetkin and McWilliams (2005).

3.3 Model Configuration

3.3.1 The South-West Indian Ocean Model (SWIM)

The SWIM model is a ROMS based configuration, which we have implemented in the South-West Indian Ocean. It has been designed specially to investigate the mesoscale circulation in the Mozambique Channel. The configuration was built using ROMSTOOLS (Penven et al., 2008). The geographical domain covers a larger extension of the South-West Indian Ocean, and parts of the South-East Atlantic (Figure 3.3a). The domain was largely extended to encompass the main oceanographic features in the Greater Agulhas Current System, namely: the South Equatorial Current, and its main branches - the South-East Madagascar Current, and the North-East Madagascar Current. It also includes the eddy field associated with the Mozambique Channel, and the south of Madagascar, as well as the Agulhas Current and its retroflection, the Agulhas Rings, the Agulhas Return Current, and the Sub-tropical convergence Front (see Figure 1.6).

3.3.2 Domain and Grid sizes

Geographically, SWIM domain lies between $0-77.5°$E, and $2.8°$S and $47.5°$S (Figure 3.3a). SWIM was configured at a relatively high resolution (longitudinal grid spacing $\Delta x \sim$ 21 km, at the mean latitude of the Mozambique Channel $\sim 19°$S). As the mesoscale eddies in the region have a typical length-scale of about $\sim$ 300 km (De Ruijter et al., 2002), the spatial resolution implemented is satisfactory to resolve these features, and their associated processes. The first baroclinic rossby radius of deformation in this region ranges from approximately 100 km in the north and 50 km in the south (Chelton et al., 1998).

To obtain an isotropic grid on Mercator projection, the latitudinal grid space in degrees was obtained by the relation $d\theta = dl.cos(\theta)$, where $dl = \frac{1}{5^\circ}$ - is the longitudinal resolution in degrees, and θ - is the latitude in degrees. The latitudinal grid size varies from $\Delta y \sim 14.89$ km at the southernmost limits, to ~ 22.17 km at the northernmost limits of the domain. The horizontal domain has an array of 256×384 grid points, in latitude and longitude respectively. In the vertical, the total number of σ-vertical layers is 45 levels. The stretching towards the surface increased the vertical resolution at the upper layers of the water column, from ~ 2.27 m at the shore, to ~ 7.87 m off-shore. At the bottom the vertical resolution ranged from ~ 7.97 m at the shore, to ~ 671.36 m off-shore (Figure 3.3b). To achieve such a vertical discretization of the grids, the stretching parameters have been chosen to ($\theta_s = 5.5$ - for the sea surface, and the $\theta_b = 0$ - for the bottom) (Beckmann and Haidvogel, 1993). The transition depth between the horizontal surface layers and the bottom σ-levels, has been set to $h_c = 10$ m.

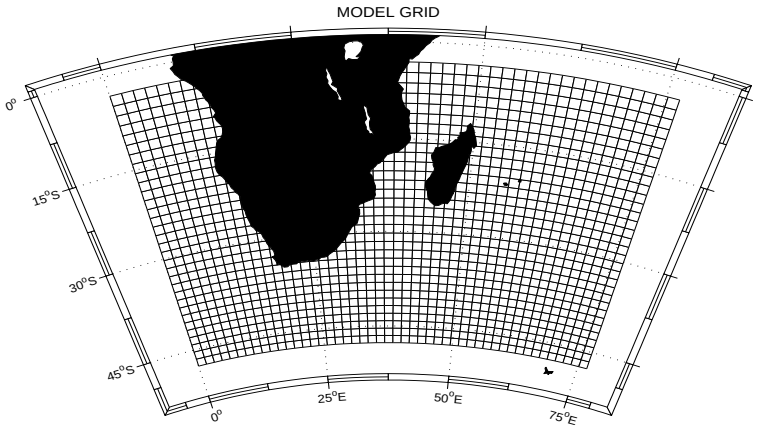

(a) Horizontal grid

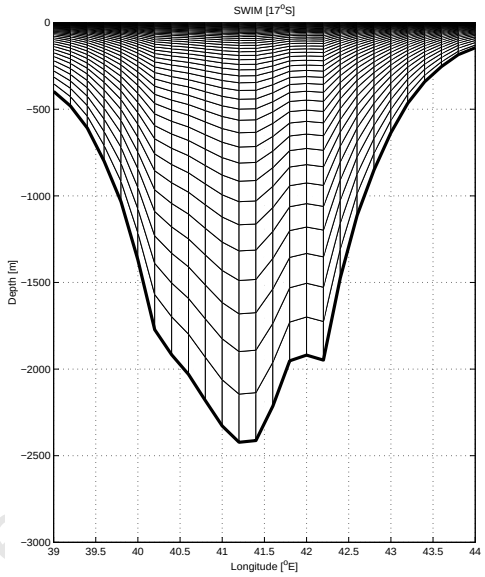

(b) Vertical grid

Figure 3.3. Extension of the SWIM domain, and the horizontal discretization of the grids, with grid cells shown at every 8 grid points, for the purposes of visualization (a). Vertical discretization of the grids in the σ-coordinate system, in SWIM configuration (b). The cross shelf section was derived at the narrower part of the Mozambique Channel (17°S).

3.3.3 Topography

The model topography was interpolated to the SWIM grid, from the high resolution dataset, gridded at 1-minute, derived from the Global Earth Bathymetric Chart of the Oceans (GEBCO1), *http* : *//www.ngdc.noaa.gov/mgg/gebco/gebco.html*.

Figure 3.4 shows the topography of the region. The upper panel (a) presents the original (raw data), and the lower panel (b), shows the model derived topography.

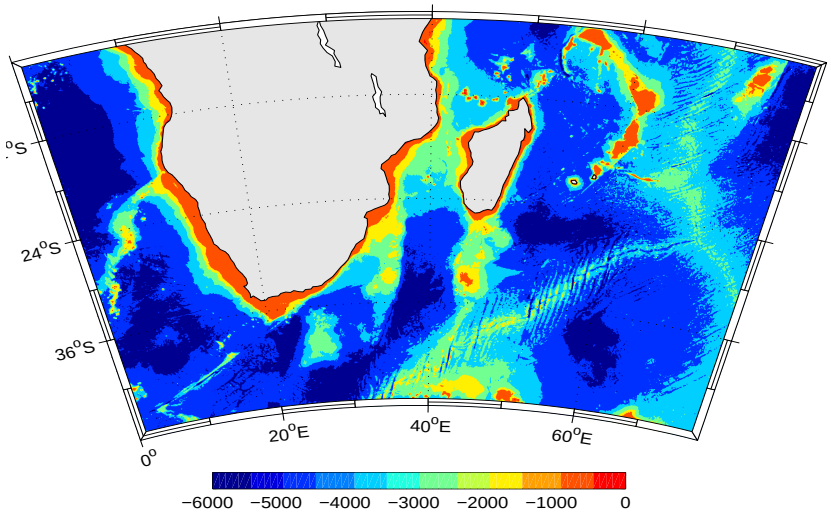

(a) Original topographic data (GEBCO1)

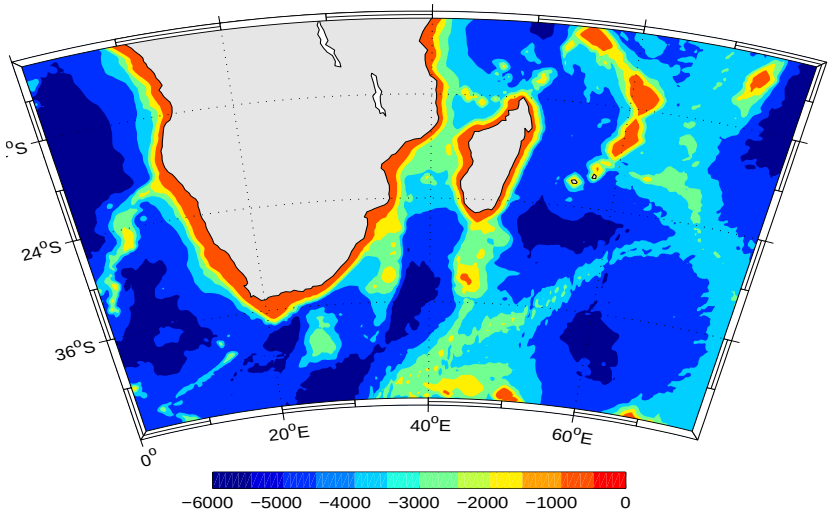

(b) Model derived topography

Figure 3.4. Original topography (a) and model derived topography (b). The background colour represent the ocean depths.

To prevent horizontal pressure gradient errors, a smoothing of the topography is required. The smoothing is performed so as to maintain the topographic slope parameter ($r=\frac{\nabla h}{2h} = \frac{h_{+1/2}-h_{-1/2}}{h_{+1/2}+h_{-1/2}}$), everywhere not superior to 0.2 (Beckmann and Haidvogel, 1993).

Although the model derived topography encompasses the main topographic features, there is a slight widening of the continental shelf area at the west coast of Madagascar, and also at the southeast coast of South-Africa, where flows the poleward propagating Agulhas Current.

At $\frac{1}{5^\circ}$ spatial resolution, we can not resolve accurately the shelf dynamics. Experiments have shown that it is preferable to crop the depth at the shore to a certain minimum value. In our case, the cropping was set at a minimum depth $h_{min} = 150$ m. A maximum depth at the shore, to prevent the generation of too big walls along the coast, was set to $h_{max} = 300$ m (see, Figure 3.5).

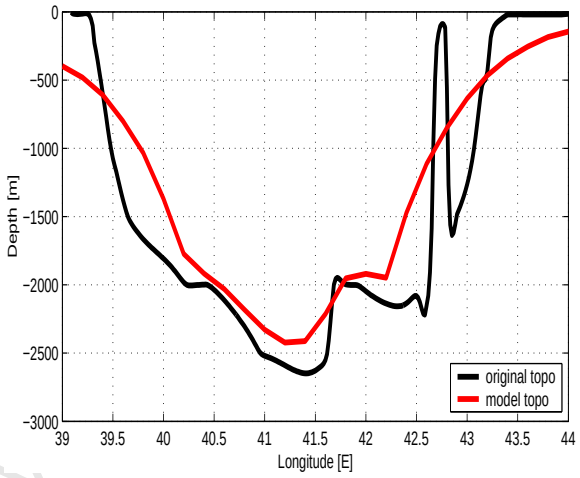

Figure 3.5. Cross-shelf section at the narrow part of the Mozambique Channel (17°S). The profiles represent the variations on the bottom topography: Black (GEBCO1), and red (SWIM model).

To remove steep topographic features in the deep ocean (e.g., seamounts), that could induce some numerical instabilities (e.g., horizontal pressure-gradient errors) into the system, a selective hanning filter was applied 4 times. Figure 3.5 gives an insight as to what extent the model derived topography after being filtered out steep features of the seafloor, can be affected. Important to mention that the smoothing is dependent on the horizontal grid resolution.

3.3.4 Surface fluxes

At the surface, SWIM is forced with monthly climatology fluxes: heat and fresh-water fluxes are at $\frac{1}{2^\circ}\times\frac{1}{2^\circ}$ grid size, derived from COADS (Da Silva et al., 1994). The wind stress is from satellite scatterometer, QuickSCAT for the period (2000-2007), gridded at $\frac{1}{2^\circ}\times\frac{1}{2^\circ}$, distributed by CERSAT ($http://www.ifremer.fr/cersat/en/index.html$). The sea surface temperature is a climatology at about ~ 9 km, pathfinder product from (Casey and Cornillon, 1999), and is used for a correction term $\frac{\partial Q}{\partial SST}$, in the heat flux calculation, accounting for the feedback of SST to the heat flux (Barnier et al., 1995).

3.3.5 Lateral boundaries and initial conditions

SWIM was prescribed with its physical lateral boundaries opened everywhere (North, South, East and West). The eastern boundary is predominantly characterized by the inflow of the South-Equatorial Current. The western boundary by the outflow, and inflow from both the Benguela Current and the South Indian Ocean Current, respectively. The northern boundary is mainly characterized by the outgoing East African Coastal Current, and the southern boundary the outflow faces the Sub-Antartic Front (SAF). At these boundaries, a mixed passive-active implicit radiation condition connects the model solution to the surrounding oceanic environment (Marchesiello et al., 2001). In an outflow condition, the outward solution is allowed to escape the model domain, whereas, in an inflow case (inward fluxes), the model solution is nudged towards the external dataset: monthly climatology, gridded at 1°×1°, World Ocean Atlas 2005 (WOA2005 Conkright et al. (2002)).

In addition, nudging of the layer at these boundaries were set to (x_{sponge}=300 km, with the viscosity value v_{sponge}=1500 m^2s^{-1}). The nudging coefficient for the tracers (for inflow and outflow), were set to (τ_{Tin}= 1.157×10^{-5} s^{-1}, and τ_{Tout}= 6.430×10^{-8} s^{-1}, respectively). The nudging coefficients for the incoming and outgoing velocities were (τ_{Min}= 3.858×10^{-6} s^{-1}, and τ_{Mout}= 6.430×10^{-8} s^{-1}, respectively). The input variables directly provided by WOA2005 were hydrographic temperature and salinity. Using these tracers, the horizontal velocities were estimated at the boundaries by the geostrophic relation, computed using a level of no motion at 1000 m. The model is initialized with the climatology of January, and 0 velocities (rest state).

3.4 Running the model and the spin-up

The model was run using Caparmor, a high performance computer, at Ifremer marine institute, France. The machine is a cluster Altix ICE 8200, SGI, with 64 nodes of calculus. Each node has 2 processors, 3.0Ghz Intel Dual-core Xeon (Woodcrest 5160). The 64 nodes are interconnected by $4\times DDR$ Infiniband. Each node has 16 G of memory.

Once all the required information to run the model was provided, SWIM was at first tested for 30 days run (for the purposes of verification). Then a 10 years run was performed, in a parallel computing regime, utilizing 64 cpus for efficiency. The partition of the domain was made in 4×16 subdomains, for longitude and latitude respectively. The total run was complete in about 4 days. The outputs were averaged at 2 days intervals. Diagnostics analysis on the integrated volume properties revealed a spin up time of the simulation (equilibrium state) after the first 3 years of run (Figure 3.6).

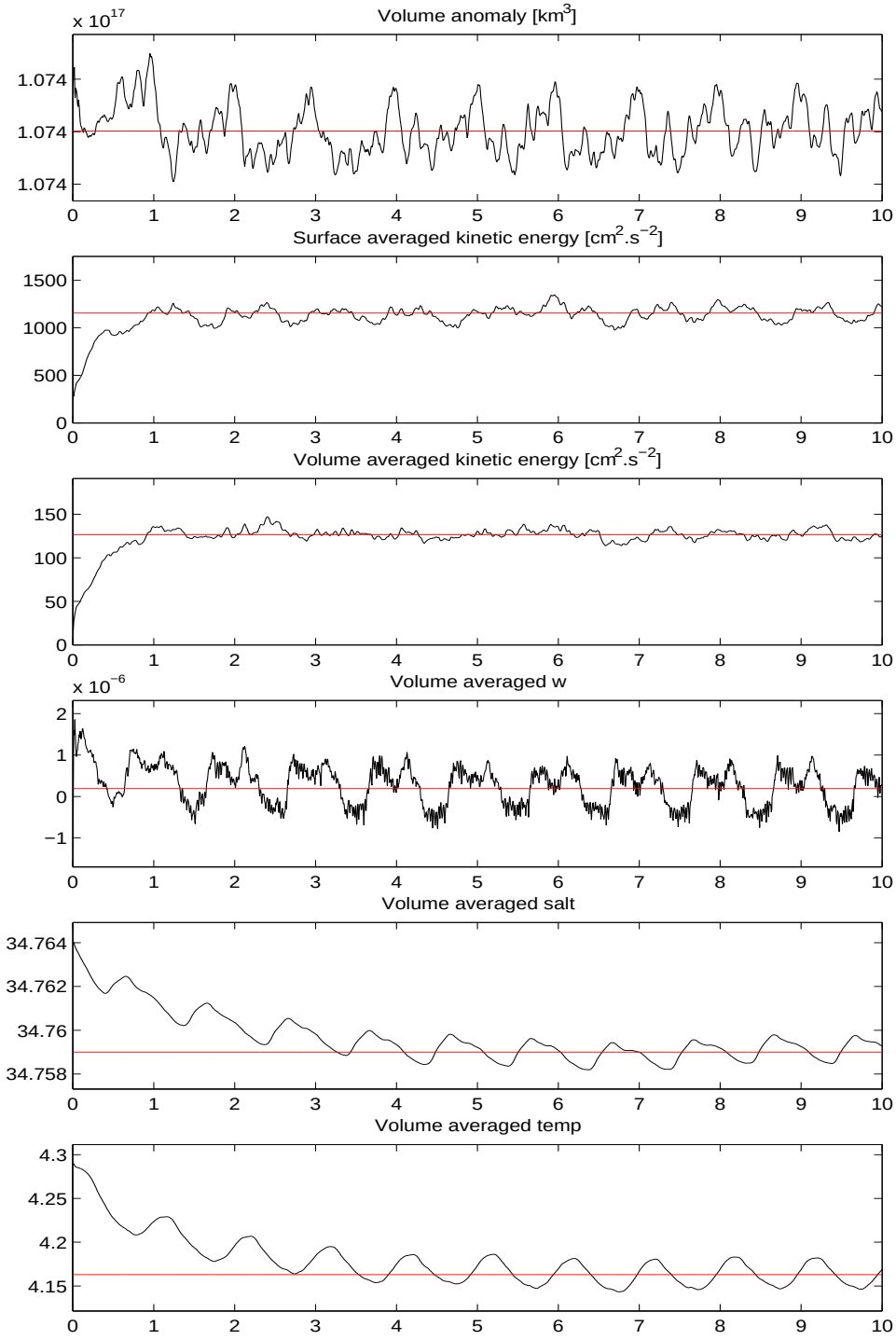

Figure 3.6. Integrated volume properties, shows that SWIM reached its equilibrium after the first 3 years of the simulation.

3.5 Data description

3.5.1 Satellite Altimetry data

Satellite altimeters provide information about variations of the sea surface height, used to study mesoscale ocean variability. In regions where in-situ observations are sparse, such as the Mozambique Channel, studies rely heavily on such altimetric observations. To-date, altimetry data spans almost 2 decades, from when it commenced in October 14, 1992. The gridded data product is produced by Ssalto/Duacs and distributed by AVISO, with support from CNES (*http* : *//www.aviso.oceanobs.com/*). It combines altimeter measurements from a number of satellites through an interpolation mapping technique (Ducet et al., 2000). In this study we use these gridded maps of absolute dynamic topography at a delayed-time (DT), that combine sea level anomaly observations merged from Jason-1, Envisat, GFO, ERS-1, ERS-2 and Topex/Poseidon with the Rio09 mean dynamic topography (Rio et al., 2011). The data are provided globally on a regular grid with a spatial resolution of $\frac{1}{4^\circ} \times \frac{1}{4^\circ}$, every 7 days.

3.5.2 LOCO Data

To evaluate the volume transport and its variability in the model, SWIM output is compared with in-situ observations from the Long-term Ocean Climate Observation program (LOCO) (De Ruijter et al., 2006, Ridderinkhof et al., 2010). The LOCO mooring array is situated across the narrow part of the channel near 17°S, and each mooring includes current meters, temperature-conductivity-pressure sensors and Acoustic Doppler Current Profilers (De Ruijter et al., 2006, Harlander et al., 2009, van der Werf et al., 2010). This array has consistently measured mass and heat transport through the Mozambique Channel since 2003, following a pilot study in 2000 - 2001, thus representing the longest time series of in-situ observations ever recorded in the Mozambique Channel. Details concerning the LOCO data, instruments and deployment strategy are given by Ridderinkhof and De Ruijter (2003), Ridderinkhof et al. (2010), Harlander et al. (2009). In the present study we used the data collected from November 23, 2003 to December 16, 2009, corresponding to four deployment periods, between which moorings were recovered, serviced and redeployed.

3.5.3 New CLS-CNES09 Data

The model annual mean SSH is compared against the mean dynamic topography (MDT) from the new CLS-CNES09 Dataset. The global MDT is computed at $\frac{1}{4^\circ}\times\frac{1}{4^\circ}$ resolution, for a time period ranging from 1993 to 1999, derived from the combination of 15 years of altimetric sea surface height and in-situ measurements, a recent geoid model computed from 4.5 years of Gravity Recovery and Climate Experiment data (GRACE). Different from RIO5 data (Rio and Hernandez, 2004), the new CLS-CNES09 Data is at relatively higher resolution, uses an updated dataset of drifting buoy velocities from 1993 to 2008, and dynamic heights from 1993 to 2007. It also uses an improved Ekman model to extract the geostrophic component of the buoy velocities. It has been shown that the new MDT resolves much stronger western boundary currents, and are in better agreement with the in-situ observations. The details of the product is given by Rio et al. (2011).

3.5.4 WOA05 Data

To evaluate the tracers distribution (Temperature and Salinity), of the model outputs, with in-situ data, we used the World Ocean Atlas 2005 (WOA05), global, monthly climatology, gridded at $1^\circ\times1^\circ$ (Conkright et al., 2002), at standard depth levels. The data is processed by the National Oceanic and Atmospheric Administration (NOAA), and archived at the National Oceanographic Data Center (NODC).

3.5.5 CARS09 Data

Another hydrographic dataset: CSIRO Atlas of Regional Seas 2009 (CARS09), also has been used in this study to reinforce our model data comparison. CARS09 is a digital global ocean climatology, or atlas of seasonal ocean water properties, gridded at $\frac{1}{2^\circ}\times\frac{1}{2^\circ}$ (Ridgway et al., 2002). The CARS09 variables, temperature and salinity, used in our study were based on several datasets, such as World Ocean Database 2005 (WOD05), surface-pressure-corrected Argo global archives, WOCE Global Hydrographic Program, etc. Different from WOA data, CARS09 applies an extra phase of quality control analysis of the input data, and also uses an adaptive length-scale scheme that maximizes the spatial resolution in regions of higher data density, while considering the topographic barriers of the ocean.

CHAPTER 4

Observational and Model data comparison

Key Question:

- **Does the SWIM model simulates satisfactorily the large and mesoscale oceanographic features of the Mozambique Channel?**

4.1 Mean-states

A comparison of observational and model data of the main oceanographic features of the system is presented here for the whole model domain, for evaluation of the SWIM model performance. However, consideration is given only to the features located in the South-West Indian Ocean, with special attention to the Mozambique Channel, our region of interest. The properties are evaluated in their annual mean-states, except for the eddy vertical structure, evaluated at an instantaneous state.

The variables compared are: surface and vertical distributions of potential temperature and salinity for representation of the water masses, meridional vertical distribution of

seawater density, SSH (proxy for geostrophic flows), meridional flow throughout the water column in the narrower part of the Mozambique Channel, volume transports in the path of the currents system, variability of SSH and eddy kinetic energy.

4.1.1 Water masses, property distribution

Water masses property distribution along the Mozambique Channel is presented. Figure 4.1 shows maps of temperature field, derived from the observational datasets (Figure 4.1a: WOA05, Figure 4.1b: CARS09), and model (Figure 4.1c: SWIM). Similarly Figure 4.2 shows their corresponding salinities. Both potential temperature and salinity were computed at 10 m depth to track the water masses and their distribution.

4.1.1.1 Surface Temperature

Comparing the maps of temperature between the different datasets: WOA05 (Figure 4.1a) and CARS09 (Figure 4.1b), within the Indian Ocean Basin, although strong similarities exist, there are also slight differences.

Similarities

The main similarities between the two dataset and SWIM outputs are observed on the following features: warmest near surface (10 m) temperatures of about 28°C, are located at the northeastern part of the domain, and are stretched zonally across the central Indian Ocean, to the east at 54°E, and to the north of 8°S. SWIM also is able to reproduce satisfactorily this structure (Figure 4.1c). This equatorial feature is part of the Pacific warm pool described by Tomczak and Godfrey (1994). On the other hand, the coolest near surface temperatures are about 6°C, observed along the southern boundary of the domain. This is a typical characteristic of subantartic mode water. Another similarity between observations and the model, is the strong temperature gradient, at the Subtropical Convergence Front (between 36°S and 40°S), known as a region of subduction (Tomczak and Godfrey, 1994), adjacent to the path of the Agulhas Return Current. In the model (Figure 4.1c), this feature seems to meander more than in the observations. Another feature also well resolved in the Indian Ocean Basin is the near zonally distributed isotherms (attributed to the lack of upwelling along the western coast of Australia (Tomczak and Godfrey, 1994)). Deflections from the zonal orientation of the isotherms occurs mainly

at the western boundary currents: South East Madagascar Current, and the Agulhas Current.

Differences

The differences between the model and observations are: the model reproduces a localized warmer temperature ($\sim 28°C$), around the central-northeastern coast of the Mozambique Channel (Figure 4.1c), that is not evident both in WOA05 and in CARS09. The model also reproduces a stronger southwestward spreading of the isotherm of 24°C at the southeast coast of South-Africa, near the Aguhas Current region. SWIM also reproduces larger south-westward penetration of temperature with about 20°C, into the South-East Atlantic Ocean (west of 20°E).

Between the two observational datasets, the isotherms of CARS09 (Figure 4.1b) are more meandering than WOA05 (Figure 4.1a). Also the southward deflection of the isotherm of 26°C, along the east coast of Madagascar, occurs much closer to the coast in WOA05 than in CARS09. In SWIM, these features are more consistent with CARS09 than with WOA05. Such a consistency could be possibly related to the relatively good resolution and interpolation schemes of CARS09 dataset relative to the WOA05.

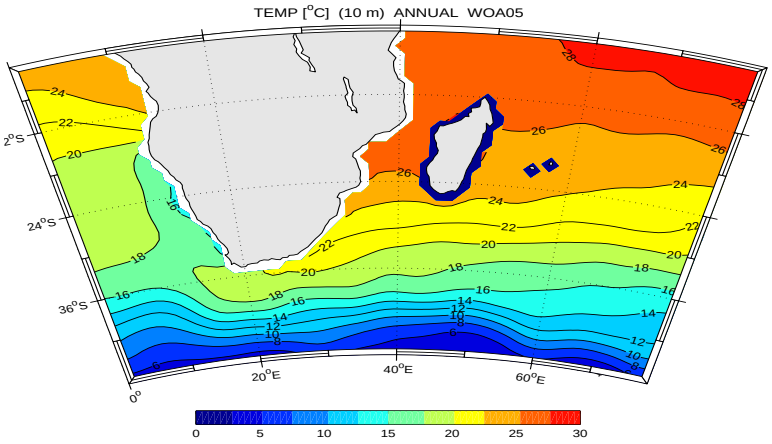

(a) WOA05

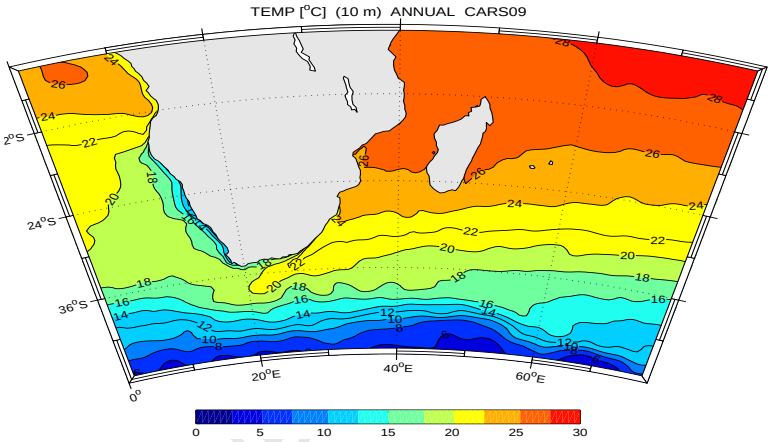

(b) CARS09

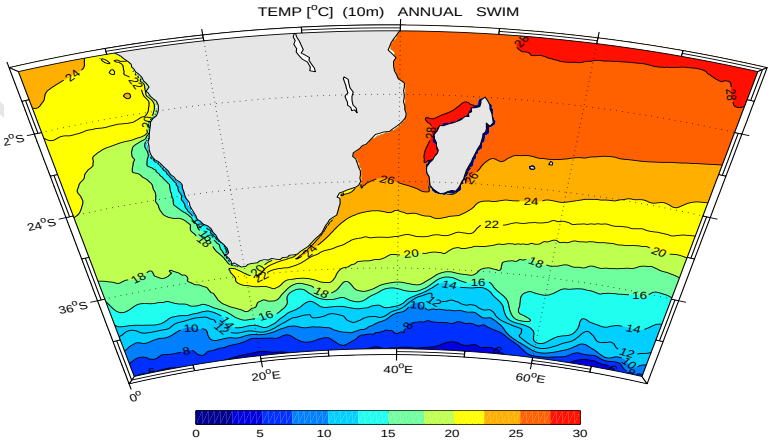

(c) SWIM

Figure 4.1. Temperature field at 10 m depth: WOA05 (a), CARS09 (b) and SWIM (c).

4.1.1.2 Surface Salinity

Maps of surface salinity distribution (Figure 4.2), shows that the features that stands-out in terms of similarities between model and observations within the Indian Ocean are many.

Similarities

Two distinct salinity tongues are observed at the eastern boundary of the domain, portraying different water masses: The north-eastern tongue is relatively fresher, water with about 34.5, and enters from the northeast sector of the domain, near 12°S, 75°E. Typical characteristics of the Indian Ocean Tropical Surface Water (TSW). Its lower salinity has been associated to the excess of precipitation over evaporation in the tropics (Wyrtki, 1971, Tomczak and Godfrey, 1994). On the other hand, the southeastern tongue, near 30°S, 75°E, is saltier water, with about 35.75. It exhibits typical characteristics of the Indian Ocean Subtropical Surface Water (STSW). Its higher salinity is known to be associated with the excess of evaporation over precipitation in the subtropics (Wyrtki, 1971), within the subtropical gyre.

Another similar pattern is the southward spreading of high salinity water with 35.25, towards the Mozambique Channel, along the african coast, and also the southward spreading of the isohaline of 35 along the east coast of Madagascar. For the southward extension of the 35.25 isohaline, it seems exaggerated in WOA05 (Figure 4.2a, where it reaches the northeastern part of Madagascar, near 17°S), and under-represented in SWIM (Figure 4.2c, where it barely reaches 6°S), when compared to CARS09 (Figure 4.2b). It is likely that such an under-representation in SWIM may be related to the boundary problems. Similarities also are evident in regard to the representation of the Subtropical Converge Front at right position, between 36°S and 40°S. With regard to the southward spreading of the isohaline with 35 along the east coast of Madagascar, WOA05 and CARS09 are in a reasonable agreement, while SWIM has failed to reproduce such a spreading. Another feature in good agreement between WOA05 and CARS09, but that SWIM shows some difficulties in reproducing is the north - south expansion of the westward water type characterized with 35.5, between 30°S and 38°S, and between 30°E and 60°E. This feature is thicker in WOA05 and CARS09, but thin in SWIM (Figure 4.2).

Differences

Differences between WOA05 and CARS09 is the westward spreading of the salinity isohaline of 35. In WOA05 such an isohaline is blocked at the east coast of Madagascar (Figure 4.2a), while in CARS09 it reaches the African continent, around the northern Mozambique Channel, between 15°S and 11°S (Figure 4.2b). In SWIM such a feature reaches its westernmost position around 44°E. Another evident difference between WOA05 and CARS09 is the representation of relatively fresher water type with 35, by CARS09, at the Sofala Bank (western boundary on the central part of the Mozambique Channel). SWIM also did not reproduce such a fresh water on the bank (Figure 4.2c). This relatively fresher water on the bank seems to be a result of dilution of the seawater by fresher waters from the Zambezi river. Although SWIM was not forced by rivers, the imprint of low salinity water on the climatology dataset around the Sofala Bank could be expected because they characterize the coastal ocean waters of the region. Note that the absence of WOA05 data closer to the coast (Figure 4.2a), makes difficult the comparison.

Though the model has reproduced the presence of these water masses, it also has some difficulties in reproducing the spatial spreading of some water types, specially that with 35 around 12°S, at the northern tip of Madagascar, and the water type with 35.25 entering into the Mozambique Channel from the northern boundary of the domain (Figure 4.2c). There, SWIM has shown lesser meridional spreading of the isohaline of 35.25, when compared against WOA05 and CARS09. On the other hand, with regards to the isohaline of 35, SWIM has shown a relatively longer zonal spreading when compared to WOA05, but lesser spreading when compared against CARS09.

The evaluation of the surface temperature and salinity suggests that the model reproduces in a reasonable manner the elements of the main water masses occupying the upper layer of the South-West Indian Ocean. Therefore the confidence in SWIM is good.

Analysis of the water masses throughout the water column is presented in Figure 4.3 and Figure 4.5. It must be noted that for the objectives of our analysis, within the Mozambique Channel, the vertical section is made at 41°E along the channel, chosen to be the suitable position to assess the property distribution throughout the channel length. The position 41°E has shown to be the favorable site where SWIM was able to capture a wider range of different water masses present in the region.

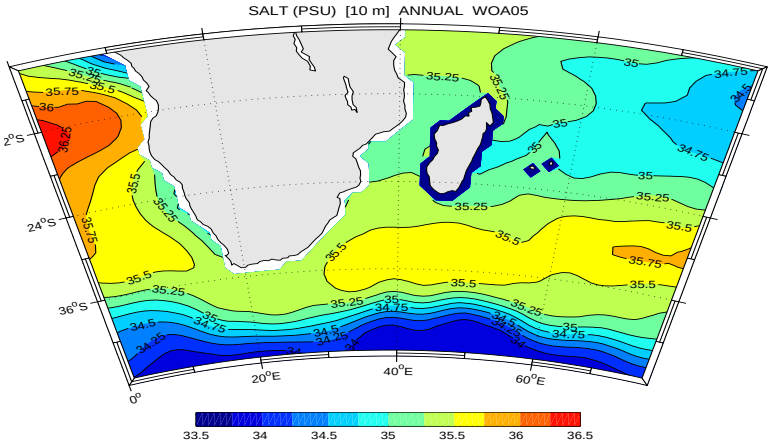

(a) WOA05

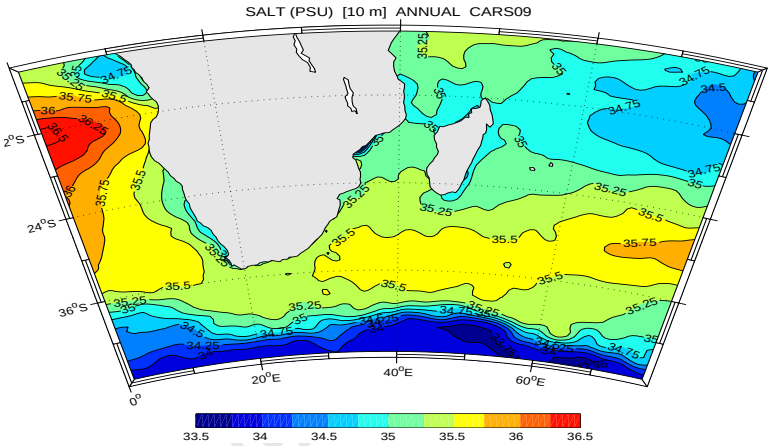

(b) CARS09

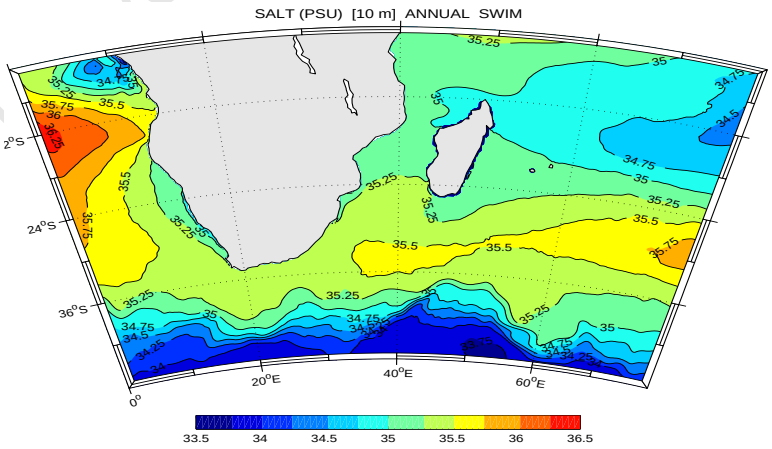

(c) SWIM

Figure 4.2. Salinity field at 10 m depth: WOA05 (a), CARS09 (b) and SWIM (c).

4.1.1.3 Vertical sections of potential temperature at 41°E

Meridional vertical distribution of potential temperature is presented. Figure 4.3a is derived from WOA05 climatology, Figure 4.3b is derived from CARS09 climatology, and Figure 4.3c is derived from SWIM, 7-year climatology of the model run.

Similarities

In all cases, the meridional distribution of the isotherms throughout the water column suggests a deeper thermocline in the south, and a shallower thermocline in the north (Figure 4.3). To the south of 35°S, the isotherms also show a deepening to about 1500 m depth, while to the north of that latitude the isotherms are nearly horizontal. This pattern is consistent with the subduction of the water masses at the Subtropical Convergence Front, near 40°S (Gupta and England, 2007), and also consistent with the presence of an eastward geostrophic flow of the Agulhas Return Current (Lutjeharms and Ansorge, 2001, Lutjeharms, 2006).

A zoom of the Figure 4.3 on the upper 500 m depth is shown in Figure 4.4. It reveals a nearly vertical profile of the isotherms at the position of the Subtropical Convergence Front, which could be attributed to mixing process. The pattern is also reproduced by the model (Figure 4.4c). Strong mixing at the Subtropical Convergence Front is consistent with the formation and interleaving of properties of the water masses, Subantartic Mode Water (SAMW) described in the literature (Wyrtki, 1971, Tomczak and Godfrey, 1994, DiMarco et al., 2002, Beal et al., 2006).

In Figure 4.4, an interesting pattern has been observed to the north of approximately 35°S: nearly between 50 m and 150 m depth, the isotherms show a sloping pattern, while from about 400 m to 200 m depth, the isotherms have a shoaling orientation. Strong perturbations on the pattern are characterized by a sloping, observed between 50 m and 400 m depth, located between 15°S and 10°S in WOA05 (Figure 4.4a), and between 20°S and 5°S in CARS09 (Figure 4.4b) and SWIM (Figure 4.4c).

The pattern reproduced by SWIM is more consistent with CARS09 than WOA05, however, with a slight exaggeration in SWIM between 20°S and 15°S. The deepening south-north orientation of the isotherms observed between 50 m and 200 m depth, could be related to the sinking of the Subtropical Surface Water (STSW) to Sub-surface layer (compare with Figure 4.6). On the other hand, the shoaling south-north orientation of the isotherms could be associated to the rising and out-cropping of the thermocline water,

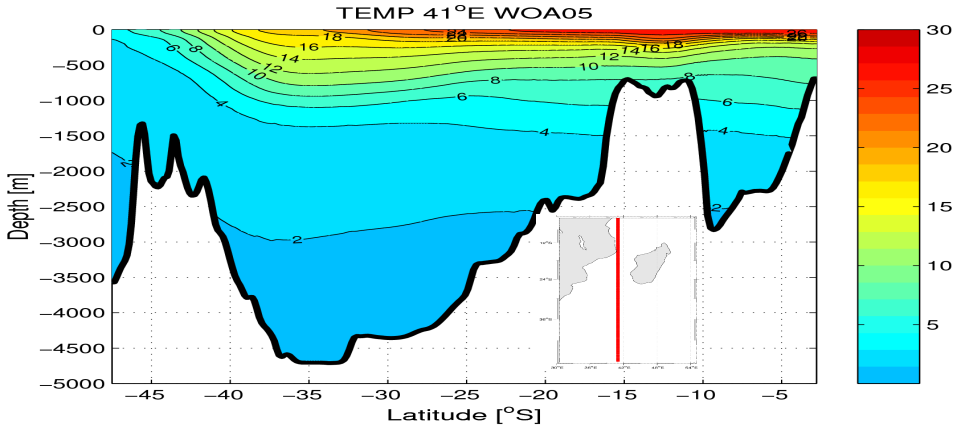

(a) WOA05

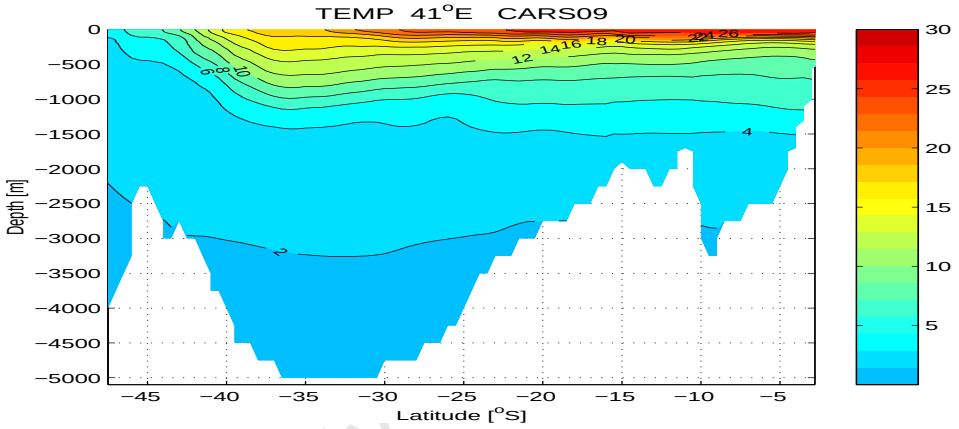

(b) CARS09

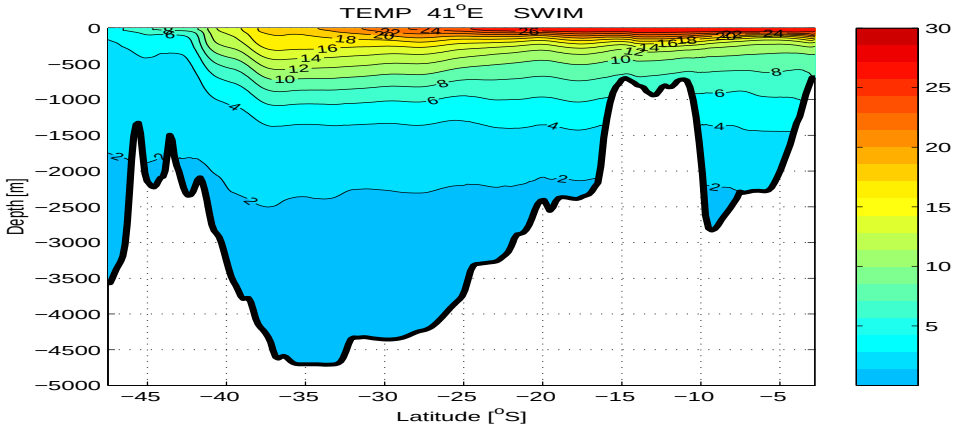

(c) SWIM

Figure 4.3. Annual vertical sections of meridional distribution of potential temperature, throughout the ocean column, computed at 41°E, to cross the whole channel length. WOA05 (a), CARS09 (b) and SWIM (c). For the transect position see the image inserted in panel (a).

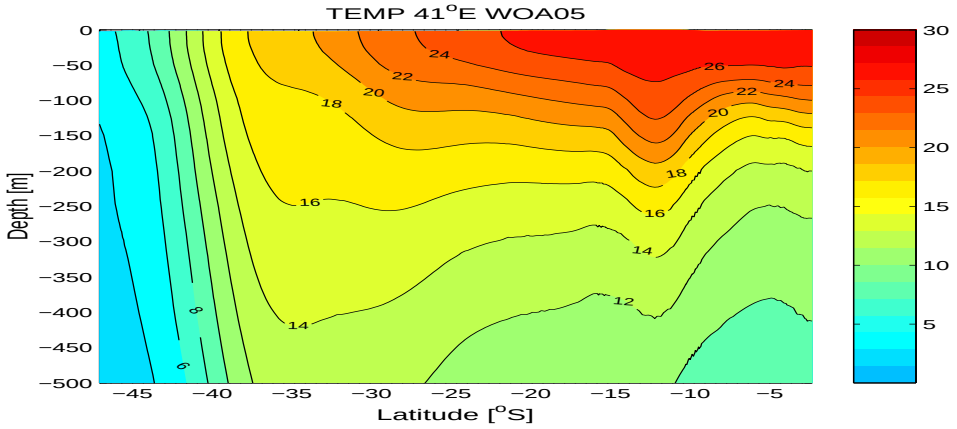

(a) WOA05

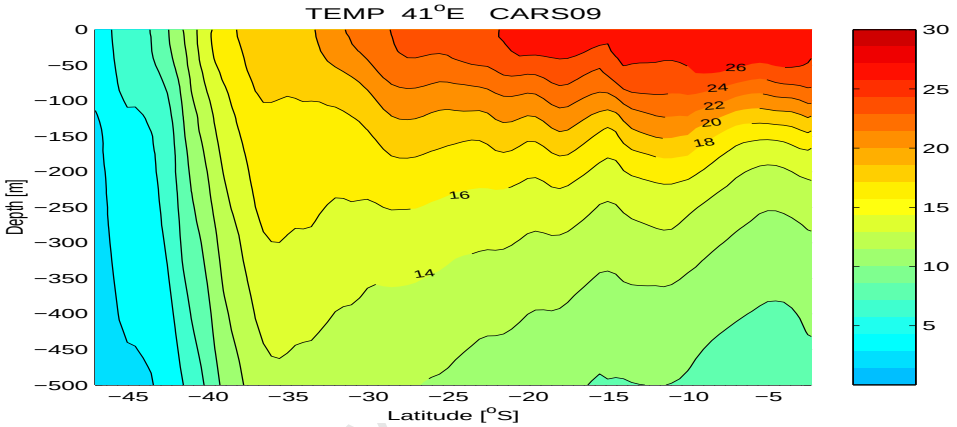

(b) CARS09

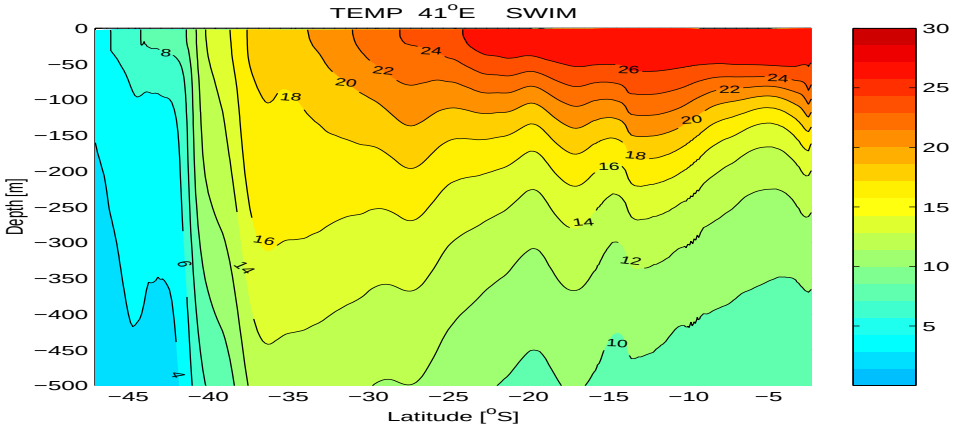

(c) SWIM

Figure 4.4. Annual vertical sections of meridional distribution of potential temperature, throughout the ocean column, computed at 41°E, to cross the whole channel length. WOA05 (a), CARS09 (b) and SWIM (c). (same as in Figure 4.3, but for the upper 500 m depth of the ocean column.

likely the SAMW (Fine, 1993, Beal et al., 2006).

The perturbation of the isotherms between 20°S and 15°S, could be associated with the shallowing of the bottom topography, due to the presence of the Davie Ridge (Figure 4.3). A warm feature of surface waters within the Mozambique Channel, to the north of about 20°S, is seen on the upper 50 m of the ocean column (Figure 4.4). Its temperature characteristics are similar to the Surface Tropical Waters (TSW), known to propagate southwards through the Mozambique Channel (Beal et al., 2006, DiMarco et al., 2002, De Ruijter et al., 2002).

Differences

The main differences observed is that SWIM reproduces a stronger uplift of colder isotherm of 4°C, between 45°S to 40°S in the upper 500 m, slightly vertically oriented isotherms near 40°S (Figure 4.4c), stronger fluctuations of the isotherms in the upper 500 m, between 25°S to 5°S (Figure 4.4c).

4.1.1.4 Vertical section of salinity at 41°E

Meridional salinity distribution throughout the water column is also investigated (Figure 4.5). Figure 4.5a shows WOA05 climatology, Figure 4.5b shows CARS09 climatology, and Figure 4.5c is derived from the 7-year climatology of SWIM model.

Similarities

Both model and observations show a good agreement. With salinity, a clear distinction of the different water masses is observed. Our analysis made previously in Figure 4.3, in combination to the property distribution presented in Figure 4.5, shows that from south to north, the following water masses can be identified: Subantartic Mode Water (SAMW), dominating the upper ocean, to the south of 40°S. Subtropical Surface Waters (STSW), also dominating the upper ocean, between 40°S and 20°S. Antartic Intermediate Waters (AAIW), present between about 2000 m and 1000 m depth of the water column, also between 40°S and 20°S. Tropical Surface Waters (TSW), dominating the upper layers, mostly between 20°S and 8°S. North Indian Deep Water (NIDW), is observed to the north of 10°S, between 500 m and 1500 m. A description of these water masses has been presented, and is consistent with the current knowledge presented by Beal et al. (2006).

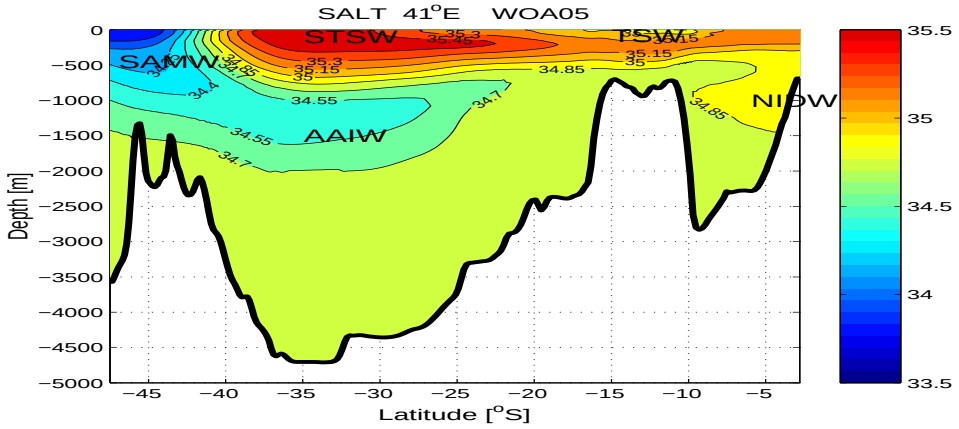

(a) WOA05

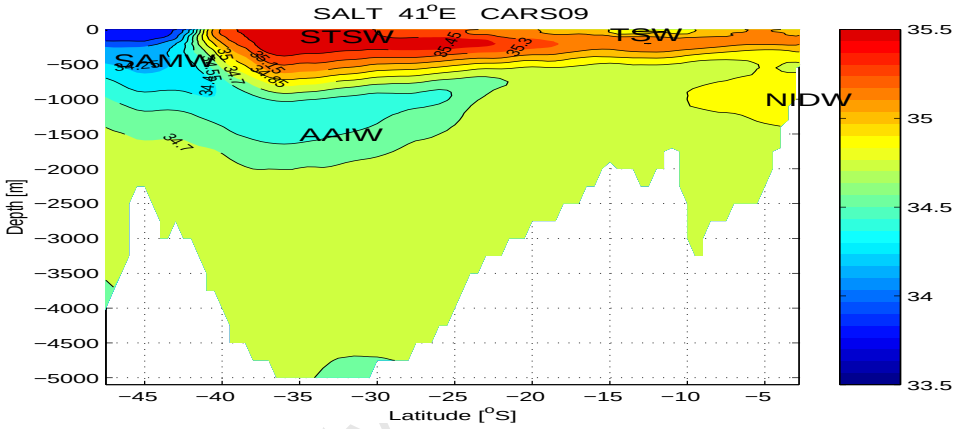

(b) CARS09

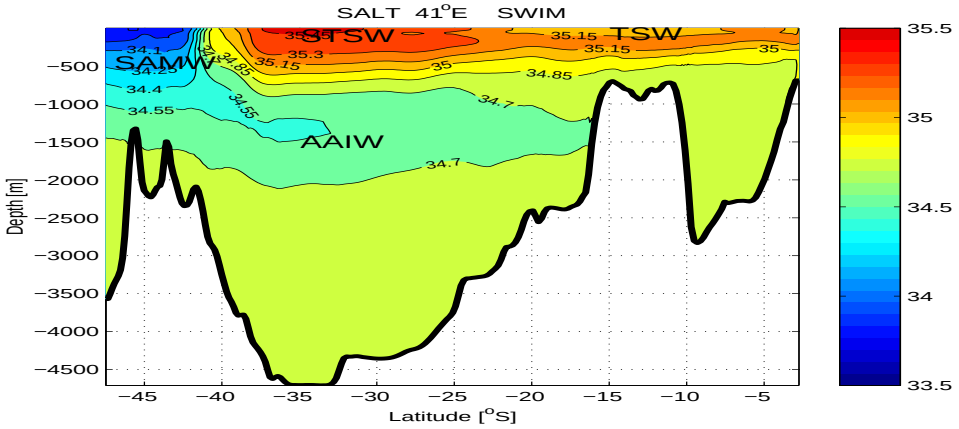

(c) SWIM

Figure 4.5. Annual vertical sections of meridional distribution of salinity, throughout the ocean column, computed at 41°E, to cross the whole channel length. WOA05 (a), CARS09 (b) and SWIM (c).

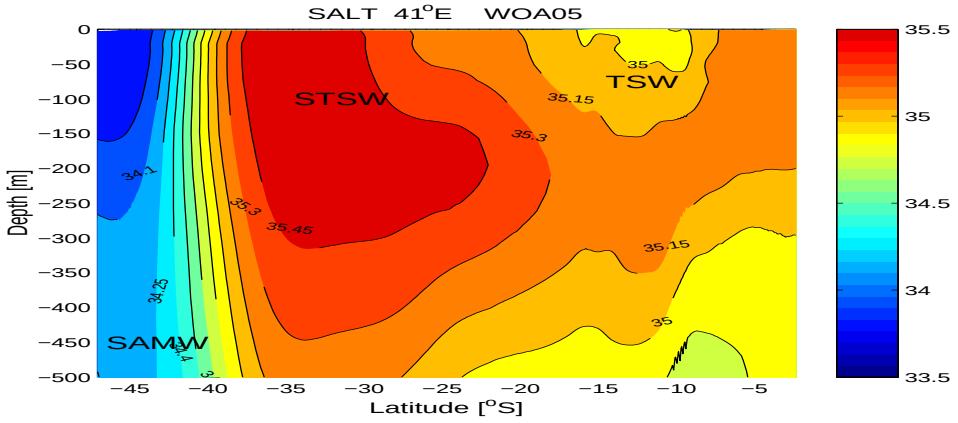

(a) WOA05

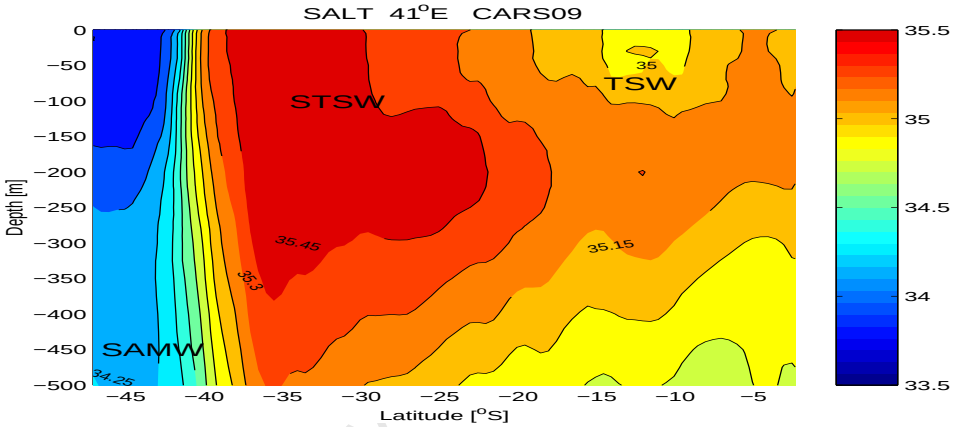

(b) CARS09

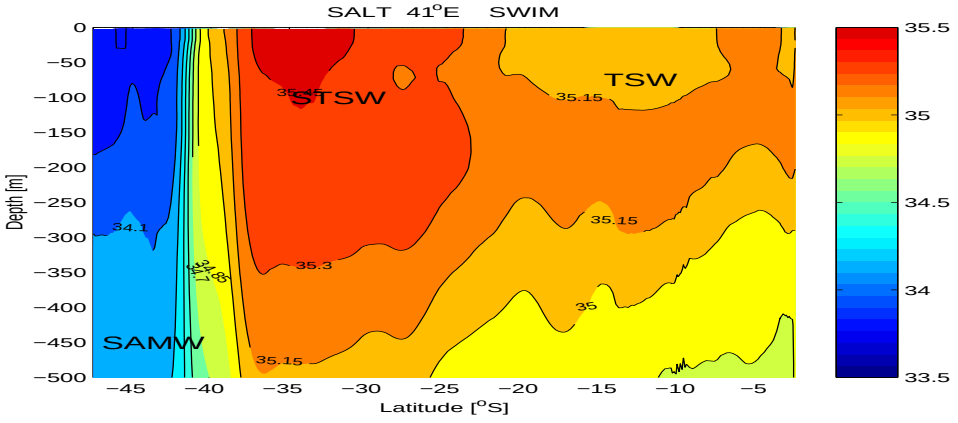

(c) SWIM

Figure 4.6. Annual vertical sections of meridional distribution of salinity, throughout the ocean column, computed at 41°E, to cross the whole channel length. WOA05 (a), CARS09 (b) and SWIM (c). (same as in Figure 4.5, but for the upper 500 m depth of the ocean column).

A zooming of the Figure 4.5, for the upper 500 m of the water column is presented in Figure 4.6. The pattern of the isohalines is consistent with the pattern of the potential temperature presented in Figure 4.4. Outstanding features are the near vertically oriented isohalines in the Subtropical Convergence Front, between 45°S and 38°S, consistent with vertical mixing; perturbations of the isohalines, between 15°S and 10°S; upwelling of a relatively low salinity water, with about 35, towards the halocline, to the south of 25°S; northward spreading to about 22°S of the STSW on the upper 300 m of the water column.

Both WOA05 (Figure 4.6a) and CARS09 (Figure 4.6b), show comparable vertical extension of the STSW with salinity 35.45, at a depth of about 300 m and 350 m respectively. On the other hand, SWIM has shown some difficulties in reproducing the STSW at comparable depths (reaching only a depth of about 100 m). Again, WOA05 and CARS09 also show comparable representation of the TSW with salinity 35, between 15°S and 10°S, while SWIM has failed to reproduce such a feature at that particular latitudinal band (Figure 4.6c).

Differences

Although the model reproduced the water masses, it has also some difficulties in reproducing accurately some features, such as the northward spreading of the water type with salinity 34.7 (likely AAIW), and also it lacks the representation of the NIDW (Figure 4.5c). The later could be related to the boundary problems (i.e: interpolations at the open boundaries of the models).

4.1.1.5 Vertical section of density at 41°E

Figure 4.7 presents the meridional density distribution on the upper 2000 m of the water column. The density has been calculated from potential temperature and salinity fields, using the seawater equation of state (Jackett and MacDougall, 1995). Figure 4.7a shows WOA05 climatology, Figure 4.7b shows CARS09 climatology, and Figure 4.7c is derived from 7-year climatology of the model run (SWIM).

Different from the potential temperature and salinity fields, the density to the south of 40°S, has shown a northward gentle slope between 47°S and 40°S, and a steep slope between 40°S and 35°S. To the north of 35°S, the isopycnals show a shoaling pattern (Figure 4.7). This pattern is also reproduced in the model (Figure 4.7c).

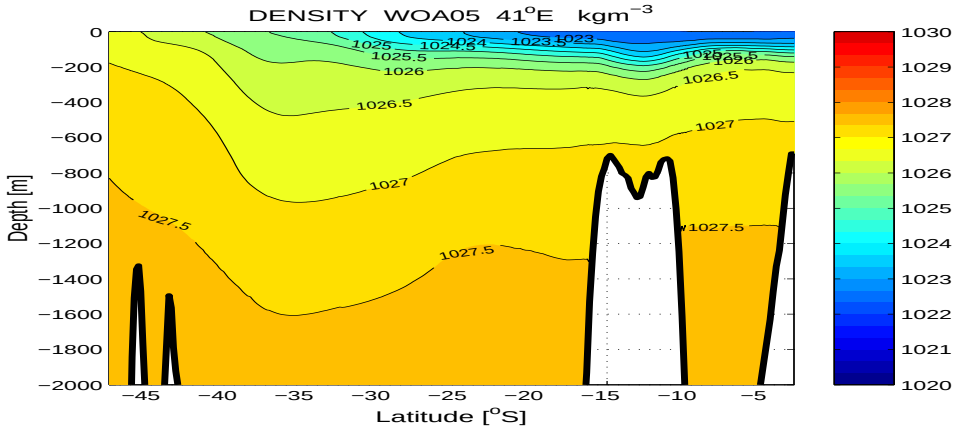

(a) WOA05

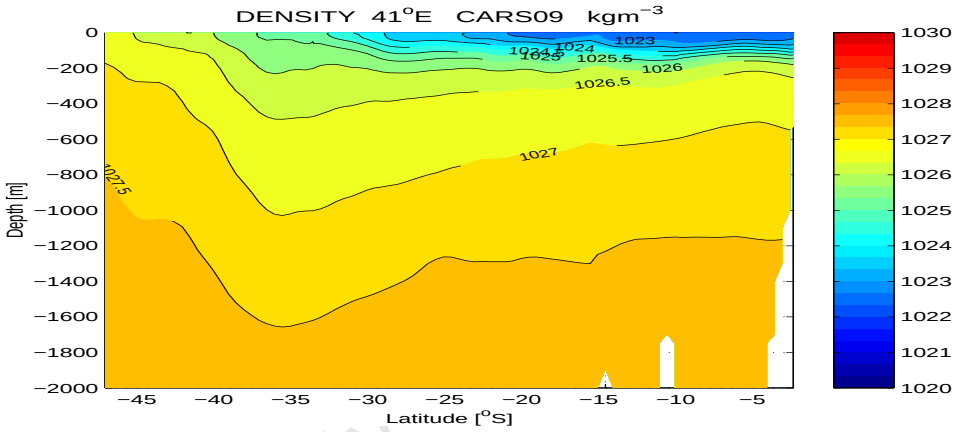

(b) CARS09

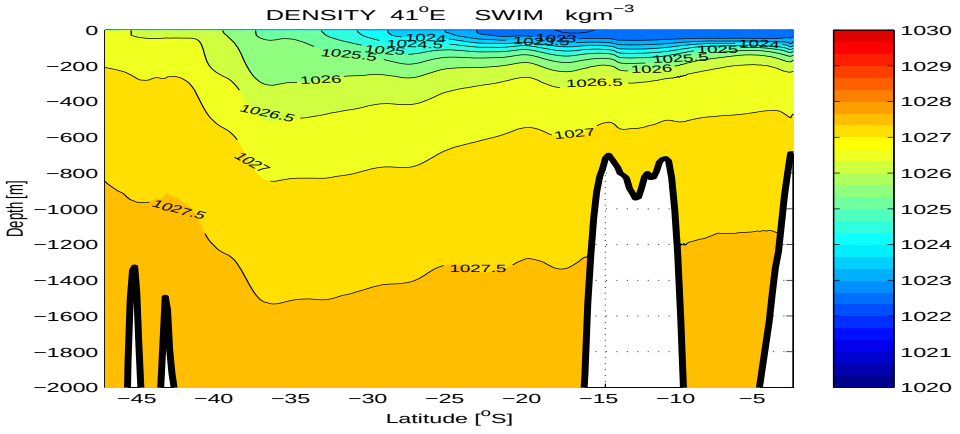

(c) SWIM

Figure 4.7. Annual vertical section of meridional distribution of density, throughout the ocean column, computed at 41°E, to cross the whole channel length. for WOA05 climatology (a), CARS09 (b), and 7-year SWIM climatology (c).

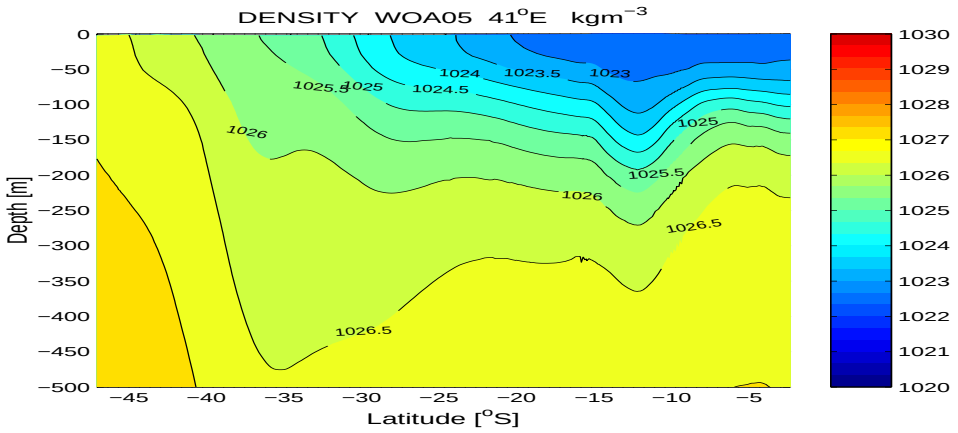

(a) WOA05

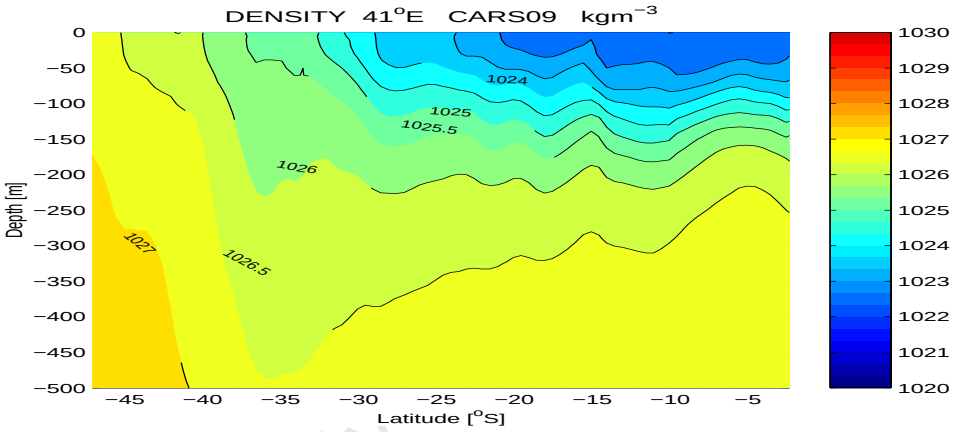

(b) CARS09

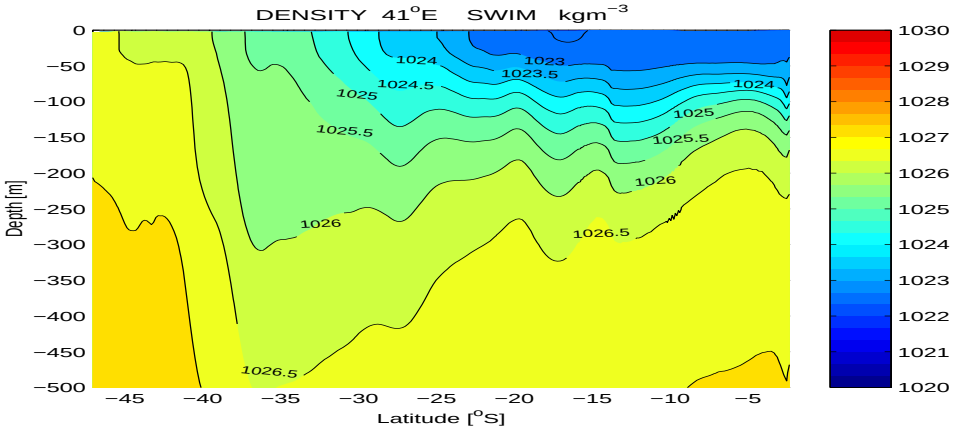

(c) SWIM

Figure 4.8. Annual vertical section of meridional distribution of density, throughout the ocean column, computed at 41°E, to cross the whole channel length. for WOA05 climatology (a), CARS09 (b), and 7-year SWIM climatology (c). (as in Figure 4.7, but for the upper 500 m).

Within the upper layers between 0 and 200 m, the isopycnals are largely spaced (likely high mixing) to the south of approximately 30°S, while to the north of 30°S, the isopycnals are closely spaced, an indicative of higher stratification. For the whole ocean column, the thickness between the isopycnals increase gradually downwards.

To the north of 35°S, the structure of the isopycnals are consistent with the structures of temperature and salinity presented previously. The steep slope of the isopycnals observed between 40°S and 35°S (Figure 4.7) is consistent with the presence of the eastward geostrophic flow of the Agulhas Return Current (Lutjeharms and Ansorge, 2001, Lutjeharms, 2006).

A zooming of the Figure 4.7 for the upper 500 m is presented in Figure 4.8. WOA05 climatology (a), CARS09 (b) and 7-year SWIM climatology (c). The zoom image clearly shows that in observations, the pattern of the northward slope of the isopycnals has more number of undulations in CARS09 (Figure 4.8b), than in WOA05 (Figure 4.8a). However, the amplitude of the undulation between 15°S and 10°S, and between 50 m and 350 m depth is higher in WOA05, than in CARS09. In SWIM, the pattern of the isopycnals is more consistent with CARS09 than with WOA05.

The overall conclusion about the model capabilities in reproducing the main hydrographic features of the system is observed by its results to be more closely aligned to climatology dataset from CARS09 than WOA05. This could be attributed to the interpolation scheme of CARS09 to be better scale selective than WOA05.

4.1.1.6 T-S diagram along 41°E

Salinity as a function of potential temperature (T-S diagram), based on the annual water properties extracted from the meridional transect along the 41°E is presented in Figure 4.9a for WOA05 climatology, Figure 4.9b for CARS09 climatology and Figure 4.9c for SWIM, 7-year climatology of the model run. From these, different water masses can be inferred.

As expected, Figure 4.9 is consistent with Figure 4.3 and Figure 4.5. The ability of the SWIM model (Figure 4.9c) in reproducing the water masses of the region is evaluated by comparing its T-S diagram against those derived from observations (CARS09 and WOA05). The comparison allows us to identify the following features:

Both for SWIM (Figure 4.9c) and observations (WOA05, Figure 4.9a and CARS09, Figure 4.9b) are observed water properties with temperature range between 18°C and 20°C, and salinity greater than 35.5, within a range of density anomaly between 24 kgm^{-3} and 26 kgm^{-3}: these are typical characteristics of the South Indian Ocean Central Water (SICW) as described by Emery (2001), which also are termed Subtropical Surface Water (STSW (You, 1997)).

Another hydrographic feature captured by the model (Figure 4.9c) is the relatively warmer water mass with temperature range between 25°C and 28°C, and salinity relatively fresher, ranging between 35 and 35.5, within a range of density anomaly between 22 kgm^{-3} and 24 kgm^{-3}: these characteristics are consistent with the presence of the Indian Ocean Surface Tropical Water (STW), as described by Schott et al. (1988) and Swallow et al. (1988).

In the range of temperature between 10°C and 15°C, and salinity between 34.5 and 35, for density of about 26.5 kgm^{-3}, the water properties suggest the presence of Subantartic Mode Water (SAMW (Gordon et al., 1987, Beal et al., 2006). Another water masses that also have been captured by SWIM is the Antartic Intermediate Water (AAIW) characterized by salinity around 34.4 and 34.6, temperature between 5°C and 7°C and density anomaly of about 27 kgm^{-3}. These characteristics are consistent with the description given by Emery (2001). The Indian Deep Water (IDW) is identified on the lowest inflection point of the diagram. It has temperature of about 2°C, salinity of about 34.8 and density of about 27.8 kgm^{-3}, consistent with hydrographic study by Gordon et al. (1987). The northern Indian Ocean water mass is also reproduced in SWIM, despite some difficulties: it has temperature of about 8°C, salinity of 35 and density anomaly of about 27 kgm^{-3}. Its property suggests the mixing of NIDW with the Red Sea Water

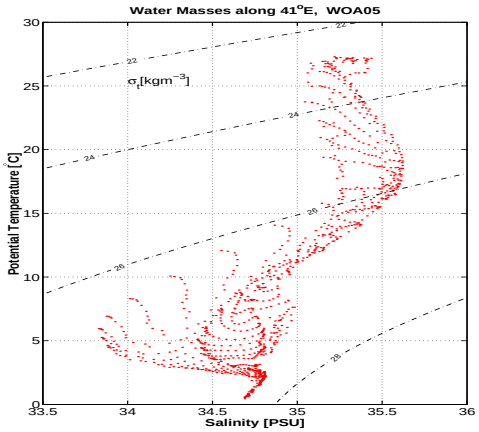

(a) WOA05

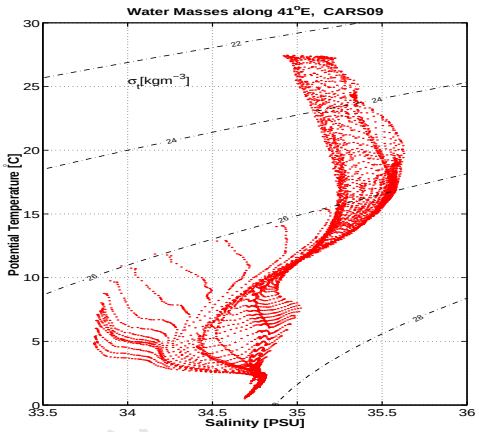

(b) CARS09

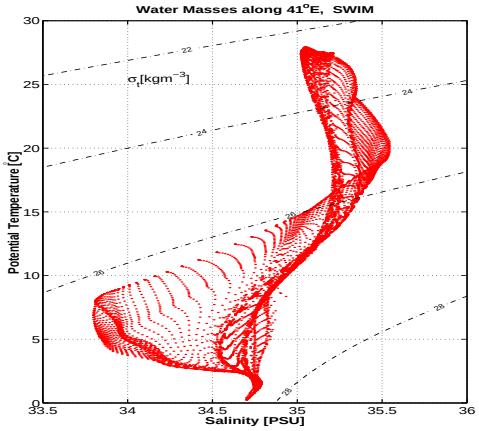

(c) SWIM

Figure 4.9. T-S diagrams, for the annual potential temperature and salinity extracted along the vertical meridional section computed at 41°E, to cross the whole channel length. for WOA05 climatology (a), CARS09 (b), and 7-year SWIM climatology (c).

(RSW), likely at intermediate depths (Gründlingh, 1985, Beal et al., 2006, Roman and Lutjeharms, 2009).

Lowest salinity (Figure 4.9) is about 33.8, with temperature range between 5°C - 8°C and density anomaly of about 26.5 kgm^{-3}. The characteristics of this water mass is similar to that presented by Gordon et al. (1987), termed by Subantartic Surface Water (SAASW), which appears to be represented to the south of the Subantartic Mode Water (SAMW) in Figure 4.5, though not indicated.

Relatively higher grid resolution in SWIM ($\frac{1}{5^\circ}$), compared to WOA05, interpolated at 1°×1° spatial grid, and CARS09 interpolated at $\frac{1}{2^\circ}\times\frac{1}{2^\circ}$ spatial grid, shows a denser sampling points (Figure 4.9c), which allows a more detailed characterization of the property distribution in SWIM than in observations (WOA05, Figure 4.9a, and CARS09, Figure 4.9b). Main differences observed in SWIM (Figure 4.9c), when compared against the observations (WOA05, Figure 4.9a, and CARS09, Figure 4.9b) are the representation of the Subantartic Surface Water (SAASW), which appears relatively warmer in SWIM, the representation of the Red Sea Water (RSW), which appears relatively fresher, and the representation of the Subtropical Surface Water (STSW), which also appears relatively fresher in SWIM. The model difficulties in reproducing accurately the temperature of SAASW and the salinity of the STSW, is likely related to the surface forcing terms of the model. On the other hand, difficulties in reproducing the salinity of the RSW could be associated with the position of the northern boundary of the SWIM configuration, blocked at 2.7°S.

The comparison of the T-S diagrams between SWIM and the observations, suggests that the model reproduces the presence of the main water masses in the southwest Indian Ocean, despite some difficulties in reproducing accurately their mixing.

4.1.2 Flow field

4.1.2.1 Surface geostrophic flow represented by mean SSH

Model derived streamlines of long-term average of variations of the sea surface height SSH (proxy of geostrophic flow field), derived from 7-year climatology (Figure 4.10b), is compared against observational data, (Figure 4.10a), absolute mean dynamic topography, derived from the new CLS-CNES09 product (Rio et al., 2011).

Similarities

Both SWIM and observation show the following features of the large-scale circulation: the westward propagation of the South Equatorial Current (SEC) between 20°S - 10°S, at the east coast of Madagascar; splitting of the SEC at the east of Madagascar in two opposite flows near 17°S; splitting of the NEMC at the east African coast, near 11°S; anticyclonic recirculation in the Comores Basin; a southward coastal flow along the whole Mozambican coast, and also eddy-like recirculation within the central part of the channel. At the south east coast of Madagascar, also is observed the excursion of the southern branch of the East Madagascar Current (SEMC); extension of the flow from the southwest of Madagascar, towards the southeast coast of South-Africa; partial retroflection and an anticyclonic recirculation of the SEMC at the South of Madagascar; flow of the Agulhas Current, along the South-East coast of South-Africa; retroflection of the Agulhas Current around 20°E, 40°S; eastward propagation of the Agulhas Return Current (ARC), near a zonal band between 35°S and 45°S, 18°E and 70°E.

Differences

Although there are many similarities between SWIM and the new CLS-CNES09 product, slight differences are apparent: the model has reproduced a relatively weaker SSH gradient of SEMC, between 26°S and 20°S; a relatively weaker recirculation loop of the Agulhas retroflection, between 20°E and 40°S; a narrower and more meandering flow of the ARC, specially between 40°E and 60°E, with its southeastern part slightly shifted to the north; and stronger anticyclonic recirculation at the offshore edge of the Agulhas Current, centered at 30°E and 35°S, nearly connecting the Agulhas Current and its return flow (ARC).

Despite such differences the model has successfully reproduced the main circulation features of the Greater Agulhas System during past investigations as presented by Lut-

jeharms (2006). Therefore SWIM model can be satisfactorily used to to achieve the objectives of the present study.

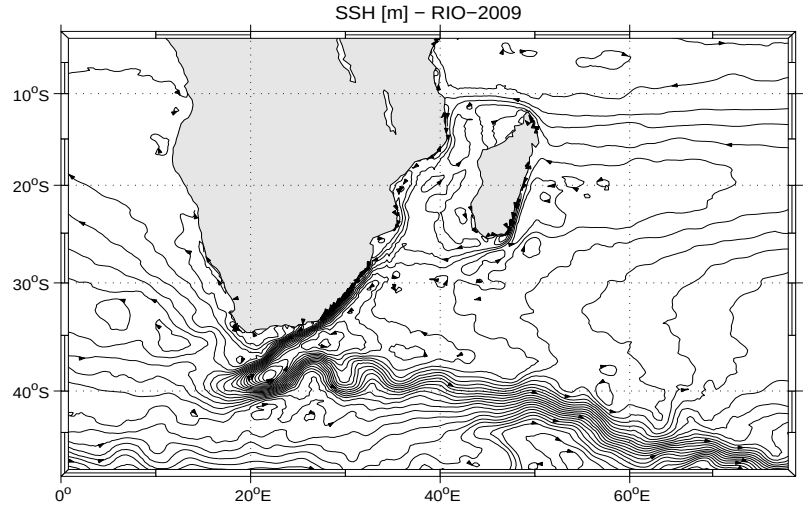

(a) RIO9

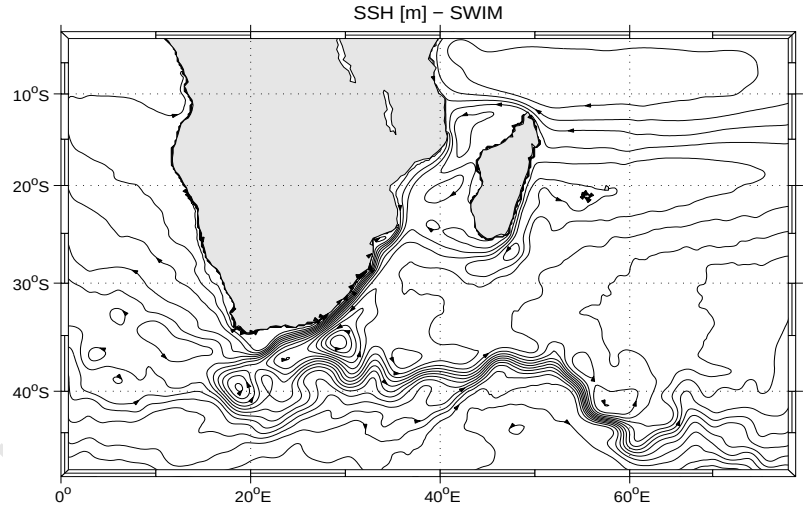

(b) SWIM

Figure 4.10. Annual mean sea surface height (SSH), proxy of the surface geostrophic flow. Upper panel (a), is derived from the new CLS-CNES09 product, lower panel is from 7-year climatology of the model run. The arrows indicate the direction of the flow, with contour intervals given at 5 cm.

4.1.2.2 Vertical structure of the mean flow at 17°S

We have evaluated the vertical structure of the meridional mean flow at 17°S, the only location in the Mozambique Channel where the longest and consistent, in-situ timeseries ever observed by LOCO moorings is available (De Ruijter et al., 2006, Ridderinkhof et al., 2010). Figure 4.11a, shows the flow field in LOCO, and Figure 4.11b shows the flow derived from 7-year climatology of the model run (SWIM).

Similarities

Consistent patterns between SWIM and LOCO can be identified on the following structures: both have shown a mean poleward flow (in blue) along the upper western boundary of the channel (Mozambican coast), and an equatorward flow (in red) on the upper eastern boundary of the channel (Madagascar coast). The poleward flow are more surface intensified than the equatorward flow, reaching a maximum velocity over 50 cm s^{-1}, and minimum velocities of about 5 cm s^{-1}, at about 1000 m depth of the ocean column. Another similarity between SWIM and LOCO is the capture of the Mozambique Undercurrent, flowing equatorward along the western boundary of the channel, below 1500 m depth (Figure 4.11b). This is consistent with in-situ observation by De Ruijter et al. (2002), who found a Mozambique Undercurrent on the continental slope of the Mozambican coast. Ridderinkhof and De Ruijter (2003) have suggested that this Undercurrent might be a continuation of the Agulhas Undercurrent reported by Beal and Bryden (1997).

Differences

Main differences between SWIM and LOCO are few, and can be identified: In regard with the equatorward component of the flow at the upper eastern boundary of the channel, it is relatively more intensified in SWIM than in LOCO. This flow also reaches about 1500 m in SWIM, while in LOCO it is shallower, reaching only about 500 m depth. The presence of a poleward flow along the western boundary of the Mozambique Channel, and an equatorward flow along the eastern boundary in the long-term averaged flow, could be attributed to the residual effect of the propagating eddies, in a flow field dominated by anticyclonic eddies. This is consistent with Harlander et al. (2009) and van der Werf et al. (2010), who have inferred that the eddies in the Mozambique Channel leave their signature on the mean flow.

The comparisons made between SWIM and LOCO suggests that SWIM is able to reproduce satisfactorily the vertical structure of the mean flow field in the Mozambique Channel.

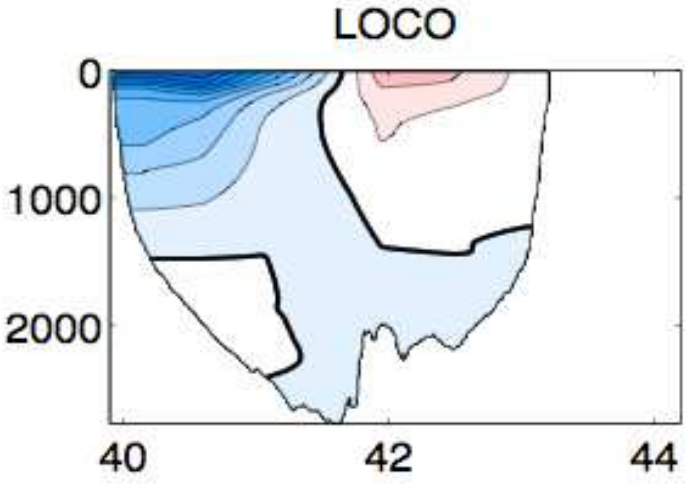

(a) LOCO

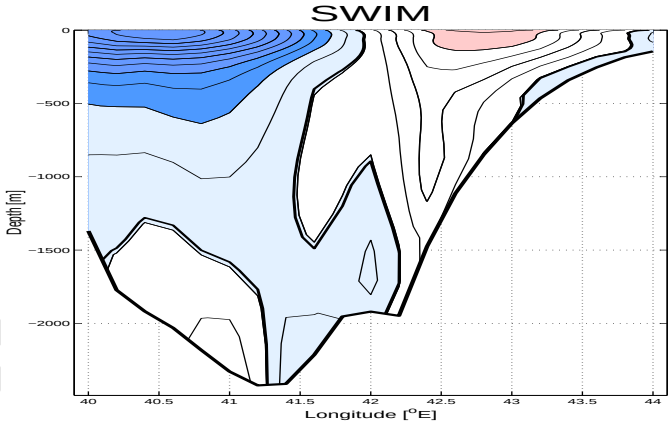

(b) SWIM

Figure 4.11. Meridional mean flow in the narrow section of the Mozambique Channel (17°S). a: LOCO, and b: SWIM 7-year climatology. Poleward flow (blue), and equatorward flow (red). Both LOCO and SWIM, the contours interval is 5 cm s^{-1}. The tick contour indicates the isoline of 0 velocity. LOCO image was extracted from van der Werf et al. (2010). Notice the slight differences on the profiles of the bottom topography associated with the horizontal grid resolution in SWIM ($\frac{1}{5}^{\circ}$).

4.1.2.3 Volume transport of the main currents

Figure 4.12 shows the SWIM derived mean volume transports across the path of the main flow structures in the greater Agulhas system: For the South-Equatorial Current (SEC), the transect has been made at 64°E, over a zonal band between 10°S and 20°S. In the North-East Madagascar Current (NEMC), the transect is made at Cape-Amber, the northern tip of Madagascar, at 49.5°E, and between 8°S and 12°S. Across the South-East Madagascar Current, the transport has been calculated at 23°S, and between 48°E and 51°E. Over the Madagascar Ridge, the transport also has been estimated across the southern extension of the SEMC, at 45°E, along the latitude band between Cape Saint-Marie and 30°S. Across the East African Coastal Current (EACC), the transport has been computed at 7°E, between 39°E and 42°E. In the Mozambique Channel, the volume transport has been investigated in two different locations: in the narrows of the channel, at 17°S, and at 24°S, both sections across the whole width of the channel. At the southeast coast of South-Africa, the transect across the Agulhas Current has been made at 32°S, following hydrographic latitude position by Beal and Bryden (1997), and Donohue and Toole (2003), and along a zonal distance between 28°E and 32°E.

The volume transports have been computed by depth-integrating the flow field structures over the upper 1500 m of the ocean column across a transversal section: $M = \int_{-z}^{0} \vec{v} dx dz$ and $M = \int_{-z}^{0} \vec{u} dy dz$, for a meridional and zonal flow fields, respectively. The calculated mean values are in many cases consistent with in-situ observations. These will be discussed in conjunction with their transport time-series, presented in Figure 4.13.

Figure 4.12 shows that across the SEC, the calculated mean volume transport on the upper 1500 m is about 40 Sv westwards, with deviations of about $\pm$ 8.13 Sv (Figure 4.13a). The maximum and minimum variations range between 60 Sv and 20 Sv westwards ($<$ 0 Sv). The mean transport of 40 Sv is about 10 Sv to 15 Sv less, when compared with in-situ observations, that suggest a westward flow of the SEC, with a mean transport of about 50 Sv to 55 Sv (Schott and McCreary, 2001, New et al., 2007). However, when considering the variation range of 60 Sv, it can be regarded as a reasonable result. For its corresponding time-series (Figure 4.13a), it can be seen the seasonal cycle, but with significant variations.

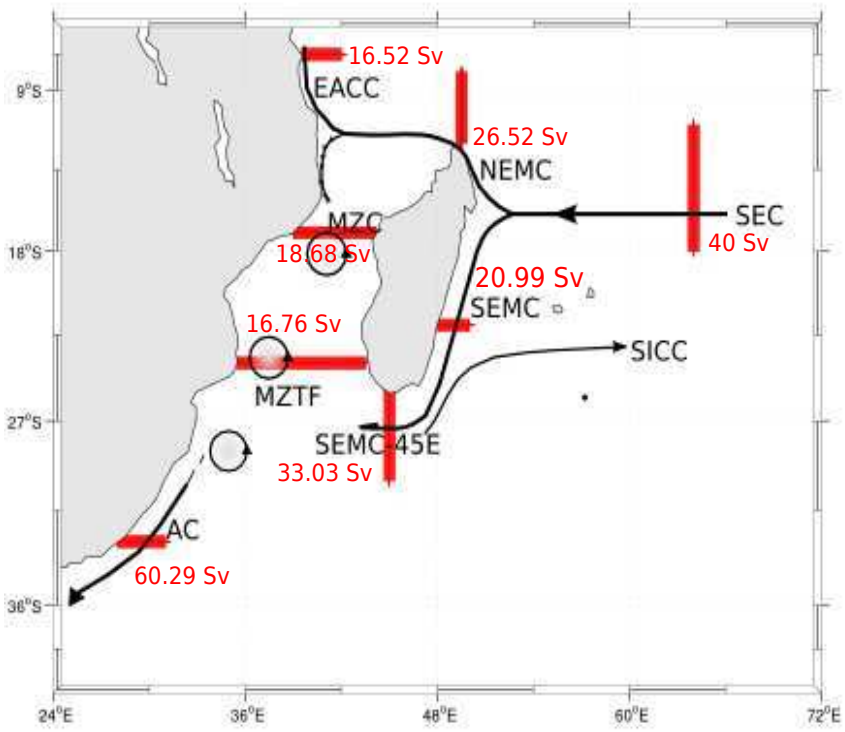

Figure 4.12. Positions and the mean volume transports in Sverdrups (Sv), of the oceanic currents, calculated on the upper 1500 m of the ocean column, derived from 7-year climatology of the model run. The acronyms: SEC (South Equatorial Current), SEC-45E (South Equatorial Current at 45°E), NEMC (North East Madagascar Current), SEMC (South East Madagascar Current), EACC (East Africa Coastal Current), MZC (Mozambique Channel Eddies), MZTF (Mozambique Channel ThroughFlow), SICC (Subtropical Indian Counter Current), and AC (Agulhas Current).

In regards to the NEMC (Figure 4.12), the calculation shows a westward mean transport of about 26.5 Sv, with standard deviations of about ± 13 Sv (Figure 4.13b). The maximum and minimum variation ranges are between 50 Sv westwards and about 15 Sv eastwards (Figure 4.13b). The westward mean transport (26.5 Sv), is in good agreement with in-situ observations, that suggest a mean transport of about 26.9 Sv (Schott et al., 1988), integrated over between 100 m - 1100 m depth of the water column. Other studies have suggested a mean transport of NEMC in about 30 Sv (Swallow et al., 1988, Schott and McCreary, 2001). Note that a positive transport in Figure 4.13b represents an eastward flow, indicative of a reversal flow in an opposite direction of the mean-flow. This reversal may be associated to the instabilities of the mean-flow (Schott et al., 1988), likely due to the eddies being generated in the northern tip of Madagascar, by barotropic

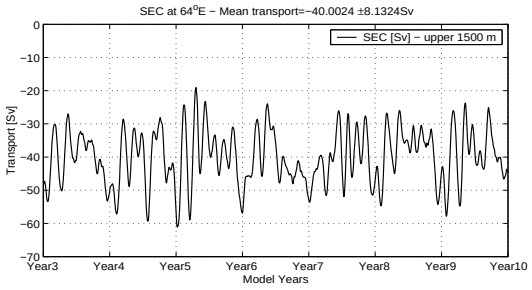

(a) SEC at 64°E

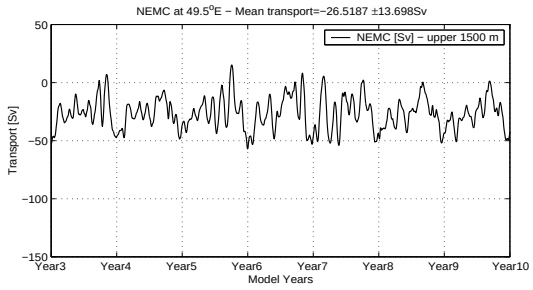

(b) NEMC at 49.5°E

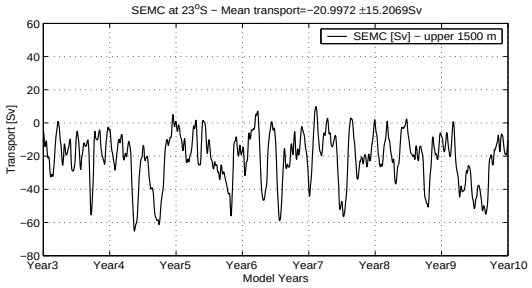

(c) SEMC at 23°S

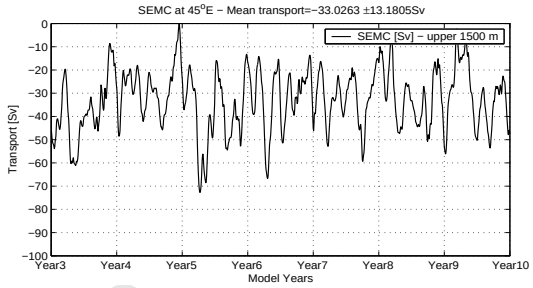

(d) SEMC2 at 45°E

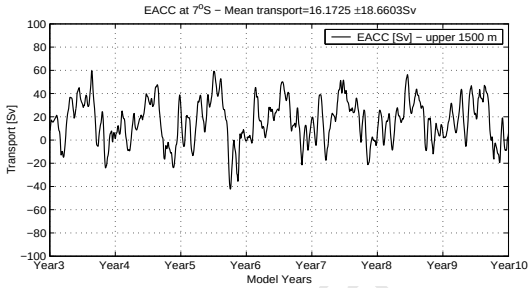

(e) EACC at 7°S

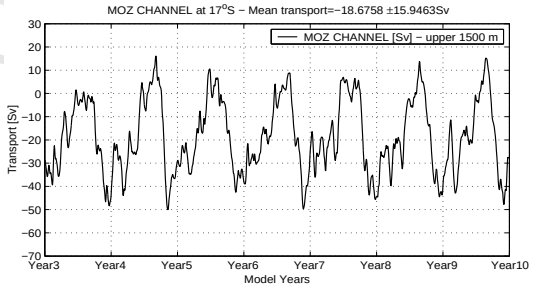

(f) MZC at 17°S

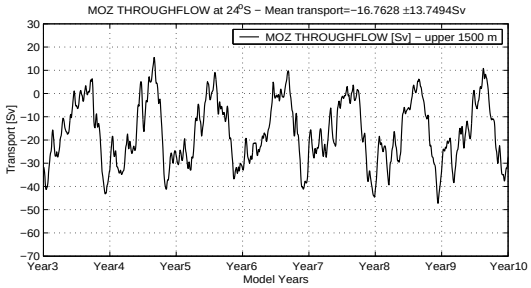

(g) MZTF at 24°S

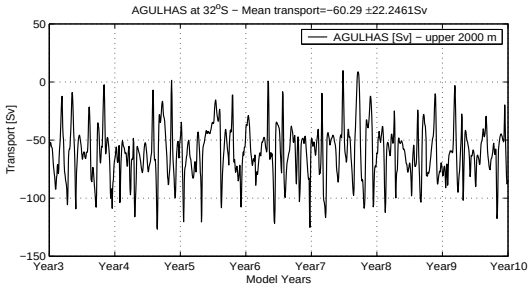

(h) AC at 32°S

Figure 4.13. Timeseries of the volume transport across the main flow structures of the greater Agulhas system shown in Figure 4.12, computed on the upper 1500 m depth of the ocean column, derived from 7-year climatology of the model run.

instabilities as reported by Biastoch and Krauss (1999).

The transect location across the SEMC, between 48°E - 51°E at 23°S (Figure 4.13c), is in agreement with the position of the hydrographic section made by Schott et al. (1988). Our calculated southward volume transport is about 21 Sv (Figure 4.12), with deviations of about ± 15 Sv (Figure 4.13c). The maximum and minimum variation range between near 60 Sv southwards, and about 10 Sv northwards, respectively. Also positive fluctuations (equatorward flow) could be attributed to the disturbances of the flow field, as eddies are locally formed, or arrive from far East Indian Ocean, as described in many studies (Quartly et al., 2006, Morrow et al., 2004, Siedler et al., 2009). The estimated southward mean transport of about 21 Sv, is in good agreement with several observational studies: 20 Sv by Donohue and Toole (2003), Schott and McCreary (2001), and 21 Sv by Swallow et al. (1988), Schott et al. (1988). To the South of Madagascar, at Cape Saint-Marie, the computed westward mean transport is about 33 Sv (Figure 4.12), with deviations of about ± 13.18 Sv (Figure 4.13d). The maximum and minimum amplitudes ranges between 70 Sv and 0 Sv westwards respectively. The calculated mean transport of 33 Sv is in good agreement with 32 Sv estimated by Nauw et al. (2008), near 47°E, but is about 4 Sv over that of 29 Sv found in hydrographic data by Donohue and Toole (2003), and OCCAM model outputs, presented by Quartly et al. (2006). However, it also differs from 52 Sv by Nauw et al. (2008), estimated at actual position 45°E. Nauw et al. (2008) attributed such an increase of the transport of about 20 Sv at 45°E to the eddy activities in the region. In our case no reversal of the transport has been observed (Figure 4.13d). Therefore the increase of the mean transport from 21 Sv at 23°S, to 33 Sv at 45°E, could be attributed to a different process, likely the recirculation in the southwest subtropical gyre as shown by Stramma and Lutjeharms (1997), and Donohue and Toole (2003), and model outputs presented by Quartly et al. (2006).

Across the EACC, the calculated mean transport is about 16.17 Sv equatorward (Figure 4.12), with deviations above the mean of about ± 18.66 Sv (Figure 4.13e). The range between the maximum and minimum variations are about 60 Sv equatorward and 40 Sv poleward. Our calculated northward mean transport of about 16.17 Sv is 3.73 Sv less, when compared to 19.9 Sv, found in hydrographic measurement by Swallow et al. (1991), measured around 4°S, on the upper 500 m depth of the oceanic water column. The strong deviations from the mean observed here (± 18 Sv), could be attributed to the seasonal variations of the EACC, due to the monsoons (Swallow et al., 1991, Tomczak and Godfrey, 1994).

In the Mozambique Channel, the mean transport at 17°S, is about 18.66 Sv poleward (Figure 4.12), with deviations of about ± 15.95 Sv (Figure 4.13f). The maximum and minimum variations, range between 15 Sv equatorward, and 50 Sv poleward respectively (Figure 4.13f). The estimated 18.66 Sv poleward is only 1.96 Sv over LOCO in-situ observations at this location (De Ruijter et al., 2006), recently estimated in about 16.7 Sv poleward (Ridderinkhof et al., 2010). It is important to infer that the mean transport at this location is quite variable: Harlander et al. (2009) using a 4 years timeseries (2003 - 2006), have found a southward mean transport of about 8.6 Sv. Fluctuations of the transport at this location are usually attributed to the mesoscale eddies, which induce about 20 Sv equatorward and 60 Sv poleward (De Ruijter et al., 2002). The transport variations (Figure 4.13f), shows a strong seasonal cycle. The models in general seems to exaggerate the seasonal cycle of the volume transport in this region, as diagnosed by van der Werf et al. (2010), inferring that such an exaggeration is due to the mis-representation of the power-spectrum at mesoscale frequencies. Farther south, at 24°S, the computed poleward mean transport has slightly changed (about 1.9 Sv less), when compared to that at 17°S. Here the transport is about 16.76 Sv (Figure 4.12), with deviations of about ± 13.75 Sv (Figure 4.13g). It is not clear why such a deacrease of the transport is observed. However, it probably could be induced by the eddies that enter into the channel, coming from the South of Madagascar (Quartly et al., 2006, De Ruijter et al., 2004). These eddies could induce some northward flow along the southwest coast of Madagascar, that imbalances the southward flow. The streamlines of mean SSH presented in Figure 4.10, shows that part of the flow from the southern extension of the East Madagascar Current may cross the latitude 24°S northwards, before its southward deflection in the Mozambique Channel. For volume conservation, it is likely that this fraction of the transport leaves the channel domain at a depth below 1500 m (note that the transports so far presented have been computed on the upper 1500 m). The maximum and minimum variations range also between 15 Sv equatorward, and 50 Sv poleward (Figure 4.13g). Similarly, the seasonal cycle is also exaggerated.

At the southeast coast of South-Africa, the calculated southward mean transport is about 60.29 Sv (Figure 4.12), with deviations from the mean of about ± 22.25 Sv (Figure 4.13h). The maximum and minimum variations range between about 120 Sv southward and nearly 10 Sv northwards (Figure 4.13h). The estimated southward mean transport is about 10 Sv lower when compared with 70 Sv of the Agulhas, observed on the upper 2000 m depth of the water column (Donohue and Toole, 2003). The strong south-

ward component reproduced in the model is consistent with a strong southward Agulhas Current (Lutjeharms, 2006). Small reversals of the flow ($\sim$ 10 Sv), could be attributed to the meandering of the flow (Lutjeharms and van Ballegooyen, 1988b, Lutjeharms et al., 2001), or mesoscale eddy activity on the Agulhas Current, as can be seen on the diagram presented by Lutjeharms and Roberts (1988a), and also recent works by Rouault et al. (2010), and Rouault and Penven (2011).

In general, the model has reproduced reasonably well the mean transport of the main oceanographic currents of the greater Agulhas System.

4.2 Eddy regime

4.2.1 Mean eddy kinetic energy

Figure 4.14a shows map of mean eddy kinetic energy (MEKE), from altimetry, from October 14, 1992 to March 31, 2010, and Figure 4.14b is derived from SWIM, for 7-year climatology of the model. According to satellite altimetric data, the most energetic place in the whole domain, is located in the Agulhas Retroflection area, with maximum energy of about 2400 cm^2 s^{-2}, and it seems to decay eastwards, along the path of the Agulhas Return Current (Figure 4.14a). After the Agulhas Retroflection area, the second most energetic place in the area, is located in the central Mozambique Channel, where it reaches about 1400 cm^2 s^{-2}. On the other hand, SWIM reproduced a maximum eddy kinetic energy of about 2000 cm^2 s^{-2}, in the central Mozambique Channel (an overestimation of about 40 %), and a relatively lower, of about 1400 cm^2 s^{-2}, in the Agulhas Retroflection region. In SWIM, the most energetic site in the Agulhas region, is shifted to the east of the retroflection zone, around 36°S, 30°E. The model has shown some difficulties in reproducing the exact energy levels: In the central channel the eddy kinetic energy produced is not adequately dissipated, and such could be associated with the some diffusive processes, or it could be related to the fact that SWIM reproduces larger Mozambique Channel eddies than those observed by the satellite altimeters, as has been shown by Halo et al. (2012) [*in review*]. Many studies have demonstrated that larger eddies are likely to have higher energy levels than smaller eddies (Rhines, 1975, McWilliams, 1984, Stammer, 1997, Eden, 2007). To the South of the channel, SWIM also appears to overestimate the energy levels along the southeastern coast of South-Africa, in the path of the Agulhas

Current (Figure 4.14b). It also can be seen that in SWIM, there is a lesser energy input from the eastern boundary of the channel, that could be associated with the boundary problems. Strong eddy kinetic energy within the channel, appears to be locally generated. Parts of this energy is being produced at the northern tip of Madagascar, and seems to spread southwards into the central Mozambique Channel (Figure 4.14b). Such a production has been associated to barotropic instabilities of the SEC (Biastoch and Krauss, 1999). SWIM also shows a stronger production of eddy kinetic energy at the South-East of Madagascar (Figure 4.14b), likely associated to a strong intensification of the SEMC.

Both SWIM and altimetry (Figure 4.14) show that the eddies play a significant role on the flow field in the Mozambique Channel, and in the greater Agulhas system as a whole. The role of such eddies on the variability of the flow is shown in Figure 4.15.

4.2.2 RMS SSH

Figure 4.15a shows root mean square (RMS) of SSH (RMS=$\sqrt{\frac{\sum SSH^2}{n}}$), from altimetry, from October 14, 1992 to March 31, 2010, and Figure 4.15b, is from SWIM, for 7-year climatology of the model run. Where n is the number of observations. Enhanced levels of RMS SSH are representative of mesoscale variability. Figure 4.15 is consistent with Figure 4.14: Strong MEKE results in a strong RMS of SSH. The stronger RMS of SSH within the channel, observed in altimetry is about 20 cm (Figure 4.15a), while in SWIM, it is about 30 cm (an overestimation of about 50 %). In the Agulhas retroflection, the maximum RMS of SSH observed in altimetry is about 45 cm, while in SWIM it is about 40 cm (an underestimation of about 11.1%). The overestimation of the RMS SSH of about 50 % in the central Mozambique Channel, could be attributed to the overestimation of about 40 % of the MEKE (Figure 4.14), as proposed by Halo et al. (2012) [*in review*]. The same process also could explain the underestimation of about 11.1% in the Agulhas retroflection region. A consistent pattern is also observed in the southwest coast of Madagascar, around 24°S, 41°E. In this site is observed that lower MEKE levels (Figure 4.14), also correspond to lower RMS SSH (Figure 4.15).

SWIM has shown also difficulties in reproducing accordingly the variability at the eastern boundary of the domain (Figure 4.15b). Similar to the MEKE, the bias in RMS SSH could be also attributed to the boundary problems.

Analysis of the maps in Figure 4.15, in conjunction with the pattern of the oceanic currents in the region (Figure 1.6), suggests that the Mozambique Channel, receives vari-

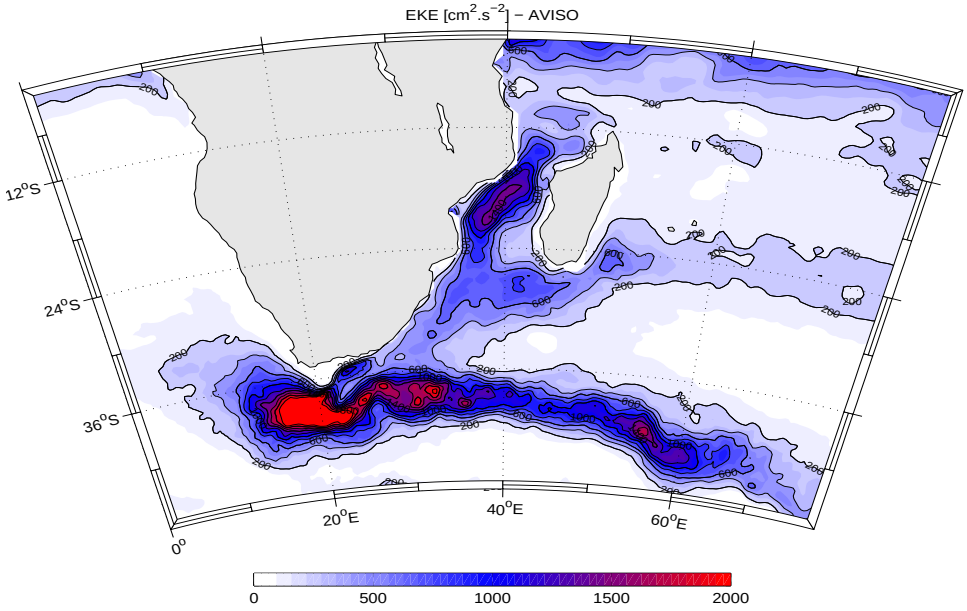

(a) AVISO

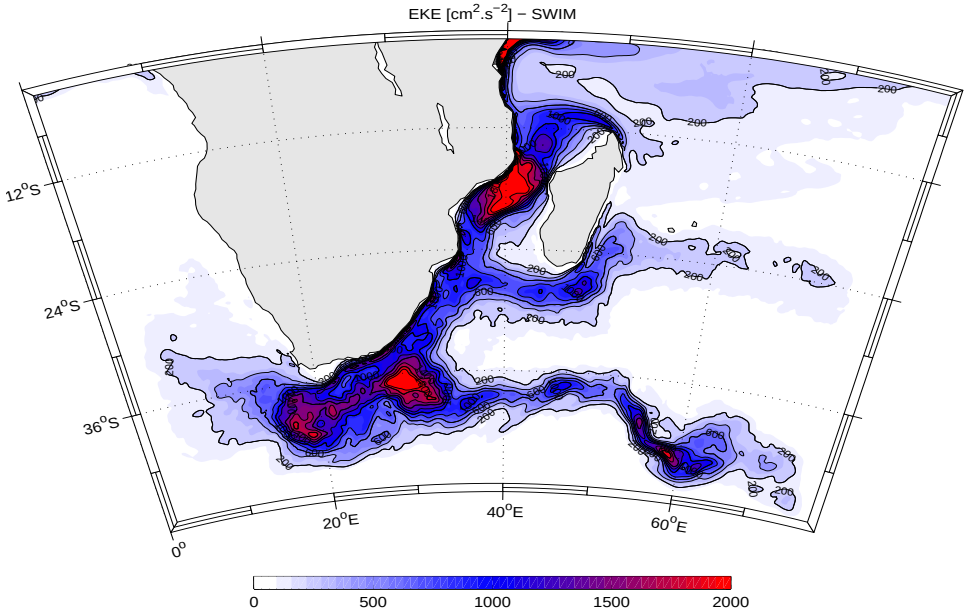

(b) SWIM

Figure 4.14. Mean eddy kinetic energy, derived from satellite altimetric observation for the period starting in October 14, 2002 to March 31, 2010, merged product (a), and from 7-year climatology of the model run (b).

ability of SSH from the East Indian Ocean, through two main gates: the north gate, in the northern Mozambique Channel, via the northern tip of Madagascar, around 12°S, and the south gate, in the southern Mozambique Channel, via the southeastern part of Madagascar, in a latitudinal band between 25°S and 28°S. Both model and altimetry reproduce such a pattern. This pattern is consistent with previous studies, that have identified two zonal bands of enhanced SSH variability, westward propagating towards the greater Agulhas system, lying across the Indian Ocean Basin at about 12°S and 25°S (De Ruijter et al., 2005, Palastanga et al., 2006).

Both in altimetry and in SWIM, the geometric features of the RMS SSH along the corridor band at 12°S, shows a different structure when compared to that at 25°S (more aggregated in the SWIM than in AVISO). Such pattern could be indicative of predominance of flow field structures of different time-scales: some studies have identified strong signals of Rossby waves entering in the Mozambique Channel through the corridor at 12°S (Schouten et al., 2002a,b, Palastanga et al., 2006), and others, have reported the predominance of several mesoscale eddies propagating through the corridor band of 25°S (Morrow et al., 2004, Quartly et al., 2006).

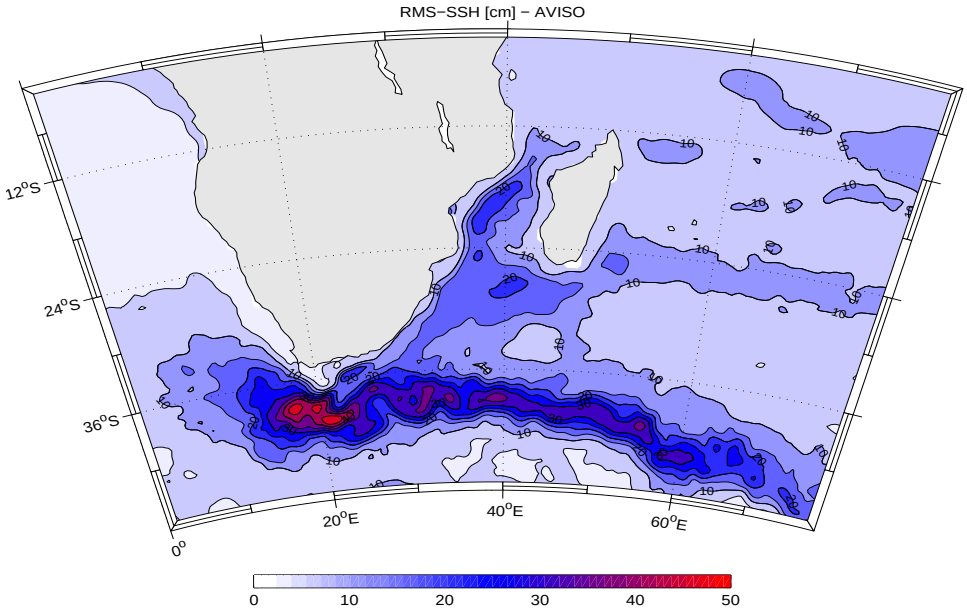

(a) AVISO

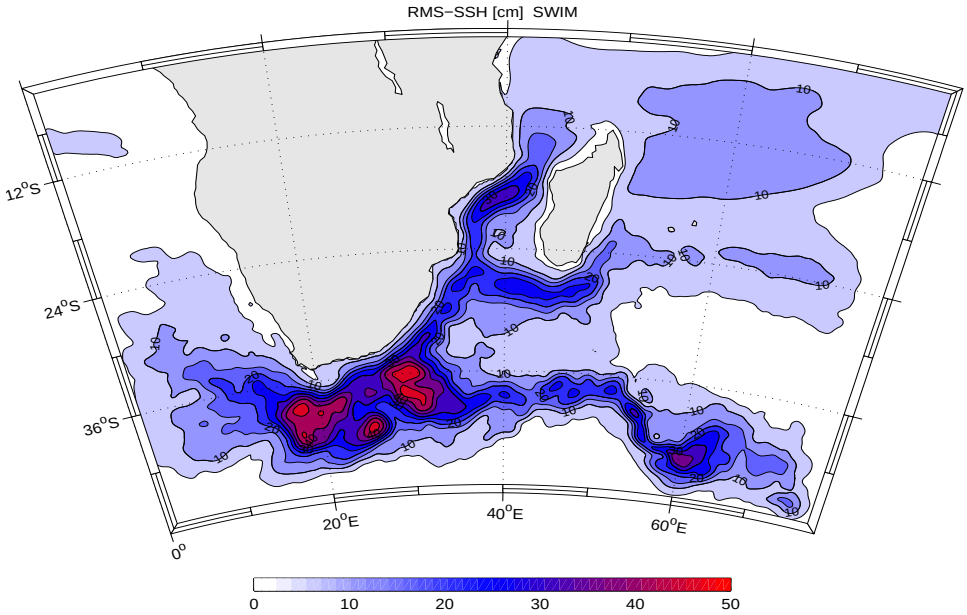

(b) SWIM

Figure 4.15. Variability of sea surface height, derived from satellite altimetric observation for the period starting in October 14, 2002 to March 31, 2010, merged product (a), and from 7-year climatology of the model run (b).

4.2.3 Eddy vertical structure at 17°S

The vertical structure of the eddies reproduced by SWIM is evaluated in the narrows of the channel, at 17°S, to allow a comparison against an eddy structure (Figure 4.16a), derived from hydrographic measurements from De Ruijter et al. (2002). The eddy in SWIM (randomly chosen, Figure 4.16b), has passed the latitude 17°S, in the year 4, month 2, day 21. The snapshots confirm that the eddies simulated in SWIM have similar vertical structures as those observed from in-situ measurements: The eddies are large, spanning almost the entire width of the narrow channel, and also reach the bottom of the channel, near 2500 m depth, consistent with observations (De Ruijter et al., 2002, Ridderinkhof and De Ruijter, 2003). The eddy in SWIM appears to be surface intensified, and exhibits a strong barotropic component as also reported in observational studies (De Ruijter et al., 2002, Ridderinkhof and De Ruijter, 2003, Schouten et al., 2003). The poleward component of the eddy at the western boundary (along the Mozambican coast), is relatively more intensified than its counter-part, observed at the eastern boundary (along the Madagascar coast). In the hydrographyc section (Figure 4.16a), the maximum poleward component of the flow at the surface is about 0.9 m s^{-1}, and the minimum near 1300 m depth, is about 0.1 m s^{-1}. In SWIM (Figure 4.16b), the maximum poleward component of the flow at the surface is relatively more intense, about 1.1 m s^{-1}, and the minimum is about 0.1 m s^{-1}, reaching the bottom of the channel. The counter-part of its poleward flow has a maximum surface velocity of about 0.8 m s^{-1}, and the minimum of about 0.1 m s^{-1}, which also reaches the bottom of the channel. The eddy in SWIM appears to be relatively more intense, with stronger barotropic signal than in the observation.

The eddy in hydrographic section of De Ruijter et al. (2002) (Figure 4.16a), and also that presented by Harlander et al. (2009), in their Figure 7, have shown two cores of an equatorward flow at the western boundary of the channel, at a depth between 700 m and 1500 m, and also near 2500 m (relatively more intense, about 0.2 m s^{-1}). De Ruijter et al. (2002) have attributed this feature as the presence of the Mozambique Undercurrent. The eddy in SWIM (Figure 4.16a), has not reproduced such a flow structure. It is likely that this might be the case only for this particular eddy. This is likely to be so, because Figure 4.11b has shown that SWIM is able to reproduce the equatorward Mozambique Undercurrent (Beal and Bryden, 1997).

Interestingly, both the hydrographic eddy section, and the SWIM (Figure 4.16), have reproduced a poleward flow to the east of the equatorward component of the eddy flow (along the Madagascar coast). This flow seems to reach the bottom of the channel, and is

relatively more intense, about 0.2 m s^{-1}, in the model than in observation. This seems to be the poleward flow mentioned by Harlander et al. (2009), as a precursor of the formation of an anticyclonic eddy in the Center of the channel.

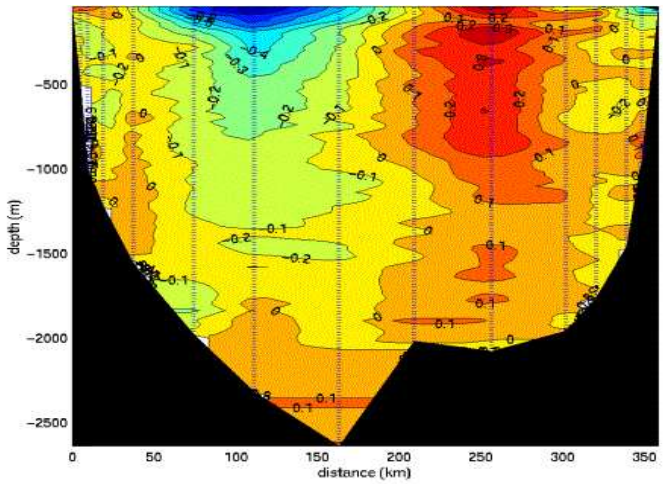

(a) Observation at 17°S

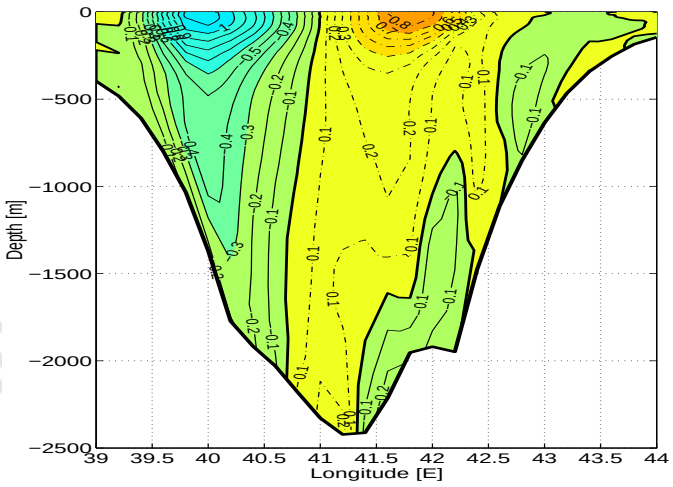

(b) SWIM at 17°S

Figure 4.16. Snap-shots of an anticyclonic eddy vertical structures, derived from hydrographic data from ACSEX cruise (a), extracted from De Ruijter et al. (2002), and SWIM (b), computed from year 4, month 2, day 21. Negative (positive) values indicate poleward (equatorward) flow.

4.2.4 Transport variability at 17°S

Transport variability throughout the water column, in the narrows of the channel at 17°S, is compared against LOCO data (Figure 4.17). The left panels show the total meridional transport for LOCO (a), and SWIM (b). The right panels show the corresponding power density spectrum, based on a Multitaper Spectral Analysis. As presented by Halo et al. (2012) [*in review*], the spectrum is presented on a logarithmic scale to highlight a wider range of variability, specially in the higher frequencies. High frequency transport fluctuations in LOCO show strong levels of variability that overwhelm the seasonal cycle. In SWIM, these high frequency signals are two orders of magnitudes below the observed power density spectrum. In the power density spectra (right panels of the Figure 4.17), the frequency range of variability can be separated into three bands of frequency: above 10 y^{-1} (high frequencies), between 3 y^{-1} and 10 y^{-1} (typical of the mesoscale regime), and below 3 y^{-1} (the annual and semi-annual cycle, and interannual variations). Considering the model representation, it appears that SWIM strongly overestimates the lower frequencies (i.e. the seasonal cycle), and underestimate the higher frequencies. The overestimation could possibly be related to the forcing fields and boundary conditions which are derived from climatology dataset, while the underestimation could be associated to the subgrid-scale of unresolved processes in the model. In the mesoscale regime (i.e. range between 3 y^{-1} and 10 y^{-1}), the magnitude of the density spectra in SWIM is in good agreement with the observations. The overestimation of the seasonal cycle appears in our case not to be related to a misrepresentation of the mesoscale variability, as has been suggested by van der Werf et al. (2010).

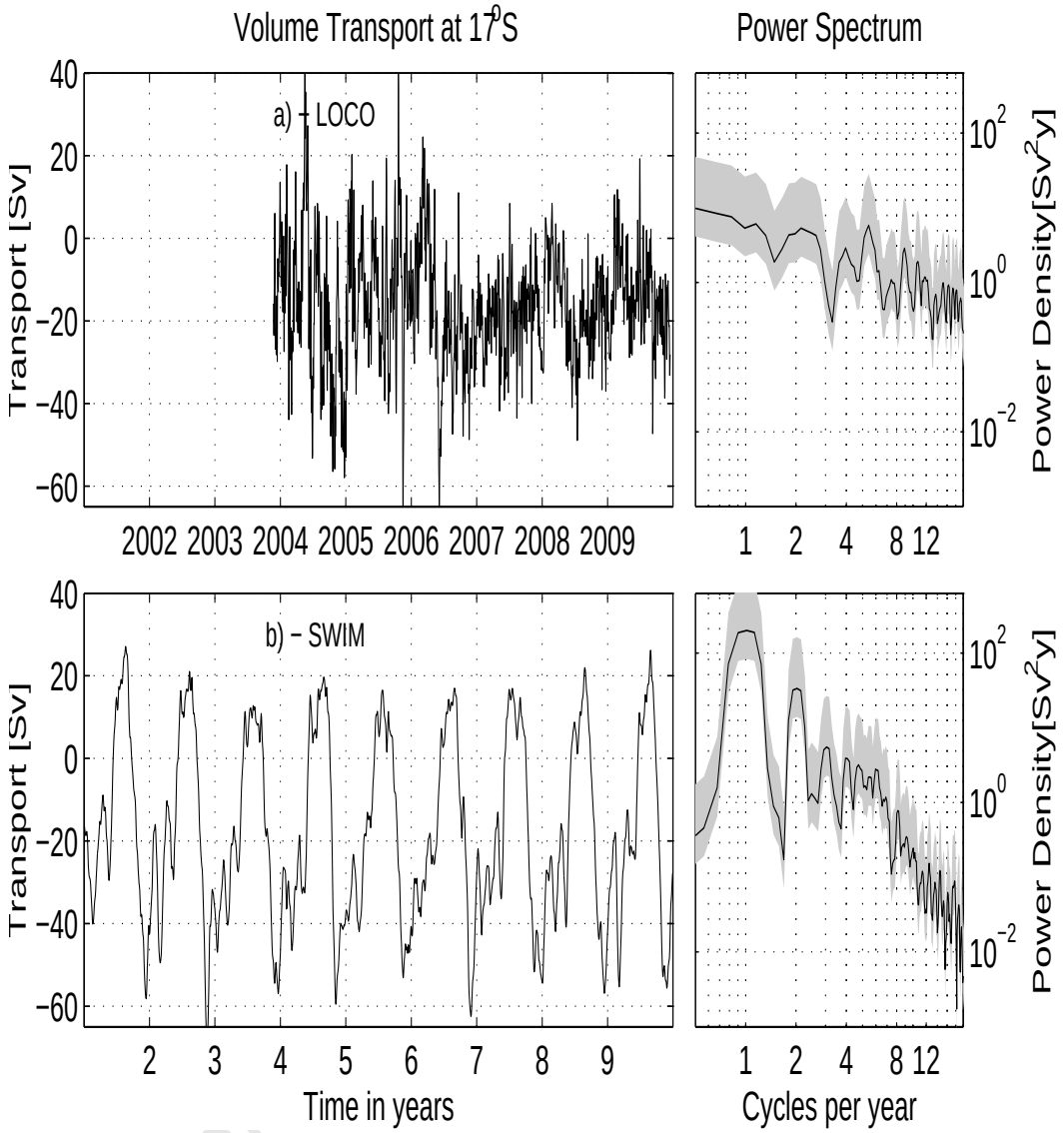

Figure 4.17. Left panels show the timeseries of the volume transport at 17°S, throughout the ocean water column, and right panels show their corresponding power spectrum. LOCO (a) and SWIM (b).

4.3 Summary of the model evaluation

An overall summary of the model performance based on the properties investigated in this chapter is presented in Table 4.1.

SWIM's performance	Oceanographic features
Similarities with observations	• Presence of the main water masses. • Presence of the currents at the right location. • Good representation of the vertical structure of the mean flow and eddy field in the narrows of the Mozambique Channel. • Relatively weaker boundary currents. • Good estimates of the volume transport of the main currents of the region. • Good representation of the power density spectrum of the transport at the mesoscale range in the narrows of the Mozambique Channel. • Right route of propagation of the RMS of SSH.
Discrepancies from observations	• weaker retroflection loop of the Agulhas Current at the retroflection region. • Narrower and highly meandering Agulhas Return Current. • Stronger recirculation at the offshore edge of the Agulhas Current proper. • Lesser mixing and spreading of the main water masses across the ocean basin. • Over-estimation of EKE and RMS in the northern and central Mozambique Channel. • Under-representation of EKE and RMS in the eastern side of the model domain. • Over-representation of the lower frequency signal of the power density spectrum of the volume transport in the narrows of the channel. • Under-representation of the higher frequency signal of the power density spectrum of the volume transport in the narrows of the channel.

Table 4.1. Summary of the model performance in reproducing the oceanographic features in the southwest Indian Ocean.

4.4 Conclusion

The outputs from our ROMS based configuration for the South-West Indian Ocean (SWIM) designed specially to resolve the mesoscale ocean dynamics in the Mozambique Channel has been compared against several observational datasets (WOA05, CARS09, LOCO, satellite altimetry and the new CLS-CNES09), for evaluation of its performance.

When the mean states for potential temperature and salinity from SWIM at the sea surface and throughout the water column is compared against climatologies from WOA05 and CARS09, it has been observed that SWIM outputs are closer to CARS09 than the WOA05. This is likely because CARS09 have a relatively better resolution than WOA05. SWIM has reproduced in a resonable manner the presence of the main water masses of the South-West Indian Ocean. However, SWIM also has shown some difficulties in reproducing accurately their spreading across the Indian Basin.

The mean flow field from SWIM at sea surface has been also compared against the mean dynamic topography from the new CLS-CNES09, portraying the surface geostrophic circulation. The comparison shows that SWIM is able to reproduce well the presence of the long-term oceanographic features of the region. Slight differences in SWIM are observed in the intensity of the main flows, such as the a relatively weaker SEMC, weaker recirculation loop of the Agulhas retroflection, and a narrower and more meandering ARC. Through the water column, the flow in SWIM has been compared against LOCO dataset. The evaluation shows that SWIM is able to reproduce satisfactorily the vertical structure of the mean flow and the eddy field in the Mozambique Channel. SWIM also has shown consistent estimates of the volume transport of the main flow of the region. Our model evaluation also reveals that SWIM has shown significant difficulties in reproducing comparable eddy kinetic energy in the region.

Despite the model difficulties, the overall evaluation of the model suggests that SWIM can be used satisfactorily to study the large and mesoscale oceanographic processes in the region. Therefore in this study we use its output to investigate in detail the eddy properties in the Mozambique Channel.

CHAPTER 5

Automatic Eddy Detection and Tracking Algorithm

5.1 Introduction

The use of an automatic algorithm to identify and track eddies in higher resolution oceanic models is of great importance: It increases the possibilities of studying eddies in more detail. There is around the world, several methods to automatically detect and track mesoscale ocean eddies (Jeong and Hussian, 1995, Portela, 1997, Sadarjoen et al., 1998, Sadarjoen and Post, 2000, Penven et al., 2005, Chakraborty et al., 2005, Isern-Fontanet et al., 2006, Chelton et al., 2007, 2011, Chaigneau et al., 2008, Nencioli et al., 2010, Chauris et al., 2011, Kurian et al., 2011, Souza et al., 2011). However, none of the existing methods are entirely satisfactory (Sadarjoen et al., 1998, Souza et al., 2011). It has been shown that different methods when applied on the same dataset, usually provide different quantitative results (Nencioli et al., 2010, Souza et al., 2011). The differences are likely related to the various assumptions taken to characterize a vortex.

Since the ocean circulation in the Mozambique Channel is dominated by the propa-

gation of mesoscale eddies (De Ruijter et al., 2002, Ridderinkhof and De Ruijter, 2003), it is important that model simulations capture their properties adequately. A new eddy detection scheme is implemented in order to compare observed eddy properties to those simulated in the models in a robust and consistent manner.

Among the numerous algorithms employed to detect eddies in the ocean, the two methods generally used with altimetry data are the methods based on geometric criteria (Chelton et al., 2011), and the methods based on local deformation properties of the flow (Okubo, 1970, Weiss, 1991, Isern-Fontanet et al., 2006).

The methods based on geometric properties of the flow field, consists in detecting closed loops in SSH (Chelton et al., 2011), provided a suitable eddy length-scale, to exclude gyre scale structures.

On the other hand, the methods based on local dynamical properties of the flow field, consists mostly in selecting regions where the Okubo-Weiss (W, or equivalent) parameter is below a negative threshold (Isern-Fontanet et al., 2006, Chelton et al., 2007) (i.e. where vorticity dominates strain: $W < 0$). The Okubo-Weiss parameter W, measures the relative importance of squared strain tensor, and squared vorticity (Okubo, 1970, Weiss, 1991), given by the relation:

$$W = S_n^2 + S_s^2 - \xi^2 \tag{5.1}$$

Where the components are expressed:

$$S_n = \frac{\partial u}{\partial x} - \frac{\partial v}{\partial y}, \quad S_s = \frac{\partial v}{\partial x} + \frac{\partial u}{\partial y}, \quad \xi = \frac{\partial v}{\partial x} - \frac{\partial u}{\partial y} \tag{5.2}$$

Where S_n, and S_s - are the normal and shear components of strain tensor respectively; ξ - is the vertical component of relative vorticity; u and v are the velocity components in the x and y directions respectively.

In the case of altimetry, W is based on second derivatives of SSH. This amplifies the errors in measurements and interpolations, resulting in a significant level of noise on SSH

field, being necessary to filter (Chelton et al., 2011, Souza et al., 2011). But the filtering applied introduces possible biases in the detected eddy properties. A second problem of this method is its sensitivity to the choice of the positive threshold used for eddy detection (Chelton et al., 2011).

Methods based on geometric criteria have appeared less problematic and have recently been preferred in comparison to the Okubo-Weiss parameter (Chelton et al., 2011, Souza et al., 2011). Nevertheless, these methods require thresholds in SSH anomalies and/or criteria based on the shape of contours in order to select proper vortices (Chelton et al., 2011, Souza et al., 2011).

Since we derive eddy properties from 2 different products with different grid resolutions ($\frac{1}{4^\circ}$ for altimetry, and $\frac{1}{5^\circ}$ for SWIM), this requires an eddy detection algorithm which does not need a specific treatment for SSH or a tunable parameter which depends on the resolution. Kurian et al. (2011), illustrate the complementarity between the Okubo-Weiss criteria and geometric methods by using successively each method depending of their need. In this study, we combine together the Okubo-Weiss and the geometric methods, resulting in a mixed-scheme, hereafter termed by the "hybrid criteria".

5.2 The hybrid criteria

5.2.1 Description and evaluation

The hybrid scheme is described as follow (steps 1 to 4):

1. The use of ocean models and the existence of an improved mean ocean dynamic topography (Rio et al., 2011) in conjunction with altimetry allow to base our hybrid criteria on absolute SSH instead of anomalies. This has 2 major advantages: First it prevents the spurious detection of current meanders which can be seen as closed loop in SSH anomalies. Second, in a system dominated by large anticyclonic Mozambique Channel Eddies, negative values of SSH anomalies could have been legitimately interpreted as an absence of an anticyclonic eddy rather than the occurrence of a cyclonic eddy (De Ruijter et al., 2002). No specific treatment such as high pass filtering is applied to SSH.

2. The Okubo-Weiss parameter is computed from the geostrophic velocities. Two passes of a Hanning filter are applied on W to reduce the grid scale noise. Regions dominated by vorticity (i.e. negative W) are selected. For evaluation purposes, SSH for 15 September 2003 (i.e. the date used by Weimerskirch et al. (2004) for comparison) is shown in Figure 5.1. The dark contours in Figure 5.1a represent the regions dominated by vorticity. As argued by Chelton et al. (2011), there is a high level of noise and several selected regions are obviously not mesoscale eddies (specially in the northern boundary, and northwestern boundary of the domain (Figure 5.1a)).

3. The regions inside closed loop of SSH are selected. The precision between the contours to detect the loops is chosen at $\Delta\text{SSH} = 2$ cm, corresponding approximately to the altimetry precision. To prevent selecting an ocean gyre as a closed loop, a limit to the equivalent diameters (i.e. the diameter of the circle corresponding to the surface as the selected region) is fixed at a maximum of 600 km. The resulting selected closed SSH loops are shown in Figure 5.1b. As noted by Chelton et al. (2011): In the case of altimetry, the geometric method appears more successful in detecting mesoscale geostrophic eddies. But several problems still remain: Several structures with multiple cores are selected (such as at 17°S in the Mozambique Channel or at 24°S along the Mozambican coast). Also elongated loops are selected (as seen at 20°S west of the Madagascar East Coast) are unlikely to be mesoscale eddies.

4. By combining the regions of negative W (step 2) and the regions embedded in SSH closed loops (step 3), we obtain a more consistent pattern where the spurious detections associated with noise in W are excluded and the ambiguities in multi-poles / elongated closed loops are cleared up. Note for example the detection of a typical anticyclonic Mozambique Channel eddy between 16°S and 18°S in Figure 5.1c and Figure 5.1d in comparison with the pattern detected in Figure 5.1a and Figure 5.1b. In addition, to ensure that the selected regions are not noise induced artifacts, they should also contain at least an extremum in SSH and a minimum in W field.

Three tunable parameters still remain: the interval between the SSH contours for closed loop detection (chosen = 2 cm), the maximum size of a closed loop (chosen = 600 km), and the number of passes of the Hanning filter on W (chosen = 2). Tests have shown

a low sensitivity to these parameters. Therefore we kept them identical when detecting eddies from altimetry and the ocean model.

5.2.2 Eddy tracking

The eddy tracking algorithm used in this study is the method proposed by Penven et al. (2005), where an eddy (e_1) detected in a first frame is the same eddy (e_2) in the subsequent frame if a generalized distance in a non-dimensional property space is minimum:

$$X_{e_1,e_2} = \sqrt{\left(\frac{\Delta X}{X_0}\right)^2 + \left(\frac{\Delta R}{R_0}\right)^2 + \left(\frac{\Delta \xi}{\xi_0}\right)^2} \tag{5.3}$$

Where

- ΔX is the spatial distance between e_1 and e_2,
- ΔR is the variation of diameter,
- $\Delta \xi$ is the variation of vorticity.
- X_0 is a characteristic length scale (here selected to be 25 km),
- R_0 is a characteristic radius (here selected to be 200 km), and
- ξ_0 is a characteristic vorticity (here selected to be 10^{-5} s^{-1}).

X_{e_1,e_2} is considered infinite if there is a change of sign in vorticity to ensure that no cyclone become an anticyclone (i.e: the eddy should preserve its polarity).

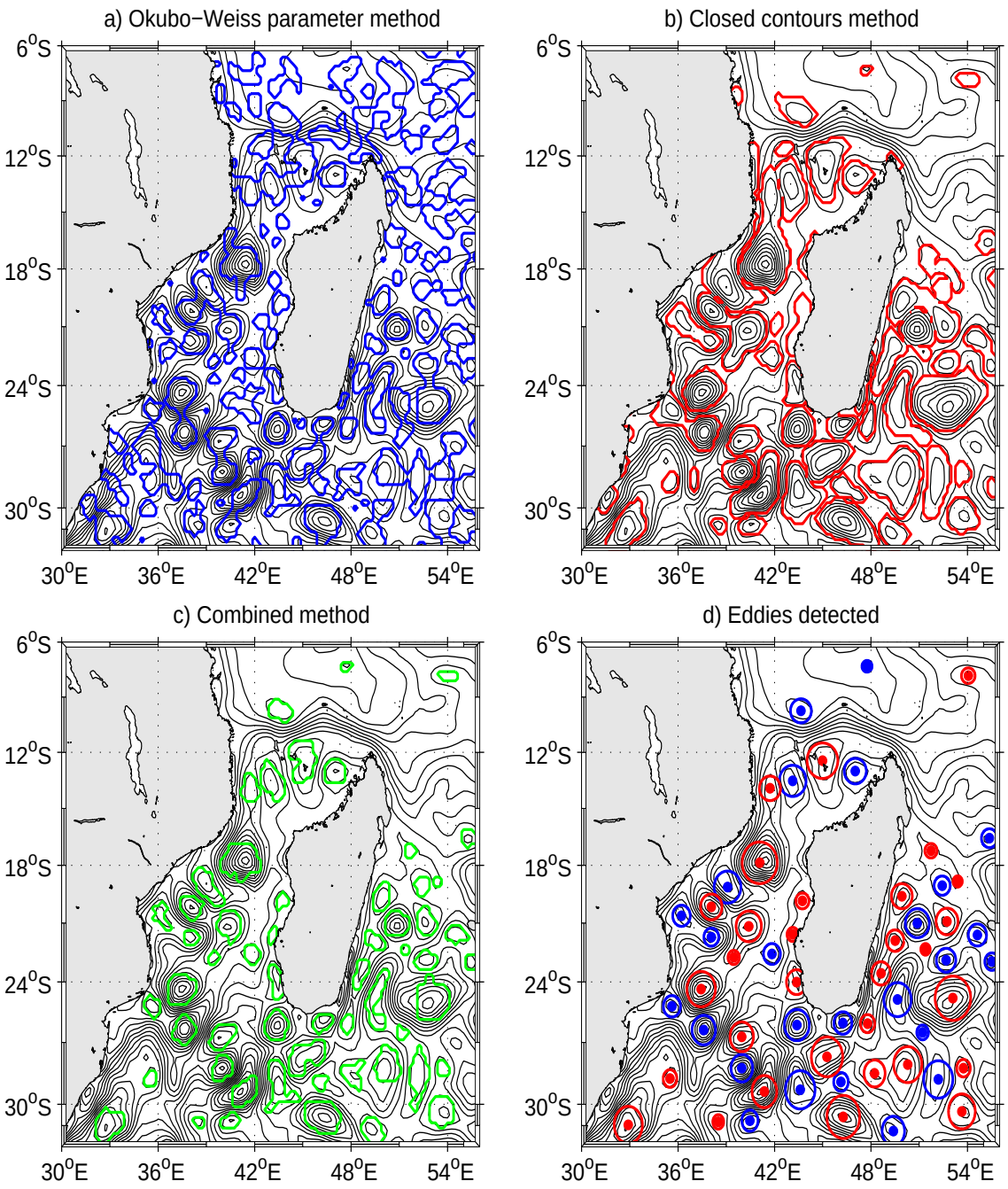

Figure 5.1. Evaluation of the different eddy detection schemes, for September 15, 2003 (date used by Weimerskirch et al.2004). Regions of negative Okubo-Weiss parameter (a); regions enclosed in closed contours of SSH loop (b); combination of regions selected in (a) and (b), resulting in a hybrid method (c). Resulting eddies selected (d): blue (cyclonic eddies), and red (anticyclonic eddies). In every panel, the grey contours are mean SSH derived from Altimetry. Note the improvement of the hybrid method, when compared with the other criterias.

5.3 Conclusion

The performance of 2 different automatic algorithms to detect and track mesoscale ocean eddies, based on geometric properties of the flow field (closed contours of SSH), and dynamical properties of the flow (Okubo-Weiss criteria), have been compared against a hybrid method, based on a mixture of the algorithms. The evaluation of the hybrid scheme has shown that by combining the closed contours of SSH and the Okubo-Weiss parameter, a geostrophic eddy is in this case defined as the flow contained in a closed loop of SSH, and where the vorticity dominates the strain. Thus we obtain a more robust eddy detection than the 2 algorithms when used separately. Therefore the hybrid scheme can be used satisfactorily to investigate the eddies in any ocean basin, derived from both altimetry and ocean models.

CHAPTER 6

Eddy Properties in the Mozambique Channel

Key Questions:

- **Are there cyclonic eddies in the Mozambique Channel?**
- **Why is the flow in the Mozambique Channel dominated by the anticyclonic eddies?**
- **What are the physical characteristics of the Mozambique Channel eddies?**
- **How do the Mozambique Channel eddy properties vary meridionally throughout the channel?**

6.1 Introduction

The flow field in the Mozambique Channel is characterized by intense mesoscale eddy activity, dominated by large anticyclonic eddies (Biastoch and Krauss, 1999, Ridderinkhof

and De Ruijter, 2003, Schouten et al., 2003). The characteristics of these eddies have been determined from a number of in-situ measurements (Ridderinkhof et al., 2001, De Ruijter et al., 2002, 2005). Observations from current meters, mooring array at $\sim$ 17°S (Ridderinkhof and De Ruijter, 2003) have shown that these eddies reach 300 km to 350 km in width, reaching all the way to the bottom of the channel, over 2000 m deep, and have a strong barotropic component (De Ruijter et al., 2002, Ridderinkhof and De Ruijter, 2003, Schouten et al., 2003). These eddies have been shown to be surface intensified, and propagate southwards parallel to the western boundary of the channel, with averaged translocation speeds of about 6 km day^{-1}. Interestingly, between 18°S and 21°S, their propagation speed reduces to 3 to 4 km day^{-1} (Schouten et al., 2003), but further to the south, at 24°S, analysis of the eddy properties by Swart et al. (2010), revealed that the eddies propagation velocities increase to over 6 km day^{-1}, with tangential velocities of about 0.5 m s^{-1}, while maintaining their large diameters (over $\sim$ 200 km). On average these eddies transport anomalous heat and salt of about 1.3×10^{20}J and 6.9×10^{12}kg, accounted as sufficient to modify the water masses downstream (Swart et al., 2010).

The frequency of occurrence of the large anticyclonic eddies in the Mozambique Channel, at 17°S, is quite regular, being about 4 to 5 per annum (Schouten et al., 2003). Their passage induce fluctuations in the mean poleward volume transport, ranging from approximately 20 Sv northward to 60 Sv southward. The mean poleward transport has been estimated to be 15 Sv (De Ruijter et al., 2002). However, this quantity seems variable. Using a relatively longer timeseries (2003 - 2006), a lower quantity of about $\sim$ 8.6 $\pm$14.1 Sv was found by Harlander et al. (2009). Due to their regular passage, and their overwhelming signature expression in anticyclonic vorticity, specially in the central Mozambique Channel, questions have been raised whether cyclonic eddies exist or not in the Mozambique Channel (De Ruijter et al., 2002). There is not yet definitive conclusion documented in the literature regarding the origin of cyclonic eddies in this region.

Cyclonic eddies are usually known as important dynamical features for the marine ecosystems (Robinson, 1983, Lathuiliere et al., 2011). They usually bring deep rich-nutrient waters into the upper ocean, thereby enhancing primary productivity. However in spite of their important role, little is known about their abundance and characteristics in the Mozambique Channel. For example, De Ruijter et al. (2002) found no cyclonic eddies in the Mozambique Channel. The apparent cyclonic anomalies observed from al-

timetry in their study were likely artifacts in the data handling, during the calculation of a mean SSH field (an inaccurate knowledge of the mean dynamic topography). Therefore they concluded that the cyclonic features are misrepresented simply because of the absence of anticyclonic eddies (De Ruijter et al., 2002). Thus the present knowledge states: *"the frequent passage of positive anomalies through the Mozambique Channel leaves a signal in the mean SSH field, leading to a negative anomaly when no anticyclone is present"* (Schouten et al., 2003).

The present generation of state-of-the-art numerical ocean circulation models have been shown to simulate the eddy regime in the Mozambique Channel with a reasonable degree of accuracy (Biastoch and Krauss, 1999, Penven et al., 2006, Biastoch et al., 2008a, Backeberg et al., 2009). As an example see Figure 6.1, reproduced by SWIM model configuration used in this study.

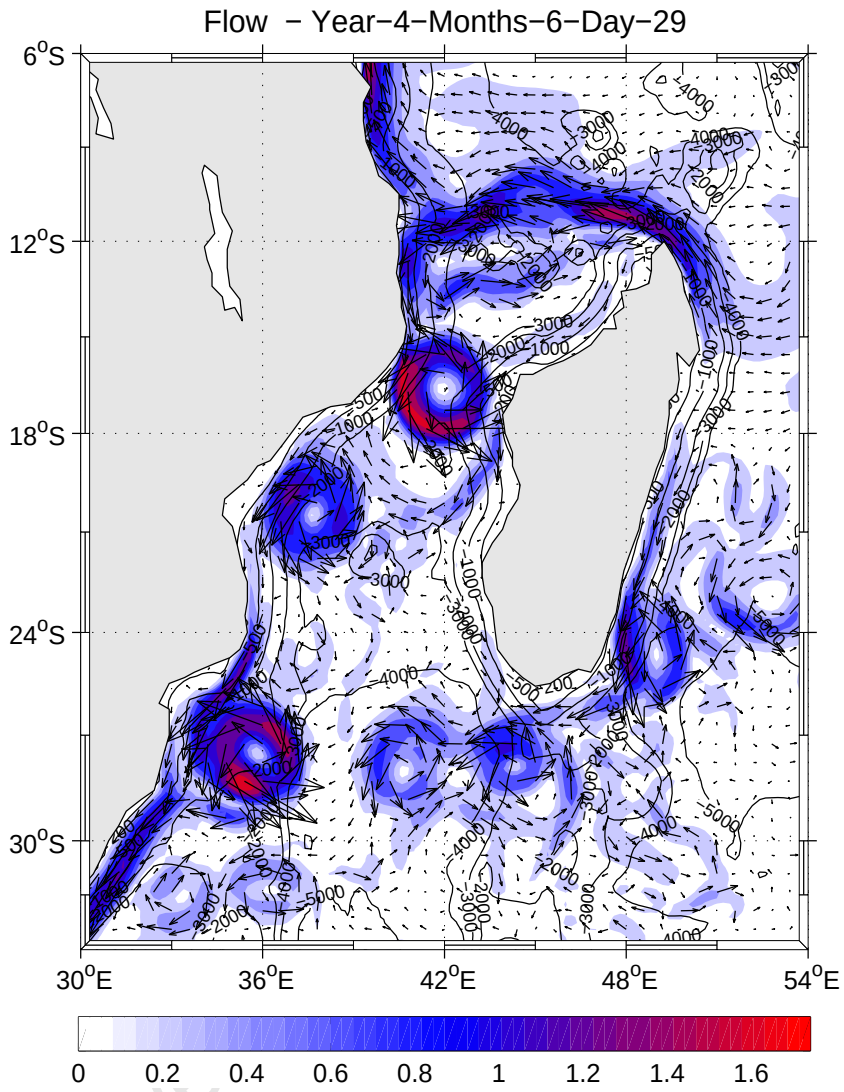

Figure 6.1. Characteristic flow field of the region, reproduced by SWIM model. The flow field has been reconstructed by depth integrated horizontal currents on the 100 m of the water column. Snap-shot of June 29, model year 4. The vectors indicates the direction of the flow, and the background colour indicates their speed expressed in [m s^{-1}]. For visualization purpose the vectors were spaced at every 3 grid points. The black contours are the isobaths in [m]. Note the key features of the circulation system in the region.

As it has been discussed in chapter 3, SWIM was configured specially to resolve realistically regional scale ocean dynamics. Thus using the eddy permitting capabilities of the model, we investigate eddy properties in the Mozambique Channel. The results are mainly compared with altimetry dataset (AVISO, 2008), for evaluation purpose.

To address the key questions presented in the outset of this chapter, we have used the

hybrid eddy detection and tracking algorithm described in the previous chapter. The eddy properties have been investigated in the Mozambique Channel, at 3 different subregions, known to exhibit distinct eddy dynamics (Schouten et al., 2003): the northern subregion, range between 10°S and 15.5°S, 39°E and 48.5°E; the central subregion, between $\sim$ 15.6°S and 24°S, 34°E and 47°E, and the southern subregion, between 24.1°S and 29.5°S, and 32°E and 46°E. The investigated eddy mean properties are: Statistical census (Number of eddies N); eddy lifetime $\bar{\tau}$; eddy amplitude $\bar{\eta}$; eddy diameter $\bar{L}$; and eddy kinetic energy ($\overline{K}$) integrated over the eddy's surface (S).

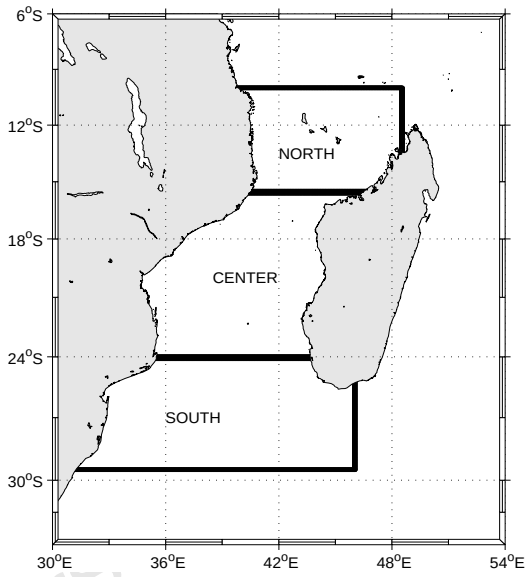

Figure 6.2. Subregions used to investigate the eddy properties. North: 10°S - 15.5°S, 39°E - 48.5°E; Center: 15.6°S - 24°S, 34°E - 47°E, and South: 24.1°S - 29.5°S, 32°E - 45°E.

6.2 Eddy properties

6.2.1 Eddy generation site and trajectory

The eddy generation site and trajectory of a fraction of the eddies (first 3-year, starting in October 14, 1992 for altimetry) are shown in Figure 6.3 (for AVISO), and in Figure 6.4 (for SWIM, first 3-year of 7-year climatology). The generation site is identified by a bold black ring, and the trajectory is indicated by continuous lines. The dots represent the pathways outside of the tracking domain.

Looking at the eddy positions, it appears that there are regions that have favored eddy generation: At the northern subregion of the channel, both for Altimetry (Figure 6.3a,b) and model (Figure 6.4a,b), it is evident that cyclonic and anticyclonic eddies are generated almost everywhere. It is also well known a favorite generation site for anticyclonic eddies to the northwest of the Cape-Amber, near 12°S, 48°E (Figure 6.3a, Figure 6.4a). The stronger gradient (closely spaced) trajectory lines, as well as the frequency of eddy occurrence in [%], in a box of $0.5° \times 0.5°$ grid size, for cyclonic and anticyclonic eddies presented in Figure 6.5, both for altimetry and model, have given insight about the pathway of the eddies: the pathway of the eddies in this region is mostly westwards along the 12°S latitude. During their westward propagation, the anticyclonic eddies have passed mainly to the north of the Comores Archipelago (Figure 6.3a), and on reaching near 42°E, the trajectory has been deflected southwards (likely due to the continental boundary), and extended towards the narrows of the channel $\sim$ 17°S, mostly along the $\sim$ 3000 m isobath. In the model (Figure 6.4a), the westward propagation of the anticyclonic eddies seems more disperse, and many eddy centres appear to pass through the gaps between the islands of the Archipelago. It is also evident for Altimetry that part of the trajectory lines of the anticyclonic eddies described a closed loop around the Archipelago (similar to the Comores Gyre). Cyclonic eddies (Figure 6.3b, Figure 6.4b) on the other hand, appears to be generated within the Comores Basin, to the south of the Archipelago: For altimetry (Figure 6.3b), this pattern seems localized, preferentially the southwest and southeast of the basin, while in SWIM, such pattern is not evident (Figure 6.4b). Interestingly, for both SWIM and altimetry, only cyclonic eddies generated to the North of Cape-Amber have shown a northwest propagation.

In the central subregion, an anticyclonic eddy generation site is evident at the eastern boundary of the channel (Figure 6.3c, Figure 6.4c), near the Madagascar Bight, between 19°S and 22°S. Another anticyclonic eddy generation site also is evident at the narrows of the channel, around 16°S. Anticyclonic eddies mostly seemed to prefer this region (at the narrows of the channel between $\sim$ 15.5°S and 17°S). Their secondary generation spot is near 20°, 44°E. The anticyclonic eddies generated at the narrows of the channel propagate mainly southwestward along the western boundary of the channel, adjacent to the Mozambican coastline. The anticyclonic eddies generated in the Madagascar Bight ($\sim$20°, 44°E), also have shown a southwestward propagation, and appears to connect the other anticyclonic path at the Mozambican coast, near 24°S. At the Madagascar Bight, cyclonic

eddies are mostly seen to be generated around 19°S (Figure 6.3d), near the Madagascar Coast. Also another site for cyclonic eddy generation is located near 23°S, 42°E (more evident in altimetry than in SWIM). The generation of the anticyclonic eddies in the northern, or central Mozambique Channel, and their southwestward trajectory along the western boundary of the channel, have been observed in many studies (Schouten et al., 2003, De Ruijter et al., 2005, van der Werf et al., 2010). On the other hand, the generation in the central eastern boundary of the channel, and their southwestward trajectory is a novel knowledge, as described by Halo et al. (2012) [*in review*]. The presence of such and other patterns, both in SWIM and altimetry, suggest a good agreement, between model and observations.

Eddy tracking in the southern subregion of the Mozambique Channel, in altimetry is shown in Figure 6.3e, for anticyclones, and in Figure 6.3f, for cyclones. Similarly, in SWIM Figure 6.4e is for the anticyclones, and Figure 6.4f is for the cyclones.

In regard to the anticyclonic eddy generation sites, in the southern Mozambique Channel, altimetric observation (Figure 6.3e) suggests three focus: at the southwest coast of Madagascar, around 25°S, 43°E; on the eastern flank of the Madagascar Ridge, around 27°S, 47°E; and on the western flank of the Madagascar Ridge, between 42°E and 46°E, 28°S and 29.5°S. This pattern is consistent with the dipole eddy structures observed by De Ruijter et al. (2004). SWIM has shown some difficulties in reproducing such focus. It has only reproduced the anticyclonic generation site on the western flank of the Madagascar Ridge, between 42°E and 46°E, 28°S and 29.5°S. It is noteworthy that SWIM (Figure 6.4e) has reproduced relatively few anticyclonic eddies in this subregion, when compared to altimetry (Figure 6.3e). The anticyclonic eddy generation site on the western flank of the Madagascar Ridge, between 42°E and 46°E, 28°S and 29.5°S, is consistent with the anticyclonic recirculation of the southern extension of the SEMC, as represented by Siedler et al. (2009). On the other hand, the anticyclonic site on the eastern flank of the ridge (around 27°S, 47°E), is also consistent with the anticyclonic recirculation of the flow field, likely associated to the retroflection of the SEMC as presented by Lutjeharms and Machu (2000), and Quartly et al. (2006).

With regard to the cyclonic eddies (Figure 6.3f), shows that their favorite generation site appears to be around the southern tip of Madagascar (Cape Saint-Marie), near $\sim 26°$S, both to the east and west of the Madagascar Ridge. The second focus, for cyclonic eddy formation, to the South of Madagascar, is located over the Madagascar Ridge, between

45°E and 46°E, 28°S and 29.5°S. The third site favoring cyclonic eddy formation, is located in the western boundary of the channel, at Delagoa Bight, near Maputo (between 25°S and 27°S).

The generation site around the Cape Saint-Marie, is consistent with cyclonic eddy formation, induced by the shear of the SEMC with the Madagascar continental shelf, as some studies have proposed (De Ruijter et al., 2004, Siedler et al., 2009). Over Madagascar Ridge, the site of cyclonic eddy formation has not been yet documented, but it seems that some eddies could be locally formed by interaction of the flow with topography. With regard to the cyclonic eddies generated at Delagoa Bight, it is consistent with the cyclonic recirculation within the Bight, as proposed by Lutjeharms and da Silva (1988).

In regard to their trajectories, both cyclonic and anticyclonic eddies have propagated southwestward towards the African coast. In the model (Figure 6.4e), anticyclonic eddies generated near ∼28°S, 46°E (Figure 6.4e), have propagated mostly, northwestwards, but when reaching the Mozambican coast (∼26°S), they appear to be deflected and propagated southwards along the coastline. The overall propagation path of the tracked eddies through the full length of the channel is evident in Figure 6.5. It shows that the main route of propagation of the eddies originated in the northern subregion is along the western boundaries of the channel. Eddies generated at the eastern boundaries, in the center of the channel also join the path at the western boundary near 24°S. A number of eddies coming from the south of Madagascar, also join the path at the western boundary near the same latitude position.

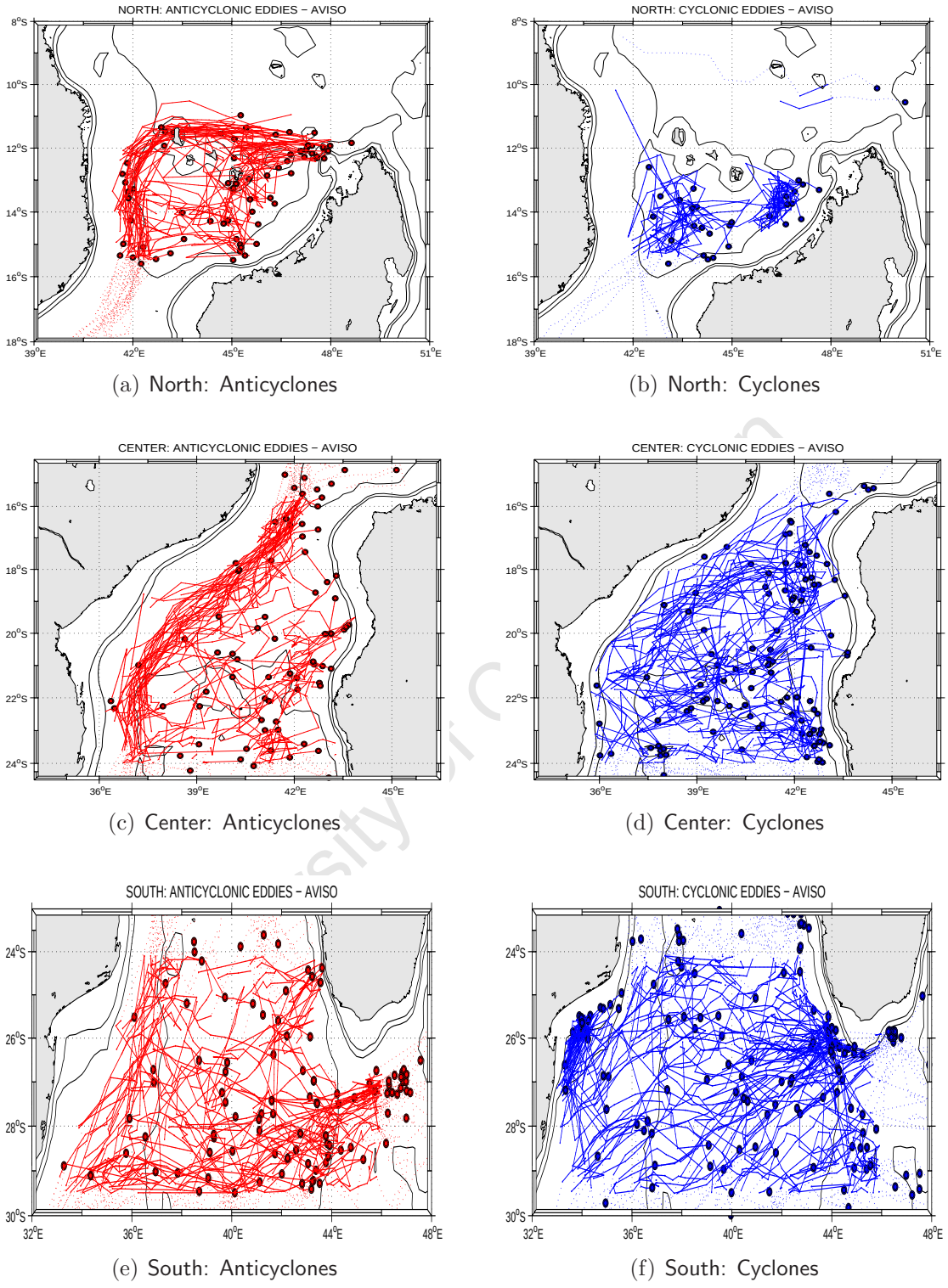

(a) North: Anticyclones (b) North: Cyclones

(c) Center: Anticyclones (d) Center: Cyclones

(e) South: Anticyclones (f) South: Cyclones

Figure 6.3. Tracks of first 3-year of anticyclonic eddies (left side panels) and cyclonic eddies (right side panels), and their formation sites at different subregions of the Mozambique Channel, based on satellite altimety data. Solid black rings indicate the formation site, and the lines show their trajectory. The background contours are the isobaths at 500 1000 3000 and 5000 m.

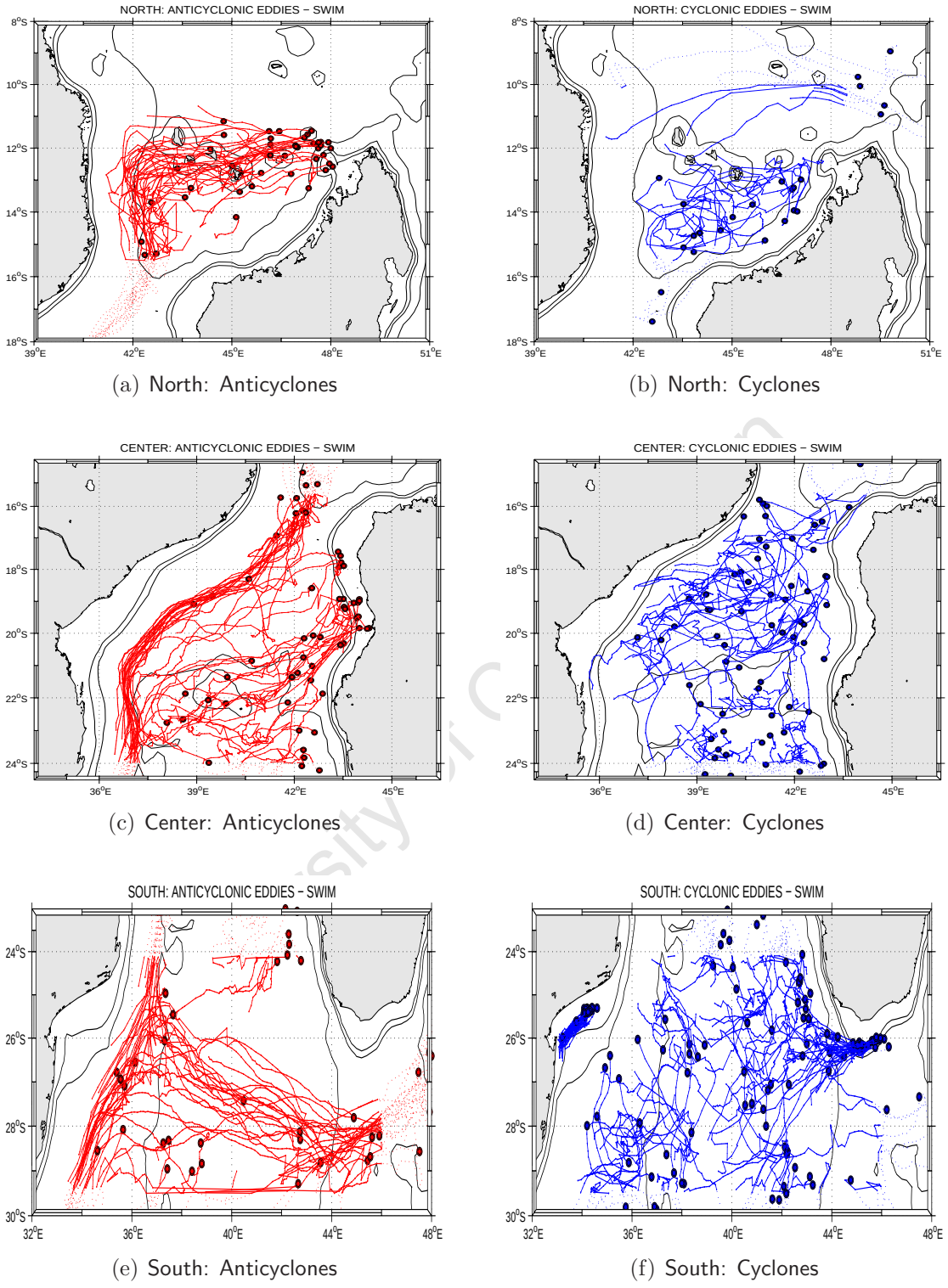

(a) North: Anticyclones (b) North: Cyclones

(c) Center: Anticyclones (d) Center: Cyclones

(e) South: Anticyclones (f) South: Cyclones

Figure 6.4. Tracks of first 3-year of anticyclonic eddies (left side panels) and cyclonic eddies (right side panels) center, and their formation sites at different subregions of the Mozambique Channel, based on SWIM outputs. Solid black rings indicate the formation site, and the lines show their trajectory. The background contours are the isobaths at 500 1000 3000 and 5000 m.

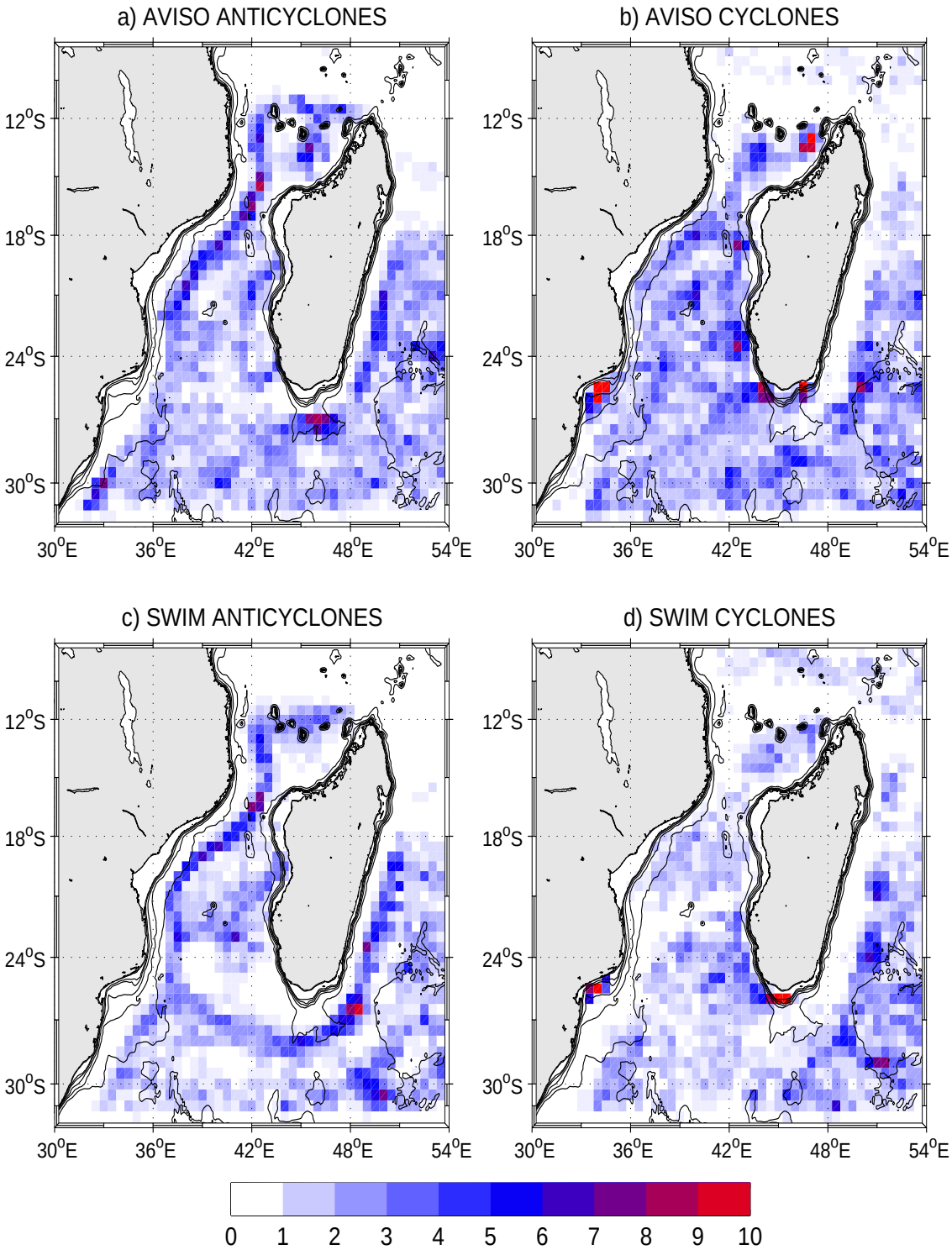

Figure 6.5. Frequency of occurrence of all tracked eddies center in [%] in a square box 0.5×0.5 grid size. Anticyclonic eddies from altimetry (October 14, 1992 to March 31, 2010) (a), and cyclonic eddies (7-year climatology) (b). Anticyclonic eddies from SWIM (c), and cyclonic eddies (d). The background bathymetric contours are isobaths at 0 100 200 500 1000 2000 5000 m.

6.2.2 Eddy census

The results obtained from both altimetric observation and model data, with regard to the mean properties of the eddies is presented in Table 6.1. The statistical eddy census performed in altimetry (dataset from October 14, 1992 to March 31, 2010), pointed that throughout the Mozambique Channel, a total of 109 eddies have been identified. About 18 eddies per year (16.5%) have been observed in the northern subregion of the channel: 6 cyclonic and 12 anticyclonic eddies. In the central subregion, a total of 37 eddies (33.9%) have been identified: 21 cyclonic and 16 anticyclonic eddies. In the south, a greater number of 54 eddies (49.5%) have been found: 29 cyclonic and 25 anticyclonic eddies.

The census in the model data (7 years) has indicated a total number of 89 eddies. 16 eddies per year (17.8%) are identified in the northern subregion: 7 cyclonic and 9 anticyclonic eddies. In the center, about 29 eddies (32.6%) have been identified: 15 cyclonic and 14 anticyclonic eddies. In the southern subregion, about 44 eddies (49.4%) have been identified: 29 cyclonic and 15 anticyclonic eddies.

The rates show a consistency between the model and observation: The number of total eddies per subregion increases southwards. Also the numbers of cyclonic eddies are higher than anticyclonics in the center and south of the channel, while in the north, the anticyclonic eddies are more numerous than cyclonic eddies.

6.2.3 Eddy polarity

The ratio of the number of cyclonic eddies and the number of the anticyclonic eddies, per year, with respect to their radius, is presented in Figure 6.6: Left panel for altimetry, and right panel for the model. The ratio provides an useful information on the length-scale at which an eddy type (either cyclonic or anticyclonic) is considered dominant (Kurian et al., 2011, Chelton et al., 2011). For altimetry, in the northern subregion of the channel (Figure 6.6a), the ratio ranges from ~ 0 to 2. In this range the number of cyclonic eddies is dominant over the number of anticyclonics, for eddy radius inferior to ~ 45 km, and also for eddy radius between ~ 75 km and 85 km. The anticyclonic eddies dominate between ~ 45 km and 75 km, and also for eddy radius larger than 85 km. In the center of the channel, the ratio ranges between ~ 0 and 2.8. In this range, cyclonic eddies dominate over anticyclonics for an eddy radius between ~ 42 km and 85 km, while anticyclonic eddies dominante over cyclonics for eddy radius inferior to 42 km, and also for eddy radius larger than 85 km. To the south of the channel, the ratio ranges between ~ 0

and 1.7. In this ratio, the number of cyclonic eddies have dominated the anticyclonics for eddy radius inferior to about $\sim$ 80 km, while the number of anticyclonic eddies have dominated the number of cyclonic eddies, for eddy radius larger than $\sim$ 80 km.

For the model (Figure 6.6b), in the northern subregion, the ratio ranges between 0 - 8.8. In this range, the number of cyclonic eddies dominate the anticyclonics, for eddies with radius smaller than $\sim$ 90 km, while for larger radius, i.e., over $\sim$ 90 km, the number of anticyclonic eddies dominate over the cyclonics. In the center of the channel, the ratio is relatively lower, it ranges between $\sim$ 0 and 1.90. In this range, the number of cyclonic eddies dominate over the anticyclonics for eddy radius also smaller than $\sim$ 90 km, while for radius larger than $\sim$ 90 km, the number of anticyclonic eddies have dominated over the number of cyclonic eddies. In the south the ratio ranges between $\sim$ 0 to 3.90. In this range, the number of cyclonic eddies dominate the number of anticyclonics, for eddies with radius smaller than $\sim$ 80 km, while for larger eddies, i.e., radius larger than $\sim$ 80 km, the number of anticyclonic eddies have dominated over the number of cyclonics.

Polarity analysis shows that in general, the anticyclonic eddies dominate over the cyclones for the largest eddies, while the cyclonic eddies dominate over anticyclonics for relatively smallest eddies.

6.2.4 Eddy life-time

The eddy lifetime (τ) has been regarded as the difference between the date when the eddy was for the first time identified within the subregion, and the date since the eddy was last seen inside of the same subregion. Only eddies with a lifetime longer than 30 days have been considered. For altimetry, Table 6.1a shows that the anticyclonic eddies have shown a relatively longer lifetime than cyclonic eddies, in the north and in the center of the channel. Whereas in the south of the channel, the lifetime of the anticyclonic eddies is relatively shorter (only 5 days) than the cyclonic eddies. For the model, Table 6.1b shows that the lifetime of the anticyclonic eddies are longer than the cyclonic eddies everywhere, in the north, center and south subregions. However, a common aspect, both for model and observation is that the cyclonic eddies in the central part of the channel, have the shortest lifetime, when compared to the lifetime of cyclonic eddies in the northern and southern subregions of the channel ($\sim$ 84 days in altimetry, and 54 days in the model). Also it appears that the lifetime of the anticyclonic eddies increases southwards, except in the southern subregion, in altimetry.

(a) AVISO

	N $[\frac{eddies}{year}]$	$\bar{\tau}$ [day]	$\bar{\eta}$ [cm]	L [km]	K [m^4s^{-2}]
NORTH					
Cyclones	6	94	8	154	$12.7*10^{10}$
Anticyclones	12	102	10	172	$26.2*10^{10}$
	N $[\frac{eddies}{year}]$	$\bar{\tau}$ [day]	$\bar{\eta}$ [cm]	$\bar{L}$ [km]	K [m^4s^{-2}]
CENTER					
Cyclones	21	84	11	136	$42*10^{10}$
Anticyclones	16	106	15	159	$58.1*10^{10}$
	N $[\frac{eddies}{year}]$	$\bar{\tau}$ [day]	$\bar{\eta}$ [cm]	$\bar{L}$ [km]	K [m^4s^{-2}]
SOUTH					
Cyclones	29	105	13	129	$45.7*10^{10}$
Anticyclones	25	100	14	139	$39.8*10^{10}$

(b) SWIM

	N $[\frac{eddies}{year}]$	$\bar{\tau}$ [day]	$\bar{\eta}$ [cm]	$\bar{L}$ [km]	K [m^4s^{-2}]
NORTH					
Cyclones	7	61	8	166	$12.1*10^{10}$
Anticyclones	9	94	20	246	$39.3*10^{10}$
	N $[\frac{eddies}{year}]$	$\bar{\tau}$ [day]	$\bar{\eta}$ [cm]	$\bar{L}$ [km]	K [m^4s^{-2}]
CENTER					
Cyclones	15	54	8	130	$11.9*10^{10}$
Anticyclones	14	101	21	175	$52.9*10^{10}$
	N $[\frac{eddies}{year}]$	$\bar{\tau}$ [day]	$\bar{\eta}$ [cm]	$\bar{L}$ [km]	K [m^4s^{-2}]
SOUTH					
Cyclones	29	60	8	109	$7.2*10^{10}$
Anticyclones	15	133	34	173	$48.7*10^{10}$

Table 6.1. Mean properties of the Mozambique Channel eddies, tracked at different subregions of the channel. From altimetry dataset for October 14, 1992 to March 31, 2010 ($\sim$ 16 years (a)), and SWIM dataset for 7 years (b): Number of eddies per year (N), mean lifetime ($\bar{\tau}$), mean amplitude ($\bar{\eta}$), mean diameter ($\bar{L}$), and total integrated energy within the eddy area K (cm^4s^{-2}).

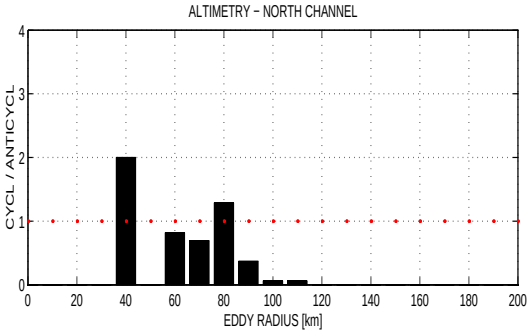

(a) Northern Channel AVISO

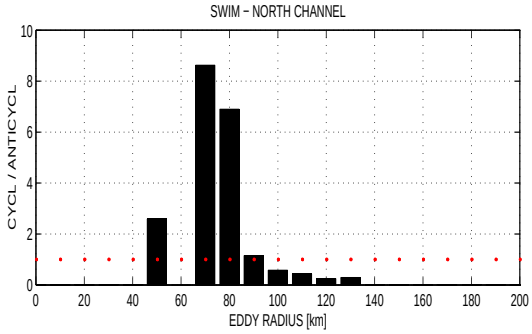

(b) Northern Channel SWIM

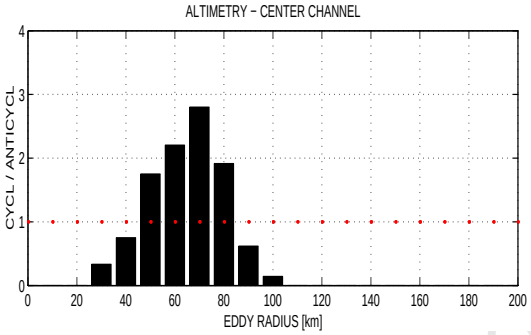

(c) Central Channel AVISO

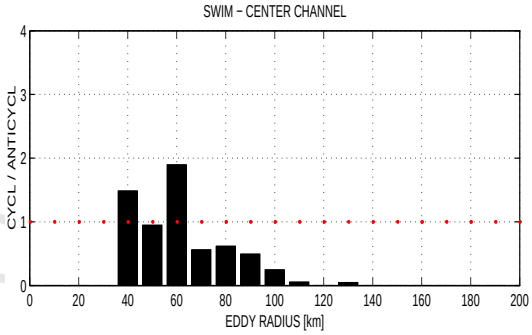

(d) Central Channel SWIM

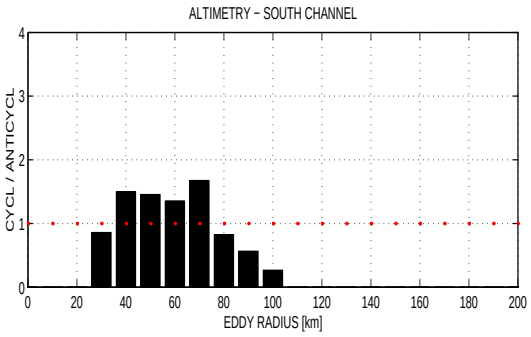

(e) Southern Channel AVISO

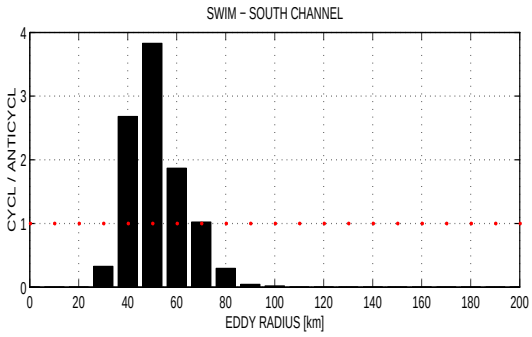

(f) Southern Channel SWIM

Figure 6.6. Ration between the number of cyclonic eddies per number of anticyclonic eddies, identified in altimetry, at different subregions of the channel. The red dots limits the numbers above and below 1.

6.2.5 Eddy amplitude

Eddy amplitude ($\bar{\eta}$), has been defined as the difference between the extremes maximum and minimum of the eddy sea surface height (Chelton et al., 2011). For altimetry, Table 6.1a shows that the amplitudes of both cyclonic and anticyclonic eddies increase from the north to south of the Mozambique Channel, except for the anticyclonic eddies in the south of the channel, where it decreases in 1 cm. Also the amplitude of the anticyclonic eddies is heigher than the amplitude of the cyclonic eddies, in the whole subregions of the channel. In the model, SWIM has shown some difficulties in reproducing the southward increase of amplitude in the cyclonic eddies (keeping the same amplitude of 8 cm throughout the channel), while the amplitude of the anticyclonic eddies have shown a consistent southward increase. The amplitudes of the anticyclonic eddies in SWIM, are almost 2× higher the amplitudes of anticyclonic eddies from altimetry. This pattern is consistent with the SWIM overestimation of the RMS SSH in about 50%, and also perhaps the observed overestimation of the EKE in about 40%, since it has been estimated from geostrophic currents computed from variations of SSH, as presented in chapter 4.

6.2.6 Eddy diameter

The eddy equivalent diameter (L), has been determined as the mean of all identified eddies per frame, with L defined by $L{=}2{\times}\sqrt{\frac{\sum S}{\pi}}$ (Souza et al., 2011). Where S is the eddy surface, assumed to have a circular geometry. Their calculated mean values, for the cyclones and anticyclones, at each subregion of the Mozambique Channel are shown in Table 6.1a, for altimetry, and in Table 6.1b, for SWIM.

For altimetry, the mean diameter $\bar{L}$ of cyclonic and anticyclonic eddies, in the northern subregion is about 154 km and 172 km respectively. For the model, they range between 166 km and 246 km, for cyclonic and anticyclonic eddies respectively. The values show that in the northern Mozambique Channel, the model has reproduced relatively larger cyclonic and anticyclonic eddies than in altimetry. In the center, for altimetry, the mean diameter $\bar{L}$ of cyclonic eddies is about 136 km, and of the anticyclonics is about 159 km. In the model, the cyclonic eddies has a $\bar{L}$ of about 130 km, and anticyclonic eddies a $\bar{L}$ of about 175 km. In the center of the channel, the calculation shows that the model has reproduced relatively smaller cyclonic eddies, and larger anticyclonic eddies, than in altimetry. In the south, for altimetry, the mean diameter $\bar{L}$ of cyclonic and anticyclonic eddies is about 129 km and 139 km, and for the model, $\bar{L}$ of cyclonic and anticyclonic

eddies is about 109 km and 173 km respectively. The values also show that the model has reproduced relatively smaller cyclonic eddies, and larger anticyclonic eddies, than in altimetry.

The result shows a good consistency between the model and altimetry: The mean diameter of the anticyclonic eddies are larger than the cyclonic eddies. Both cyclonic and anticyclonic eddies decrease their diameter from the north to south of the channel. This southward decrease of the eddies diameter, is in agreement with the north to South decrease of the first baroclinic Rossby radius of deformation in the region, as shown by Chelton et al. (1998).

In general the model has reproduced larger eddies than in altimetry. It has been observed in the model, the lowest minimum and highest maximum eddy diameters range ($\sim$ 109 km and 246 km), than altimetry, where the minimum and maximum diameter captured range between 129 km and 172 km. The ability of the model to capture the lowest minimum diameter could be attributed to the relatively higher resolution of the SWIM configuration ($\sim$ 21 km), than the altimetric data resolution ($\sim$ 25 km).

6.2.7 Eddy surface integrated kinetic energy

The eddy kinetic energy is calculated by the expression $K=\frac{u_g^2+v_g^2}{2}$. Where u and v are the zonal and meridional components of the geostrophic velocities, computed using the sea surface height (i.e. $u_g=-\frac{g\partial\eta}{f\partial y}$), and $v_g=\frac{g\partial\eta}{f\partial x}$. Here g is the acceleration due to gravity, taken to be (g=9.81 m s^{-2}), and $f=2\Omega\sin\theta$ is the Coriolis parameter, where Ω is the Earth rotation frequency ($\Omega=7.3\times10^{-5}$s^{-1}), and θ is the latitude. The total eddy kinetic energy is here considered as K stored in cyclonic eddies plus K in the anticyclonic eddies, integrated within the eddy's surface ($\iint Kds$). For the northern subregion of the channel, the total eddy kinetic energy derived from the altimetry is about 38.9×10^{10} m^4 s^{-2}: about 12.7×10^{10} m^4 s^{-2} for cyclonic, and 26.2×10^{10} m^4 s^{-2} for anticyclonic eddies. In the central region, the total energy is about 100.1×10^{10} m^4 s^{-2}: about 42×10^{10} m^4 s^{-2} for cyclonic eddies, and 58.1×10^{10} m^4 s^{-2} for anticyclonic eddies. In the south, the total energy is about 85.5×10^{10} m^{4}s^{-2}: about 45.7×10^{10} m^4 s^{-2} for cyclonic eddies, and 39.8×10^{10} m^4 s^{-2} for the anticyclonic eddies. For the model, the total energy in the northern subregion is estimated in about 51.4×10^{10} m^4 s^{-2}: about 12.1×10^{10} m^4 s^{-2} for cyclonic eddies, and 39.3×10^{10} m^4 s^{-2} for anticyclonic eddies. In the central subregion, the total energy is about 64.8×10^{10} m^4 s^{-2}: about 11.9×10^{10} m^4 s^{-2} for cyclonic eddies and 52.9×10^{10} m^4

s^{-2} for anticyclonic eddies. In the southern subregion, the total energy is estimated in about 55.9×10^{10} m^4 s^{-2}: 7.2×10^{10} m^4 s^{-2} for cyclonic eddies, and 48.7×10^{10} m^4 s^{-2} for anticyclonic eddies.

The estimated energy levels have shown a good consistency between SWIM and altimetry: both have shown the highest peak of the total K in the center of the Mozambique Channel. This is in agreement with the maps of MEKE shown in Figure 4.14, where the most energetic site in the whole channel is in the center. In general energy of the anticyclonic eddies is greater than the cyclonic eddies (except in the southern channel, for altimetry, where the energy of the cyclones is greater than the anticyclonic eddies, in about 5.9×10^{10} m^4 s^{-2}). The bulk of the total K in each subregion, have the greatest contribution from the anticyclonic eddies. The total K at each subregion are higher in altimetry than in SWIM, except in the northern subregion. The energy of cyclonic eddies from the altimetry are greater than the energy of the cyclonic eddies reproduced in SWIM. This could be due to the fact that cyclonic eddies are relatively larger in altimetry than in SWIM. Similarly, the energy of the anticyclonic eddies produced in SWIM are greater than the anticyclonic energy produced in altimetry (except in the center of the channel). Also this could be related to the fact that SWIM produces relatively larger anticyclonic eddies than the altimetry.

6.2.8 Eddy frequency distribution

Figure 6.7, and Figure 6.8 show the histogram of frequency distribution in [%] of the Mozambique Channel eddies, with respect to their radius (R=$\frac{\bar{L}}{2}$), at different subregions of the channel (see the top labels in each panel for reference of the eddy type). Figure 6.7, is for altimetry, and Figure 6.8 is for SWIM. For altimetry (Figure 6.7), the radius of the cyclonic eddies range from 40 km to 110 km in the north of the channel; 30 km to 100 km in the center and southern subregions. For anticyclonic eddies, their radius range from 40 km to 130 km in the north; 30 km to 130 km in the center; and 30 km to 120 km in the South of the channel.

At the scale of the first baroclinic Rossby radius of deformation for the region, known to range between 100 km in the northern Mozambique Channel, to about 40 km in the southern Mozambique Channel ((Chelton et al., 1998), see their Figure 6), it can be seen in Figure 6.7a, that the most dominant frequency of the cyclonic eddies ($\sim$ 16%) identified in the northern Mozambique Channel, are centered around a mean radius of 80

km. In the center of the channel (Figure 6.7b), the dominant frequency of the cyclonic eddies ($\sim$ 18%) have their radius centered around 70 km; and in the south (Figure 6.7c), the dominant peak ($\sim$ 15%) of the cyclonic eddies are centered around 70 km and 60 km radius. Therefore, it is observed a southward decrease of the eddy radius in cyclones. This is consistent with the southward decrease of the mean diameter of the cyclonic eddies presented in Table 6.1a. The decrease of the cyclonic eddy radius from north to south of the channel, appears to follow the decrease of the first baroclinic Rossby radius of deformation.

With regard to the anticyclonic eddies, their dominant frequency ($\sim$ 15%) is centered at 90 km radius in the northern Mozambique Channel (Figure 6.7a). In the center (Figure 6.7b), their dominant frequency is observed at two different radius range: the first peak ($\sim$ 7%) is centered around 70 km radius, and the second peak ($\sim$ 7.5%) is centered around 100 km radius. In the south of the channel (Figure 6.7c), the anticyclonic eddies have their dominant frequency ($\sim$ 11%) centered at 60 km radius. Similar to the cyclonic eddies, it is also observed a southward decrease of the eddy radius in anticyclonic eddies, which also appears to follow the first baroclinic Rossby radius of deformation for the region.

In the model (Figure 6.8), the radius of the cyclonic eddies range from 50 km to 130 km in the northern Mozambique Channel; 30 km to 130 km in the Center; and 30 km to 100 km in the South. For the anticyclonic eddies, their radius range from 50 km to 190 km in the north; 40 km to 150 km in the center; and 30 km to 150 km in the south. The cyclonic eddies in the north of the channel (Figure 6.8a), have their dominant frequency ($\sim$ 8%) centered at 70 km radius. In the center (Figure 6.8b), their dominant frequency ($\sim$ 12%) is also centered at 70 km. In the south (Figure 6.8c), the dominant frequency ($\sim$ 25%) is centered around a relatively smaller radius of about 50 km. It is observed a southward increase of their dominant frequency, in 8%, 12%, and 25%, respectively. The southward decrease of their radius is only observed between the central and southern subregions of the channel. With regard to the anticyclonic eddies, in the north Mozambique Channel (Figure 6.8a), they have their most dominant frequency ($\sim$ 12%) centered at 140 km radius. Note that this is beyond the first baroclinic Rossby radius of deformation for this region. However, at the scale of the typical baroclinic Rossby radius, a secondary dominant frequency ($\sim$ 8%) is observed at 100 km radius. In the center of the channel (Figure 6.8b), at the range scale of the first Baroclinic Rossby radius of deformation (50 km to 100 km), as suggested by Chelton et al. (1998), the anticyclonic eddies have

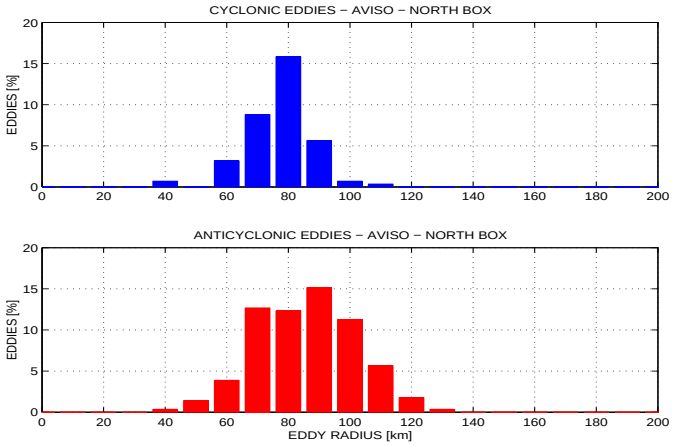

(a) Northern Channel

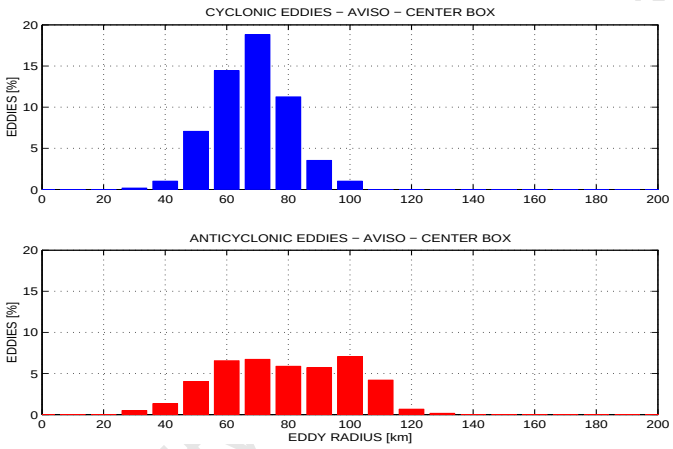

(b) Central Channel

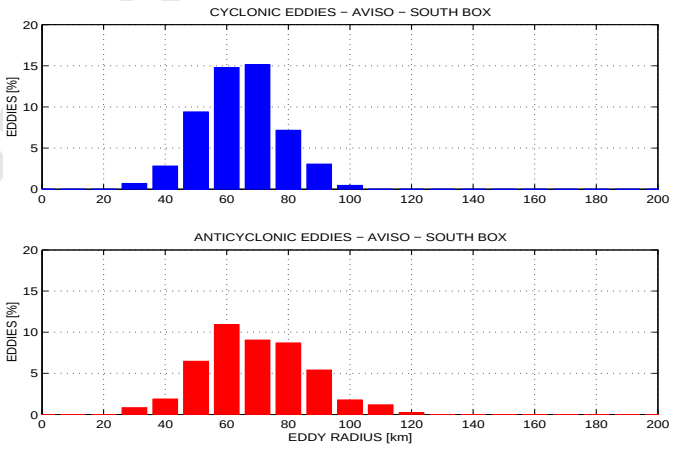

(c) Southern Channel

Figure 6.7. Histogram of frequency distribution for the eddies from the altimetry, at different subregions of the Mozambique Channel. In all panels, blue is for cyclones and red is for anticyclones.

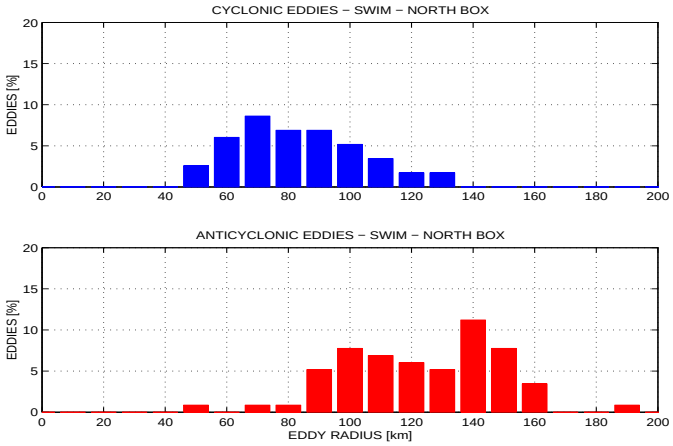

(a) Northern Channel

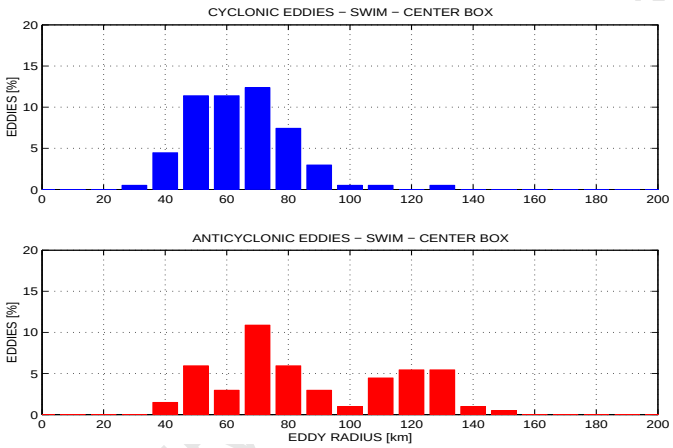

(b) Central Channel

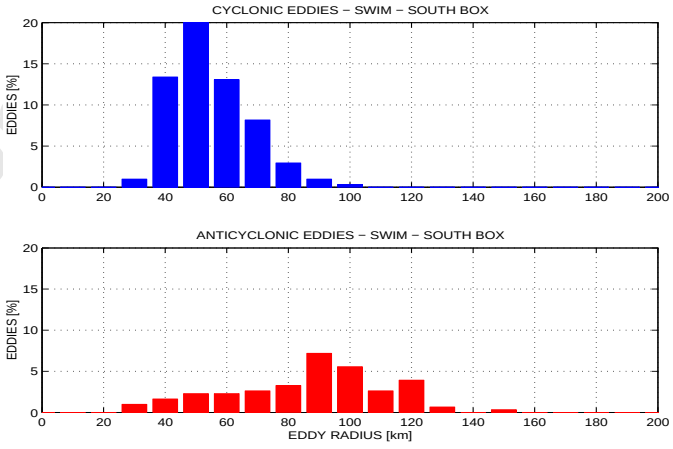

(c) Southern Channel

Figure 6.8. Histogram of frequency distribution of eddies SWIM, at different subregions of the Mozambique Channel. Blue is for cyclones and red is for anticyclones.

their dominant frequency ($\sim$ 11%) centered at 70 km. Beyond the first baroclinic Rossby radius, it is also observed another peak, centered between 120 km and 130 km eddy radius. Similarly, in the south of the channel (Figure 6.8c), the anticyclonic eddies also have shown a bimodal distribution, with the dominant frequency ($\sim$8%) at the range scale of the first Baroclinic Rossby radius centered at 90 km, while at a larger scale, beyond the first baroclinic Rossby radius, the peak is centered at 120 km radius.

Similar to altimetry, it is also observed a decrease of the anticyclonic eddy radius, from north to south of the channel. In the model, such a southward decrease is observed both in the first, and second turbulent modes. Different from the altimetry, the second turbulent mode (beyond the first baroclinic Rossby radius), in SWIM is observed in whole subregions of the channel, while in altimetry is evident only in the center of the channel.

Our analysis on the frequency of anticyclonic eddies per year, with respect to the range of the first baroclinic Rossby radius for the region presented by Chelton et al. (1998), shows that for altimetry, in the north of the channel, about 7.4 eddies per year are present within the range of baroclinic Rossby radius (between 40 km to 100 km (Chelton et al., 1998)), and about 3.0 eddies per year, have their radius beyond the baroclinic Rossby radius (over 100 km). In the center of the channel, about 10.5 eddies per year are in the first mesoscale mode, with radius within the baroclinic Rossby radius, and about 4.1 eddies per year are present in the second mode, have their radius beyond 100 km. In the south of the channel, about 21.1 anticyclonic eddies per year have their radius within the range of the first baroclinic Rossby radius, and only about 1.6 per year are beyond 100 km radius. Similar analysis for the anticyclonic eddies from the model shows that in the north of the channel, about 1.3 anticyclonic eddies per year are present in the first mesoscale mode, and about 8.3 anticyclonic eddies per year are present in the second mode. In the center of the channel, about 8.8 anticyclonic eddies per year are present in the first mode, and about 5 anticyclonic eddies per year are present in the second mode. In the south, about 9 anticyclonic eddies per year are present in the first mode, and about 6 anticyclonic eddies are present in the second mode. The anticyclonic eddy frequency of about 4.1 per year (in the second mode), observed in altimetry, is in agreement with the frequency of about 5 per year (in the second mode), observed in SWIM. This is also consistent with hydrographic observations across the narrows of the Mozambique Channel, which suggests that the regular passage of the large anticyclonic eddies at 17°S, is about 4 - 5 eddies per year (De Ruijter et al., 2002, Ridderinkhof and De Ruijter, 2003, Schouten et al., 2003).

Comparisons of the eddy diameter between altimetry and SWIM shows that SWIM

reproduces relatively larger eddies than altimetry. This is consistent with the eddy mean diameters shown in Table 6.1. Nevertheless, there is a good consistency between SWIM and altimetry, in reproducing the southward decrease of the eddy radius in the Mozambique Channel.

6.2.9 Eddy energy spectrum

The spectrum of the eddy energy distribution with respect to their size (radius), in each subregion of the Mozambique Channel, is presented in Figure 6.9, for altimetry, and in Figure 6.10, for SWIM (see the labels on top of the panels for reference). For altimetry, in the north of the channel (Figure 6.9a), the cyclonic eddies have their dominant energy peak ($\sim 6\times10^{10}$cm^2 s^{-2}) centered at 80 km radius. In the center, their energy peak ($\sim 14\times10^{10}$cm^2 s^{-2}) also is centered at 80 km radius, while in the south, their peak ($\sim 16\times10^{10}$cm^2 s^{-2}) is centered at a relatively smaller radius, at 70 km radius. The estimate shows that the energy of the cyclonic eddies have increased from the north to the south of the channel. Throughout the channel, the most dominant energy peak in the cyclonic eddies is located in the eddies with a 70 km radius. The anticyclonic eddies on the other hand, in the north of the channel (Figure 6.9a), have shown their dominant energy peak ($\sim 8\times10^{10}$cm^2 s^{-2}) centered around 100 km radius. In the center (Figure 6.9b), their dominant energy peak ($\sim 19\times10^{10}$cm^2 s^{-2}) also is centered at 100 km. In the south (Figure 6.9c), their energy peak ($\sim 10.5\times10^{10}$cm^2 s^{-2}) is centered at a relatively smaller radius of 90 km. Different from cyclonic eddies, the most dominant energy peak throughout the channel, is in the center of the channel, for eddies with about 100 km radius. This is in agreement with Table 6.1. In the model (Figure 6.10), for the north of the channel (Figure 6.10a), the cyclonic eddies have shown their dominant energy peak ($\sim 2.5\times10^{10}$cm^2 s^{-2}), centered at 90 km radius. In the center, their energy peak ($\sim 3\times10^{10}$cm^2 s^{-2}), have been observed centered at 80 km radius. In the south, their dominant energy peak ($\sim 2.5\times10^{10}$cm^2 s^{-2}), is centered at a relatively smaller radius of 50 km.

As can be seen from the estimates, the most dominant energy peak in the SWIM cyclonic eddies throughout the channel is located in the center of the channel, at 80 km eddy radius. However, it is seen that the energy of the cyclonic eddies in general do not have significant geographical changes. Our estimates also show that the energy levels in the cyclonic eddies from SWIM are relatively lower when compared against the energies

of the cyclonic eddies from the altimetry. With regard to the anticyclonic eddies, in the north of the channel, they have their dominant energy peak ($\sim 10\times10^{10}$cm^2 s^{-2}), centered at 150 km. In the center, the dominant energy peak (over 20×10^{10}cm^2 s^{-2}), is centered at 130 km radius. In the south of the channel, the dominant energy peak ($\sim 13.5\times10^{10}$cm^2 s^{-2}), have been observed at 100 km radius. As observed in altimetry, most dominant energy peak throughout the channel, in the anticyclonic eddies is also located in the central part of the channel, at 130 km radius. This is consistent with Figure 4.14. The energy of the anticyclonic eddies is stronger than the energy of the cyclonic eddies. This is also consistent with Table 6.1.

In general, the model has shown comparable dominant energy levels for the anticyclonic eddies, but underestimates the energy levels for the cyclonic eddies.

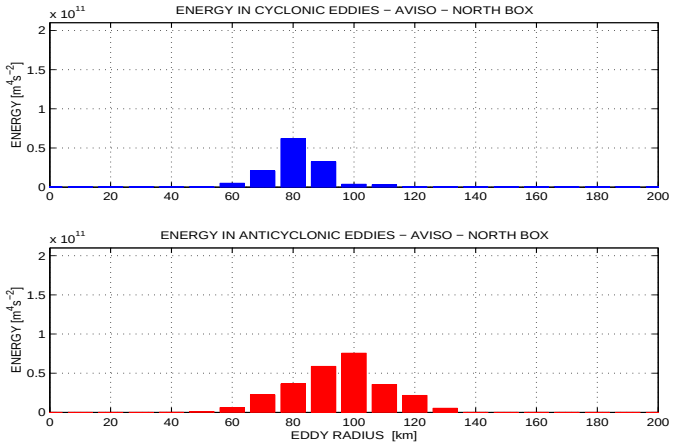

(a) Northern Channel

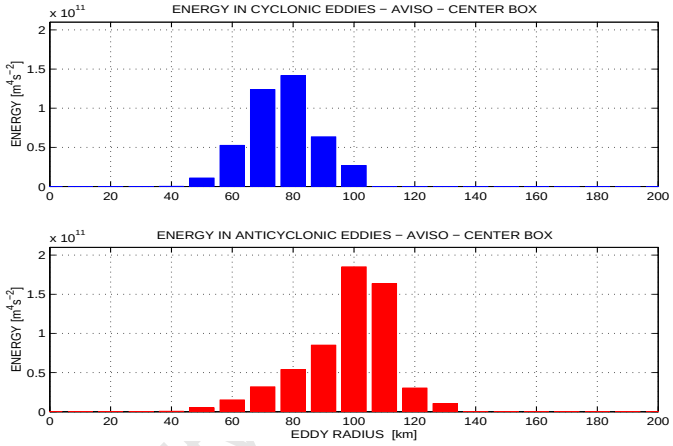

(b) Central Channel

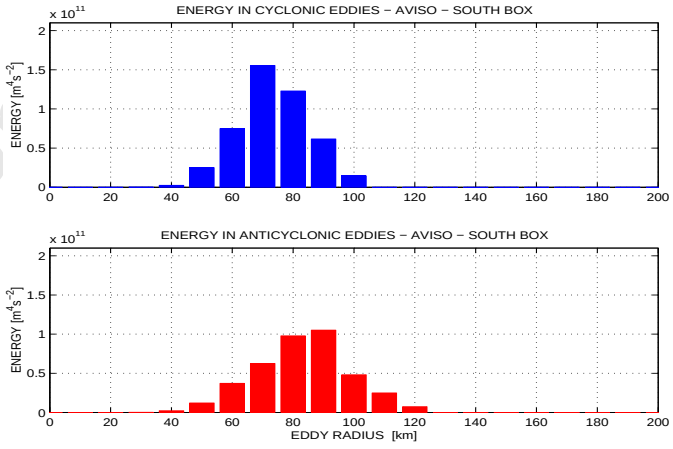

(c) Southern Channel

Figure 6.9. Histogram of energy distribution of the eddies from altimetry, at different length scales, in different subregions of the Mozambique Channel. In all panels, blue is for cyclones and red is for anticyclones.

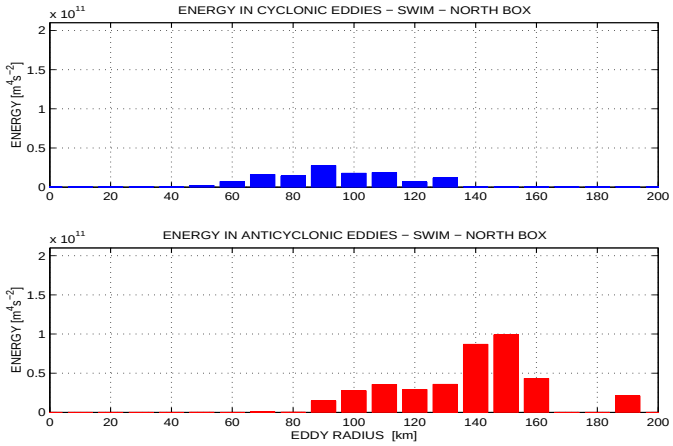

(a) Northern Channel

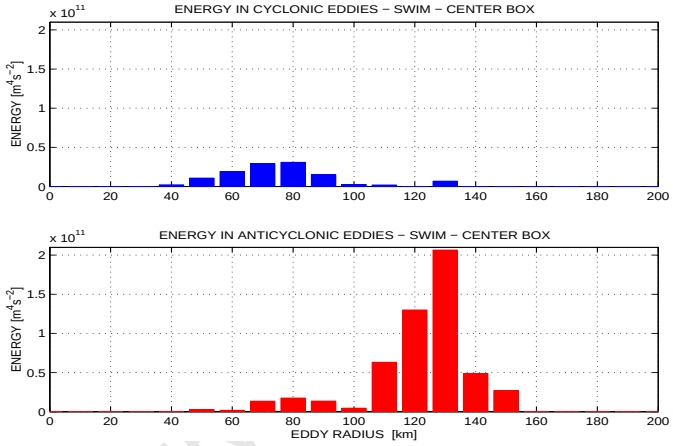

(b) Central Channel

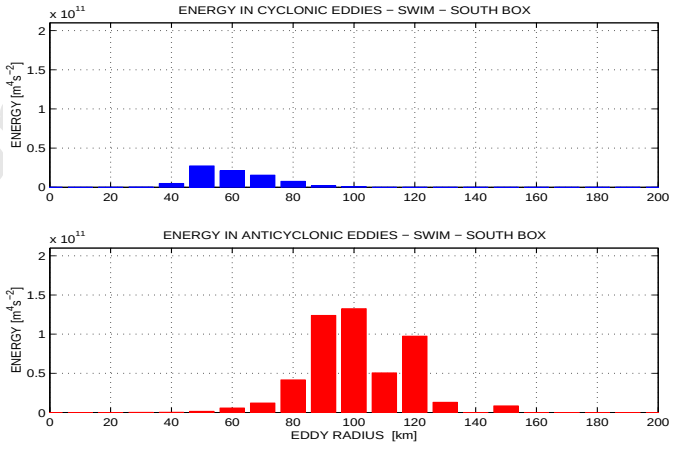

(c) Southern Channel

Figure 6.10. Histogram of energy distribution for the eddies in SWIM, at different length scales, in different subregions of the Mozambique Channel. In all panels, blue is for cyclones and red is for anticyclones.

6.3 A long-lived anticyclonic eddy

A single eddy event, long-lived, model derived anticyclone, strong enough to pass through the whole length of the Mozambique Channel has been selected and traced, for analysis of its physical characteristics, and property changes during its meridional southward propagation throughout the water column. Figure 6.11, shows the evolution of such an eddy at different positions within the channel, chosen for its investigation.

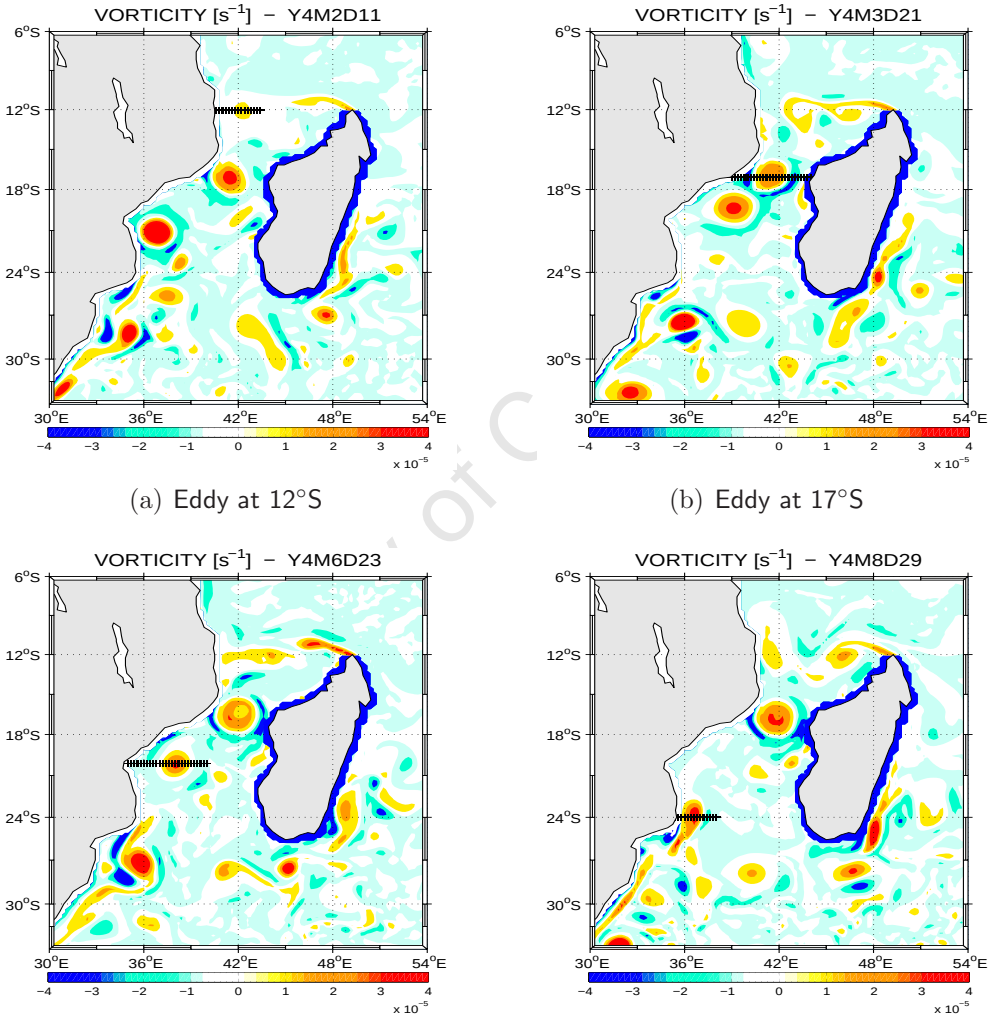

(a) Eddy at 12°S (b) Eddy at 17°S

(c) Eddy at 20°S (d) Eddy at 24°S

Figure 6.11. Eddy time evolution represented by surface expression of the vorticity field. The transects across show the positions used to investigate the eddy properties, during its southward propagation. Upper panels: left (eddy at 12°S, 40.5°E - 43.3°E), right (eddy at 17°S, 39°E - 44°E). Lower panels: left (eddy at 20°S, 35°E - 42°E), right (eddy at 24°S, 35.5°E - 38.5°E).

6.3.1 Eddy vertical flow structure

The eddy vertical structure is investigated at 4 different zonal transects across the Mozambican coast: in the north, the transect has been made at 12°S, 40.5°E and 43.3°E; in the center, the transect is across the narrows of the channel, at 17°S, 39°E and 44°E, and on the Sofala Bank, at 20°S, 35°E and 42°E. In the south, the transect has been made at 24°S, 35.5°E and 38.5°E (see Figure 6.11). Our choice of the latitude positions is made to allow comparisons between the model with the published information about the eddy characteristics, and water properties, based on in-situ observations (DiMarco et al., 2002, De Ruijter et al., 2002, 2006, Donohue and Toole, 2003, Swart et al., 2010). The longitude range of the transects is dependent of the eddy size. The selected eddy has been identified around the northwest coast of Madagascar, and appears to be generated by instabilities on the free-jet of the SEC after it has passed the Cape-Amber. The eddy passed through the transect at 12°S, on day 11, month 2 of the model year 4 (Figure 6.11a). At this time, the eddy seemed to lie on the offshore edge of the narrow, poleward, boundary flow along the northern Mozambican coast. The eddy zonal extension ranges between 41.5°E and 43.5 5°E, with its center near 42.5°E (Figure 6.12a). The eddy shows a relatively weak signal throughout the water column: its equatorward component has shown a maximum meridional velocity at surface of about 0.2 m s^{-1}, while its counter-part (poleward component) was relatively more intense, slightly over 0.4 m s^{-1}, however, it appeared strongly influenced by the northern Mozambican boundary flow. The eddy was deep reaching, extended to the bottom of the channel, of about 3000 m depth, with poleward velocities of about 0.1 m s^{-1}, while the equatorward velocities with about 0.1 m s^{-1}, was observed around 2000 m deep. About 40 days after, the eddy had reached the narrows of the channel at 17°S, on the day 21, month 3 (Figure 6.11b). The size of the eddy has ranged between longitudes 39.5°E to 43°E, and its core was centered near 41.5°E (Figure 6.12b). It appeared also strongly surface intensified, with maximum poleward velocities over 1.5 m s^{-1}, and its equatorward velocities was about 1.2 m s^{-1}. The eddy appeared to have conserved its barotropic signal, extended throughout the water column, with velocities up to 0.1 m s^{-1} near 1500 m depth. At this time, the equatorward Mozambique Undercurrent has been captured (De Ruijter et al., 2002), and was lying over the Mozambican continental slope (Figure 6.12b). This corroborates our previous analysis, about the capabilities of the eddies in SWIM in capturing the Mozambique Undercurrent (see chapter 4, section: "Eddy vertical structure at 17°S"). The Undercurrent has shown 2 cores: the upper core was around 500 m - 1500 m depth, and has shown velocities of about 0.1 m

s^{-1}, while the lower core was below 2000 m depth, and has shown velocities below 0.1 m s^{-1}. The eddy has spent a considerable time in the central part of the channel, and crossed the transect at 20°S, on the day 23, of the month 6 (after 3 months, Figure 6.11c). At 20°S, the eddy's center has been observed around 38°E (Figure 6.12c). The maximum poleward and equatorward velocities are about 1.1 m s^{-1} and 1 m s^{-1}, respectively. The eddy still reached the bottom of the channel $\sim$ 2500 m, with velocities up to 0.1 m s^{-1}, observed near 2000 m. Two-months later, on the day 29, of the month 8, the eddy has drifted farther south, and crossed the transect at 24°S (Figure 6.11d). Here the eddy size has ranged between 35.5°E and 38.5°E, and its center was around 36.5°E. The eddy also appeared strongly surface intensified, and has shown the strongest poleward and equatorward velocities, around 1.7 m s^{-1} and 1 m s^{-1}, respectively (Figure 6.12d). The poleward component was considerably shallower ($\sim$ 1000 m), while the equatorward component has reached the bottom of the ocean ($\sim$ 2500 m), lying over the Mozambican continental slope. During its southward propagation, this long-lived anticyclonic eddy has shown its core across the transects, centered at the following zonal positions: 42.5°E, 41.5°E, 38°E, and 36.5°E, indicating a westward deflection of the eddy. This is consistent with the south-westward propagation of the large anticyclonic Mozambique Channel eddies, as described in the literature (De Ruijter et al., 2002, Ridderinkhof and De Ruijter, 2003). Also this is consistent with our Figure 6.5c, which shows the main route of the anticyclonic eddies, adjacent to the Mozambican coast. At 24°S, the vertical structure of the eddy has shown considerable change, when compared against its structure at previous positions. Such a change is likely related to the strong interaction of the eddy with the continental shelf-break, as suggests Figure 6.12d. Eddy-shelf interaction is a complex dynamical process: it can generate and/or dissipate an eddy (Sutyrin and Grimshaw, 2010) (details about the eddy production and dissipation along the Mozambican coast is discussed in chapter 7). At 24°S the equatorward Mozambican Undercurrent has been also observed, between 1500 m and 2500 m depth, with relatively stronger velocity of about 0.2 m s^{-1}. These characteristics are consistent with the description of this current presented by De Ruijter et al. (2002).

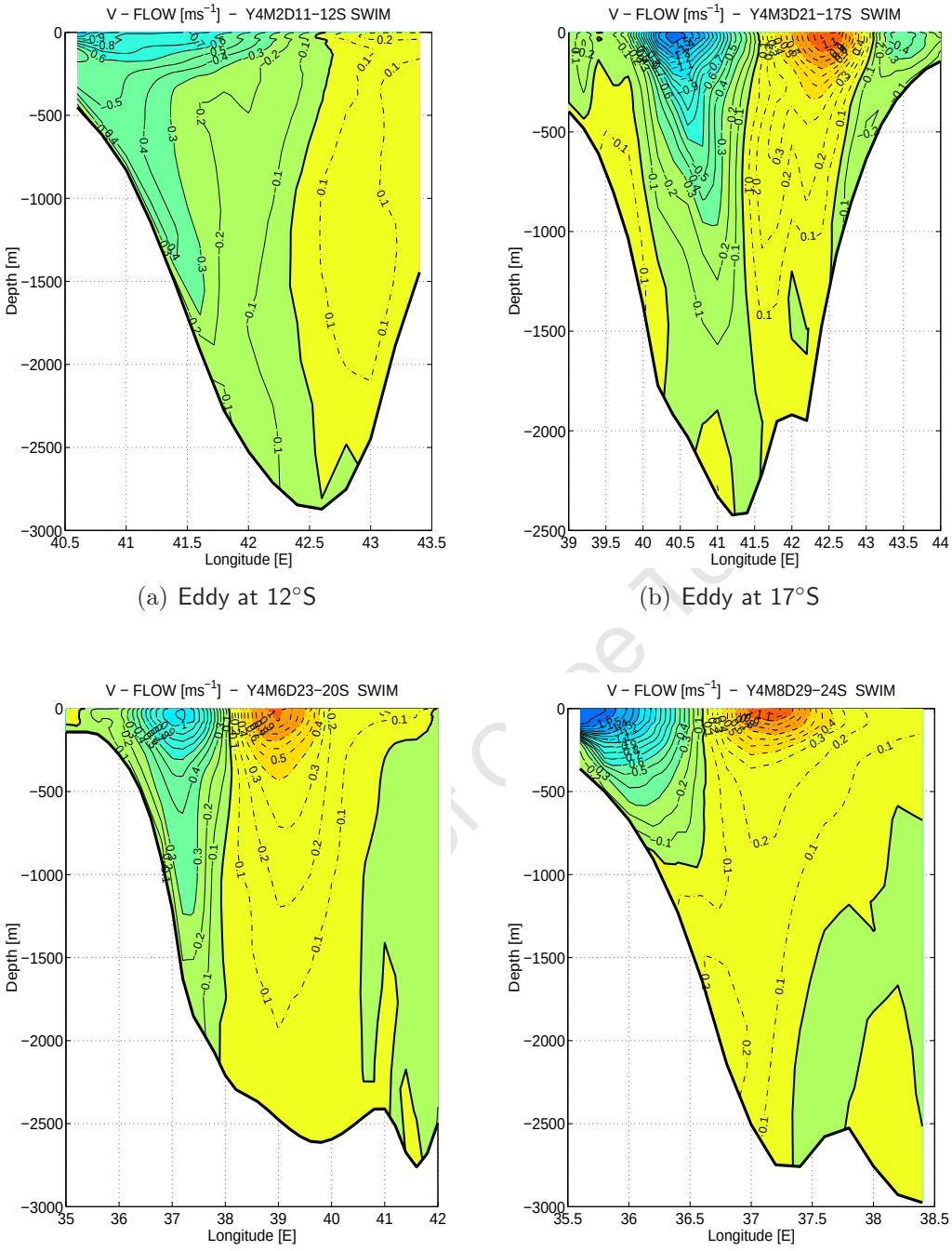

(a) Eddy at 12°S

(b) Eddy at 17°S

(c) Eddy at 20°S

(d) Eddy at 24°S

Figure 6.12. Vertical structure of a long-lived anticyclonic eddy from SWIM, at different locations within the channel, during its southward propagation. Upper panels: left (eddy at 12°S, 40.5°E - 43.3°E), right (eddy at 17°S, 39°E - 44°E). Lower panels: left (eddy at 20°S, 35°E - 42°E), right (eddy at 24°S, 35.5°E - 38.5°E). Negative or continuous line (poleward flow), and positive or dashed-line (equatorward flow). The tick contour indicates the zero isoline. To be compared with Figure 6.11.

6.3.2 Eddy water properties

6.3.2.1 Eddy vertical temperature and salinity

An analysis of water properties in the core of the anticyclonic eddy in study (a long-lived eddy able to cross the whole length of the channel) is now made. The left panels in Figure 6.13 and Figure 6.16, show the vertical distributions of temperature and salinity, throughout the ocean column. The right panels show a zoom on the upper 500 m depth, to facilitate the analysis where the stronger gradients are.

The eddy temperature distribution in the northernmost section at 12°S (Figure 6.13a) shows closely spaced isotherms, with temperatures over 10°C characterizing the upper 500 m of the eddy's water column. At intermediate depths (between 1000 m and 2000 m), the temperature distribution within the eddy ranges between 7°C and 3°C, respectively, while at greater depths (below 2500 m), the eddy temperature has been below 2°C. A closer inspection on the upper 500 m of the eddy (Figure 6.13b), reveals warmer waters with temperature over 29°C, on the upper 50 m of the water column. The mid-thermocline isotherms (taken to be the isotherms of 17°C in tropical oceans), range between $\sim$ 120 m and 170 m depth, for the western and eastern sectors of the transect respectively. In fact, the general temperature distribution within the eddy in the upper 500 m shows the isotherms slopping downward to the east, while below 1500 m depth, it shows isotherms slopping downward to the west.

The salinity distribution within the eddy (Figure 6.13c), shows a more complicated pattern: from the eddy's surface down to about 200 m, salinity increases, ranging from 35.0 to about 35.25, likely Tropical Surface Waters (Swallow et al., 1988). As as been described, TSW enters in the Mozambique Channel through SEC. This may support that the eddy was formed by instabilities of the SEC. In the upper 50 m the presence of relatively fresher water (with salinity slightly below 35.0, AAMW) is confined between 41.58°E and 42.58°E. On the other hand, to the west of 41.58°E, relatively saltier water dominated at the sea-shore. The isohalines throughout the upper 50 m have appeared vertically oriented (indicative of surface mixing). A relatively stronger salinity gradient has been observed near 50 m, and is characterized by horizontal distribution of the isohalines, ranging between 35.05 and 35.15. The core of maximum salinity $\sim$ 35.25 was centered around 140 m to 240 m depth, and between 41.3°E and 42.6°E. Below 200 m depth, down to the ocean bottom, the salinity within the eddy shows a decreasing tendency, with cores of minimum salinity around 34.75, centered at intermediate depths of about 1000 m, at

42°E, likely the RSW, as has been shown in many studies (Gründlingh, 1985, Beal et al., 2006, Roman and Lutjeharms, 2009). The second core of minimum salinity is located to the east, and is lined up nearly at the same intermediate depth, but different from the first core, it is deep reaching, extended to the ocean bottom. The horizontal structure of salinity between $\sim$ 100 m and 800 m depth, also have shown a slopping isohalines, downward towards the eastern sector of the transect.

Nevertheless, both temperature and salinity patterns in Figure 6.13b, and Figure 6.13d, suggest that the eddy signature is rather weak. This is consistent with our previous Figure 6.12a. It is likely that the eddy is at its earliest stage.

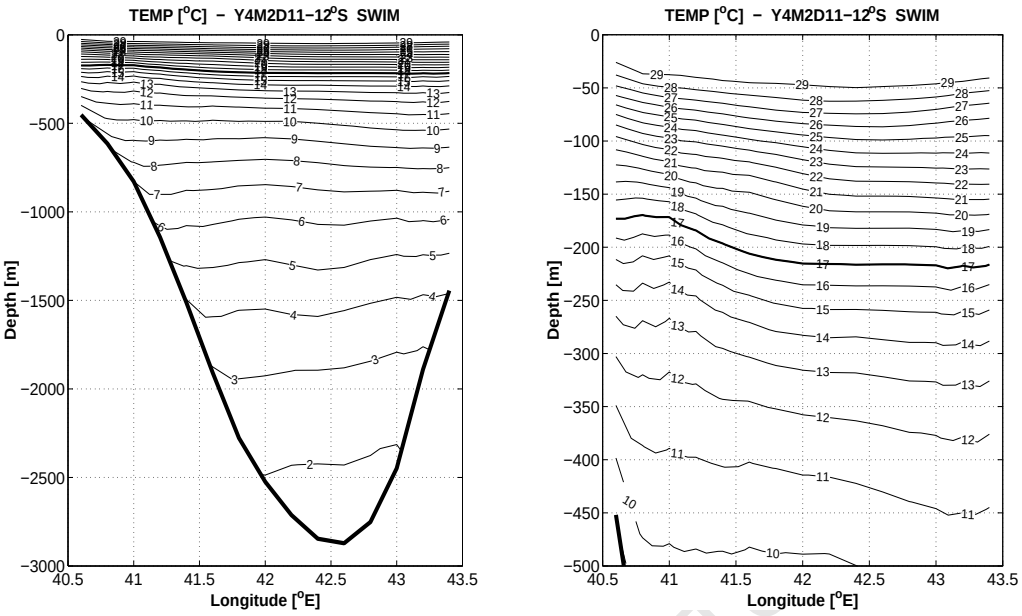

(a) Eddy Temperature at 12°S.

(b) Eddy Temperature above 500 m at 12°S.

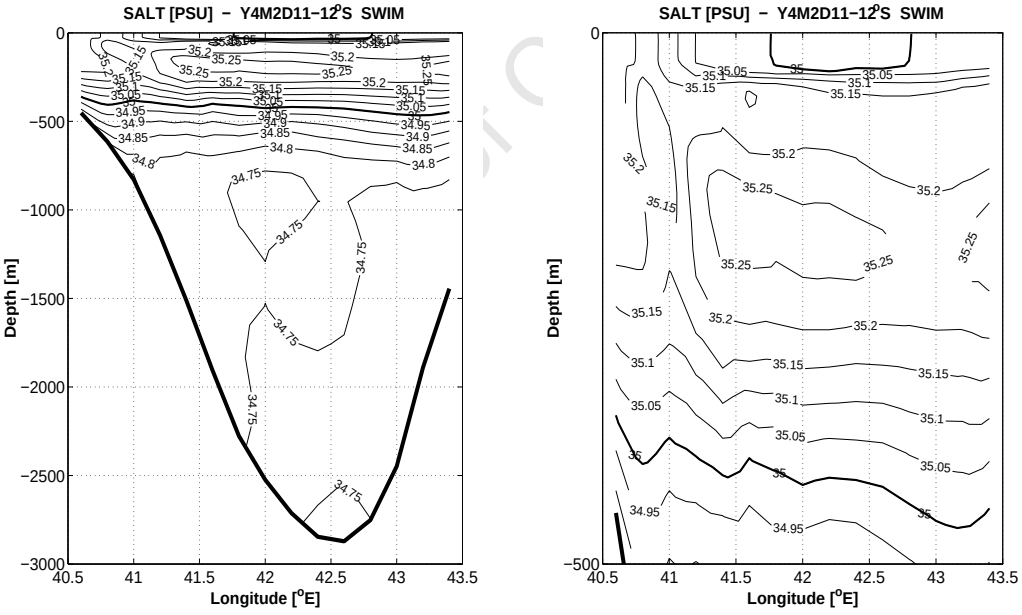

(c) Eddy Salinity at 12°S.

(d) Eddy Salinity above 500 m at 12°S.

Figure 6.13. Vertical temperature and salinity structure across a long-lived anticyclonic eddy at the northern transect, located at 12°S, 40.5°E - 43.3°E. Upper panels: left is temperature through the whole ocean column, and right is above 500 m depth. Lower panels: left is salinity through the whole ocean column, and right is above 500 m depth. The tick contour indicates the temperature of 17°C, and salinity of 35.0 isoline.

The transect in the narrows of the channel at 17°S (Figure 6.14), shows a stronger deepening of the near surface isotherms and isohalines within the core of the eddy (a typical signature of an anticyclonic eddy), centered at 41.5°E. For the case of temperature (Figure 6.14), inspections on the eddy's upper layer shows a tongue of warmer surface water with temperature over 30°C lowered about 50 m depth, located between 41°E and 41.5°E (Figure 6.14b). The mid-thermocline isotherm (17°C) ranges between 100 m and 250 m depth. At intermediate depths, temperature ranges between 3°C and 6°C, while at greater depths (below 2000 m), the temperature is near 2°C (Figure 6.14a). The temperature structure below 2000 m, suggests that the eddy has reached the bottom of the channel.

The corresponding salinity distribution (Figure 6.14c) within the eddy also shows similar characteristics to that observed in the previous transect: vertically oriented isohalines in the upper 50 m, with a tongue of relatively fresher water (salinity slightly below 35.0, likely AAMW) centered between 40.8°E and 42°E. Also a relatively stronger eddy salinity gradient, identified by their closely spaced and horizontally stretched isohalines is located near 50 m. The isohalines also are characterized by a downward increase of salinity, within the eddy's core between 50 m and 250 m depth, with a core of maximum salinity (about 35.25), located at 200 m depth, between 41°E and 41.5°E. Below 250 m depth down to near 1000 m depth, salinity shows a consistent decrease from 35.25 to 34.75. Between 1000 m and 1500 m, the water mass within the eddy is characterized by a core of salinity about 34.7, likely AAIW, located at the western sector of the transect, lying over the Mozambican continental slope. Whereas below 2000 m depth down to the ocean bottom, the water mass within the eddy is relatively saltier, about 34.75 PSU.

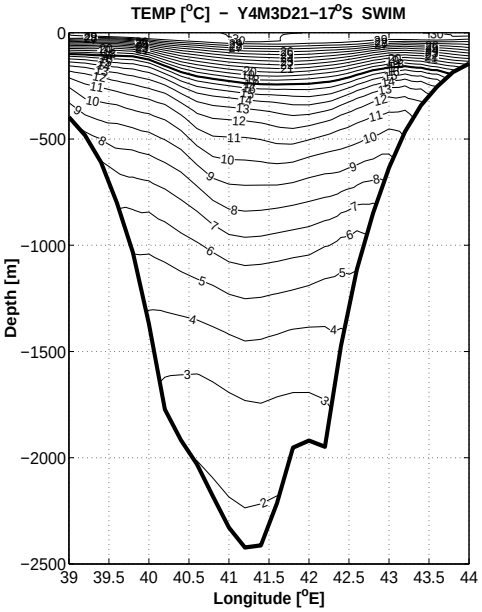

(a) Eddy Temperature at 17°S.

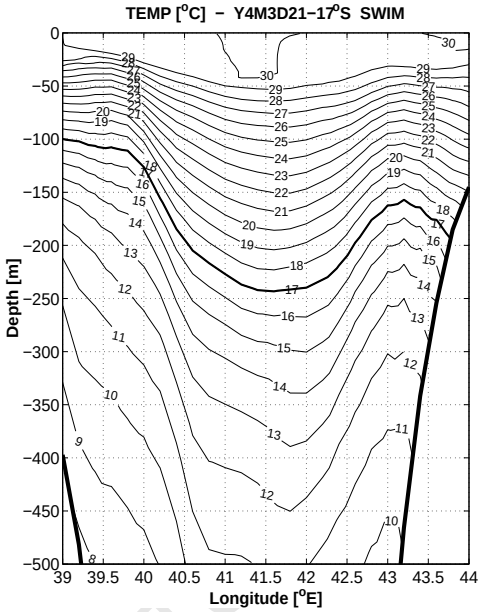

(b) Eddy Temperature above 500 m at 17°S.

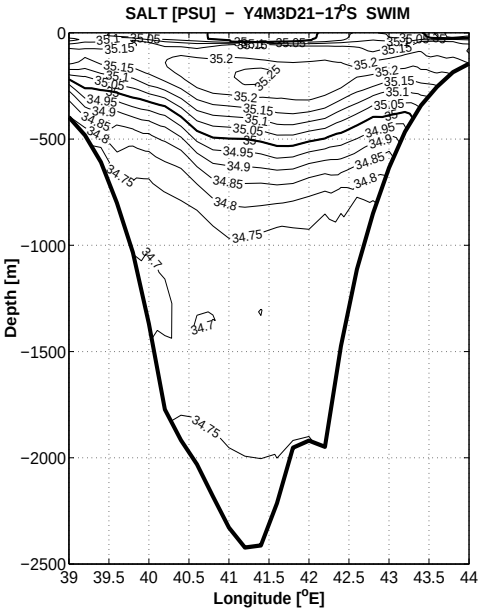

(c) Eddy Salinity at 17°S.

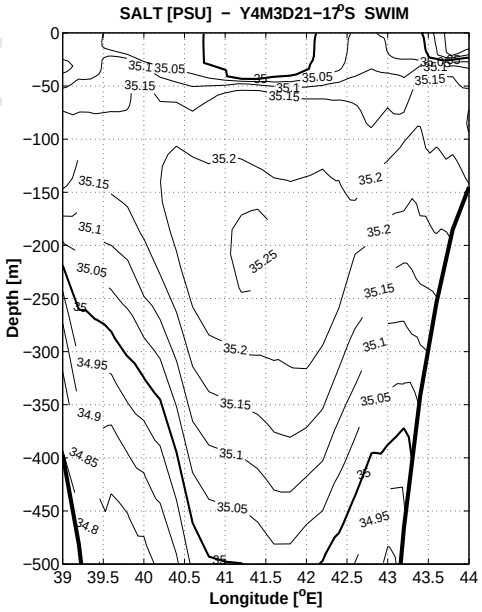

(d) Eddy Salinity above 500 m at 17°S.

Figure 6.14. Vertical temperature and salinity structure across a long-lived anticyclonic eddy at the central transect, located at 17°S, 39°E - 44°E. Upper panels: left is temperature through the whole ocean column, and right is above 500 m depth. Lower panels: left is salinity through the whole ocean column, and right is above 500 m depth. The tick contour indicates the temperature of 17°C, and salinity of 35.0 isoline.

The transect on Sofala Bank at 20°S is shown in Figure 6.15. Similar to the previous cases, the upper ocean column within the eddy also presents vertically oriented isotherms (Figure 6.15a), suggesting a well mixed layer, with a core of maximum temperature near 27°C located between 37.5°E and 38.5°E, reaching about 80 m depth, while to the west of the eddy section (towards African continent), the temperature have decreased in 1°C. The mid-thermocline isotherms (17°C) within the eddy, ranges between 140 m and 280 m depth, centered at 38°E. Below the thermocline, down to about 500 m depth, the temperature within the eddy decreased to about 11°C. At intermediate depths, between 1000 m and 1700 m depth, the temperature varies gradually between 7°C and 3°C, while towards the deep layers, below 2300 m, the water column within the eddy is characterized by temperatures below 2°C.

The corresponding salinity distribution (Figure 6.15c) within the eddy also shows a well mixed layer on upper 100 m of the water column, characterized with a minimum salinity of about 35.1, on upper 50 m depth, located at the western sector of the transect. Also similar to the previous transect, a core of maximum salinity of about 35.25 is trapped within the eddy at 250 m depth, centered at 38°E. A gradual decrease of the eddy's salinity to a minimum of 34.7 (AAIW), is located at intermediate depths between 1200 m and 2000 m. At such depths, the isohalines show a significant upward deflection over the western sector of the transect, at Mozambican continental slope, suggesting the presence of an oceanic current (discussed later). Below 2000 m depth towards the ocean bottom, salinity shows an increasing tendency, reaching a maximum of about 34.8, likely (IDW).

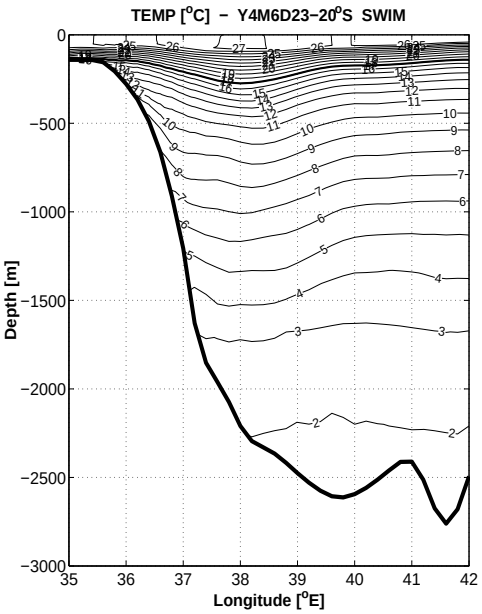

(a) Eddy Temperature at 20°S.

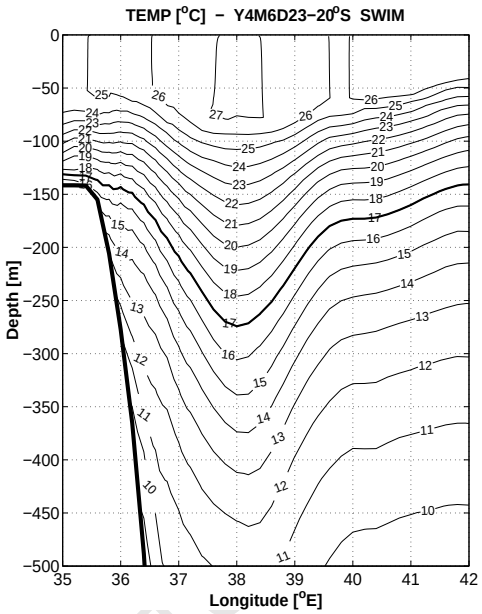

(b) Eddy Temperature above 500 m at 20°S.

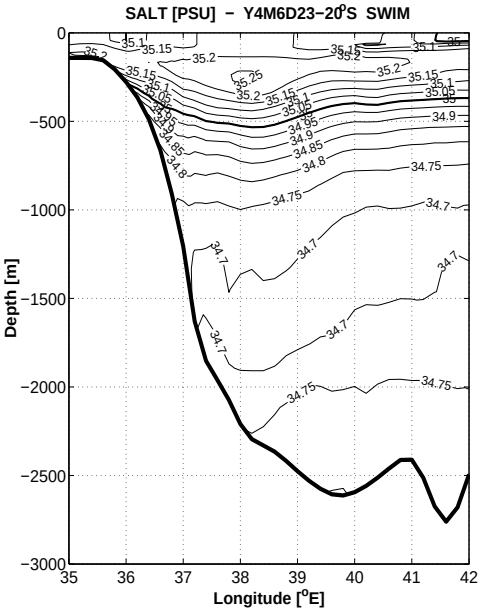

(c) Eddy Salinity at 20°S.

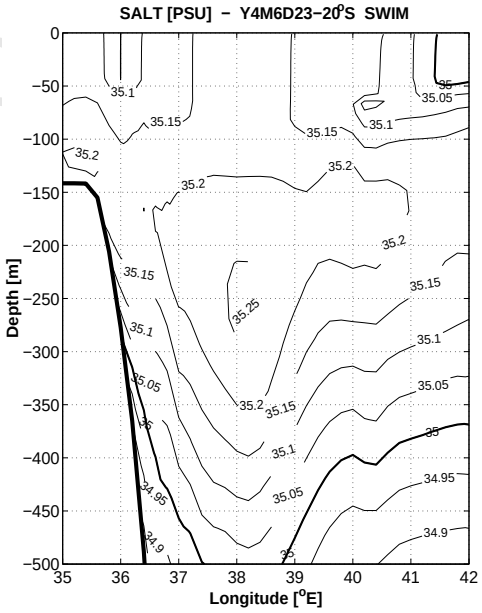

(d) Eddy Salinity above 500 m at 20°S.

Figure 6.15. Vertical temperature and salinity structure across a long-lived anticyclonic eddy at the central transect, located at 20°S, 35°E - 42°E. Upper panels: left is temperature through the whole ocean column, and right is above 500 m depth. Lower panels: left is salinity through the whole ocean column, and right is above 500 m depth. The tick contour indicates the temperature of 17°C, and salinity of 35.0 isoline.

To the south, the transect across the eddy at 24°S is shown in Figure 6.16. At this location the eddy occupies the westernmost position, with a core centered at 36.5°E. The upper 100 m within the eddy shows vertically oriented isotherms, suggesting a well mixed layer, characterized by temperatures slightly over 25°C. In the core of the eddy, the mid-thermocline isotherms (17°C) is depressed by 100 m, reaching a depth of about 220 m. Within the eddy, the temperature shows a gradual decrease with increasing depth, reaching 3°C, at about 1500 m (intermediate depth). Over 500 m tick layer, between 1500 m and 2000 m depth, the temperature shows smaller variation, only of 1°C. Below 2000 m depth within the eddy, the water column is characterized with temperature below 2°C.

The corresponding salinity structure (Figure 6.16c) within the eddy shows nearly vertically oriented isohalines on upper 300 m of the water column, confined to the west of 37°E. Notice that no relatively fresher water dominates the upper ocean column at this transect. The core of maximum salinity within the eddy is about 35.35, ranging between 150 m and 250 m, located to the east of 37°E. Below 250 m to about 1200 m depth, through the eddy, the salinity decreases gradually, getting fresher as to 34.55 at intermediate layers, about 1200 m depth, between 37°E and 38.5°E (AAIW). Below 1200 m, the eddy's salinity shows a gradual increase with increasing depth, reaching a maximum salinity of about 34.75 at 2000 m depth. Note also the presence of a relatively lower salinity core of about 34.6 at 1000 m depth, lying on the western flank of the section, over Mozambican continental slope. The core is located at same depth where the temperature ranges between 7°C and 4°C (typical characteristics of intermediate waters).

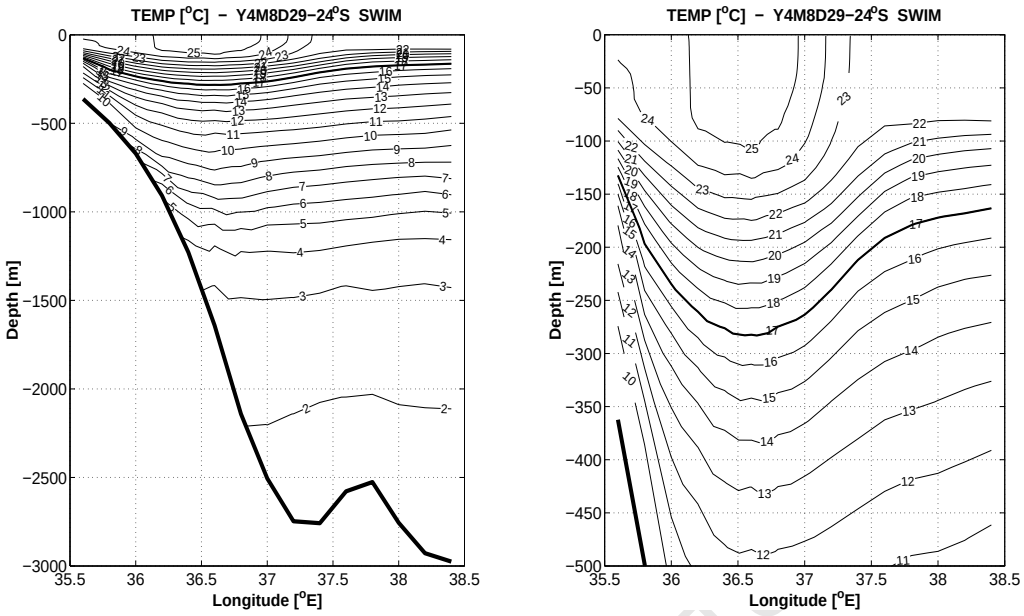

(a) Eddy Temperature at 24°S. (b) Eddy Temperature above 500 m at 24°S.

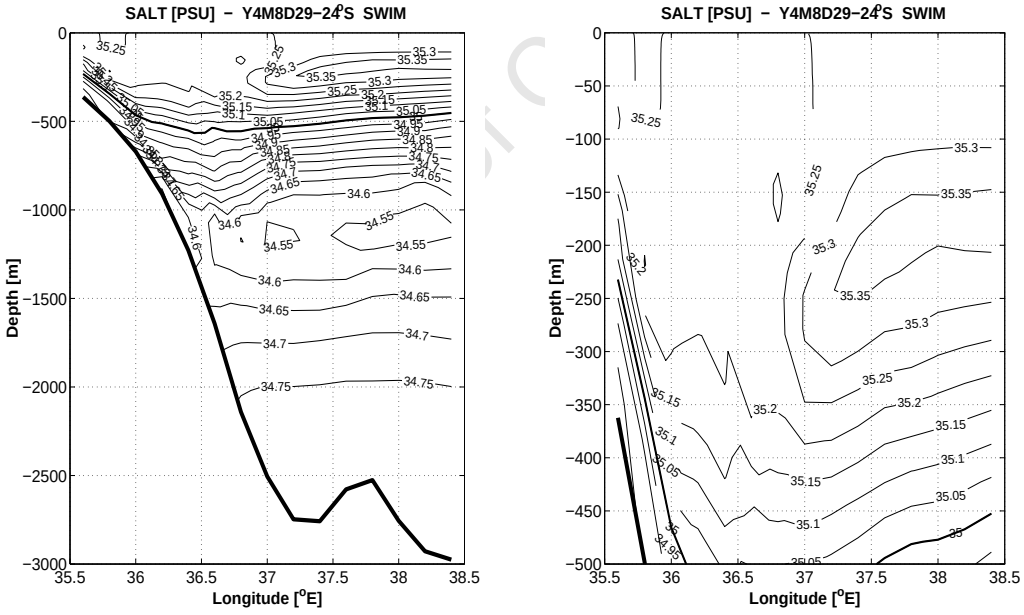

(c) Eddy Salinity at 24°S. (d) Eddy Salinity above 500 m at 24°S.

Figure 6.16. Vertical temperature and salinity structure across a long-lived anticyclonic eddy at the central transect, located at 24°S, 35.5°E - 38.5°E. Upper panels: left is temperature through the whole ocean column, and right is above 500 m depth. Lower panels: left is salinity through the whole ocean column, and right is above 500 m depth. The tick contour indicates the temperature of 17°C, and salinity of 35.0 isoline.

6.3.2.2 Water masses

Salinity as a function of temperature (T-S diagram), based on the water properties obtained across the eddy transects in study is presented in (Figure 6.17). We use the T-S relationship to delineate and infer water types, water masses, and their spatial distribution, and also to infer mixing among the water masses within the long-lasting anticyclonic eddy in study. The profiles shown in Figure 6.17 allows us to isolate different water masses trapped within the eddy: A water type with temperature above 15°C, salinity range between 35 and 35.3, and density anomaly between 23 kg m^3 - 26 kg m^3. These characteristics suggest the presence of Indian Ocean Equatorial water masses (IEW). Another water mass also identified has the following properties: temperature range between 10°C and 15°C, salinity between 34.8 and 35.2, and a density anomaly between 26 kg m^3 - 27 kg m^3. These characteristics suggest the presence of the South Indian Ocean Central water masses (SICW). A minimum salinity water mass of about 34.6, temperature of about 5°C, and a density anomaly between 27 kg m^3 - 28 kg m^3, characterizes the Antartic Intermediate Water mass (AAIW). Also at intermediate deph is evident properties of the RSW. At the bottom tip of the profil (Figure 6.17), a minimum temperature water mass of about 2°C, and salinity of about 34.8, characterizes the Indian Ocean Deep Water (IDW).

The IEW profil outcrops about 4 isopycnals: 23 kg m^3 - 26 kg m^3, nearly in a vertical orientation. This may suggest occurrence of a strong diapycnal mixing. On the other hand, the SICW is slightly slanted along a density anomaly layer of 27 kg m^3, which may suggest a mixing along the isopycnal.

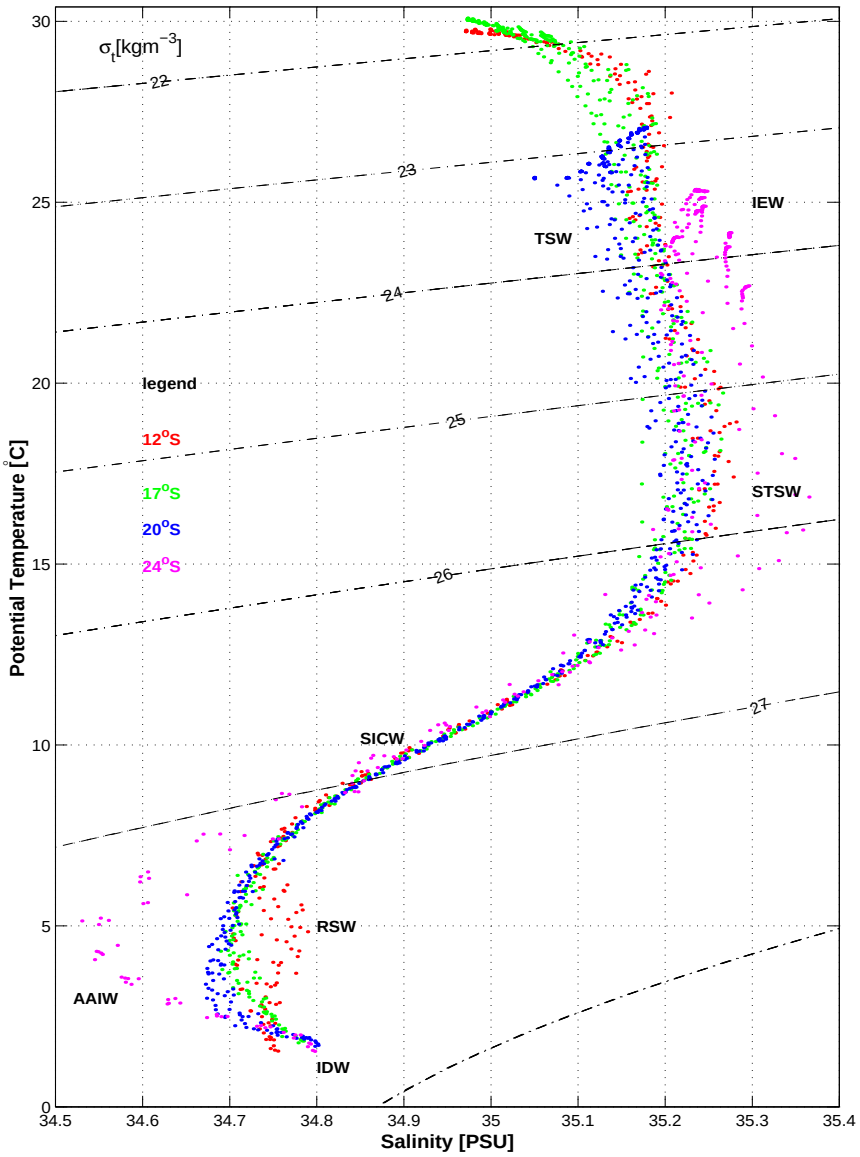

Figure 6.17. The diagram represents the relationship between potential temperature and salinity obtained at different latitudes in the Mozambique Channel, across a long-lived anticyclonic eddy, during the southward course of propagation. The relationship identifies different water masses: Antartic Intermediate Water (AAIW), Indian Deep Water (IDW), Indian Equatorial Water (IEW), Tropical Surface Water (TSW), Subtropical Surface Water (STSW), South Indian Central Water (SICW). The colours indicate the transect positions: see the inserted legend for reference.

6.4 Discussion

6.4.1 Eddy generation site, trajectory, census and polarity, lifetime, amplitude, diameter, frequency, surface integrated kinetic energy, velocity structure and water masses

- Eddy generation site

In Figure 6.3 and Figure 6.4, showing eddy tracks from altimetry and from SWIM respectively, the beginning of the eddy trajectories is defined by the bold black rings, indicating the generation site. Denser concentrations of these bold black rings in a specific region, may suggest a preference of eddies being generated at such a site.

In the northern Mozambique Channel (10°S and 15.5°S, 39°E and 48.5°E), we have identified a localized site at the northwest of Cape-Amber (around 12°S, 46.5°E - 48°E), favoring anticyclonic eddy formation. Both model and observation, show such an eddy generation site (Figure 6.3a and Figure 6.4a), and our analysis suggests this to be a primary site of an anticyclonic eddy formation. The Cape-Amber, the northernmost tip of Madagascar, is regarded a region of shear flow production, in the South Equatorial Current (SEC) (Quadfazel and Swallow, 1986, Schott et al., 1988). (one may find also informative to see vortex formation as suggested by Soares (1975), his Figure 42). Biastoch and Krauss (1999), using a numerical ocean circulation model, with z-coordinate in the vertical, nested at $\frac{1}{3^\circ}\times\frac{1}{3^\circ}$ horizontal grid resolution in the greater Agulhas system, have suggested that the shear production at the Cape-Amber is due to barotropic instability of the SEC. Penven et al. (2006c), using a different ocean model, with a generalized σ-coordinate in the vertical, and at a relatively higher spatial grid resolution, $\frac{1}{4^\circ}$ in longitude, also covering the greater Agulhas system, have demonstrated that the geographical location of the Madagascar land mass, relative to the path of the SEC, plays a decisive role on the generation of the flow instabilities, hence favoring anticyclonic eddy formation that propagate southward, throughout the Mozambique Channel (Penven et al., 2006c). The northern region of the Mozambique Channel has been characterized as a region of an irregular formation of mesoscale variability (Schouten et al., 2003). Inspection in Figure 6.3a and Figure 6.4a, show that the site favoring the eddy formation does not occurs exactly at Cape-Amber, where the friction of the SEC and the northern tip of the Island takes place, rather, the eddies are formed slightly to the west of the Cape, between

46.5°E and 48°E. The eddies appear to be formed after the SEC has passed the Cape-Amber, flowing westwards as a meandering jet, after losing the topographic/coastline control (see Figure 6.1). The region around 12°S, 46.5°E to 48°E, is characterized by a shallow topography, involving several oceanic banks and Islands (Figure 2.1), such as, the Leven Bank (near 12°S, 48°E), the Gayser Bank (11.75°S, 46.5°E), and the Gloriouses Island (11.75°S, 47°E) (for reference see Figure 2.1). These elements seems to provide the region favourable conditions for eddy formation.

Between Geyser Bank and the African continent, nearly at the same latitude (12°S), lies the Comores Arquipelago $\sim$ 270 km long, set of 4 islands: Mayotte (12.5°S, 45°E), Anjouan (12.2°S, 44.5°E), Moheli (13.7°S, 43.5°E), and the Grande Comores (11.75°E, 43.38°E). The tracks suggest that some of the eddies there may be also generated when the flow field squeezes through the gaps between the islands.

A relatively few number of the cyclonic eddies are seen also to be generated in the northern Mozambique Channel (Figure 6.3b and Figure 6.4b). Both model and altimetry, suggest that their preferential site of formation is at the eastern and western boundaries of the Comores Basin, along the isobath of 3000 m. In SWIM they are mostly at the western boundary.

In the central subregion of the Mozambique Channel (15.6°S - 24°S, 34°E - 47°E), another site favoring anticyclonic eddy generation is located at the northern entrance of the narrows of the channel, near 16°S (Figure 6.3c, and Figure 6.4c). This site of anticyclonic eddy generation is corroborated by in-situ observations (Ridderinkhof and De Ruijter, 2003), as well as altimetric remote sensed observations (Schouten et al., 2003). (one may find also informative to see the pattern of the surface currents derived from ship observations presented by Soares (1975), his Figure 42, for February-March, 1974). Anticyclonic eddies at the northern entrance of the narrow channel are known to be formed by conservation of potential vorticity of the flow field, involving the beta-effect (Ridderinkhof and De Ruijter, 2003). These eddies cross the narrows to the center of the channel, and propagate along the western boundary, adjacent to the Mozambican coastline (De Ruijter et al., 2002). This pattern is quite well illustrated by both SWIM and altimetry. Our results in the center of the channel also suggest a secondary anticyclonic eddy generation site at the eastern boundary of the channel, near the Madagascar coastline, at 20°S, 43°E. Little is known about this secondary anticyclonic eddy generation site. However, a portrayal of an anticyclonic recirculation of the flow at this site has been presented by Soares (1975) (again, one may find informative to see his Figures. 43, 44, for the Austral

summer season). Inspection in Figure 6.3d and Figure 6.4d, also suggest another 2 other sites favoring cyclonic eddy formation, along the eastern boundary of the channel (near Madagascar coast). For these 2 sites, the northernmost site is located around 19°S, 42°E, and the southernmost site is around 23°S, 42°E. The existence of these cyclonic eddy generation sites could possibly explain the origin of cyclonic eddies discussed previously (Gründlingh, 1995, Quartly and Srokosz, 2004, De Ruijter et al., 2004), but without a definite conclusion. Given the trajectory of the cyclonic eddies reported by Gründlingh (1995) (see his Figure 11), as propagating in the vicinities of the Mozambique Current, and also comparing with the trajectory of the cyclonic eddies originated at 19°S, 42°E (Figure 6.3d and Figure 6.4d), one may legitimately associate the origin of Gründlingh eddies with the formation site at 19°S, 42°E. This may contradict De Ruijter et al. (2002), who associated the origin of cyclonic eddies present in the channel, with the region to the south of Madagascar. Generation site of cyclonic eddies at 19°S, 42°E, also could explain the origin of cyclonic eddies reported by Quartly and Srokosz (2004), as possibly being pre-formed eddies drifting south or south-eastwards, coming from somewhere to the north of 22°S (see Top row of their Figure 6). The eddy generation site identified near 23°S, 42°E, is less controversial: Quartly and Srokosz (2004), have found a number of cyclonic features in this location, somewhat suggesting their local generation, as lee-eddies, at the so-called Madagascar Shelter.

In the southern subregion of the channel (24.1°S - 29.5°S, 32°E - 46°E), the site of cyclonic eddy generation at the eastern boundary of the channel, adjacent to the southern tip of Madagascar, also is corroborated by Quartly and Srokosz (2004) (see their Figure 6h). The presence of this site is also in agreement with other studies (Gründlingh, 1995, De Ruijter et al., 2004, Siedler et al., 2009), which suggest the formation of cyclonic eddies by friction at the inshore edge of the South-East Madagascar Current with the continental shelf at the southern tip of Madagascar (Cape Saint-Marie), a mirror of what happens at the Cape-Amber.

Inspection in Figure 6.3e,f and Figure 6.4e,f, also shows a number of cyclonic and anticyclonic eddies in the southern subregion of the channel. They appear to be formed outside of the channel (e.g. east of the Madagascar Ridge, and in the southern boundary, likely by the instabilities in the Agulhas Return Current (Figure 4.10)). These flow instabilities migrate into our region of study. Morrow et al. (2004), have shown that some anticyclonic eddies generated far east as to Australia, propagate westward, nearly at latitude 25°S, and eventually enter in the southern Mozambique Channel. Quartly

et al. (2006), also have shown similar results to those found by Morrow et al. (2004). Buck (2004) (not accessed material), has been quoted by Quartly et al. (2006) as using an automatic algorithm in the region south of Madagascar, and identified local generation of eddies in the region.

At the western boundary of the channel, cyclonic eddy generation site at the Delagoa Bight, (near 26°S, 34°E), is evident (Figure 6.3f and Figure 6.4f). This corroborates previous studies pointing this place as a suitable location for the formation of lee-eddies (Lutjeharms and da Silva, 1988, Quartly and Srokosz, 2004).

- Eddy trajectory

Both model and altimetric results show that anticyclonic eddies generated in the northern Mozambique Channel, near 12°S, 48°E (Figure 6.3a and Figure 6.4a), initially propagate westwards along the latitude 12°S. Their trajectory is similar to the path of the westward flowing SEC. On approaching the western boundary of the channel, the trajectory of the eddies is deflected southwards. Their southward deflection resembles that of the northern Mozambique Coastal Current, reported by De Ruijter et al. (2002). It is likely that interaction between eddy and mean-flow occurs there. Cyclonic eddies also originated in the northern subregion (Figure 6.3b and Figure 6.4b), at the southern entrance between the Geyser Bank and Leven Bank, exhibit mostly a south-westward propagation. In the central subregion of the channel (Figure 6.3c and Figure 6.4c), anticyclonic eddies generated at the northern entrance of the narrow channel ($\sim$ 16°S), propagate mostly southwards parallel to the western boundary (Schouten et al., 2003). It is important to mention that the trajectory of these eddies at this path is similar to the trajectory of the anticyclonic eddies tracked manually, derived both from observation and ocean models in previous works (Schouten et al., 2003, De Ruijter et al., 2005, van der Werf et al., 2010). Both cyclonic and anticyclonic eddies generated at the eastern boundary of the channel propagate mostly south-westwards. The same is true for the eddies generated in the southern subregion of the channel (De Ruijter et al., 2004, 2005).

The direction of propagation and trajectory of the eddies identified in our study is consistent with theories of non-linear turbulence (McWilliams and Flierl, 1979, Chelton et al., 2007), which infer that eddies should be propagating mainly westwards, with a slight meridional deviation (pole-ward or equator-ward associated with the direction of rotation). The overall trajectory of the eddies, throughout the full length of the Mozam-

bique Channel is summarized in Figure 6.5, which shows the frequency of occurrence of cyclonic and anticyclonic eddy center in $0.5^\circ \times 0.5^\circ$ grid size boxes.

- Eddy Census and Polarity

The statistical census of the eddies (Table 6.1) and analysis of their polarity (Figure 6.6) shows that for both altimetry and the model, the total numbers of eddies (cyclonic + anticyclonic), as well as the total numbers of each eddy types (total number of cyclonic eddies) and (total number of anticyclonic eddies) per subregion, show an increase from the northern subregion of the channel to the southern subregion. The northern subregion of the channel is a region where eddies are initially generated (Biastoch and Krauss, 1999). Once they have been generated, a fraction of them enter in the center of the channel (Ridderinkhof and De Ruijter, 2003, Schouten et al., 2003). In the center Mozambique Channel, some eddies are generated at the northern entrance of the narrow channel, near 16°S (Ridderinkhof and De Ruijter, 2003, Schouten et al., 2003). Some eddies also are generated along the eastern boundary of the channel, near Madagascar coast, thus increasing the abundance of eddies in the region. This is consistent with previous studies (Schouten et al., 2003, De Ruijter et al., 2004). A fraction of eddies originated both from the north and center of the channel pass through the southern subregion during their southward migration. In the south of the channel, some eddies also are locally generated and some have their origins outside of the channel Morrow et al. (2004), Quartly et al. (2006). The contributions of all these sources may account for a greater abundance of eddies in the southern Mozambique Channel. The results also show that, for both altimetry and model, the northern subregion of the channel is the only place where the total numbers of anticyclonic eddies is over the numbers of cyclonic eddies. Such an abundance of anticyclonic over cyclonic eddies, could be explained by the geographical settings of the Madagascar land mass (Penven et al., 2006c): The Cape-Amber at the southern edge of the South Equatorial Current, favors greatly an anticyclonic, rather than a cyclonic recirculation of vorticity (Biastoch and Krauss, 1999), leading to a dominance of an anticyclonic eddy formation. Notice that the opposite happens at Cape Saint-Marie, the southern tip of the Madagascar. Few cyclonic eddies generated to the north of 12°S, near the latitude 10°S, around the Gloriouses Islands, propagate mostly north-westward, and do not enter into the Mozambique Channel. Contrary to what is generally thought, part of the cyclonic and anticyclonic eddies are locally formed. This corroborates the hypothesis that sug-

gests that cyclonic eddies in the Mozambique Channel should be expected, but relatively weaker and less consistent when compared with the anticyclonic eddies (Harlander et al., 2009). Interestingly, we have found in the center and south of the channel, more cyclonic than anticyclonic eddies, but they appear to be relatively smaller. However, even within the same subregion, the analysis of eddy polarities (Figure 6.6), has shown that the dominance of one eddy type over the other depends on the eddy-length scale at which the eddies are compared.

- Eddy life-time

For both model and altimetry, our analysis shows that the anticyclonic eddies are longer-lived than the cyclonic eddies. This probably could be explained by looking at their energy content and their larger size. In general anticyclonic eddies are more energetic and larger than cyclonic eddies. This is not an exception in our case: higher energy peaks within the larger anticyclonic eddies seem to provide them longivity over the cyclonic eddies. An interesting example to mention is observed in the center of the channel: The region stands out as the place where cyclonic eddies have lived shorter, when compared to the other subregions. The center of the channel is also the place where the anticyclonic eddies have their highest energy peak. This may suggest that the overwhelming signature of the anticyclonic eddies may play a role on the dissipation of cyclonic eddies.

- Eddy diameter

Model and altimetry (Table 6.1) show that cyclonic and anticyclonic eddies decrease their size, during their north-south meridional variation. Studies have shown that there is a direct relationship between the eddy length-scale and the first baroclinic Rossby radius (Krauss et al., 1990). Relating the eddy length-scale (maximum and minimum) observed in our study (for altimetry: range between 110 km and 30 km in cyclones, and 130 km and 30 km in anticyclones; and for the model: it ranges between 130 km and 30 km in cyclones, and 190 km and 30 km in anticyclones), with the global map of distribution of the first baroclinic Rossby radius, presented by Chelton et al. (1998), (see their Figure 6: for the southwest Indian Ocean sector, from the northern to the southern tip of Madagascar, the first baroclinic Rossby radius range between 100 km and 40 km respectively). We find a good agreement between these length-scales, specially in connection with the cyclonic

eddies. It is tempting to conclude that the size of the cyclonic eddies in our region of study may be controlled by the first baroclinic Rossby radius (typical characteristics of mesoscale ocean turbulence Penven et al. (2005)). From north to south of the Mozambique Channel, the anticyclonic eddies have a larger diameter than the cyclonic eddies. Their size could be influenced by other factors such as the geometry of the channel. Nevertheless both cyclonic and anticyclonic eddies in altimetry and in the SWIM decrease their size when going south.

- Eddy frequency

Analysis of the eddy frequency distribution, with respect to their radius (Figure 6.7 and Figure 6.8), per subregions of the channel shows: while cyclonic eddies generally have a modal distribution (one dominant peak), the anticyclonic eddies on the other hand, have a bimodal distribution (2 dominant peaks: One within the range of the first baroclinic Rossby radius for the region, and the other, beyond the Rossby radius), more evident in SWIM (in all subregions) than in altimetry. In altimetry the second mesoscale mode is only clearly observed in the center of the channel. In the center of the channel, the frequency of the anticyclonic eddies per year observed in the second mode, for both altimetry and model are consistent with in-situ observations (De Ruijter et al., 2002, Ridderinkhof and De Ruijter, 2003, Schouten et al., 2003, Harlander et al., 2009), and also are in agreement with other modelling studies (van der Werf et al., 2010). In the south, the model shows a slight decay on the dominance of the second mesoscale mode. Decay of the density of the modes may be associated with the local dynamics of the background flow: migration of eddies from upstreams of the channel, and those from the east, in south of Madagascar (De Ruijter et al., 2004, Morrow et al., 2004, Quartly et al., 2006) makes the flow field in this area complex. The background flow of the region is described as being characterized by eddy-eddy interaction, which results in eddy merging or splitting of the structures, eddy dissipation, dipolar vortex formation (De Ruijter et al., 2004), rossby waves dynamics (Schouten et al., 2002b), etc...etc. These processes affect the characteristics of the flow field of the region.

- Eddy SSH amplitude

Different from the eddy diameters, the amplitude of the eddies appear to increase with their north-south meridional variation. In altimetry, it increases from 8 cm to 13 cm for cyclonic eddies, and from 10 cm to 14 cm for anticyclonic eddies. In the model, it only has increased for anticyclonic eddies, from 8 cm in the north to 34 cm in the south. There is no amplitude increase in the cyclonic eddies in the model. It is not obvious why such a property conservation is manifested. It is also not obvious in the model why significant amplitude variation of the anticyclonic eddies is observed at the transition between the center to the southern subregions, while in altimetry, great deal of change is observed at the transition between the northern to the center of the channel. Significant amplitude increase from the north to the center of the channel is to be expected: Studies have shown that the meridional (north - south) displacement of eddies, from the north of the channel (near 12°S) to the center of the channel (near 20°S), through a meridional planetary vorticity gradient, would increase the height anomaly of an eddy with a constant rotational velocity by 60% (Schouten et al., 2003).

The stronger SSH eddy amplitude observed in the model is consistent with the overestimation of RMS SSH observed in the region, as shown in Figure 4.15.

- Eddy surface integrated energy

For the eddy energy, the statistics show that for both model and altimetry (Table 6.1), the anticyclonic eddies are more energetic than cyclonic eddies. Also stands out that dominant peaks of energy are located at larger eddies. This is in agreement with theories of mesoscale turbulence (McWilliams and Flierl, 1979, Stammer, 1997). Also it is shown that the strongest energy of the anticyclonic eddies is located in the central part of the channel. This is consistent with the increase of RMS SSH, because the geostrophic velocities used in the calculation of the eddy kinetic energy are computed from variation of SSH. The bulk of eddy kinetic energy in the Mozambique Channel is mostly supplied by anticyclonic eddies. In altimetry the cyclonic eddies increase their energy from the north to south of the channel, while in the model their energy decreases. The southward decrease of the eddy energy in SWIM is consistent with the southward decrease of the eddy size, likely related with the first baroclinic Rossby radius of deformation.

- Eddy temperature and salinity

The description of temperature and salinity distributions throughout the eddy vertical structure made previously (Figure 6.13 to Figure 6.16), suggests that the investigated eddy, involved several water masses, from different origins. For instance, at the northernmost transect, 12°S, (Figure 6.13b), the relatively fresher and warmer, surface water (with salinity slightly below 35.0, and temperature over 29°C), identified in the upper 50 m (a well mixed layer) of the water column within the eddy, is similar to that observed in hydrographic data presented by Wyrtki (1971), for Austral summer conditions (January - February), and also presented by Tomczak and Godfrey (1994), representing the Tropical Surface Water mass (TSW). For this particular season, the water mass is characterized with the following property range: temperature between 28°C and 29°C, and salinity between 34.5 and 35.0 (DiMarco et al., 2002). Coincidently, our transect across the eddy at 12°S, is made in February. It is the same latitude position where hydrographic data collected by an Australian cruise in 1965, are presented by DiMarco et al. (2002). Interestingly, the fresher salinities (< 35.0), exactly at the same range depth $\sim$ upper 50 m, also found by the Australian cruise, was previously regarded as a puzzling feature (DiMarco et al., 2002). However, it is now known that the presence of this surface lower salinity water mass at this location is expected, because it is linked with the advection and diffusion in the South Equatorial Current (Wyrtki, 1971, Gordon et al., 1997, DiMarco et al., 2002). Rather than being regarded as an anomalous water mass, this surface lower salinity water (< 35.0), appears to characterize the system throughout the year (Wyrtki, 1971). The TSW is formed at the central equatorial region of the Indian Ocean (see Beal et al. (2006), their Figure 5), thus constitutes part of the Indian Equatorial Waters (IEW). Its relatively low salinity results from the excess of precipitation over evaporation in the tropics (Toole and Warren, 1993, Tomczak and Godfrey, 1994), specially in the Bay of Bengal. It also is due to the influence of the low salinity waters from Indonesian Through Flow (ITF) (Gordon et al., 1997, Donohue and Toole, 2003), also known as the Australasian Mediterranean Waters AAMW (Tomczak and Godfrey, 1994), which have fractions of the fresher Equatorial West Pacific waters. The presence of the fresher TSW water mass in the core of the eddy suggest that the eddy has a direct link with the SEC. This is further evidenced with the aid of Figure 6.11, showing the eddy time-evolution, and its connection with the instabilities of the SEC. Barotropic shear instability is induced by the friction of SEC with the Cape-Amber, the northern tip of Madagascar (Schott et al., 1988, Biastoch and Krauss, 1999).

Our analysis at 12°S, below the eddy's mixed layer depth, between ∼ 130 m and 220 m, also identifies a subsurface water mass, with a core of maximum salinity near 35.25, and temperature range between 17°C and 20°C, centered around 41.5°E to 42.5°E (Figure 6.13d). Its relatively higher salinity and its depth range is similar to that found by DiMarco et al. (2002), using the dataset collected by WOCE Hydrographic Program in January 1996, in a transect extended between the northern tip of Madagascar and Mombassa City, Kenya. Their study has identified this water parcel as the TSW (salinity range between 35.1 and 35.3), although located at 300 m depth. The presence of a water parcel with similar properties (temperature and relatively higher salinity range, as well as subsurface depth range) within the eddy, observed farther south, at different latitude positions across the eddy in study i.e., 17°S (Figure 6.14d), 20°S (Figure 6.15d), and 24°S (Figure 6.16d), suggests that the parcel owes its origin at subtropical regions. This is corroborated by observations (Donohue and Toole, 2003), which have revealed that equatorward of 28°S, the Subtropical Surface Water (STSW), subducts below the TSW, producing a subsurface salinity maximum near 200 m depth. STSW is known to be formed and subducted in the subtropics, at subtropical convergence (Toole and Warren, 1993, Tomczak and Godfrey, 1994), to the east of 90°E (Wyrtki, 1971), (see also Beal et al. (2006), their Figure 5), and between 25°S and 35°S, within the Subtropical gyre, by excessive evaporation over precipitation (Toole and Warren, 1993, Tomczak and Godfrey, 1994). This process makes the STSW a parcel of relatively higher salinity when compared to TSW. Considering its geographical source region (to the east of 90°E), it becomes evident that the presence of STSW within the eddy at our section locations (southwestern Indian Ocean), indicates that this water mass has been firstly advected equatorward by the anticyclonic circulation of the Subtropical gyre, and secondly transported westward to the South-West Indian Ocean by the South Equatorial Current, in agreement with Beal et al. (2006). In our analysis, the strongest salinity core of STSW within the eddy is located at the southernmost transect, 24°S. This could be explained by the proximity of the eddy transect to the subtropics, or stronger influence of the outflow from the southern extension of the East Madagascar Current, regarded as the main transporter of the STSW towards the Agulhas Current region (Donohue and Toole, 2003, Beal et al., 2006). The STSW is also regarded as part of the South Indian Central Waters (SICW). SICW has been characterized with the following property range for temperature and salinity between 8°C and 25°C, and 34.6 and 35.8 respectively (Emery, 2001). A cross-shore hydrographic section at 12°S, by De Ruijter et al. (2002) and Swart et al. (2010) also have suggested

the presence of SICW, with temperature above 10°C, salinity above 34.9, density anomaly below 26.8 kg.m^{-3}. It has been located in the upper 450 m.

For all our transects, the analysis at mid-depth ranges between 300 m and 900 m, reports a gradual decrease of salinity with depth, to a minimum of about 34.75. At this depth range, the SICW is influenced by parcels of tropical waters, such as AAMW/ITF (near 600 m depth (Tomczak and Godfrey, 1994)). As mentioned, this water mass brings relatively fresher waters into the South-West Indian Ocean. This could explain the gradual decrease of salinity formerly reported.

Below the eddy's mid-depth layer, at intermediate water depths, between 1000 m and 2500 m, for the eddy transect at 12°S (Figure 6.13c); between 1000 m and 1500 m depth, for the eddy transect at 17°S (Figure 6.14c); between 1300 m and 1800 m depth, for the eddy transect at 20°S (Figure 6.15c); and between 800 m and 1500 m depth, for the eddy transect at 24°S (Figure 6.16c), are observed cores of salinities with 34.75, and minimum of 34.7, 34.7 and 34.55, respectively. Water mass with similar properties: core of this salinity, at intermediate ocean depths have been also observed in hydrographic sections in the region (De Ruijter et al., 2002, DiMarco et al., 2002, Swart et al., 2010). The characteristics defines the presence of the Red Sea Water (RSW) and Antartic Intermediate Water (AAIW) (Tomczak and Godfrey, 1994, Donohue and Toole, 2003), specially that at 17°S, 20°S and 24°S. At 12°S (northernmost transect), the core of minimum salinity at referred depth, is the saltier when compared with the rank of minimum salinities identified at other transects. This could be associated with the influence of southward spreading Red Sea Water (RSW), regarded as the saltier water masses of the intermediate layers (Wyrtki, 1971). The RSW has been observed in the waters of the Mozambique Channel, moving towards the Agulhas Current (Wyrtki, 1971, Beal et al., 2000, De Ruijter et al., 2002, DiMarco et al., 2002, Donohue and Toole, 2003). RSW owes its higher salinity by the excess of evaporation over precipitation in the Red Sea Basin (Wyrtki, 1971, Tomczak and Godfrey, 1994). Its southward propagation is made mainly along the African coast. However, absence of oxygen in the model data, makes difficult to draw a definitive conclusion whether the relatively higher minimum salinity core of 34.75 observed at 12°S, is from RSW or AAIW origin, since AAIW has been observed as far north as to near 10°S (Tomczak and Godfrey, 1994, DiMarco et al., 2002). The AAIW is generated in the South-East Pacific Ocean and is advected eastward into the Atlantic and Indian Oceans (Wyrtki, 1971, Fine, 1993). Once in the South-West Indian Ocean, AAIW is known to be transported equatorward at intermediate depth, along the western boundaries. Within

the Mozambique Channel, AAIW is transported equatorward by the Mozambican Undercurrent (De Ruijter et al., 2002, Donohue and Toole, 2003). Corresponding eddy vertical flow structure shown in Figure 6.12, also is consistent with this fact.

Below the depth of the AAIW, our analysis show a minimum and maximum of temperature and salinity ranges across the eddy between 1.3°C and 1.8°C, and 34.75 and 34.8 respectively. According to hydrographic studies, this property range could represent characteristics of the Indian Deep Waters, IDW (Tomczak and Godfrey, 1994, Emery, 2001), or North Atlantic Deep Water, NADW. Emery (2001), gives the range of the IDW properties with respect to temperature and salinity, between 1°C and 2°S, and 34.62 and 34.73 respectively. The IDW moves northwards mainly concentrated along the western boundaries, reaching far north as to the Arabian Seas (Tomczak and Godfrey, 1994). This may explain their presence at our eddy transects. Studies also have revealed the presence of NADW in the South-West Indian Ocean (van Aken et al., 2004, De Ruijter et al., 2002). Again, it is important to mention that the absence of oxygen data in the model also makes difficult to differentiate IDW from NADW.

The presence of different water masses investigated across the long-lived anticyclonic eddy suggests that the eddy has trapped water masses from different origins. The constant observation (property conservation) of the same water masses involved within the eddy may indicate that the eddy transports materials southwards as it moves downstream, in agreement with previous studies (DiMarco et al., 2002, De Ruijter et al., 2002, Swart et al., 2010).

The Temperature - Salinity diagram presented in Figure 6.17, also shows small spreading of the water types (points in the plot. Compare our Figure 6.17, with De Ruijter et al. (2002), their Figure 4; Swart et al. (2010), their Figure 4). This may indicate that the eddy has mostly conserved its inward properties, isolating himself from the background oceanic environment. In fact Mozambique Channel eddies are strongly non-linear, thus have higher potential to trap materials (Chelton et al., 2011).

6.5 Conclusion

Our analysis from altimetry and SWIM model, about the eddy statistics, frequency, generation site, pathways, polarity, lifetime, amplitude, size and energy at the different regions of the Mozambique Channel, give an important information about the nature of the flow field in the region: Both cyclonic and anticyclonic eddies have been found to be generated within the channel. Cyclonic eddies appeared to be more abundant and smaller compared to the anticyclonic eddies. Cyclonic eddies seemed more ubiquitous than anticyclonic eddies, while the later were preferencially formed in the northern part of the channel, near 12°S, 48°E, between Madagascar and the African continent. In the center of the channel, they appeared to be preferentially formed in the narrow part of the channel, near 16°S, and at the eastern boundary of the central channel, near Madagascar Bight, around 20°S, and 44°E. In the south of the channel, preferential eddy generation sites for cyclonic eddies were identified at the eastern boundary of the channel, adjacent to the southern tip of Madagascar, and at the Delagoa Bight (between 25°S and 27°S), near Maputo, at the south-east coast of Mozambique. On the other hand, anticyclonic eddies have also their favorite generation site outside of the channel (e.g. east of the Madagascar Ridge, and in the southern boundary, likely by the instabilities in the Agulhas Return Current).

For both model and observation, we have identified 2 mesoscale turbulent modes on the anticyclonic eddies in the central part of the channel. The first mode was within the first baroclinic Rossby radius, centered around 70 km - 90 km radius, while the second mode was larger (beyond the first baroclinic Rossby radius), and was centered around 100 km - 140 km. Their frequency (5 - 6 anticyclonic eddies per year), observed in the second mode, is consistent with in-situ observations (De Ruijter et al., 2002, Ridderinkhof and De Ruijter, 2003, Schouten et al., 2003, Harlander et al., 2009), and other modelling studies (van der Werf et al., 2010).

With regard to their trajectories, the eddies identified in our study appeared to propagate mostly in south-westward direction, consistent with theories of non-linear turbulence (McWilliams and Flierl, 1979, Chelton et al., 2007), which infers that eddies should be propagating mainly westwards, with a slight meridional deviation (pole-ward or equator-ward associated with the direction of rotation).

Our analysis on the eddy polarities, has shown that the dominance of one eddy type over the other depends on the eddy-length scale at which the eddies are compared. The anticyclonic eddies have shown to be larger than the cyclones. However, both cyclonic

and anticyclonic eddies decrease their size with their north to south propagation, and appears to follow the baroclinic Rossby radius for the region (Chelton et al., 1998).

With regard to the eddy lifetime, the anticyclonic eddies have shown to last longer than cyclonic eddies, everywhere in the channel, and it seems to be related to their larger size, higher amplitude and large energy content.

Analysis on the temperature and salinity within a long-lived anticyclonic eddy that propagated throughout the length of the channel have shown that the eddy had trapped different water masses from different origins, such as IEW, TSW, STSW, SICW, AAIW, RSW and IDW. Its T-S diagram has shown a less spreading of its properties, suggesting that the eddy had conserved its properties for a considerable time.

CHAPTER 7

Eddy-Mean Flow Interaction in the Mozambique Channel

Key Questions:

- **What role the eddy-mean flow interaction plays on the circulation in the Mozambique Channel?**
- **What dominant eddy formation mechanisms can be inferred at the different subregions of the channel?**

7.1 Introduction

Interaction of motions with different timescales, such as oceanic eddies, and general ocean currents, can be investigated by energy transfer mechanisms using the Lorenz diagram (Cronin and Watts, 1996, Azevedo et al., 2008). The Lorenz diagram allows one to diagnose a specific dynamical process (e.g. energy transport, turbulence production, buoyancy production, energy dissipation), associated with the event of energy conversion (Kundu,

1990). The types of energy involved in the Lorenz diagram associated with these processes are kinetic and potential energies, distributed in their time-mean and turbulent states, namely, mean kinetic energy, turbulent or eddy kinetic energy, mean potential energy and eddy potential energy.

As was discussed in chapter 6, the Mozambique Channel is a region of strong mesoscale eddy activity (De Ruijter et al., 2002, Ridderinkhof and De Ruijter, 2003, Schouten et al., 2003). The understanding of the mechanisms of formation of such eddies still remain an on-going study (Harlander et al., 2009). Some studies have proposed several mechanisms: For instance, Biastoch and Krauss (1999), have investigated the formation of the Mozambique Channel eddies, using outputs of an eddy permitting ocean model, at $\frac{1}{3^\circ}$ horizontal grid resolution, within the greater Agulhas system. In their analysis, they have considered 2 components of the Lorenz diagram: The conversion of the mean kinetic to eddy kinetic energy, and the conversion of the mean potential to eddy kinetic energy. Their result has shown that the eddies in the Mozambique Channel were formed at the northern tip of Madagascar, by barotropic instability in the South Equatorial Current (Biastoch and Krauss, 1999). The generated eddies drifted southward throughout the channel, and reached the downstream region of the Agulhas Current.

Schouten et al. (2002b, 2003), using satellite altimetry data, found a correlation between the arrival of baroclinic Rossby waves generated in the eastern Indian Ocean, with the frequency of eddy formation in the central Mozambique Channel, rated at about 4 to 5 eddies per year, thus suggesting that the eddy formation in the channel was related with such a Rossby wave activity.

Ridderinkhof and De Ruijter (2003), have used in-situ observations of about 19 months, collected at the narrowest part of the Mozambique Channel, near $\sim 17^\circ$S, to investigate the nature of the flow field in the region. Their study has suggested that the generation of the eddies at this location, was related with the separation towards off-shore of a southward, western boundary current at the Mozambican coast, confined to the north of $\sim 17^\circ$S. By conservation of potential vorticity, and vortex stretching over the shallower topography at the narrow of the channel lead to a local formation of eddies (Ridderinkhof and De Ruijter, 2003). The contribution of the local topography seems to play an important role on such process. The study has shown that such process occurs when the SEC reaches its strongest transport. Local eddy formation associated with the intensification of the SEC volume transport has been recently corroborated by Backeberg and Reason (2010), using

a nested model configuration at $\frac{1}{10^{\circ}}$ spatial grid resolution of the greater Agulhas system.

Another study by Harlander et al. (2009), based on 4 years timeseries, from 2003 to 2006, of the dataset retrieved at the narrows of the channel (Ridderinkhof and De Ruijter, 2003, De Ruijter et al., 2006), have shown that the generation of the Mozambique Channel eddies in the center of the channel, was influenced by a so-called Mozambique Channel Rossby normal mode (an off-shore deflection to the center of the channel of a poleward flow along the Madagascar coast). However, the dynamical processes involved remained uncertain (Harlander et al., 2009).

Penven et al. (2006c), also used a numerical model, configured at $\frac{1}{4^{\circ}}$ horizontal grid resolution, to investigate the ocean dynamics in the Agulhas system. The model simulated the oceanic circulation in the region, and has run as if Madagascar Island was not present. Their study have shown that the absence of the island has led to no formation of the Mozambique Channel eddies. Thus, suggesting that the presence of such eddies are strongly dependent of the geographical location of Madagascar (in the path of the South Equatorial Current). Their results also corroborates the findings of Biastoch and Krauss (1999), that infers that the Mozambique Channel eddies are generated at the northern tip of Madagascar.

As becomes evident from the various possible mechanisms presented (Biastoch and Krauss, 1999, Schouten et al., 2002b, Ridderinkhof and De Ruijter, 2003, Schouten et al., 2003, Penven et al., 2006c, Harlander et al., 2009, Backeberg and Reason, 2010), at present, the origin of the Mozambique Channel eddies is not fully understood, as also has been pointed by Harlander et al. (2009), Backeberg and Reason (2010). More studies in this direction are required. In the present chapter, we use SWIM outputs to further investigate the formation of the Mozambique Channel eddies. We analyze energy conversion terms connecting the blocks of energies composing the Lorenz diagram, namely: mean kinetic, mean potential, eddy kinetic and eddy potential.

7.2 Energetics of the flow field

7.2.1 Energy conversion terms

The review of the volume-integrated energy budgets composing the classical Lorenz diagram (Cronin and Watts, 1996, Azevedo et al., 2008), have shown that the different energy types in a controlled volume, are connected by four main energy conversion terms: The conversions from mean kinetic to eddy kinetic energy, from the mean kinetic to mean potential energy, from the mean potential to eddy potential, and finally from the eddy potential to eddy kinetic energy. Following Miller and Lee (1995) notation $C(X, Y)$, indicating the conversion of an energy type X to a type Y (also from Y to X, if the term $C(X, Y)$ is negative), the conversion terms are expressed by the equations (7.1) to (7.4), derived from the evolution equation of potential and kinetic energy budget:

$$C(\overline{K}, K') = -\left[\overline{u'u'}\frac{\partial \overline{u}}{\partial x} + \overline{u'v'}\left(\frac{\partial \overline{u}}{\partial y} + \frac{\partial \overline{v}}{\partial x}\right) + \overline{v'v'}\frac{\partial \overline{v}}{\partial y}\right] \tag{7.1}$$

$$C(\overline{P}, \overline{K}) = -\overline{w}.\overline{\rho}\frac{g}{\rho_0} \tag{7.2}$$

$$C(\overline{P}, P') = -\frac{g}{\rho_0}\frac{\overline{u'\rho'}\frac{\partial \overline{\rho}}{\partial x} + \overline{v'\rho'}\frac{\partial \overline{\rho}}{\partial y}}{\frac{d\tilde{\rho}}{dz}} \tag{7.3}$$

$$C(P', K') = \overline{-\rho' w'}\frac{g}{\rho_0} \tag{7.4}$$

In these equations u, v and w - are the zonal, meridional, and vertical components of the flow, in x, y and z directions. g - is the acceleration due to gravity, ρ - is the seawater density, computed via non-linear equation of state (Jackett and MacDougall, 1995), ρ_0 - is the seawater density of reference, and $\tilde{\rho}(z)$ - is the reference state for potential density.

The conversion term (7.1) can be obtained from the time-derivative of the kinetic energy budget of the mean flow (Kundu, 1990). Because the conversion term (7.1) involves

both turbulent and mean-flow, it stems from the interaction between these two motions with different time-scales. Cushman-Roisin and Beckers (2009) calls the term (7.1) by the "*shear production*", because of the presence of the shear of the large-scale flow. The literature (Kundu, 1990, Cronin and Watts, 1996, Azevedo et al., 2008) shows that in case that the conversion term (7.1) is positive, it indicates an occurrence of a barotropic instability in the system. Note that this is the same term used by Biastoch and Krauss (1999), while investigating eddy generation mechanisms in the source regions of the Agulhas Current. The kinetic energy of the mean flow is converted to turbulence or eddy kinetic energy. If the conversion term is negative, the energy is converted from the eddies to the mean-flow (Dewar and Bane, 1985).

The term (7.2), indicates the conversion of the mean potential to mean kinetic energy. It represents the production (or destruction) of mean kinetic energy by a buoyant force on the mean flow (Kundu, 1990). This term has been used by Veitch et al. (2010), as an indication of a path of a baroclinic instability process. Baroclinic instability is a process resulting in a redistribution of the density field, which tends to lead the system to a more stable state. Azevedo et al. (2008) and Cronin and Watts (1996), in a 2-layer model, with a QG-approximation, have also represented this term by ($-g\alpha\overline{w_a}\overline{\Delta T}$), when temperature is regarded as the only driver of density variations. (Where g is the acceleration due to gravity, α - is the thermal expansion coefficient, w_a - is the vertical component of an ageostrophic flow, and ΔT - the temperature difference between the upper and lower layers). This term (7.2) also can be obtained from the time-derivative of the kinetic energy budget of the mean flow (Kundu, 1990, Azevedo et al., 2008). Considering that the term (7.2) is generated by consequence of mass field distribution, due to the slope change of the isopycnals, Cronin and Watts (1996), have demonstrated that this term becomes very important for the energy balance in the ocean, as it modifies the local hydrostatic pressure. The modified hydrostatic pressure generates a horizontal pressure gradient, that produces a vertical pressure work on the mean flow (Cronin and Watts, 1996). Note that no eddy production is linked to this term. Therefore it will not be considered in our study.

The term (7.3), represents the conversion of energy from the mean potential to eddy potential. Tsugawa and Hasumi (2010) and Biastoch and Krauss (1999), have used similar relation, as indicative of a baroclinic instability, hence eddy production. Cronin and Watts (1996), Azevedo et al. (2008), in their 2-layers model, with QG- approximation have represented this term by the expression ($-\frac{g\alpha}{\theta_z}\overline{u'T'}^{div}\nabla_h\overline{T}$). (Where θ_z - is a temperature profile horizontally uniform, and time-independent, regarded as the basic stratification.

The upper-script "*div*" represents the divergent part of the flow field, and ∇_h - is the horizontal gradient operator). The term (7.3) can be obtained from the time-derivative of the potential energy, either from the mean or from the turbulent flow field (Kundu, 1990). This term, represents a rate of a baroclinic conversion. If the conversion rate is positive, it indicates a first phase (or conversion path) of a baroclinic instability (Azevedo et al., 2008).

With regard to the last term (7.4), it stands for the conversion from the eddy potential to eddy kinetic energy. It represents a "*buoyancy production*" by the work performed by turbulent buoyancy forces on the vertical stratification, leading to changes on the potential energy (Cushman-Roisin and Beckers, 2009). Cushman-Roisin and Beckers (2009) and Marchesiello et al. (2003), have regarded this term as an estimate of a baroclinic conversion rate, indicative of a second phase of a baroclinic instability. The term (7.4) can be found from the time-derivative of the kinetic or potential energy budget of a turbulent flow (Azevedo et al., 2008). Cronin and Watts (1996), also have represented this term in the form $g\alpha\overline{w'_a T'}$.

To investigate the eddy generation processes associated to the energy transfer, the conversion terms that we will be looking are: terms (7.1), (7.3) and (7.4).

Figure 7.1 shows the subregions within the Mozambique Channel, used to compute the regional energy conversion terms, and Table 7.1, shows their quantified rates. The conversion terms are vertically integrated throughout the oceanic water column.

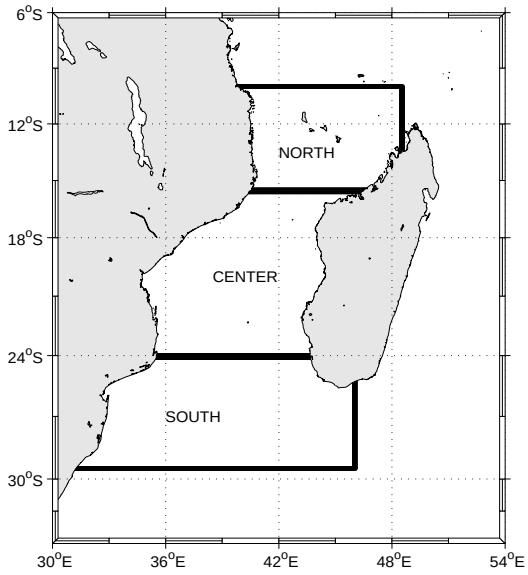

Figure 7.1. Subregions of the Mozambique Channel, used to compute the mean energy conversion terms, presented in Table 7.1. North: 15.5°S - 10°S, 39°E - 48.5°E; Center: 24°S - 15.6°S, 34°E - 47°E, and South: 29.5°S - 24.1°S, 32°E - 45°E.

Subregion	Transfer rate [m^3s^{-3}]		
	$C(\overline{K},K')$	$C(\overline{P},P')$	$C(P',K')$
North	3.32×10^{-6}	-7.01×10^{-6}	1.70×10^{-6}
Center	7.88×10^{-6}	3.87×10^{-6}	-1.73×10^{-6}
South	7.56×10^{-6}	19.76×10^{-6}	3.0×10^{-6}

Table 7.1. Energy conversion terms in m^3s^{-3} at the different regions of the Mozambique Channel. The conversion terms have been vertically integrated throughout the ocean column, and averaged over each subregion. The quantities have been estimated from the 7-year climatology of the model run. For the conversion rates: $C(\overline{K},K')$ - is the conversion from mean kinetic to eddy kinetic energy, $C(\overline{P},P')$ - is the conversion from mean potential to eddy potential energy, and $C(P',K')$ - is the conversion from eddy potential to eddy kinetic energy.

The northern subregion of the channel, is extended from 15.5°S to 10°S, 39°E to 48.5°E (Figure 7.1). In this region, the production of the eddy kinetic energy by a direct energy transfer (barotropic instability) is about 3.32×10^{-6} m^3s^{-3}, while the indirect production is about 1.70×10^{-6} m^3s^{-3}. The strongest conversion rate observed in this region is about -7.01×10^{-6} m^3s^{-3}, energy transfer from eddy potential to mean potential energy (negative signal in $C(\overline{P},P')$), suggesting an eddy dissipation.

In the center of the channel, the subregion spans from 24°S to 15.6°S, 34°E to 47°E (Figure 7.1). The strongest conversion term is the direct production of eddy kinetic energy (barotropic instability), estimated in about 7.88 $\times$ 10^{-6} m^3s^{-3}. The dissipation of the eddy kinetic energy, characterized by a negative conversion term in $C(P', K')$ is about 1.73 $\times$ 10^{-6} m^3s^{-3}. Different from the northern subregion, here there is a production of eddy potential energy of about 3.87 $\times$ 10^{-6} m^3s^{-3}.

The subregion in the south ranges between 29.5°S and 24.1°S, 32°E and 45°E (Figure 7.1). The strongest eddy kinetic energy production is the direct transfer from mean kinetic to eddy kinetic energy, estimated in about 7.56 $\times$ 10^{-6} m^3s^{-3}. The other form of production via a transfer from eddy potential to eddy kinetic is about 3.0 $\times$ 10^{-6} m^3s^{-3}. The strongest energy conversion rate observed in this region, and in the channel as a whole is about 19.76 $\times$ 10^{-6} m^3s^{-3}, transfer from mean potential to eddy potential energy ($C(\overline{P},P')$), indicative of baroclinic instability.

In general, Table 7.1, suggests that the dynamical process with strongest energy transfer rate is the first phase of the baroclinic instability process, where the energy is converted from the mean potential to the eddy potential ($C(\overline{P},P')$). While with regard to the formation of the eddy kinetic energy, the strongest dynamical process is the transfer of energy from the mean kinetic to the eddy kinetic ($C(\overline{K},K')$), suggesting a dominance of the barotropic instability process.

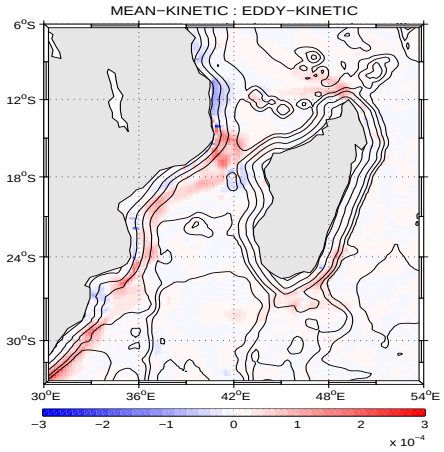

(a) C($\overline{K}$,K')

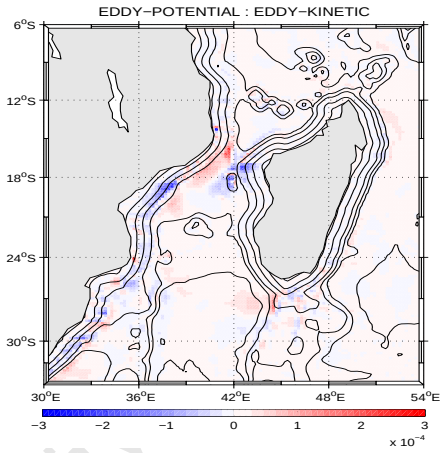

(b) C(P',K')

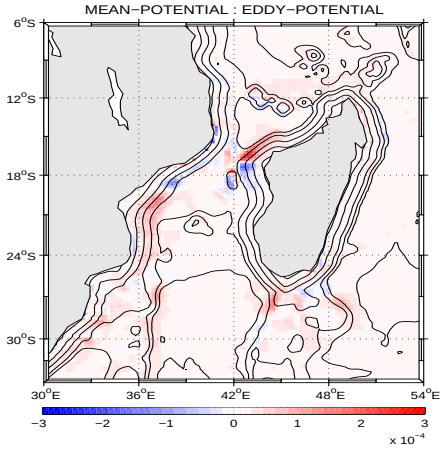

(c) C($\overline{P}$,P')

Figure 7.2. Maps of the spatial distribution of the different energy conversion terms in Wm^{-2}, associated to the eddy formation. The terms were vertically integrated throughout the ocean column, and were computed from 7-year climatology of the model run.

7.3 Eddy Generation Processes

7.3.1 Barotropic and baroclinic instabilities

Figure 7.2 shows maps of a spatial distribution of the energy conversion terms, associated to the eddies. The transfer terms were vertically integrated throughout the oceanic water column.

Figure 7.2a, portrays a dynamical process in which kinetic energy of the system is directly converted from its mean-state to its turbulent form (eddy), and represents a barotropic instability of the flow. According to this panel, shear production (i.e. positive conversion rate) preferentially occurs at following locations: at the northern tip of Madagascar (Cape-Amber), with an approximated rate of about 2×10^{-4} Wm^{-2} ; in the narrower part of the channel, at the western boundary, near 16.5°S, about 2.5×10^{-4} Wm^{-2}; and along a southwest band, starting to the west of about 18°S, 42°E, extended along the western boundary of the channel. In this band, the strongest conversion rate occurs near 20°S, 37°E; near 24°S, 37°E; and to the south of 29°S, over the northern extension of the Agulhas Current. Another region characterized by a shear production, but with a relatively lower rate (about 1.5×10^{-4} Wm^{-2}), when compared to the previous sites already mentioned, is located to the south-east of Madagascar, around 24°S to 26°S, 48°E. On the other hand, a negative conversion rate (eddy dissipation) is observed along the western boundary of the channel, between 11°S and 14°S. The spatial distribution of the energy conversion terms presented are in good agreement with the current description of the flow field found in recent literature: Shear production observed at Cape-Amber (Figure 7.2a), is consistent with barotropic instability of the westward flowing South-Equatorial Current, at the northern extremity of the Island, leading to eddy shedding events at the Cape, as reported in some studies, where hydrographic data (Schott et al., 1988), and also model simulations were used (Quadfazel and Swallow, 1986, Biastoch and Krauss, 1999).

Eddy dissipation observed at the northwestern boundary of the channel, between 12°S and 14°S (Figure 7.2a), indicates that the energy is transferred from the eddies to the mean-flow. This suggests that the eddies are dissipating, and their energy is mainly used to maintain the mean-flow at this latitudinal band. This is also in agreement with the presence of a western boundary current to the north of the narrower part of the channel, as reported by hydrographic measurements (De Ruijter et al., 2002). It corroborates the possibility that this boundary current may not be a permanent feature as proposed by

Schouten et al. (2003). This could be expected for a flow field sustained by passing eddies. Although this southward boundary current derives its waters mainly from the same source (i.e. SEC) as the northward East African Coastal Current (EACC), is likely that these opposite flowing currents are modulated by different processes. The northward EACC is known to be a wind driven (Wyrtki, 1971, Tomczak and Godfrey, 1994), while the southward flow is suggested here to be modulated by the mesoscale eddy activity.

The strongest positive conversion rate (shear production, over 2.5×10^{-4} Wm^{-2}), in the narrow sector of the channel, near 16.5°S, is consistent with the concept of local formation of anticyclonic eddies at this location, produced by an off-shore overshooting of the southward boundary flow as proposed by Ridderinkhof and De Ruijter (2003), Harlander et al. (2009). Their studies have suggested that by conservation of potential vorticity, involving a large β-effect, and vortex stretching over the shallow oceanic topography of Davie Ridge, could generate anticyclonic eddies (Schouten et al., 2003, De Ruijter et al., 2002). The latitude near 15°S marks the location where the energy transfer changes its sign towards a positive conversion rate. Note that this geographical point stands as the easternmost point of the Mozambican coast, suggesting that the coastline may also play a role on the production of turbulent kinetic energy.

To the south of the narrows of the channel, along the western boundary, there are two other localized sites with relatively strong shear production: near 21°S, 37°E, at the central sector of the Sofala Bank; and the other, near 24°S, 36°E. The barotropic instability signal at 21°S, 37°E, seems closely related to shear induced by the continental slope of the bank, while the signal at 24°S, 36°E, seems related to the shear flow induced by a change of coastline orientation, leading to eddy formation, in a mechanism similar to that described by Thorpe (1998). Should also be noted that the region near 24°S, 36°E, is regarded in literature as a site of strong shear flow that induces the generation of a cyclonic recirculation at the Delagoa Bight, near Maputo, around 26°S, 33°E (Lutjeharms and da Silva, 1988, Lutjeharms, 2006, Lamont et al., 2010). See also Quartly and Srokosz (2004), their Figure 1.b. This is also in agreement with the generation of cyclonic eddies, as suggested in chapter 6.

With regard to the shear production observed at the south-eastern coast of Madagascar, around 24°S to 26°S, 48°E, the signal is also in agreement with literature, that characterize this place as a site of strong disturbances of the flow field (Quartly et al., 2006, Siedler et al., 2009), when the South-East Madagascar Current partly separates from the continental shelf.

Figure 7.2b shows eddies being formed with a different mechanism from that proposed in Figure 7.2a. In Figure 7.2b, eddy potential energy is converted to eddy kinetic via buoyancy production, an indication of a baroclinic instability process. Here, the strongest baroclinic conversion rate occurs also in the central part of the channel, nearly between 15°S and 21°S, specially at the shallower part of the narrow sector of the channel, where the bottom topography is characterized by the presence of the Davie Ridge. This topographic feature seems to play a significant role on the process. At this site (between 15°S and 21°S, Figure 7.2b), the conversion term is characterized by a buoyancy production at the western boundary, while the eastern boundary is characterized by eddy buoyancy dissipation (negative conversion term). Note that the rate of buoyancy production is relatively lower (1×10^{-4} Wm^{-2}), than the destruction rate (2×10^{-4} Wm^{-2}). Here the location of buoyancy production signature coincides with the location of a cyclonic recirculation of the flow field, related with the formation of coastal trapped lee eddies, and also development of the Angoche upwelling as described by Lutjeharms (2006).

The Mozambique Channel eddies are large (diameter over 300 km (De Ruijter et al., 2002, Schouten et al., 2003, Ridderinkhof and De Ruijter, 2003)), and at the narrows of the channel, they usually fill the whole width of the channel. Interaction of these eddies with the Madagascar continental shelf, at Pracel Bank, near 17°S, 43°E, may explain the eddy buoyancy dissipation signature observed at that position. A close inspection also in Figure 7.2b, at the eastern edge of the Juan de Nova Island, near 18°S, 42°E, shows a relatively smaller signature of buoyancy production. This position of eddy formation by buoyancy production coincides with the secondary anticyclonic eddy formation site, described in chapter 6, and also reported by Halo et al. (2012) [*in review*]. The size of the eddies identified at this location (radius $\sim$ 70 km), as discussed by Halo et al. (2012) [*in review*], is also consistent with the first baroclinic Rossby radius of the region, proposed by Chelton et al. (1998). This corroborates with the finding of this study, where we infer that the eddies in the eastern part of the central channel are generated by baroclinic instability of the flow.

Another site in the channel dominated by an eddy buoyancy dissipation is located at Sofala Bank, near 19°S, 38°E. The kinetic energy of the eddies at this site, is significantly converted to its potential energy. Again, it may suggest that the eddies formed as shown in Figure 7.2a, interacts with the continental slope at Sofala Bank, leading to an eddy decay event (Figure 7.2b).

The energy transfer from the mean potential to eddy potential, also known as the first phase of baroclinic conversion (Azevedo et al., 2008), is presented in Figure 7.2c. Here, the strongest conversion rate in the whole channel domain occurs at the eastern boundary of the narrow sector of the channel. This is consistent with Figure 7.2b. The exception is that at Sofala Bank, near 21°S, 36°E, there is an evidence of production of eddy potential energy. A significant shift of sign of the conversion term is observed over the narrow sector of the channel. The transition from the mean potential to eddy potential occurs at the northeastern flank of the narrow sector of the channel, inferring to be an eddy production site, while the transition from the eddy potential to the mean potential, occurs at the southeastern flank of the Pracel Bank, near 15°S to 20°S, 43°E, inferring some eddy destruction, likely by the continental slope of the bank. A similar dynamical process is also observed at Sofala Bank, occuring in the central part of the western boundary of the channel, near 18°S to 22°S, 36°E to 38°E. At the northern part of the Bank, the potential energy flows from the eddy towards the background flow (indicative of eddy dissipation), while the opposite occurs at the southern part of the bank.

A comparison between two energy conversion terms involved in the generation of eddy kinetic energy (i.e: C($\overline{K}$, K′), and C(P′, K′)), is presented in Figure 7.3a. The depth-integrated conversion terms were zonally averaged over the three subregions of the channel domain. The meridional profiles of these terms show that the barotropic instability generally dominates the second phase of the baroclinic instability. This is in agreement with the Table 7.1. However, there are also localized sites within the channel, where the signal of baroclinic instability is greater than the barotropic instability, such as between, the latitudes 12°S and 14°S, at 18°S, and near 22°S (Figure 7.3a). Inspection on the profile of the barotropic instability shows a strongest conversion rate (over -2×10^{-6} m^3s^{-3}), occuring between 15°S and 17°S, while a lowest rate is observed between 12°S and 14.3°S, specially near 14.3°S, where the peak is about -2×10^{-6} m^3s^{-3}. Note that the eddy dissipation (negative C($\overline{K}$, K′)) at this latitude band is consistent with Figure 7.3b, previously explained (where the eddies sustain the mean flow). On the other hand, the strongest signal of baroclinic instability is observed near 17°S, $\sim$ 2.4×10^{-6} m^3s^{-3}, and near 27.5°S, of about 2.5×10^{-6} m^3s^{-3}, while the lowest signal (-3.8×10^{-6} m^3s^{-3}), is observed near 17.5°S. Note that between 18°S to 20°S, the energy of the baroclinic conversion is transfered from the eddy kinetic to the eddy potential. Interestingly, this conversion coincides with the site of the highest SSH variability of the region, as described by Halo et al. (2012) [*in review*],

(see their Figure 3). In the south, between 22°S and 28°S, both barotropic and baroclinic transfers of energies towards eddy kinetic energy increase southwards.

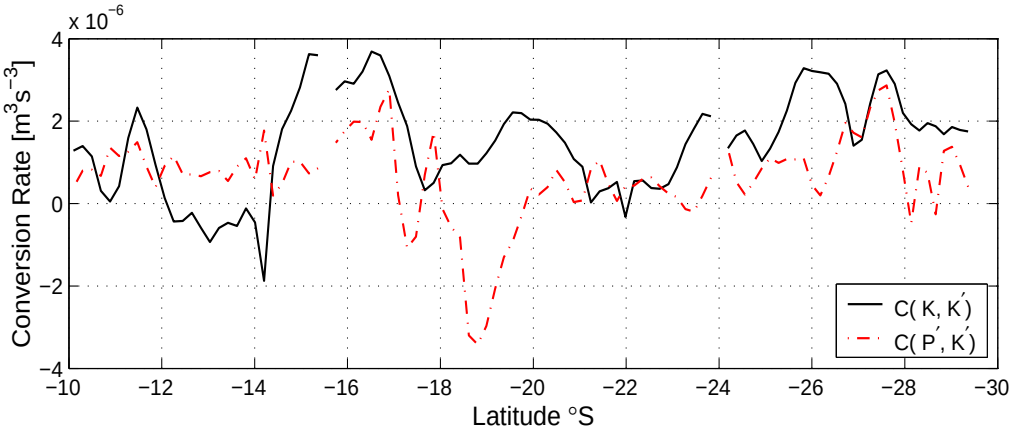

(a) Profiles of C($\overline{K}$,K') and C(P',K') conversion terms

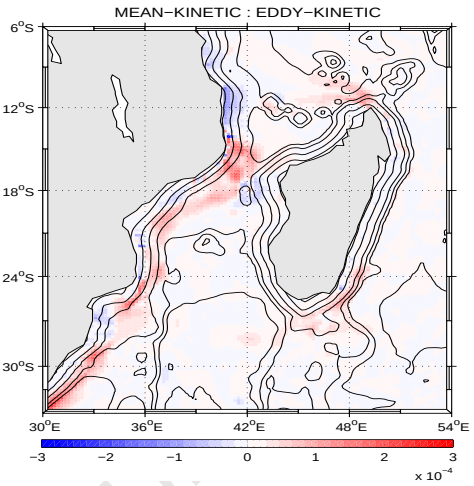

(b) C($\overline{K}$,K')

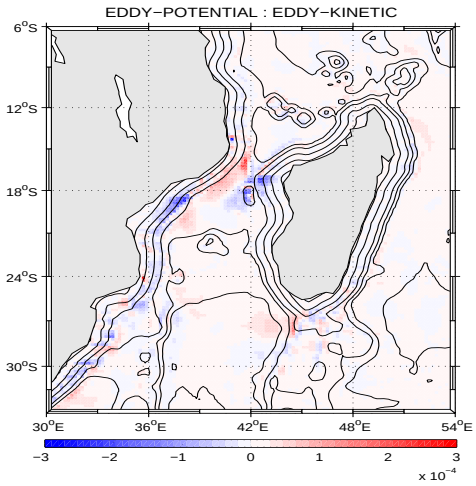

(c) C(P', K')

Figure 7.3. Profiles of conversion terms in m^3s^{-3} (a): Black (barotropic instability) and Red (baroclinic instability), vertically integrated and zonally averaged in the whole channel domain. Spatial distribution of barotropic C($\overline{K}$,K') (b) and baroclinic C(P',K') instabilities (c) in Wm^{-2}, vertically integrated at the whole ocean water column, and computed from 7-year climatology of the model run. Note that the panels Figure 7.3b and Figure 7.3c are the same as in Figure 7.2a and Figure 7.2b

7.4 Discussion

7.4.1 Eddy generation processes

Figure 7.2a suggests that in the northern subregion of the Mozambique Channel, anticyclonic eddies were formed by barotropic instabilities of the SEC, when the flow pass at the Cape-Amber. This is in agreement with previous studies (Schott et al., 1988, Biastoch and Krauss, 1999). Instabilities of the SEC at the northern tip of Madagascar has also been reported in hydrographic data, and attributed to mesoscale dynamics (Schott et al., 1988). In a modelling study, Biastoch and Krauss (1999), have demonstrated that positive vorticity (anticyclonic rotation) and shear instabilities are generated at Cape-Amber by the friction between the SEC with the coastline, triggering eddies. More recently, also it has been shown that the anticyclonic eddy formation at this location may be directly linked with the dynamics of the SEC at the northern tip of Madagascar (Backeberg and Reason, 2010). The barotropic instability signal produced at the northern tip of Madagascar (Figure 7.2a), has shown a westward extension, suggesting that the flow propagates southwestwards. Interestingly, on approaching the African coast, it is evident a negative energy conversion rate, extended paralel to the coastline, along the northwestern boundary of the channel, nearly between 11°S and 14°S. The signal of such conversion rate which suggests the production of the mean-flow by the eddies is consistent with the presence of a southward western boundary current (Figure 7.2a), as proposed by De Ruijter et al. (2002). Interestingly, the possible presence of a mean-flow controlled by the eddy field could also corroborate the arguments presented by Schouten et al. (2003), regarding the nature of this flow. According to Schouten et al. (2003), this flow is not a permanent feature, and is strongly variable. Our results have shown that this is likely to be true, as the flow seemed to be sustained by southward passing mesoscale eddies.

In the central part of the channel 15°S to 24°S, our results have suggested that the interaction of the eddies with the mean-flow, results on generation of eddies by barotropic and baroclinic instabilities (Figure 7.2a,b). In Figure 7.2a, between 15°S and 18°S, is evident that the southward mean-flow observed at the northwestern boundary of the channel as previously discussed, changed its signal, from negative to a positive conversion rate, indicative of an eddy production, by destruction of the mean-flow. This is consistent with previous studies that have reported a local formation of mesoscale eddies at this site (Ridderinkhof and De Ruijter, 2003, Harlander et al., 2009, Backeberg, 2010, van der Werf et al., 2010). The generation of the anticyclonic eddies at this location, have been related

to an off-shore deflection of a southward, coastal western boundary current, confined to the north of approximately 17°S. By conservation of potential vorticity, and vortex stretching over the shallower topography at the narrow of the channel lead to a local formation of eddies. Ridderinkhof and De Ruijter (2003) have suggested that such process occurs when the SEC reaches its strongest transport.

Figure 7.2b, also suggests that some eddies formed at this site are generated by a different mechanism of that proposed by Ridderinkhof and De Ruijter (2003). However, the lateral boundaries of the channel, also seems to play a significant role on the decay of the eddies (eddy-shelf interaction), as suggested by the negative signatures in Figure 7.2b, inferring eddy destruction. Interaction of eddies with the slopped continental shelf has been recently investigated in the framework of a barotropic model by Sutyrin and Grimshaw (2010). Their result has shown that the eddy-shelf interaction, has generated topographic coastally trapped waves, and secondary cyclonic eddies due to an off-shelf advection of water with high potential vorticity, and enhanced vortex decay due to deformations of the vortex core (Sutyrin and Grimshaw, 2010). A similar process to this could also explain the generation of cyclonic eddies, both in the eastern and western parts of the Mozambique Channel, as described by Halo et al. (2012) [*in review*]. Interestingly, such a sink of eddy kinetic energy, results in an energy transfer towards eddy potential energy. The production of eddy potential energy in the central subregion of the Mozambique Channel, could explain why the central part of the channel is regarded as a region characterized by a strongest SSH variability, as shown by Halo et al. (2012) [*in review*], (see their Figure 3). Note that the eddy potential energy is linked to variations of the SSH (mimic of the vertical displacement of the thermocline).

The results show that both barotropic and baroclinic instabilities play an important role. Barotropic instabilities are responsible for the generation of anticyclonic eddies on the western boundary of the channel (Figure 7.3b). This also is in agreement with previous studies (De Ruijter et al., 2002, Ridderinkhof and De Ruijter, 2003, Schouten et al., 2003, Backeberg, 2010). Note that the barotropic instability signal at this site can be associated with the eddies dominating the second turbulent mesoscale mode of larger eddies $\sim$ radius 100 km, described in the previous chapter, and also presented by Halo et al. (2012) [*in review*]. On the other hand, baroclinic instabilities seemed to be responsible for the generation of the eddies in the eastern part of the channel (Figure 7.3c). This is in agreement with the results presented in the previous chapter, also discussed by Halo et al. (2012) [*in review*], and was regarded as a novel result. Note also that the

eddies generated in this region are related with the first turbulent mesoscale mode of relatively smaller eddies $\sim$ radius 80 km, as presented by Halo et al. (2012) [*in review*]. In the western boundary of the channel, over Sofala Bank, both baroclinic and barotropic instabilities play an important role on the generation of mesoscale eddies (Figure 7.3b,c).

In the southern Mozambique Channel, both baroclinic and barotropic instabilities are also responsible for eddy formation (Figure 7.3a). Barotropic instabilities dominate over the western boundary of the channel (Figure 7.3b), while baroclinic instabilities dominate on the eastern boundary (Figure 7.3c), to the southwest of Madagascar. The generation of eddies in the southwest of Madagascar (Figure 7.3c) is also in agreement with the previous studies, reporting enhanced mesoscale dynamics of eddies and dipoles, as reported in the literature (Gründlingh, 1995, Quartly and Srokosz, 2004, De Ruijter et al., 2004, Siedler et al., 2009). Note that to the south of 28°S, there is a decrease of the profiles (Figure 7.3a), which may be interpreted as eddy decay, likely absorbed in the Agulhas Current (Gründlingh, 1995).

7.5 Conclusion

Analysis performed with regard to the role of the eddy-mean flow interaction in the circulation in the Mozambique Channel, and identification of the important eddy formation mechanisms, at the different subregions of the channel, have shown that in the northern Mozambique Channel, eddies were generated by barotropic instabilities of the SEC, at the northern tip of Madagascar, in agreement with previous studies. However, the generated eddies on the other hand seemed to release part of their turbulent energy to sustain a southward mean flow, at the north western boundary of the channel, between 14°S and 12°S. At this latitudinal band, baroclinic instabilities were the dominant eddy formation mechanism. To the south of 14°S, barotropic instabilities of the southward western boundary flow also has led to the eddy formation in the narrows of the channel, over Davies Ridge. On the other hand, baroclinic instabilities dominated over barotropic, specially at 18°S, and 21°S to 22°S. To the south of the 22°S, barotropic instabilities dominated over baroclinic instabilities. In spite the localized dominance of baroclinic instabilities observed in the region, the overall dominant process in the whole channel domain is the barotropic instability.

CHAPTER 8

Thesis Conclusion: Main findings and the way forward

The main Research Questions addressed in this study were:

- **Does the SWIM model simulate satisfactorily the large and mesoscale oceanographic features of the Mozambique Channel? (Chapter-4)**
- **Are there cyclonic eddies in the Mozambique Channel? (Chapter-6)**
- **Why is the flow in the Mozambique Channel dominated by the anticyclonic eddies? (Chapter-6)**
- **What are the physical characteristics of the Mozambique Channel eddies? (Chapter-6)**
- **How do the Mozambique Channel eddy properties vary meridionally throughout the channel? (Chapter-6)**
- **What role the eddy-mean flow interaction plays on the circulation in the Mozambique Channel? (Chapter-7)**

- **What dominant eddy formation mechanisms can be inferred at the different subregions of the channel? (Chapter-7)**

8.1 Concluding summary of the Thesis

A model based configuration for the South-West Indian Ocean (SWIM) has been designed to simulate the mesoscale oceanic circulation in the Mozambique Channel, and by extension in the greater Agulhas Current system. An extensive model data comparison has been performed for evaluation on the performance of the SWIM configuration.

When the mean states of temperature and salinity from SWIM at the sea surface and throughout the water column was compared against climatologies from WOA05 and CARS09, it has been observed that SWIM outputs were more compared to CARS09 than the WOA05, possibly due to CARS09's better interpolation schemes. The T-S diagrams have shown that SWIM has reproduced the presence of the main water masses of the region, while failing to resolve accurately their mixing and spreading across the Indian Basin.

When the time-mean streamlines of SSH field from SWIM was compared against the mean dynamic topography from the CLS-CNES09 product, for evaluation of the large-scale surface geostrophic circulation, it was observed that SWIM reproduced well the presence of the long-term oceanic currents of the region. In contrast to the observations, SWIM reproduced a relatively weaker SEMC, a weaker recirculation loop of the Agulhas retroflection, a narrower and more meandering ARC and a stronger recirculation at the offshore edge of the Agulhas Current proper.

Throughout the water column, the flow in SWIM has been compared against the LOCO mooring dataset. SWIM was able to reproduce satisfactorily the vertical structure of the mean flow and the eddy field in the narrows of the Mozambique Channel. SWIM also has shown consistent estimates of the volume transport of the main ocean currents. The diagnostics have shown that SWIM has shown significant difficulties to reproduce comparable eddy kinetic energy and SSH variability in the Mozambique Channel, with a $\sim 50\%$ overestimation.

Despite the model difficulties, the overall evaluation has suggested that SWIM can be successfully used to study the large and mesoscale oceanographic processes of the region. Confident with the model results, we have designed a robust automatic eddy detection

and tracking algorithm (able to discriminate meanders from eddies), that can be used for both model outputs and altimetry. The scheme was designed by combining the closed loop of SSH criteria and the Okubo-Weiss parameter, where the vorticity dominates the strain. The evaluation of the mixed scheme ("hybrid criteria") suggested that the hybrid scheme is more robust than the closed contours of SSH criteria and the Okubo-Weiss parameter used separately. Using this scheme we have investigated the eddy properties in the Mozambique Channel. The automatic eddy detection scheme was able to identify and track both cyclonic and anticyclonic eddies generated within the channel. The statistical census revealed that there have more cyclonic than anticyclonic eddies here found. Analysis of their size suggested that cyclonic eddies in the Mozambique Channel are relatively smaller compared to their anticyclonic counterpart. Cyclonic eddies appeared more ubiquitous than anticyclonic eddies. North to south investigation of the eddy properties with regard to their generation site have shown that larger anticyclonic eddies were preferencially formed in the northern part of the channel, near 12°S, 48°E, between Madagascar and the African continent. In the center of the channel, they appeared to be preferentially formed in the narrows of the channel, near 16°S, and at the eastern boundary of the central channel, near the Madagascar Bight, around 20°S, and 44°E. Anticyclonic eddy formation site also appeared outside of the channel (e.g. east of the Madagascar Ridge, and in the southern boundary, likely by the instabilities in the Agulhas Return Current). In the south of the channel, preferential eddy generation sites for cyclonic eddies were identified at the eastern boundary of the channel, adjacent to the southern tip of Madagascar, and at the Delagoa Bight (between 25°S and 27°S), near Maputo, at the south-east coast of Mozambique.

For both model and observation, we have identified 2 modes on the size distribution for the anticyclonic eddies in the central part of the channel. The first mode ranged within the first baroclinic Rossby radius of deformation of the region, centered around 70 km - 90 km radius, while the second mode was larger (beyond the first baroclinic Rossby radius of deformation), and was centered around 100 km - 140 km. Their frequency (5 - 6 anticyclonic eddies per year), observed in the second mode, was consistent with in-situ observations (De Ruijter et al., 2002, Ridderinkhof and De Ruijter, 2003, Schouten et al., 2003, Harlander et al., 2009), and other modelling studies (van der Werf et al., 2010). With regard to their trajectories, the eddies identified in our study appeared to propagate mostly in a south-westward direction, consistent with theories of non-linear turbulence (McWilliams and Flierl, 1979, Chelton et al., 2007). This knowledge allows us

to portray the flow field in the Mozambique Channel as presented in Figure 8.1.

Our analysis on the eddy polarity distribution with regard to their size (radius), has shown that the dominance of one eddy type over the other depends on the eddy-length scale at which the eddies are compared. The anticyclonic eddies have shown to be larger than the cyclones. However, both cyclonic and anticyclonic eddies decrease in size with their north to south propagation, and appear to follow the first baroclinic Rossby radius of deformation for the South-West Indian Ocean region (Chelton et al., 1998).

With regard to the eddy lifetime, the anticyclonic eddies have shown to last longer than cyclonic eddies, everywhere in the channel, and it seemed to be related to their larger size, higher amplitude and larger energy content.

Analysis on the temperature and salinity within a long-lived anticyclonic eddy that propagated throughout the length of the channel have shown that the eddy had trapped different water masses from different origins, such as IEW, TSW, STSW, SICW, AAIW, RSW and IDW. A T-S diagram has shown a less spreading of its properties, suggesting that the eddy had conserved its properties for a considerable time.

Investigations into the different energy conversion terms in order to evaluate the role of the eddy-mean flow interaction in the circulation of the Mozambique Channel, and the dignostic of the important eddy formation mechanisms, at the different subregions of the channel, have shown that in the northern Mozambique Channel, anticyclonic eddies were generated by barotropic instabilities of the SEC at the northern tip of Madagascar, in agreement with previous studies. However, the generated eddies appeared to release part of their kinetic energy in order to sustain a southward mean flow, at the north-western boundary of the Mozambique Channel, between 14°S and 12°S. To the south of 14°S, barotropic instabilities of the southward western boundary flow also played a role on the eddy formation in the narrows of the channel, over the Davies Ridge. On the other hand, baroclinic instabilities dominated over barotropic at localized sites: specially at 18°S, and 21°S - 22°S. To the south of the 22°S, barotropic instabilities dominated over baroclinic instabilities. In general, cyclonic eddies appeared to be associated with baroclinic instabilities, while the anticyclonic eddies appeared associated with barotropic instabilities.

Despite the localized dominance of baroclinic instabilities observed in the region, the overall dominant process in the whole channel domain is the barotropic instability.

The key scientific questions are addressed one by one in the following section:

Chapter-4

- **Does the SWIM model simulate satisfactorily the large and mesoscale oceanographic features of the Mozambique Channel?**

SWIM reproduces in a resonable manner the presence of the main water masses of the region, but fails to resolve accurately their mixing and spreading along the channel. It reproduces well the presence of the mean ocean currents of the region, but fails to reproduce accurately their intensity. Stronger deviations from observation is the reproduction of comparable eddy kinetic energy and SSH variability in the central part of the Mozambique Channel. However, despite the model difficulties, the overall evaluation suggest that SWIM can be used to study the large and mesoscale oceanographic processes of the region.

Chapter-6

- **Are there cyclonic eddies in the Mozambique Channel?**

Both SWIM and altimetry show that there are cyclonic eddies being generated within the Mozambique Channel. The statistical census suggest a greater abundance of cyclonic over anticyclonic eddies.

- **Why is the flow in the Mozambique Channel dominated by the anticyclonic eddies?**

Despite the statistical census suggesting that there are relatively more cyclonic than the anticyclonic eddies within the Mozambique Channel, the flow in this region is regarded as dominated by the anticyclonic eddies because the anticyclonic eddies are relatively larger, more energetic, and have a longer life-time when compared to the cyclonic eddies.

- **What are the physical characteristics of the Mozambique Channel eddies?**

For altimetry, both cyclonic (anticyclonic) eddies in the Mozambique Channel have shown the following mean characteristics: mean diameter over 139 (155) km, a mean amplitude of about 11 (13) cm, a mean life-time over 94 (100) days, and an annual frequency of about 19 (18), respectively. On the other hand for SWIM, the mean properties for

cyclonic (anticyclonic) eddies are: mean diameter of 135 (198) km, mean amplitude of about 8 (25) cm, a mean life-time over 58 (109) days, and an annual frequency of about 17 (13), respectively.

The cyclonic eddies are ubiquitous, while the anticyclonic eddies have a favorite site for their formation within the channel, and exhibit a bi-modal distribution of their size. They are highly energetic, propagate in a southwest direction, they reach the bottom of the channel, and appear to be strongly influenced by the Mozambican continental shelf.

- **How do the Mozambique Channel eddy properties vary meridionally throughout the channel?**

Both, model and altimetry show that from the north to the south, the Mozambique Channel eddies decrease in size, while increasing their mean amplitude (except for cyclonic eddies in SWIM). Similarly the annual frequency of the eddies increase from the north to the south of the channel. No consistent pattern between model and observation was found for the north to south variation of the mean life-time of the eddies. Consistent pattern between SWIM and altimetry with regard to the eddies energy, is that the anticyclonic eddies increase their energy from north to center, but decrease from the center to the south of the channel. Tracer distribution within the an anticyclonic eddy event has shown that the eddy conserved its water mass properties during the north to south propagation.

Chapter-7

- **What role the eddy-mean flow interaction plays on the circulation in the Mozambique Channel?**

The eddy-mean flow interaction in the Mozambique Channel generates large anticyclonic eddies in the northern sector of the channel. These anticyclonic eddies appear to release their kinetic energy which sustain a mean flow along the northwestern boundary of the channel. Such a mean flow undergoes through further instabilities generating anticyclonic eddies in the narrows of the channel. In the central Mozambique Channel the interaction eddy-mean flow reveals the dissipation of anticyclonic eddies, while favoring the formation of cyclonic eddies.

- **What dominant eddy formation mechanisms can be inferred at the different subregions of the channel?**

The diagnostics made suggest that despite the localized dominance of baroclinic instabilities observed in the region between 12°S to 14°S, the overall dominant process in the whole channel domain is the barotropic instability.

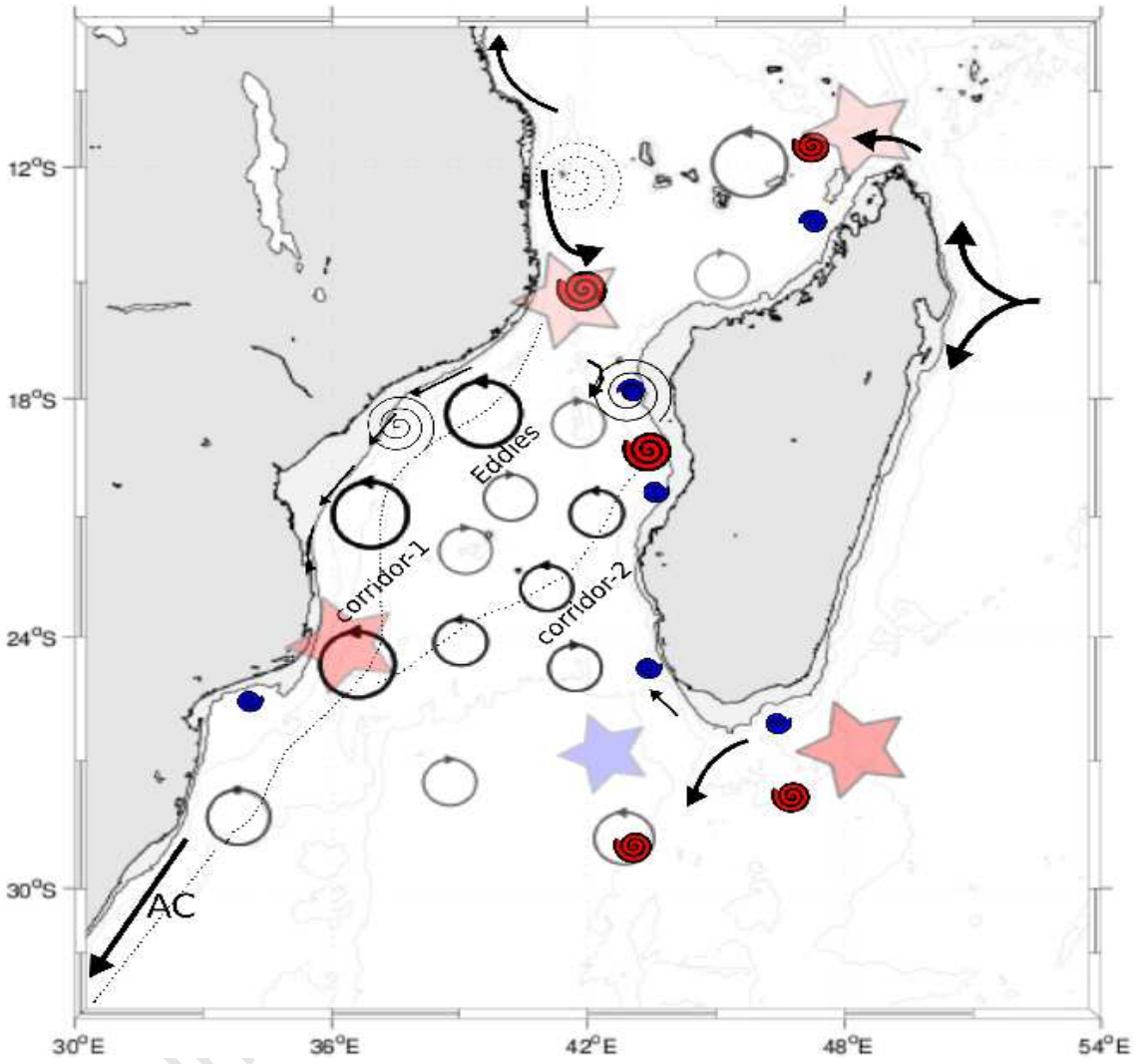

Figure 8.1. Schematic of the main findings of the study. Meaning of the symbols: Red stars: sites dominated by barotropic instabilities, blue starts: sites dominated by baroclinic instabilities, dotted spirals: site of energy conversion from eddy kinetic to mean kinetic energy, continuous spirals: sites of anticyclonic eddy dissipation, blue shaded spirals: generation sites of cyclonic eddies, and red shaded spirals: generation sites of anticyclonic eddies. Clockwise closed circles represent cyclonic eddies and anticlockwise closed circles is for anticyclonic eddies. The arrows indicate the direction of the flow. The dotted-lines indicate the eddy corridor (trajectories). The background contours indicate the ocean bathymetry. Shaded bathymetry is shallower than 200 m.

8.2 The way forward

The ROMS based configuration SWIM, designed to simulate the mesoscale ocean dynamics on the South-West Indian Ocean, appeared to reproduce resonably well the main oceanographic features of the greater Agulhas Current system. Despite its performance, one major constrain of the configuration is the production of higher levels of EKE and SSH variability in the Mozambique Channel (overestimation $\sim 50\%$). Therefore, to minimize this, SWIM requires further improvements. Likely a special treatment on the subgrid-scale representation of the flow viscosity which will enhance the dissipation will be necessary to achieve a more realistic simulation of the mesoscale eddy field of the region. Also a change of the surface forcings, from climatology to interannual, may be required to improve the model solution. Because SWIM is intended to be used to force small-scale, coastal model configurations in the Mozambique Channel, important to study the coupling between the physical dynamics and biological properties (which could ensure a better management of the marine ecosystems), study of shelf dynamics, e.g: Sofala-Bank, its improvement is urgent.

A robust automatic eddy detection scheme has been designed. It is important to use this scheme to explore other eddy properties that were not investigated in this study (such as the relation of the eddy-size with their life-time, propagation distance, amplitude, strength, etc) to make the description of the eddy field in the Mozambique Channel more detailed.

Despite the finding of this study that has brought a new knowledge of the system (e.g: favorite eddy formation sites, bi-modes of the anticyclonic eddies, local formation of cyclonic eddies in the channel and their properties, etc), several questions remain unanswered, such as, what drives the southward propagation of the Mozambique Channel eddies? What role the local topography plays on the formation of the Mozambique Channel eddies? What role the eddy shelf interactions play on the dynamics of the flow field? What is the role of the Mozambique Channel eddies on the biogeochemical cycle of nutrients in the Mozambique Channel? Will the different modes of the mesoscale anticyclonic eddies present in the Mozambique Channel affect differently the mesoscale structuring of pelagic ecosystem of the channel? A study in this direction is also important if a more detailed description of the flow field in the Mozambique Channel is required.

APPENDIX A

The Model Coordinates

A.1 The Vertical Sigma σ - coordinate system

The terrain-following (σ) - coordinate is suitable for representation of the shelf and bottom dynamics (e.g. bottom currents), as well as for the surface processes (e.g. mixed layer), provided a satisfactory stretching parameters: see (Song and Haidvogel, 1994). The system is obtained essentially by transforming the Cartesian z coordinate in a stretched vertical system ($\sigma = \frac{z-\zeta}{H+\zeta}$).

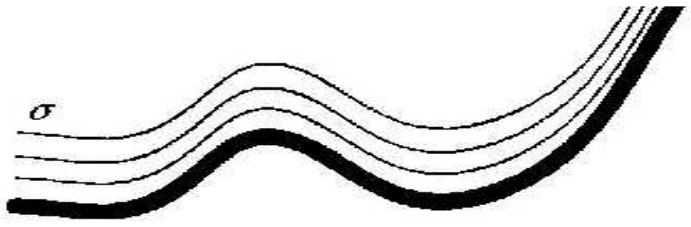

Figure A.1. An illustration of the vertical coordinate in a terrain-following system.

The coordinate transformation reads: $\hat{x} = x$, $\hat{y} = y$, and $\sigma = \sigma(x, y, z)$. It implies that $z = z(x, y, \sigma)$, and σ values ranges between -1 (at the bottom $z = -H(x, y)$) to 0 (at the top $z = \zeta(x, y)$). i.e. -1 $\leq \sigma \leq$ 0. The chain rule of the transformations has been presented by Hedström (2009), and is written as:

$$\left(\frac{\partial}{\partial x}\right)_z = \left(\frac{\partial}{\partial x}\right)_\sigma - \left(\frac{1}{H_z}\right)\left(\frac{\partial z}{\partial x}\right)_\sigma \left(\frac{\partial}{\partial \sigma}\right)$$

$$\left(\frac{\partial}{\partial y}\right)_z = \left(\frac{\partial}{\partial y}\right)_\sigma - \left(\frac{1}{H_z}\right)\left(\frac{\partial z}{\partial y}\right)_\sigma \left(\frac{\partial}{\partial \sigma}\right)$$

$$\frac{\partial}{\partial z} = \left(\frac{\partial s}{\partial z}\right)\frac{\partial}{\partial \sigma} = \frac{1}{H_z}\frac{\partial}{\partial \sigma}$$

where $H_z \equiv \frac{\partial z}{\partial \sigma}$

The dynamic equations written in this frame (σ-coordinate) takes the form:

$$\frac{\partial u}{\partial t} - fv + \vec{v}.\nabla u = -\frac{\partial \phi}{\partial x} - \left(\frac{g\rho}{\rho_o}\right)\frac{\partial z}{\partial x} - g\frac{\partial \zeta}{\partial x} + \frac{1}{H_z}\frac{\partial}{\partial \sigma}\left[\frac{K_v}{H_z}\frac{\partial u}{\partial \sigma}\right] + Fu + Du \qquad \text{(A.1)}$$

$$\frac{\partial v}{\partial t} - fu + \vec{v}.\nabla v = -\frac{\partial \phi}{\partial y} - \left(\frac{g\rho}{\rho_o}\right)\frac{\partial z}{\partial y} - g\frac{\partial \zeta}{\partial y} + \frac{1}{H_z}\frac{\partial}{\partial \sigma}\left[\frac{K_v}{H_z}\frac{\partial v}{\partial \sigma}\right] + Fv + Dv \qquad \text{(A.2)}$$

$$\frac{\partial T}{\partial t} + \vec{v}.\nabla T = \frac{1}{H_z}\frac{\partial}{\partial \sigma}\left[\frac{K_T}{H_z}\frac{\partial T}{\partial \sigma}\right] + F_T + D_T \qquad \text{(A.3)}$$

$$\frac{\partial S}{\partial t} + \vec{v}.\nabla S = \frac{1}{H_z}\frac{\partial}{\partial \sigma}\left[\frac{K_S}{H_z}\frac{\partial S}{\partial \sigma}\right] + F_S + D_S \qquad \text{(A.4)}$$

$$\rho = \rho\left(T, S, P\right) \tag{A.5}$$

$$\frac{\partial \phi}{\partial \sigma} = \left(\frac{-gH_z\rho}{\rho_o}\right) \tag{A.6}$$

$$\frac{\partial H_z}{\partial t} + \frac{\partial (H_z u)}{\partial x} + \frac{\partial (H_z v)}{\partial y} + \frac{\partial (H_z \Omega)}{\partial \sigma} = 0 \tag{A.7}$$

where $\vec{v} = (u, v, \Omega)$ and $\vec{v}.\nabla = u\frac{\partial}{\partial x} + v\frac{\partial}{\partial y} + \Omega\frac{\partial}{\partial \sigma}$
The vertical velocity in this frame is expressed as:

$$\Omega(x, y, \sigma, t) = \frac{1}{H_z}\left[\omega - \left(\frac{z+h}{\zeta+h}\right)\frac{\partial \zeta}{\partial t} - u\frac{\partial z}{\partial x} - v\frac{\partial z}{\partial y}\right] \tag{A.8}$$

where

$$\omega = \frac{\partial z}{\partial t} + u\frac{\partial z}{\partial x} + v\frac{\partial z}{\partial y} + \Omega H_z \tag{A.9}$$

In this coordinate the equations (A.1) and (A.2) express the horizontal momentum balance. (A.3) and (A.4) are the advection-diffusion equation for the tracer T and S respectively. The equation (A.5) is the seawater equation of state, and the equation (A.6) is the hydrostatic balance. The continuity equation is expressed by the equation (A.7). The vertical boundary conditions are expressed:

- **at the sea surface:** $\sigma = 0$

$$\left(\frac{K_v}{H_z}\right)\frac{\partial u}{\partial \sigma} = \tau_s^x(x,y,t) \tag{A.10}$$

$$\left(\frac{K_v}{H_z}\right)\frac{\partial v}{\partial \sigma} = \tau_s^y(x,y,t) \tag{A.11}$$

$$\left(\frac{K_T}{H_z}\right)\frac{\partial T}{\partial \sigma} = \frac{Q_T}{\rho_o c_P} \tag{A.12}$$

$$\left(\frac{K_S}{H_z}\right)\frac{\partial S}{\partial \sigma} = \frac{Q_S}{\rho_o c_P} \tag{A.13}$$

$$\Omega = 0 \tag{A.14}$$

- **at the seafloor:** $\sigma = -1$

$$\left(\frac{K_v}{H_z}\right)\frac{\partial u}{\partial \sigma} = \tau_b^x(x,y,t) \tag{A.15}$$

$$\left(\frac{K_v}{H_z}\right)\frac{\partial v}{\partial \sigma} = \tau_b^y(x,y,t) \tag{A.16}$$

$$\left(\frac{K_T}{H_z}\right)\frac{\partial T}{\partial \sigma} = 0 \tag{A.17}$$

$$\left(\frac{K_S}{H_z}\right)\frac{\partial S}{\partial \sigma} = 0 \tag{A.18}$$

$$\Omega = 0 \tag{A.19}$$

A.2 The Orthogonal-Curvilinear coordinate system

Orthogonal-Curvilinear coordinates under a laterally varying grid is used in ROMS to resolve accurately coastal ocean processes (e.g. boundary currents) over an irregular coastlines. Their velocities u, v are expressed as:

$$\vec{v}.\hat{\xi} = u \tag{A.20}$$

and

$$\vec{v}.\hat{\eta} = v \tag{A.21}$$

Both ξ and η are funtions of x and y: $\xi(x, y)$ and $\eta(x, y)$. ξ and η are a set of horizontal orthogonal coordinates (Figure A.2). The dependency of the differential distance and the lenght of the curve is written as:

$$(ds)_\xi = (\frac{1}{m})d\xi \tag{A.22}$$

$$(ds)_\eta = (\frac{1}{n})d\eta \tag{A.23}$$

$\hat{\xi}, \hat{\eta}$ - is the vectorial notation of ξ and η. $m(\xi, \eta)$ and $n(\xi, \eta)$ - are the scalar factors which relate the differential distances ($\Delta\xi$, $\Delta\eta$) to the actual arc lengths (for details see

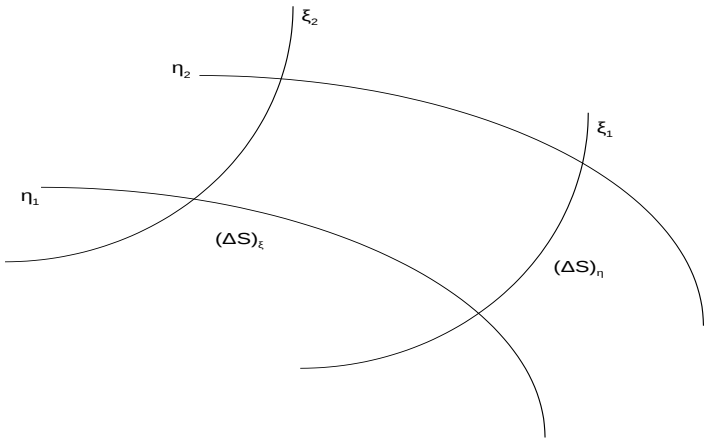

Figure A.2. An illustration of the Orthogonal-Curvilinear coordinate system.

Hedström (2009).

Expressing the dynamic equations in Orthogonal-Curvilinear coordinate (Arakawa and Lamb, 1977) takes the form:

$$\frac{\partial}{\partial t}\left(\frac{H_z u}{mn}\right)+\frac{\partial}{\partial \xi}\left(\frac{H_z u^2}{n}\right)+\frac{\partial}{\partial \eta}\left(\frac{H_z uv}{m}\right)+\frac{\partial}{\partial \sigma}\left(\frac{H_z u\Omega}{mn}\right) \tag{A.24}$$
$$-\left\{\left(\frac{f}{mn}\right)+v\frac{\partial}{\partial \xi}\left(\frac{1}{n}\right)-u\frac{\partial}{\partial \eta}\left(\frac{1}{m}\right)\right\}H_z v=$$
$$-\left(\frac{H_z}{n}\right)\left(\frac{\partial \phi}{\partial \xi}+\frac{g\rho}{\rho_o}\frac{\partial z}{\partial \xi}+g\frac{\partial \zeta}{\partial \xi}\right)+\frac{1}{mn}\frac{\partial}{\partial \sigma}\left[\frac{K_v}{H_z}\frac{\partial u}{\partial \sigma}\right]+\frac{H_z}{mn}\left(F_u+D_u\right)$$

$$\frac{\partial}{\partial t}\left(\frac{H_z v}{mn}\right)+\frac{\partial}{\partial \xi}\left(\frac{H_z uv}{n}\right)+\frac{\partial}{\partial \eta}\left(\frac{H_z v^2}{m}\right)+\frac{\partial}{\partial \sigma}\left(\frac{H_z v\Omega}{mn}\right) \tag{A.25}$$
$$+\left\{\left(\frac{f}{mn}\right)+v\frac{\partial}{\partial \xi}\left(\frac{1}{n}\right)-u\frac{\partial}{\partial \eta}\left(\frac{1}{m}\right)\right\}H_z u=$$
$$-\left(\frac{H_z}{m}\right)\left(\frac{\partial \phi}{\partial \eta}+\frac{g\rho}{\rho_o}\frac{\partial z}{\partial \eta}+g\frac{\partial \zeta}{\partial \eta}\right)+\frac{1}{mn}\frac{\partial}{\partial \sigma}\left[\frac{K_v}{H_z}\frac{\partial v}{\partial \sigma}\right]+\frac{H_z}{mn}\left(F_v+D_v\right)$$

$$\frac{\partial}{\partial t}\left(\frac{H_z T}{mn}\right)+\frac{\partial}{\partial \xi}\left(\frac{H_z u T}{n}\right)+\frac{\partial}{\partial \eta}\left(\frac{H_z v T}{m}\right)+\frac{\partial}{\partial \sigma}\left(\frac{H_z \Omega T}{mn}\right)= \frac{1}{mn}\frac{\partial}{\partial s}\left[\frac{K_T}{H_z}\frac{\partial T}{\partial \sigma}\right]+\frac{H_z}{mn}\left(F_T+D_T\right) \tag{A.26}$$

$$\frac{\partial}{\partial t}\left(\frac{H_z S}{mn}\right)+\frac{\partial}{\partial \xi}\left(\frac{H_z u S}{n}\right)+\frac{\partial}{\partial \eta}\left(\frac{H_z v S}{m}\right)+\frac{\partial}{\partial \sigma}\left(\frac{H_z \Omega S}{mn}\right)= \frac{1}{mn}\frac{\partial}{\partial s}\left[\frac{K_S}{H_z}\frac{\partial S}{\partial \sigma}\right]+\frac{H_z}{mn}\left(F_S+D_S\right) \tag{A.27}$$

$$\rho=\rho\left(T,S,P\right) \tag{A.28}$$

$$\frac{\partial \phi}{\partial \sigma}=-\left(\frac{gH_z\rho}{\rho_o}\right) \tag{A.29}$$

$$\frac{\partial}{\partial t}\left(\frac{H_z}{mn}\right)+\frac{\partial}{\partial \xi}\left(\frac{H_z u}{n}\right)+\frac{\partial}{\partial \eta}\left(\frac{H_z v}{m}\right)+\frac{\partial}{\partial \sigma}\left(\frac{H_z \Omega}{mn}\right)=0 \tag{A.30}$$

All the boundary conditions remains unchanged (Hedström, 2009).

The equations (A.24) and (A.25) express the horizontal momentum balance in ξ and η directions respectively. (A.26) and (A.27) are the advection-diffusion equation for the tracer T and S respectively. The equation (A.28) is the seawater equation of state, and the equation (A.29) is the hydrostatic balance. The continuity equation is expressed by the equation (A.30).

Bibliography

Antonov, J. I., Levitus, S., Boyer, T. P., Conkright, M. E., O'Brien, T., Stephens, C., Trotsenko, B., 1988. :World Ocean Atlas 1998, Vol. 3, Temperature of the Indian Ocean. NOAA Atlas NESDIS 29. Tech. rep., U. S. Gov, Printing Officce, Washington, DC.

Arakawa, A., Lamb, V. R., 1977. :Computational design of the basic dynamical processes of the UCLA general circulation model. In: Methods in Computational Physics. Journ. Comput. Phys 17, 173–265.

AVISO, 2008. :SSALTO DUACS User Handbook. (M)SLA and (M)ADT Near-Real Time and Delayed Time Products. Ssalto. Duacs 1.9.

Azevedo, J. L. L., de Oliveira., L. R., de Sousa., J. F. A., Soares., I. D., Mata, M. M., 2008. :Os Processos de Conversao de Energias nos Oceanos, uma Revisao do Diagrama de Lorenz. Rev. Brasileira. Geophys. 26, 153–172.

Backeberg, B. C., 2010. :Modelling the mesoscale variability in the greater Agulhas Current System using a Hybrid Coordinate Ocean Model. Ph.D. thesis, University of Cape Town.

Backeberg, B. C., Bertino, L., Johannessen, J. A., 2009. :Evaluating two numerical advection schemes in HYCOM for eddy-resolving modelling of the Agulhas Current 5, 173–190.

Backeberg, B. C., Reason, C., 2010. :A connection between the South Equatorial Current north of Madagascar and Mozambique Channel. Geophys. Res. Lett 37, L04604, doi:10.1029/2009GL041950.

Barnier, B., Siedfridt, L., Marchesiello, P., 1995. :Thermal forcing for a global ocean circulation model using a three-year climatology of ECMWF analyses. Journ. Mar. Syst 6, 363–380.

Beal, L. M., De Ruijter., W. P. M., Biastoch., A., Zahn., R., 136, S. W. G., 2011. :On the role of the Agulhas System in ocean circulation and climate. Rev. Nature. 472, 429–436.

Beal, M. L., Bryden, H. L., 1997. :Observations of an Agulbas Undercurrent. Deep Sea Res., Part I 41, 1715–1724.

Beal, M. L., Bryden, H. L., 1999. :The velocity and vorticity structure of the Agulhas Current at 32^circS. Journ. Geophys. Res 104, 5151 – 5171.

Beal, M. L., Chereskin, T. K., Lenn, Y. D., Elipot, S., 2006. :The Sources and Mixing Characteristics of the Agulhas Current. Journ. Phys. Oceanogr 36, 2060–2074.

Beal, M. L., Ffield, A., Gordon, A. L., 2000. :Spreading of the Red Sea Overflow waters in the Indian Ocean. Journ. Geophys. Res 105, 8549 – 8564.

Beckmann, A., Haidvogel, D. B., 1993. :Numerical simulation of flow around a tall isolated seamount. part I: Problem formulation and model accuracy. Journ. Phys. Oceanogr 23, 1736–1753.

Biastoch, A., Böning, C. W., Lutjeharms, J. R. E., 2008a. :Agulhas leakage dynamics affects decadal variability in Atlantic overturning circulation. Nature 456, 489–492.

Biastoch, A., Böning, C. W., Schwarzkopf, F. U., Lutjeharms, J. R. E., 2009. :Increase in Agulhas leakage due to poleward shift of Southern Hemisphere westerlies. Nature 462, 495–498, doi:10.1038.

Biastoch, A., Krauss, W., 1999. :The role of mesoscale eddies in the source regions of the Agulhas Current. Journ. Phys. Oceanogr 29, 2303–2317.

Biastoch, A., Lutjeharms, J. R. E., Böning, C. W., Scheinert, M., 2008b. :Mesoscale perturbations control inter-ocean exchange south of Africa. Geophys. Res. Lett 35, doi:10.1029/2008GL035132.

Blaas, M., Dong, C., Marchesiello, P., McWilliams, J. C., Stolzenbach, K. D., 2007. :Sediment-transport modeling on Southern Californian shelves: A ROMS case study. Cont. Shelf Res 27, 832–853.

Boyer, T. P., Levitus, S., Antonov, J. I., Conkright, M. E., O'Brien, T., Stephens, C., Trotsenko, B., 1988. :World Ocean Atlas 1998, Vol. 6, Salinity of the Indian Ocean. NOAA Atlas NESDIS 32. Tech. rep., U. S. Gov, Printing Officce, Washington, DC.

Casal, T. G. D., Beal, L. M., Lumpkin, R., Johns, W. E., 2009. :Structure and downstream evolution of the Agulhas Current system during a quasi-synoptic survey in February-March 2003. Journ. Geophys. Res 114, C03001, doi:10.1029/2008JC004954.

Casey, K. S., Cornillon, P., 1999. :A comparison of satellite and in situ based sea surface temperature climatologies. Journ. Clim. 12, 1848–1863.

Chaigneau, A., Gizolme, A., Grados, C., 2008. :Mesoscale eddies off Peru in altimeter records: Identification algorithms and eddy spatio-temporal patterns. Prog. Oceanog. 79, 106–119.

Chakraborty, P., Balachandar, S., Adrian, R. J., 2005. :On the relationships between local vortex identification schemes. Journ. Fluid. Mech 535, 189 – 214.

Chapman, P., DiMarco, S. F., Davis, R. E., Coward, A. C., 2003. :Flow at intermediate depths around Madagascar based on ALACE float trajectories. Deep Sea Res., Part II 50, 1957 – 1986.

Chauris, H., Karoui, I., Garreau, P., Wackernagel, H., Craneguy, P., Bertino, L., 2011. :The circlet transform: A robust tool for detecting features with circular shapes. Comput. Geosc. 37, 331–342.

Chelton, D. B., deSzoeke, R. A., Schlax, M. G., Naggar, K. E., Siwertz, N., 1998. :Geographical variability of the first-baroclinic Rossby radius of deformation. Journ. Phys. Oceanogr 28, 433–460.

Chelton, D. B., Schlax, M. G., Samelson, R. M., 2011. :Global observations of nonlinear mesoscale eddies. Prog. Oceanog. 91, 167–216.

Chelton, D. B., Schlax, M. G., Samelson, R. M., Szoeke, R. A., 2007. :Global Observations of large oceanic eddies. Geophys. Res. Lett 34, L15606, doi:10.1029/2007GL030812.

Conkright, M. E., Locarnini, R. A., Garcia, H. E., O'Brien, T. D., Boyer, T. P., Stephens, C., Antonov, J. I., 2002. :World Ocean Atlas 2001: Objective analyses, data statistics, and figures, CD-ROM documentation. Tech. rep., National Oceanographic Data Center, Silver Spring, MD.

Cronin, M., Watts, D. R., 1996. :Eddy-Mean Flow Interaction in the Gulf Stream at 68°W. Part 1: Eddy Energetics. Journ. Phys. Oceanogr 26, 2107–2131.

Cushman-Roisin, B., Beckers, J.-M., 2009. :Introduction to Geophysical Fluid Dynamics. Physical and Numerical Aspects. Academic Press, Thayer School of Engineering Dartmouth College Hanover, New Hampshire 03755, USA, 777pp.

Da Silva, A. M., Young, C. C., Levitus, S., 1994. :Atlas of surface Marine data 1994, Vol. 1, algorithms and procedures. Tech. rep., U. S. Department of Commerce, NOAA.

De Ruijter, W. P. M., Brummer, G. J. A., Drijfhout, S. S., Lutjeharms, J. R. E., Peeters, F., Ridderinkhof, H., van Aken, H., van LeeuwenSchouten, P. J., 2006. :Observations of the Inter-Ocean Exchange Around South Africa. Eos Trans. AGU 87, 97–101.

De Ruijter, W. P. M., Ridderinkhof, H., Lutjeharms, J. R. E., Schouten, M. W., Veth, C., 2002. :Observations of the flow in the Mozambique Channel. Geophys. Res. Lett 29, 1401–1403.

De Ruijter, W. P. M., Ridderinkhof, H., Schouten, M. W., 2005. :Variability of the southwest Indian Ocean. Philos. Trans. R. Soc. London A 363, 63–76, doi:10.1098/rsta.2004.1478.

De Ruijter, W. P. M., van Aken, H. M., Beier, E. J., Lutjeharms, J. R. E., Matano, R. P., Schouten, M. W., 2004. :Eddies and dipoles around South Madagascar: formation, pathways and large-scale impact. Deep Sea Res., Part I 51, 383–400.

De Ruijter, W. P. M., van Leeuwen, P. J., Lutjeharms, J. R. E., 1999. :Generation and evolution of Natal Pulses: solitary meanders in the Agulhas Current. Journ. Phys. Oceanogr 29, 3043–3055.

Debreu, L., Blayo, E., 2008. :Agrif: Adaptive grid refinement in fortran. Comput. Geosc. 34, 8–13.

Debreu, L., Marchesiello, P., Penven, P., Cambon, G., 2012. :Two-Way nesting in split-explicit ocean models: Algorithms, implementation and validation. Ocean Modelling 49-50, 1–21.

Defant, A., 1961. :Physical Oceanography. Pergamon Press, New York, Oxford, London., Paris, 626pp.

Dewar, W. K., Bane, J. M., 1985. :Sub-surface Energetics of the Gulf-Stream near the Charleston Bump. Journ. Phys. Oceanogr 15, 1771–1789.

DiMarco, S. F., Chapman, P., Jr, W. D. N., Donohue, K., Luther, M., Johnson, G. C., Toole, J., 2002. :Volume transport and property distribution of the Mozambique Channel. Deep Sea Res., Part II 49, 1481–1511.

Domopoulos, A. W. J., Smith, C. R., Tyler, P. A., 2003. :Ecology of the deep Indian Ocean floor. In: Elsevier (Ed.), Ecosystems of the World. Vol. 28. Chapman and Hall Ltd., Amsterdam, p. 569.

Donguy, J.-R., Piton, B., 1991. :The Mozambique Channel Revisited. Oceanol. Acta 14, 549–558.

Donohue, K. A., Toole, J. M., 2003. :A near synoptic survey of the SouthWest Indian Ocean. Deep Sea Res., Part II 50, 1893–1931.

Ducet, N., Le Traon, P. Y., Reverdin, G., 2000. :Global high-resolution mapping of ocean circulation from TOPEX/Poseidon and ERS-1 and -2. Journ. Geophys. Res 105, 19,477–19,498.

Eden, C., 2007. :Eddy length scales in the North Atlantic Ocean. Journ. Geophys. Res 112, C06004.

Emery, W. J., 2001. :Water Types and Water Masses. Academic Press, 3179–3187Doi:10.1006/rwos.2001.0108.

Fine, R. A., 1993. :Circulation of Antartic Intermediate Waters in the South Indian Ocean. Deep Sea Res., Part I 40, 2021 – 2042.

Goni, G., DeMaria, M., Knaff, J., Sampson, C., I. Ginis, F. B., Mavume, A., Lauer, C., Lin, I. I., Ali, M. M., Sandery, P., Ramos-Bauarque, S., Kang, K., Mehra, A., Chassignet, E., Halliwell, G., 2009. :Ocean Measurements to Tropical Cyclone Intensity Forecasting. Ocean. Society 22.No.3, 190–197.

Gordon, A. L., 1986. :Interocean exchange of Thermocline Water. Journ. Geophys. Res 91.NO.C4, 5037–5046.

Gordon, A. L., Lutjeharms, J. R. E., Gründlingh, M. L., 1987. :Stratification and circulation at the Agulhas Retroflection. Deep Sea Res. 34.NO.4, 565–599.

Gordon, A. L., Ma., S., Olson, D. B., Hacker, P., Ffield, A., Talley, L. D., Wilson, D., Baringer, M., 1997. : Advection and Diffusion of Indonesian throughflow water within the Indian Ocean South Equatorial Current. Geophys. Res. Lett 24, 2573–2576.

Gordon, A. L., McClean, J. L., 1999. :Thermocline stratification of the Indonesian Seas - Models and Observations. Journ. Phys. Oceanogr 29, 198 – 216.

Gruber, N., Frenzel, H., Doney, S. C., Marchesiello, P., McWilliams, J. C., Moisan, J. R., Oram, J. J., Plattner, G. K., Stolzenbach, K. D., 2006. :Eddy-resolving simulation of plankton ecosystem dynamics in the California Current System. Deep Sea Res., Part I 53, 1483–1516.

Gründlingh, M. L., 1978. :Drift of a satellite tracked buoy in the Southern Agulhas Current and Agulhas Return Current. Deep Sea Res. 25, 1209–1224.

Gründlingh, M. L., 1980. :On the volume transport of the Agulhas Current. Deep Sea Res. 27, 557 – 563.

Gründlingh, M. L., 1985. :Occurrence of the Red Sea Water in the Southwest Indian Ocean, 1981. Amer. Meteor. Soc. 15, 207–212.

Gründlingh, M. L., 1993. :On the winter flow in the southern Mozambique Channel. Deep Sea Res., Part I 40, 409 – 418.

Gründlingh, M. L., 1995. :Tracking eddies in the southeast Atlantic and southwest Indian Oceans with TOPEX-POSEIDON. Journ. Geophys. Res 100. NoC12, 24,977–24,986.

Gupta, A. S., England, M. H., 2007. :Evaluation of Interior Circulation in a High-Resolution Global Ocean Model. Part II: Southern Hemisphere Intermediate, Mode, and Thermocline Waters. Journ. Phys. Oceanogr 37, 2612–2636.

Halo, I., Backeberg, B., Penven, P., Ansorge, I., Reason, C., Ullgren, J. E., 2012. :Eddy Properties in the Mozambique Channel: A comparison between Observations and two Numerical Ocean Circulation Models. Deep Sea Res., Part II *submitted*.

Harlander, U., Ridderinkhof, H., Schouten, M. W., De Ruijter, W. P. M., 2009. :Long-term observation of transport, eddies, and Rossby waves in the Mozambique Channel. Journ. Geophys. Res 114, c02003.

Hedström, K. S., 1997. :User's Manual for an S-Coordinate Primitive Equation Ocean Circulation Model (SCRUM) Version 3.0. Tech. rep., Institute of Marine and Coastal Sciences, Rutgers University, USA.

Hedström, K. S., 2009. :DRAFT Technical Manual for a Coupled Sea-Ice/Ocean Circulation Model . Tech. rep.

Hoguane, A., 2007. :Perfil Diagnostico da Zona Costeira de Mozambique. Gestao. Costeira 7, 69–82.

IHO, 1953. :limits of the Oceans and Seas. Tech. rep., Internation Hydrographic Organization, Imp, Monte Carlo.

Isern-Fontanet, J., Garcia-Ladona., E., Font, J., 2006. :Vortices of the Mediterranean Sea: An Altimetric Perspective. Journ. Phys. Oceanogr 36, 87–103.

Jackett, D. R., MacDougall, T. J., 1995. :Stabilization of hydrographic data. Journ. Atmos. Ocean 12, 381–389.

Jackett, D. R., MacDougall, T. J., 1997. :A Neutral Density Variable for the World's Oceans. Amer. Meteor. Soc. 27, 237–263.

Jeong, J., Hussian, F., 1995. :On the identification of a vortex. Journ. Fluid. Mech 285, 69 – 94.

Krauss, W., Döscher, R., Lehmann, A., Viehoff, T., 1990. :On eddy scales in the eastern and northern North Atlantic Ocean as a function of latitude. Journ. Geophys. Res 23, 2729–2732.

Kundu, P. K., 1990. :Fluid Mechanics. Vol. 1. acp.

Kurian, J., Colas., F., Capet., X., McWilliams., J. C., Chelton, D. B., 2011. :Eddy properties in the California Current System. Journ. Geophys. Res 116, C08027, doi:10.1029/2010JC006895.

Lamont, T., Roberts, M. J., Barlow, R. G., Morris, T., vander Berg, M. A., 2010. :Circulation patterns in the Delagoa Bight, Mozambique, and the influence of deep ocean eddies 32, 553–562.

Large, W. G., McWilliams, J. C., Doney, S. C., 1994. :Oceanic vertical mixing: a review and a model with a nonlocal boundary layer parameterization 32, 363–403.

Lathuiliere, C., Levy, M., Echevin, V., 2011. :Impact of eddy-driven vertical fluxes on phytoplankton abundance in the euphotic layer. Journ. Plankton. Res 33, 827–831.

Levitus, S., Boyer, T. P., 1994b. :World Ocean Atlas 1994, Vol. 4, Temperature. Tech. rep., NOAA Atlas NESDIS 4, U. S. Gov, Printing Office, Wash, D.C.

Levitus, S., Burger, R., Boyer, T. P., 1994. :World Ocean Atlas 1994, Vol. 3, Salinity. Tech. rep., NOAA Atlas NESDIS 3, U. S. Gov, Printing Office, Wash, D.C.

Lutjeharms, J., 2006. :The Agulhas Current. Springer-Verlag, Berlin Heidelberg, New York.

Lutjeharms, J. R. E., 2007. :Three decades of research on the greater Agulhas Current. Ocean. Sci 3, 129–147.

Lutjeharms, J. R. E., Ansorge, I., 2001. :The Agulhas Return Current. Journ. Mar. Syst 30, 115–138.

Lutjeharms, J. R. E., Bang, N. D., Duncan, C. P., 1981. :Characteristics of the currents east and south of Madagascar. Deep Sea Res. 28, 879–899.

Lutjeharms, J. R. E., Boebel, O., P. C. F. van der Vaart, W. P. M. De Ruijter, T. H. R. H. L. B., 2001. :Evidence that the Natal Pulse controls the Agulhas Current over its full depth. Geophys. Res. Lett 28, 3449–3452.

Lutjeharms, J. R. E., da Silva, A. J., 1988. :The Delagoa Bight eddy. Deep Sea Res. 35, 619–634.

Lutjeharms, J. R. E., Machu, E., 2000. :An upwelling cell inshore of the East Madagascar Current. Deep Sea Res., Part I 47, 2405–2411.

Lutjeharms, J. R. E., Roberts, H. R., 1988a. :The Natal Pulse; an extreme transient on the Agulhas Current. Journ. Geophys. Res 93, 631–645.

Lutjeharms, J. R. E., van Ballegooyen, R. C., 1988b. :The retroflection of the Agulhas Current. Journ. Phys. Oceanogr 18, 1570–1583.

Marchesiello, P., Debreu, L., Couvelard, X., 2009. :Spurious diapycnal mixing in terrain-following coordinate models: The problem and solution 26, 156–169.

Marchesiello, P., McWilliams, J. C., Shchepetkin, A., 2001. :Open boundary condition for long-term integration of regional oceanic models 3, 1–21.

Marchesiello, P., McWilliams, J. C., Shchepetkin, A., 2003. :Equilibrium structure and dynamics of the California Current System. Journ. Phys. Oceanogr 33, 753–783.

McCarthy, M. S., 1977. :Subantartic Mode Water. In: Angel, M. (Ed.), A voyage of Discovery, George Deacon 70^{th}, Anniversary Volume . Pergamon. 8, 103 – 119.

McWilliams, J. C., 1984. :The emergence of isolated coherent vortices in turbulent flow. Journ. Fluid. Mech 146, 21–43.

McWilliams, J. C., Flierl, G. R., 1979. :On evolution of isolated non-linear vortices. Dynamics of Atmospheres and Oceans 5, 43–66.

Miller, J. L., Lee, T. N., 1995. :Gulf Stream Meanders in the South-Atlantic Bight. Part I - Scalling and Energetics. Journ. Geophys. Res 100, 6687–6704.

Morrow, R., Birol, F., Griffin, D., Sudre, J., 2004. :Divergent pathways of cyclonic and anticyclonic eddies. Geophys. Res. Lett 31, L24311.

Nairn, A. M., Stehli, F., 1982. :The Ocean Basins and Margins: Volume 6 The Indian Ocean. Plenum Press., New York.

Nauw, J. J., van Aken, H. M., Webb, A., Lutjeharms, J. R. E., de Ruijter, W. P. M., 2008. :Observations of the southern East Madagascar Current and Undercurrent and Countercurrent system. Journ. Geophys. Res 113, C08006, doi:10.1029/2007JC004639.

Nencioli, F., Dong, C., Dickey, T., Washburn, L., McWilliams, J. C., 2010. :A Vector Geometry Based Eddy Detection Algorithm and Its Application to a High-Resolution Numerical Model Product and High-Frequency Radar Surface Velocities in the Southern California Bight. Journ. Atm. Ocean. Tech 27, 564–579.

New, A. L., S. G. Alderson, D. A. S., Stansfield, K. L., 2007. :On the circulation of water masses across the Mascarene Plateau in the South Indian Ocean. Deep Sea Res., Part I 54, 42–74, doi:10.1016/j.dsr.2006.08.016.

Okubo, W., 1970. :Horizontal dispersion of floatable particles in the vicinity of velocity singularities such as convergencies. Deep Sea Res. 17, 445–454.

Olson, D., Evans, R. H., 1986. :Rings of the Agulhas Current. Deep Sea Res. 33, 27–42.

Olson, D., Fine, R., Gordon, A., 1992. :Convective modifications of water masses in the Agulhas. Deep Sea Res. 39, 163–181.

Omta, A. W., J, L., Garcon, V., Kooijman, S. A. L. M., Dijkstra, H. A., 2009. :The interpretation of satellite chlorophyll observations: The case of the Mozambique Channel. Deep Sea Res., Part I 56, 974–988, doi:10.1016/j.dsr.2009.01.011.

Palastanga, V., van Leeuwen, P. J., de Ruijter, W. P. M., 2006. :A link between low-frequency mesoscale eddy variability around Madagascar and the large-scale Indian Ocean variability. Journ. Geophys. Res 111, C09029.

Palastanga, V., van Leeuwen, P. J., Schouten, M. W., de Ruijter, W. P. M., 2007. :Flow structure and variability in the subtropical Indian Ocean. Journ. Geophys. Res 112, C01001.

Penven, P., Chang, N., Shillington, F., April 2-7 2006. :Modelling the Agulhas Current using SAfE (Southern Africa Experiment). In: Proc. EGU General Assembly, Vienna, Austria.

Penven, P., Échevin, V., Pasapera, J., Colas, F., Tam, J., 2005. :Average circulation, seasonal cycle, and mesoscale dynamics of the Peru Current System: A modeling approach. Journ. Geophys. Res 110, C10021, doi:10.1029/2005JC00294.

Penven, P., Lutjeharms, J. R. E., Florenchie, P., 2006c. :Madagascar: a pacemaker for the Agulhas Current system? Geophys. Res. Lett 33, L17609, doi:10.1029/2006GL026854.

Penven, P., Marchesiello, P., Debreu, L., Lefèvre, J., 2008. :Software tools for pre- and post-processing of oceanic regional simulations. Env. Model. Soft 23, 660–662, doi:10.1016/j.envsoft.2007.07.004.

Piton, B., Pointeau, J. H., Ngoumbi, J. S., 1981. :Atlas hydrologique du Canal de Mozambique (Ocean Indien). Trav. Doc. ORSTOM 132, 41pp.

Plattner, G. K., Gruber, N., Frenzel, H., McWilliams, J. C., 2005. :Decoupling marine export production from new production. Geophys. Res. Lett 32, L11612, doi:10.1029/2005GL022660.

Portela, L. M., 1997. :Identification and Characterization of Vortices in the Turbulent Boundary Layer. Ph.D. thesis, Stanford University, School of Mechanical Engineering.

Provenzale, A., 1999. :Transport by Coherent Barotropic Vortices. Annu. Rev. Fluid. Mech 31, 55–93.

Quadfazel, D. R., Swallow, J. C., 1986. :Evidence for 50 day period planetary waves in the South Equatorial Current of the Indian Ocean. Deep Sea Res. 33, 1307–1312.

Quadfazel, D. R., Swallow, J. C., 1996. :The circulation of the South Equatorial Current in the eastern Indian Ocean. Journ. Geophys. Res 101, 12.483–12.488.

Quartly, G. D., Buck, J. J. H., Srokosz, M. A., Coward, A. C., 2006. :Eddies around Madagascar - The Retroflection re-considered. Journ. Mar. Syst 63, 115–129, doi:10.1016/j.jmarsys.2006.06.001.

Quartly, G. D., Srokosz, M. A., 2002. :SST Observations of the Agulhas and East Madagascar Retroflections by TRMM Microwave Imager. Journ. Phys. Oceanogr.

Quartly, G. D., Srokosz, M. A., 2004. :Eddies in the southern Mozambique Channel. Deep Sea Res., Part II 51, 69–83.

Reason, C. J. C., Lutjeharms, J. R. E., Hermes, J., Biastoch, A., Roman, R. E., 2003. :Inter-ocean fluxes south of Africa in an eddy-permitting model. Deep Sea Res., Part II 50, 281 – 298.

Rhines, P. B., 1975. :Waves and turbulence on a β plane. Journ. Fluid. Mech 69, 417–443.

Ridderinkhof, H., De Ruijter, W. P. M., 2003. :Moored Current Observations in the Mozambique Channel. Deep Sea Res., Part II 50, 1933–1955.

Ridderinkhof, H., Lutjeharms., J. R. E., de Ruijter, W. P. M., 2001. :A research cruise to investigate the Mozambique Current. S. Afr. J. Sci 27, 461–464.

Ridderinkhof, H., van der Werf, P. M., Ullgren, J. E., van Aken, H. M., van Leeuwen, P. J., De Ruijter, W. P. M., 2010. :Seasonal and interannual variability in the Mozambique Channel from moored current observations. Journ. Geophys. Res 115, C06010.

Ridgway, K. R., Dunn, J. R., Wilkin, J. L., 2002. :Ocean Interpolation by four-dimensional least squares -Application to the waters around Australia. Journ. Atm. Ocean. Tech 19, 1357–1375.

Rio, M.-H., Guinehut, S., Larnicol, G., 2011. :The new CNS-CLS09 global mean dynamic topography computed from the combination of GRACE data, altimetry and in-situ measurements. Journ. Geophys. Res 116, C07018.

Rio, M.-H., Hernandez, F., 2004. :A mean dynamic topography computed over the world ocean from altimetry, in situ measurements, and a geoid model. Journ. Geophys. Res 109, C12032, doi:10.1029/2003JC002226.

Robinson, A. R., 1983. :Eddies in Marine Science. Springer-Verlag, Berlin Heidelberg, New Tork, Tokyo.

Roman, R., Lutjeharms, J. R. E., 2009. :Red Sea Intermediate Water in the source regions of the Agulhas Current. Deep Sea Res., Part I 56(6), 939–962.

Rouault, M. J., Mouche, A., Collard, F., Johannessen, J. A., Chapron, B., 2010. :Mapping the Agulhas Current from space: An assessment of ASAR surface current velocities. Journ. Geophys. Res 115, C10026, doi:10.1029/2009JC006050.

Rouault, M. J., Penven, P., 2011. :New Perspectives on Natal Pulses from satellite observations. Journ. Geophys. Res 116, C07013, doi:10.1029/2010JC006866.

Sadarjoen, I. A., Post, F. H., 2000. :Detection, quantification, and tracking of vortices using streamline geometry. Vis. Comp. Graph 24, 333 – 341.

Sadarjoen, I. A., Post, F. H., Ma, B., Banks, D. C., Pagendarm, H.-G., 1998. :Selective visualization of vortices in hydrodynamic flows, 419 – 422.

Saëtre, R., 1985. :Surface currents in the Mozambique Channel. Deep Sea Res. 32, 1457 – 1467.

Saëtre, R., da Silva, A. J., 1984. :The Circulation of the Mozambique Channel. Deep Sea Res. 31, 485 – 508.

Schott, F. A., Fieux, M., Kindle, J., Swallow, J., Zantopp, R., 1988. :The boundary currents east and north of Madagascar: 2 Direct measurements and model comparisons. Journ. Geophys. Res 93, 4963 – 4974.

Schott, F. A., McCreary, J. J. P., 2001. :The monsoon circulation of the Indian Ocean. Prog. Oceanog. 51, 1–123.

Schott, F. A., Xie, S.-P., Jr, J. P. M., 2009. :Indian Ocean Circulation and Climate Variability. Rev. Geophys. 47, 1–46.

Schouten, M. W., De Ruijter, W. P. M., van Leeuwen, P. J., 2002b. :Upstream control of Agulhas ring shedding. Journ. Geophys. ResDoi:10.1029/2001JC000804.

Schouten, M. W., De Ruijter, W. P. M., van Leeuwen, P. J., H, D., 2002a. :A Teleconnection between the equatorial and southern Indian Ocean. Geophys. Res. Lett 107, doi:10.1029/2001GL014542.

Schouten, M. W., De Ruijter, W. P. M., van Leeuwen, P. J., Lutjeharms, J. R. E., 2000. :Translation, decay and splitting of Agulhas rings in the south-eastern Atlantic ocean. Journ. Geophys. Res 105, 21,913–21,925.

Schouten, M. W., De Ruijter, W. P. M., van Leeuwen, P. J., Ridderinkhof, H., 2003. :Eddies and variability in the Mozambique Channel. Deep Sea Res., Part II 50, 1987–2003.

Shchepetkin, A. F., McWilliams, J. C., 2003. :A method for computing horizontal pressure gradient force in an ocean model with a non-aligned vertical coordinate. jgr 108.

Shchepetkin, A. F., McWilliams, J. C., 2005. :The regional oceanic modeling system (ROMS): a split-explicit, free-surface, topography-following-coordinate oceanic model. Ocean Modelling 9, 347–404.

Siedler, G., Rouault, M., Biastoch, A., Backeberg, B., Reason, C. J. C., Lutjeharms, J. R. E., 2009. :Modes of the southern extension of the East Madagascar Current. Journ. Geophys. Res 114, C01005.

Siedler, G., Rouault, M., Lutjeharms, J. R. E., 2006. :Structures and origin of the subtropical South Indian Ocean. Geophys. Res. Lett 33, L24609.

Soares, G., 1975. :Contribution a létude de le hydrologie et la circulation du Canal de Mozambique en hiver austral. These de Doctorat 3^{eme} cycle, Université, Paris V, 89pp.

Song, Y., Haidvogel, D. B., 1994. :A Semi-implicit Ocean Circulation Model Using a Generalized Topography-Following Coordinate System. Journ. Comput. Phys 115, 228–244.

Souza, J. M. A. C., Montegut, C. d., Le Traon, P. Y., 2011. :Comparison between three implementations of automatic identification algorithms for the qualification and characterization of mesoscale eddies in the South Atlantic Ocean. Ocean Sci 7, 317–334.

Stammer, D., 1997. :Global characteristics of ocean variability estimated from regional TOPEX/POSEIDON altimeter measurements. Journ. Phys. Oceanogr 27, 1743–1769.

Stramma, L., Lutjeharms, J. R. E., 1997. :The flow field of the subtropical gyre in the South Indian Ocean into the Southeast Atlantic Ocean: A case study. Journ. Geophys. Res 99, 14053 – 14070.

Sutyrin, G. G., Grimshaw, R., 2010. :The long-time interaction of an eddy with shelf topography. Ocean Modelling 32, 25–35.

Swallow, J., Fieux, M., Schott, F. A., 1988. :The boundary currents east and north of Madagascar 1: Geostrophic currents and transports. Journ. Geophys. Res 93, 4951 – 4962.

Swallow, J., Schott, F. A., Fieux, M., 1991. :Structure and Transport of the East African Coastal Current. Journ. Geophys. Res 93, 4951 – 4962.

Swart, N. C., Lutjeharms, J. R. E., Ridderinkhof, H., De Ruijter, W. P. M., 2010. :Observed characteristics of Mozambique Channel eddies. Journ. Geophys. Res 115, C09006, doi:10.1029/2009JC005875.

Tew-Kai, E., Marsac, F., 2009. :Patterns of variability of sea surface chlorophyll in the Mozambique Channel: A quantitative approach. Journ. Mar. Syst 77, 77–88, doi:10.1016/j.jmarsys.2008.11.007.

Thorpe, S. A., 1998. :Turbulence in the Stratified and Rotating World Ocean. Theoret. Comput. Fluid. Dynam 11, 171–181.

Tomczak, M., Godfrey, J. S., 1994. :Regional Oceanography: An Introduction. Bull. Amer. Meteor. Soc 2, 390.

Toole, M. J., Warren, B. A., 1993. :A hydrographical section across the subtropical South Indian Ocean. Deep Sea Res. 40 (10), 1973 – 2019.

Tsugawa, M., Hasumi, H., 2010. :Generation and Growth Mechanism of the Natal Pulse. Amer. Meteor. Soc. 40, 1597–1612.

UCLA, USGS, 2003. :Application of the Regional Ocean Modelling System (ROMS) to Water and Sediment Quality issues in the Southern California Bight. Tech. rep., The Coastal Center of the UCLA Institute of the Environment and The Coastal and Marine Geology Program U.S. Geological Survey, USA.

van Aken, H. M., Ridderinkhof, H., De Ruijter, W. P. M., 2004. :North Atlantic deep water in the south-western Indian Ocean. Deep Sea Res., Part I 51, 755–776.

Van Ballegooyen, R. C., Gründlingh, M. L., Lutjeharms, J. R. E., 1994. :Eddy fluxes of heat and salt from the southwest Indian Ocean into the southeast Atlantic. Journ. Geophys. Res 99, 14053–14070.

van der Werf, P. M., van Leeuwen, L. J., Ridderinkof, H., de Ruijter, W. P. M., 2010. :Comparison between observations and models of the Mozambique Channel transport: Seasonal cycle and eddy frequencies. Journ. Geophys. Res 115, CO2002, doi:10.1029/2009JC005633.

van Leeuwen, P. J., De Ruijter, W. P. M., Lutjeharms, J. R. E., 2000. :Natal Pulses and the formation of Agulhas rings. Journ. Geophys. Res 105, 6425–6436.

Veitch, J. A., Penven, P., Shillington, F. A., 2010. :Modelling equilibrium dynamics of the Benguela Current system. Ph.D. thesis, University of Cape Town.

Walker, N. D., Mey, R. D., 1988. :Ocean-Atmosphere heat fluxes within the Agulhas Retroflection region. Journ. Geophys. Res 93, 15474–15483.

Weeks, S. J., Shillington, F., 1996. :Phytoplankton pigments distribution and frontal structures in the Subtropical Convergence region south of Africa. Deep Sea Res., Part I 43, 739–768.

Weijer, W., De Ruijter, W. P. M., Dijkstra, H. A., van Leeuwen, P. J., 1999. :Impact of interbasin exchange on the Atlantic overturning circulation. Journ. Phys. Oceanogr 29, 2266–2284.

Weijer, W., De Ruijter, W. P. M., Sterl, A., Drijfhout, S., 2002. :Response of the Atlantic Overturning circulation to South Atlantic sources of buoyancy. Global. Plan. Change 34, 293 – 311.

Weimerskirch, H., LeCorre, M., Jaquemet, S., Potier, M., Marsac, F., 2004. :Foraging strategy of a top predator in tropical waters: great frigatebirds in the Mozambique Channel. Mar. Ecol. Prog. Ser 275, 297–308.

Weiss, J., 1991. :The dynamics of enstrophy transfer in two-dimensional hydrodynamics. Physica D 48, 273–294.

Wyrtki, K., 1971. :Oceanographic Atlas of the International Indian Ocean Expedition. National Science Foundation., Washington. DC, p. 531.

You, Y., 1997. :Seasonal variations of thermocline circulation and ventilation in the Indian Ocean. Journ. Geophys. Res 102, 10391–10422.

Vita

Issufo Halo

The details of my childhood are inconsequential.